Imaging Stars Through The Atmosphere

PETER GEORGE TUTHILL

CAVENDISH LABORATORY
CAMBRIDGE
and
CHURCHILL COLLEGE

September 1994

A dissertation submitted for the degree of Doctor of Philosophy in the University of Cambridge

Preface

Research presented in this thesis was carried out under the supervision of Professor John E. Baldwin between January 1991 and September 1994 at the Cavendish Laboratory, Cambridge. Except where clear reference is made in the text, the work presented is the author's own and no part of it has previously been submitted for any degree or qualification at any university.

This thesis does not exceed 60 000 words.

Peter Tuthill

September 1994

Acknowledgements

The world does not, in my experience, avidly devour astronomy Ph.D. theses, and despite their author's best intentions, usually only one page gets read. This is the page. So, before you flick through all the squiggles and numbers in the rest of this book, I will briefly stray into the human side of this work.

Professional Acknowledgements:
Many different people have been more or less directly involved in various aspects of the production of this thesis. First and foremost, I would like to thank John Baldwin and Chris Haniff for constant help, advice, supervision and encouragement. A number of other members of the COAST group, and of the university have also helped in various ways, and in particular I would like to mention Martin Beckett, Stuart Dalziel, Dave Green and Martin Oldfield. Organizations outside the university which have provided much assistance and useful information are the Royal Greenwich Observatory, the American Association of Variable Star Observers and the British Astronomical Association. In addition, I am extremely grateful for valuable data and discussions provided by Ken Nordsieck at the University of Wisconsin, Michael Scholz of the University of Heidelberg and Mike Feast of the University of Cape Town. I would also like to express my gratitude to the Cambridge Commonwealth Trust for the Packer Cambridge Scholarship which provided support during the course of this research.

Unprofessional Acknowledgements:
Here I find myself once again obliged to thank John Baldwin who has been almost as laid back as an Australian (what higher complement is there ?) and Chris Haniff for demonstrating that you don't have to be too serious to do something well (most famously with a roll of tinfoil and a flat cap). In addition, the rest of the COASTies and the Radio Astronomers have all made the Cavendish a good place to be. Long may the extended discursive friday afternoon COAST meetings in JB's sunny office endure!

My deepest thanks to my friends in Cambridge – they know who they are – without whom my sanity and my sense of humour might otherwise have found the going rocky; especially over the last few months. It was extremely reassuring to have the safe havens against the natives provided by Patty and Derek Pearce and also Alf Cousins. To Ob: thanks for everything, and most of all, for your smile. It would have been an infinitely paler world without you. Finally, most of all I thank my family, for putting up without me for the years it took to perform this work, for encouragement from afar and for generally being the best Mum, Dad and Brother anyone could wish for.

To my parents

VICTOR AND ELIZABETH TUTHILL

Contents

C.4 μ Cep 160

With us ther was a doctour of phisik
In al this world ne was ther noon hym lik,
To speke of phisik and of surgeyre,
For he was grounded in astronomye.

Geoffrey Chaucer
from 'The Canterbury Tales'

Chapter 1

Introduction

1.1 Perspective

How big is a Star ? What would one look like 'close up' ? These questions must predate the science of astronomy and yet have proved particularly tenacious as they are still not completely answered today.

The first experiment to measure a star's diameter (other than that of our own sun) was made by Galileo about 370 years ago. He suspended a fine cord vertically and measured the distance at which he had to stand from the cord so that it just occulted the image of the first magnitude star Vega. A brief account of the experiment is given in his *Dialogue concerning the Two Chief World Systems* and it is interesting to read how carefully it was done. Galileo concluded that the angular diameter of Vega was 5 seconds of arc. We now know that Galileo's result was roughly 1500 times too large, and it is instructive to understand why such a simple experiment gave the wrong answer. As was realized by Newton, the atmosphere does not allow images to pass through with perfect clarity – light is distorted causing the stars to appear blurred. Presumably Galileo's was not a measurement of the angular size of Vega, but rather was influenced by terrestrial effects, one of which was the local blurring due to the atmosphere (although diffraction around the string may also have played some role).

To Newton also goes the credit for making the first estimate of the angular size of a star which was close to modern accepted values. He argued that if one is prepared to assume that the sun is a body similar to the fixed stars, and if it were removed to a distance at which it appears as a first magnitude star, then its angular diameter would be about 2×10^{-3} seconds of arc. Remarkably (considering the difficulties involved), this is only about 30% smaller than modern estimates for Vega's diameter.

The next important development did not arrive until 1920, when Michelson and Pease made the first successful experimental measurement of the angular diameter of a star. Their method relied upon the interference of two beams of starlight collected at points separated in space (as first suggested by Fizeau 1868). With the 20 ft stellar interferometer on Mount Wilson, they were able to measure the diameters of a half-dozen cool giant and supergiant stars; however later attempts to extend the work to other stars and longer baselines failed. Discouraged by these difficulties, high resolution imaging languished until the 1960's and the novel intensity interferometry approach of Hanbury Brown and Twiss. In a series of classic experiments, the Narrabri Intensity Interferometer provided the first measurements of the sizes of a number of main-sequence stars. Observations were, however, limited to only the brightest stars.

Much of the recent explosion of interest in high resolution imaging can be traced to the early 1970's when the nature of images degraded by the atmosphere was first realized by Labeyrie (1970) to be an interference pattern formed by a randomly distorted wavefront – *i.e.* a *speckle pattern*. He suggested that speckle interferometry, a technique used in laser optics, could be used to retrieve high angular resolution information from short-exposure images. This technique was found to be highly successful, and is now widely used in the visible and infrared. The basic principle is fairly straightforward, and relies on exposures such as those shown in Figure ??, which are short enough to freeze the effects induced by the atmosphere. The sharp granular structure produced when light from a point source passes through the atmospheric phase screen (left panel) can be seen to be blurred when the light originates from an extended source (right panel). This blurred image can be considered as a set of sharp patterns, each due to light from a single point on the star, but slightly shifted before being added to the total.

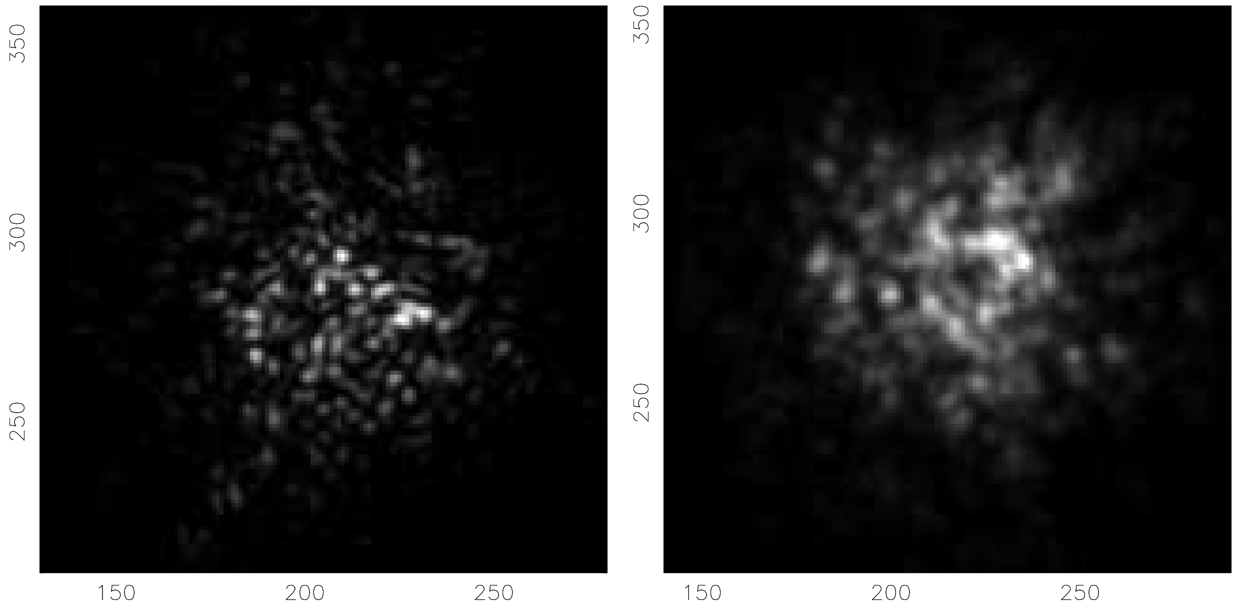

Figure 1.1: Short-exposure (10 msec) images taken whilst observing α Oph (left) and α Her (right). The wavelength of observation was 710 nm and the frames are $1.5''$ squares. Clear differences between the unresolved α Oph and the resolved α Her can be seen from 'speckle patterns' such as these without the aid of any image processing.

Modern developments encompass a range of techniques. In addition to interferometric methods mostly based on Michelson-Fizeau and speckle interferometry, other active fields of research currently include adaptive optics, heterodyne interferometry and space astronomy. Adaptive optics seeks to measure and rapidly correct wavefront distortions with the use of a flexible element (or 'rubber mirror') in the optical path. Heterodyne interferometry uses a laser as a reference beam in a way directly analogous to a local oscillator in modern radio telescopes. Meanwhile, more conventional interferometry has not stood still, with modern descendants of the Michelson-Fizeau interferometer achieving baselines measured in the hundreds of metres by linking separate telescopes into an array.

1.2 Introduction to Imaging

For a telescope operating with no atmospheric or optical aberrations, the theoretical angular resolution is set by the Rayleigh criterion:

$$\Omega = \frac{1.22\lambda}{D} \tag{1.1}$$

where Ω is the smallest angle (in radians) for which separate objects can be distinguished, λ is the wavelength of the light and D is the diameter of the primary mirror. At first sight, it might be thought that building telescopes with larger apertures would enable them to resolve smaller objects. For a large (5 m) modern telescope operating in the visible (500 nm) the diffraction limit set by Equation ?? is $0.025''$. In practice, even at good high-altitude sites the performance of such telescopes rarely exceeds $0.5 - 1''$, and is independent of the diameter of the mirror. This limitation in spatial resolution is imposed by atmospheric refractive index fluctuations or *seeing*. 'The seeing' can also be used to refer to the value of the atmospheric resolution limit.

Atmospheric turbulence and its relation to image quality has been the topic of much theoretical and experimental investigation in recent years. The 'standard model' for providing a statistical description of the wavefront distortions is based on two quantities. The first of these is Fried's parameter, usually denoted by r_0, and is the diameter of a circular aperture over which the root-mean-square (rms) variation in phase is one radian. The second parameter is a measurement of the atmospheric coherence time t_0, and although a number of different definitions exist, all provide an estimate of the evolutionary timescale of the wavefront distortions. Values of these spatial and temporal scales which are characteristic of seeing at a good site are $10 - 20$ cm and $10 - 20$ msec respectively for observations made in the visible. More detailed descriptions of astronomical seeing can be found in Chapter 5 and in the reviews by Roddier (1981) and Goodman (1985).

A number of methods for overcoming the seeing-induced distortions and recovering diffraction-limited performance have been devised. Those of interest here are mostly based upon the Michelson-Fizeau interferometer, but we also draw upon techniques from speckle interferometry and radio astronomy.

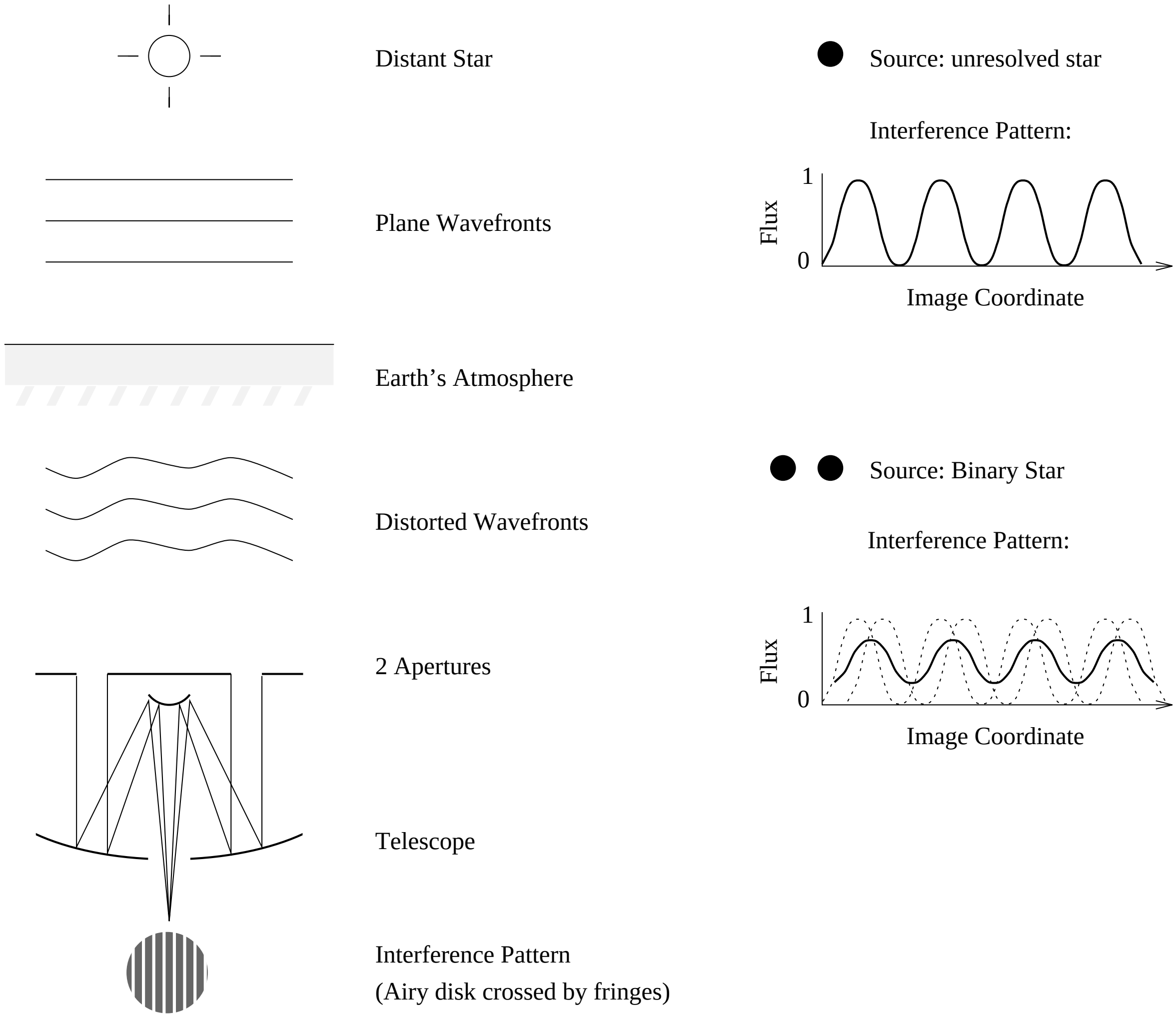

Figure 1.2: Cartoon demonstrating the Michelson-Fizeau interferometer (left). Plane wavefronts arriving at the atmosphere from a distant star are distorted by refractive index fluctuations. Light is collected from two spatially-separated apertures, and focused to form an image. This image will be an Airy disk from the circular apertures crossed by fringes due to interference between light arriving via the two different paths. For a single unresolved source (top right) the contrast in this pattern will be high. For a binary star, however, each component separately produces a high-contrast pattern but with a shift in phase between them (lower right). Summing these together, the net effect is to lower the contrast so that there are no longer regions in the image where the flux is zero. This loss of contrast or *visibility* indicates that the source is resolved.

High resolution information is preserved in short exposures taken with a Michelson-Fizeau interferometer (Figure ??). As was noted earlier for the speckle patterns of Figure ??, one of the most important features is the contrast in the image, with lower contrasts corresponding to more resolved objects. For sinusoidal patterns such as those shown for the Michelson-Fizeau interferometer in Figure ??, this can be measured quantitatively in terms of the *visibility amplitude* (hereafter simply denoted the 'visibility') defined as:

$$|V_b| = (i_{max} - i_{min})/(i_{max} + i_{min}) \tag{1.2}$$

where $|V_b|$ is the visibility on the baseline b (given by the vector separation of the two apertures) and i_{max} and i_{min} are the maximum and minimum intensities in the fringe pattern. Visibilities are important to interferometric imaging as they are directly proportional to the Fourier amplitudes in the transform of the true object flux distribution. A great deal of information about source morphologies such as diameters, profiles and separations of binary components can be recovered from the visibilities alone. For example, the experiments of Michelson, Hanbury Brown and Labyerie mentioned in the previous section all recovered only visibility information.

In addition to Fourier amplitudes, an ideal strategy would recover Fourier *phase* information as this is vital for unambiguous image reconstruction. The problem is to overcome the random fluctuations in phase induced at each telescope by the atmospheric turbulence. One technique for doing this has been borrowed from radio astronomy and relies on measuring a quantity known as the *closure phase*. Suppose that we have a set of three antennae 1, 2 and 3. The true (uncorrupted) instantaneous fringe phases measured on the three baselines between the antennae are ϕ_{12}, ϕ_{23} and ϕ_{31}, whilst the random wavefront errors induced by the atmosphere at each antenna are given by ϵ_1, ϵ_2 and ϵ_3. These error terms occur in pairs in the phase measured along each baseline between two antennae. Then the closure phase Φ_{123} is given by:

$$\begin{aligned}
\Phi_{123} &= \phi_{12} + \epsilon_1 - \epsilon_2 \\
&+ \phi_{23} + \epsilon_2 - \epsilon_3 \\
&+ \phi_{31} + \epsilon_3 - \epsilon_1 \\
&= \phi_{12} + \phi_{23} + \phi_{31}
\end{aligned} \tag{1.3}$$

which can be seen to be independent of the ϵ_i error terms. Note that it is necessary to have at least three antennae forming a closed loop of baselines to measure one single closure phase, thus two-aperture interferometers such as the original Michelson-Fizeau of Figure ?? cannot implement this technique. The way in which this closure quantity is used in the image reconstruction process is described in more detail later.

1.3 The Astronomy of Candidate Objects

The first objects to have their diameters measured interferometrically were not stars, but Jupiter's Galilean satellites and the minor planet Vesta. Close binary stars such as Capella also figured amongst the early successes. It was not until Michelson and Pease extended the baseline of their interferometer, by means of a steel beam supporting flat mirrors in front of their telescope, that they were able to measure the angular sizes of some cool giant and supergiant stars. Precisely the same constraints of resolution apply to our astronomical program for high-resolution imaging based on a four metre telescope, which forms much of the work presented in later chapters. This leads to the observations being restricted to exactly those categories of objects given above – namely solar-system objects (moons and minor planets), binary stars and very large cool stars. Although some binary stars were included in the astronomical program, most work has concentrated upon the latter category; cool giants and supergiants.

As a main sequence star ages, the hydrogen nuclear fuel which has sustained it becomes depleted in the centre. The mostly helium core shrinks and hydrogen burning accelerates in a surrounding shell. The stellar envelope then expands and the luminosity increases, both by many orders of magnitude; however, the temperature of the tenuous outer layers decreases which causes the spectrum to shift to the red. The star evolves away from the bulk of stars on the main sequence, and moves to regions on the HR diagram which are populated by red giants. Helium core burning, then helium shell burning succeed hydrogen during this relatively brief but eventful period in the star's lifetime. The study of two subsets of these stars – one occupying a region known as the Asymptotic Giant Branch (AGB) consists of the Mira Variables, whilst the other group are the Supergiants – forms a significant proportion of the work in the body of this dissertation.

Red giant stars have high luminosities over the sensitivity range of our detectors (500 – 900 nm), and have apparent diameters up to $\sim$ 50 milli-arcseconds (mas) – large enough to be resolved at the diffraction limit of a 4 m telescope. It is fortuitous that they also happen to exhibit a range of interesting yet poorly understood phenomena which are particularly amenable to study with high resolution methods. A number of these are outlined below.

One of the most direct measurements afforded by interferometry is that of an angular diameter. In addition to combining this with a distance estimate and thus arriving at the *physical diameter* of the star, it is also possible to obtain the *stellar temperature* (with the additional use of photometry data). The star's hot central core surrounded by the extended cool atmosphere results in another phenomena whose study may be addressed by imaging – *convection.* Most of the heat transport through the atmosphere is due to this, with large convective zones being sufficiently powerful to raise the local surface temperature thus causing 'hotspots' on the stellar disk. These provide the most popular explanation for the observed bright regions detected in high-resolution images. A further complicating factor in the atmospheres of many red giants, particularly those of lower ($\sim 1M_{\odot}$) mass, is *pulsation.* This is thought to be brought on by an instability known as the 'κ mechanism' involving the cyclic ionisation and deionisation of hydrogen and helium at certain layers in the atmosphere. It has been found to be possible to study aspects of stellar pulsation with interferometry and this is discussed at length in later sections. To the already complex picture of the extended atmosphere driven by pulsation and convection must be added the phenomena of *mass loss*, and the presence of dust plus molecular and atomic species both in the atmosphere and in the circumstellar environment. Monochromatic radial profiles which sample the stellar disk in various spectral features and in the continuum can go some way towards unravelling the puzzles posed in understanding such stars.

Evolved giants occupy a fairly important place in stellar and galactic evolution. The process of mass loss is responsible for the enrichment of the interstellar medium (ISM), and the formation of planetary nebulae. The mass loss process also 'defuses' a large number of potential supernovae and so has implications for the observed supernova rate. As this class of object contains some of the most luminous known stars, there is interest in their use as a yardstick for measuring the distance to distant galaxies in much the same way as is popular with variables of the Cepheid type. Finally, it is important cosmologically to account for mass processed through stars and into its resting place in the ISM or compact dwarf stars.

1.4 Overview

Subsequent chapters describe research associated with high angular resolution imaging of astronomical targets in the visible and near infrared regions of the spectrum. Interferometric methods, implemented both on a monolithic telescope and on separated-element telescopes, are considered. Topics ranging from instrumental design, experimental procedure, data analysis, observational results and the interpretation of the results in an astrophysically relevant context figure in the discussion.

Chapter 2 describes an imaging experiment performed on a number of occasions at the William Herschel Telescope (WHT). After a brief theoretical introduction of the basic principles, a full description of the experiment from the instrumentation through to the data analysis is given. Extensive discussion of the optimisation of the technique and experimental difficulties encountered follows, concluding with a section looking towards future improvements.

Chapter 3 gives a discussion of the results of the WHT experiments for one class of object known as Mira Variables. These are a type of Long Period Variable (LPV). The ramifications of the measurements for the astrophysics of these stars is investigated in detail – with the stellar pulsations, effective temperatures, brightness profiles, surface structures and other atmospheric behaviours all coming under scrutiny.

Chapter 4 treats those results from stars in the supergiant class obtained during the WHT imaging experiments. Much of the discussion in this case centres around the surface morphologies of these stars and interpretations of the origins of image structure. Following this, further evidence is drawn from polarimetry measurements taken over a period concurrent with the imaging observations.

Chapter 5 concerns the seeing and its effect upon high-resolution imaging. The contribution to image motion from instrumental effects and from the atmosphere, as well as the likely improvement to the long-exposure image quality for tip-tilt guided images are discussed. The results of algorithms designed to obtain diffraction limited performance are presented and compared. Finally, the design and results of a Hartmann-type wavefront sensor dedicated to the study of the atmosphere are given.

Chapter 6 describes the Cambridge Optical Aperture Synthesis Telescope (COAST). As this instrument was at a developmental stage throughout the course of the work presented here, aspects discussed are of a more practical nature associated with the instrumentation.

Chapter 7 briefly summarizes the major conclusions of this work and points out, where appropriate, future directions for research.

Appendix A contains a summary of all observations of giant stars, along with the results of fitting uniform-disks and Gaussian profiles to the data.

Appendix B gives results and raw data concerning the morphologies and surface structures of a number of LPV's. To be included, stars had to be moderately resolved (> 30 mas) and to have yielded at least some data of sufficient quality for an analysis of the morphology to be made.

Appendix C gives results and raw data concerning the morphologies and surface structures for all supergiants observed.

Others with Optick Tubes the Moons scant face
(Vaste Tubes, which like long Cedars mounted lie)
Attract through glasses to so neer a space,
As if they came not to survey but prie.

Nine hasty Centuries are now Fulfill'd,
Since Opticks first were known to Astragon;
By whom the Moderns are become so skill'd,
They dream of seeing to the Maker's Throne.

Sir William D'Avenant (1606–68)
from 'Gondibert'

Chapter 2

Aperture Masking at the WHT

2.1 Introduction

The basic problem in high-resolution astronomical imaging is to recover the object intensity distribution $O(\underline{x})$, given that the actual intensity pattern one measures $I(\underline{x})$ has been corrupted by the passage of the light through an inhomogeneous medium. As was mentioned in Chapter 1, one method for achieving this relies on the analysis of very short exposure images. We start by making the approximation that the object is small enough so that light emitted from all points on it suffers essentially identical aberrations, *i.e.* it is *isoplanatic*. For conditions relevant here, this region was typically a few arc-seconds in size, and as all the objects observed were much smaller than this, the assumption of isoplanatism was almost certainly valid.

The short-exposure intensity pattern $I(\underline{x})$ may be represented as the convolution of the object intensity pattern $O(\underline{x})$ with the instantaneous point-spread function for the atmosphere-telescope combination $\tau(\underline{x})$:

$$I(\underline{x}) \;=\; O(\underline{x}) * \tau(\underline{x}) \tag{2.1}$$

$I(\underline{x})$ is often referred to as a 'speckle pattern' and in the case where $O(\underline{x})$ is an unresolved source, simply reduces to a measurement of the point-spread function $\tau(\underline{x})$. Following the approach of Labyrie (1970), we take a Fourier transform of 2.1 giving:

$$\hat{I}(\underline{f}) \;=\; \hat{O}(\underline{f}) \,.\, \hat{\tau}(\underline{f}) \tag{2.2}$$

where $\underline{f}$ is a reciprocal co-ordinate to the angular sky co-ordinate $\underline{x}$. The power spectrum is computed and averaged over many short exposures to enhance the signal-to-noise ratio:

$$\left\langle |\hat{I}(\underline{f})|^2 \right\rangle = |\hat{O}(\underline{f})|^2 \left\langle |\hat{\tau}(\underline{f})|^2 \right\rangle \tag{2.3}$$

If we obtain $\left\langle |\hat{\tau}(\underline{f})|^2 \right\rangle$ from observations of an unresolved star, Equation 2.3 then provides an estimate of the power spectrum $O(\underline{x})$. For simple sources such as binary stars, this information is enough to determine important parameters such as the separation, flux ratio and position angle (with a 180° ambiguity) of the stars. However, unambiguous image reconstruction is generally not possible since Fourier phase information is lost in taking the squared modulus of the image transform.

Many schemes have been devised to recover both phase and amplitude information from speckle interferograms; two of the most developed of these are the Knox-Thompson method (Knox and Thompson 1974, Knox 1976) and Speckle Masking, originally proposed by Weigelt (1977). These schemes rely upon higher-order moments of the image transform, such as the second order cross-spectrum in the case of the Knox-Thompson method. Speckle Masking extracts phase information from the third order moment, also known as the triple product or the *Bispectrum*:

$$\left\langle \hat{I}(\underline{f}_1)\hat{I}(\underline{f}_2)\hat{I}^*(\underline{f}_1+\underline{f}_2) \right\rangle = \hat{O}(\underline{f}_1)\hat{O}(\underline{f}_2)\hat{O}^*(\underline{f}_1+\underline{f}_2) \left\langle \hat{\tau}(\underline{f}_1)\hat{\tau}(\underline{f}_2)\hat{\tau}^*(\underline{f}_1+\underline{f}_2) \right\rangle$$

where $\left\langle \hat{\tau}(\underline{f}_1)\hat{\tau}(\underline{f}_2)\hat{\tau}(\underline{f}_1+\underline{f}_2) \right\rangle$ is the 'bispectral transfer function'. These methods need not be examined in detail here (for reviews see Dainty 1987 or Roddier 1988); however, it should be pointed out that the extraction of phase information from the bispectrum is entirely analogous to the concept of closure phase mentioned in Chapter 1.

The majority of theoretical studies of speckle imaging have concentrated on the photon-starved regime in order to ascertain the fundamental limitations of image reconstruction techniques. For bright objects in the visible or near-IR, these conditions rarely apply since the dominant noise contribution arises not from statistical photon fluctuations but rather from atmospherically induced noise. One way to reduce the atmospheric noise contribution to the measurements is to mask off large portions of the pupil, recording interferograms formed only from selected parts. This technique is referred to as *aperture masking.*

At first sight it might seem counterproductive to use pupils which collect only a small fraction of the light incident upon the primary mirror and therefore measure a correspondingly small fraction of the available Fourier information. However, theoretical investigations of the performance of masking schemes (see *e.g.* Readhead 1988), along with recent analyses based largely on numerical simulations (Haniff and Buscher 1992, Buscher and Haniff 1993), indicate that such observing configurations can compare favourably with fully-filled aperture schemes under a range of conditions. In situations where dense Fourier coverage is not required (for 5 m class telescopes in the visible, this includes all extra-solar system objects), the masked pupil geometries can offer significant advantages such as:

1. reduced atmospheric noise;

2. improved resistance to seeing variations which affect the fidelity of the calibration of the atmospheric transfer function;

3. less stringent requirements on detectors for high count rates or frame readout times.

Further arguments about the benefits of various pupil geometries will be presented later. However, as will be explained in the next section, the overriding argument in favour of a masked pupil was a practical one based on the capabilities of the detector and data archival system.

2.2 The Experiment

High angular resolution imaging experiments were carried out at the 4.2 metre William Herschel Telescope (WHT) on the island of La Palma. The main optical components are shown schematically in Figure 2.1. This equipment was mounted on an optical table in the Ground Based High Resolution Imaging Laboratory (GHRIL), a purpose-built facility supported at one of the $f/11$ Nasmyth foci.

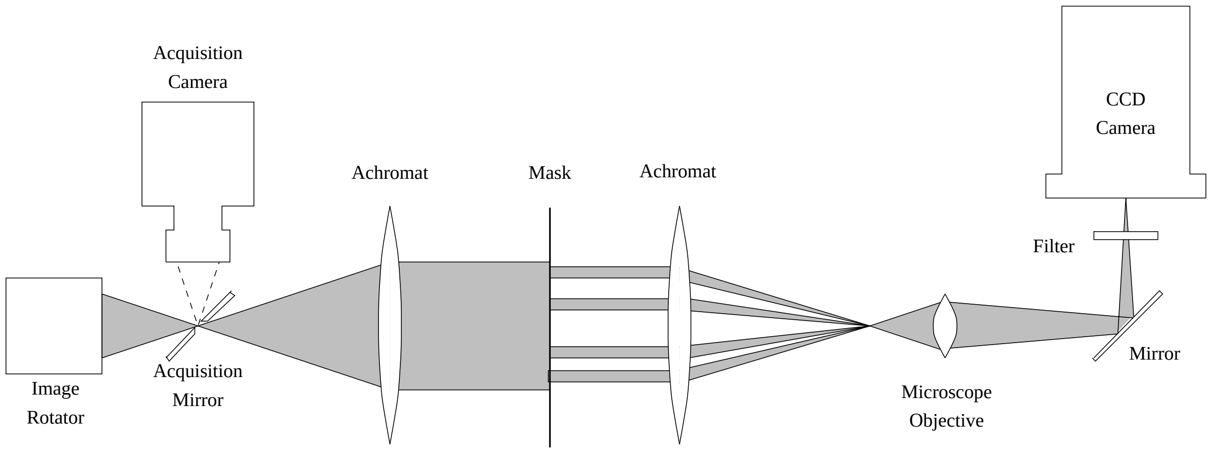

Figure 2.1: Schematic diagram of optical layout for high-resolution imaging.

Before arriving at the Nasmyth focus, starlight passed through an image rotator mounted on the elevation bearing of the telescope. At focus, a polished plate with a small hole was positioned on the optical axis of the apparatus so that non-axial light was sent into a video camera, providing an acquisition field. The telescope pointing was fine-adjusted until the optical axes of the starlight and the imaging apparatus were coincident. Light then passed through the hole and onto an achromat ($f = 300\,\mathrm{mm}$), which re-imaged the primary mirror demagnified to a diameter of 27mm. Aperture masks fabricated from thin aluminium sheet were placed in the parallel beam beyond this achromat. An image was formed by a second achromat, which, after magnification by a $\times 10$ microscope objective and wavelength selection by a narrow-band interference filter, was finally recorded on a cooled Charged Couple Device (CCD). The intensity pattern at the detector was an Airy disk crossed by interference fringes, the detailed nature of which depended upon the pupil mask used.

Both the interference filter and the aperture mask could be changed quickly to allow the observing configuration to be adapted to varying sources and conditions. The image scale on the CCD was set so that the longest baselines possible in the mask plane formed fringes which were sampled by the detector at about 3.5 pixels per fringe. The field-of-view of the CCD then corresponded to approximately 3 seconds of arc on the sky.

Although CCD's have low read noise and high quantum efficiency, they are not popular as detectors for speckle interferometry due to the long time required to read a sufficiently large two-dimensional area (up to several seconds for 300×300 pixels). Such a two-dimensional readout, however, was not required in this case, as the aperture masks only passed one-dimensional high resolution information. During the initial alignment of the system, it was arranged that this dimension was perpendicular to the transfer columns on the CCD. This enabled the recorded signal to be compressed into a single row of pixels by on-chip binning; this row could then be read out normally. Whilst this procedure preserved all the important high-resolution information in the image, it was possible to reduce the readout time so that exposure times of around t_0 could be attained.

Typically, observations were made with the camera taking around 100 exposures per second continuously over 5 to 10 second periods. About 5 such datasets, each consisting of over 500 one-dimensional exposures, were recorded on the source object. The telescope was then pointed to a nearby unresolved star where a similar amount of data was collected. There was an inevitable lag of about two minutes between the observations of the target object and the point-source. The image rotator was then moved to sample a different position angle on the sky, and the data acquisition procedure repeated. Two-dimensional coverage of the Fourier plane was built up in this fashion, with data usually being taken at six or nine evenly spaced position angles. A total of some 15 000 to 30 000 independent 1-dimensional exposures, usually requiring about 45 minutes of telescope time to collect, formed the total for one observation. Conventional two-dimensional speckle interferometry often relies upon some tens or hundreds of

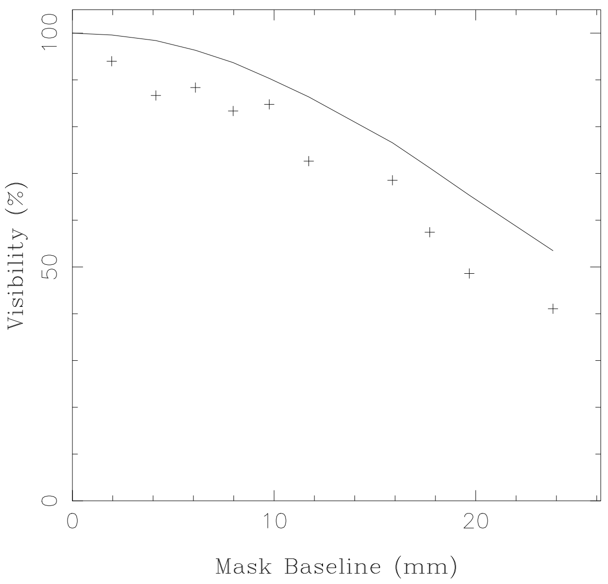

Figure 2.2: Visibility data (crosses) were obtained whilst observing a 5 micron pinhole illuminated by a tungsten lamp. The solid line is a plot of the theoretical visibility curve expected at 700 nm given the optical setup. This predicted curve also includes the effects of two processes which lower the measured visibility: the non-zero (10 nm) bandpass of the filter and the loss of visibility due to sparse fringe sampling. These are both more significant at longer baselines.

specklegrams to reconstruct an image and thus is not able to gain such good statistical isolation from atmospheric noise.

A useful test of the quality of the optical train is to measure the loss of coherence whilst observing a known laboratory reference source. This was done for all the filters and aperture masks used. Typical data are presented in Figure 2.2, where it can be seen that the measured visibilities fall some 10% lower than the theoretical ideal. This loss of coherence is probably due to slight aberrations, mis-alignments and defocus in the optical system.

2.3 Data Processing

Data acquired at the telescope were saved onto magnetic tape for transport and subsequently analyzed in Cambridge. Figure 2.3 shows two typical datasets. One-dimensional exposures

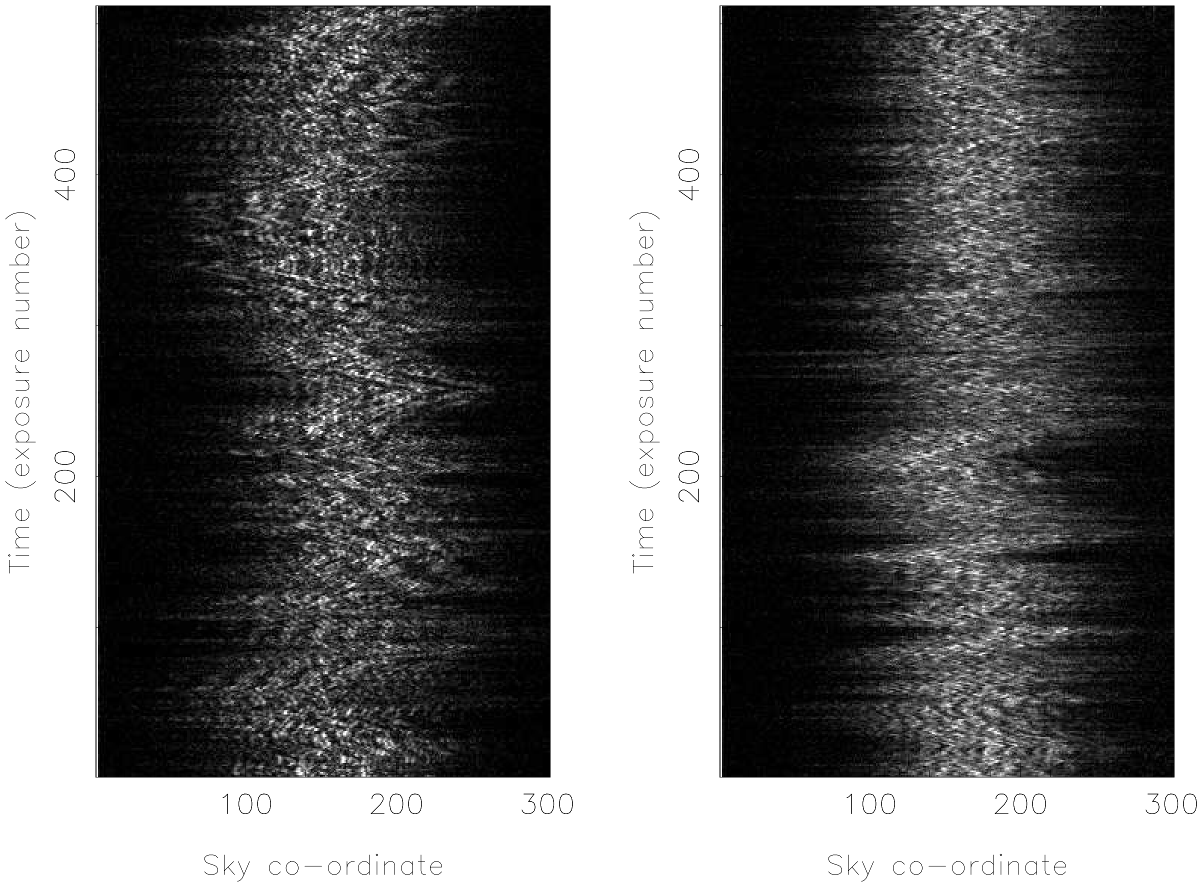

Figure 2.3: Time-series of 512 one-dimensional speckle exposures taken at 710nm observing α Oph (left) and α Her (Right) with a five-hole aperture mask. The exposure time was 17 msec, whilst the width of each frame corresponds to approximately $3''$ on the sky.

are stacked vertically to give a time sequence, with the wander of the centroid arising from the seeing and telescope tracking errors. As with the speckle exposures in Chapter 1, the relative lack of power at high spatial frequencies for α Her, as compared to the point-source α Oph, can be discerned visually in the raw data. For each dataset, the mean power spectrum was accumulated by summation of the squared modulus of the Fourier transform of each one-dimensional specklegram. The resultant power spectra are shown in Figure 2.4.

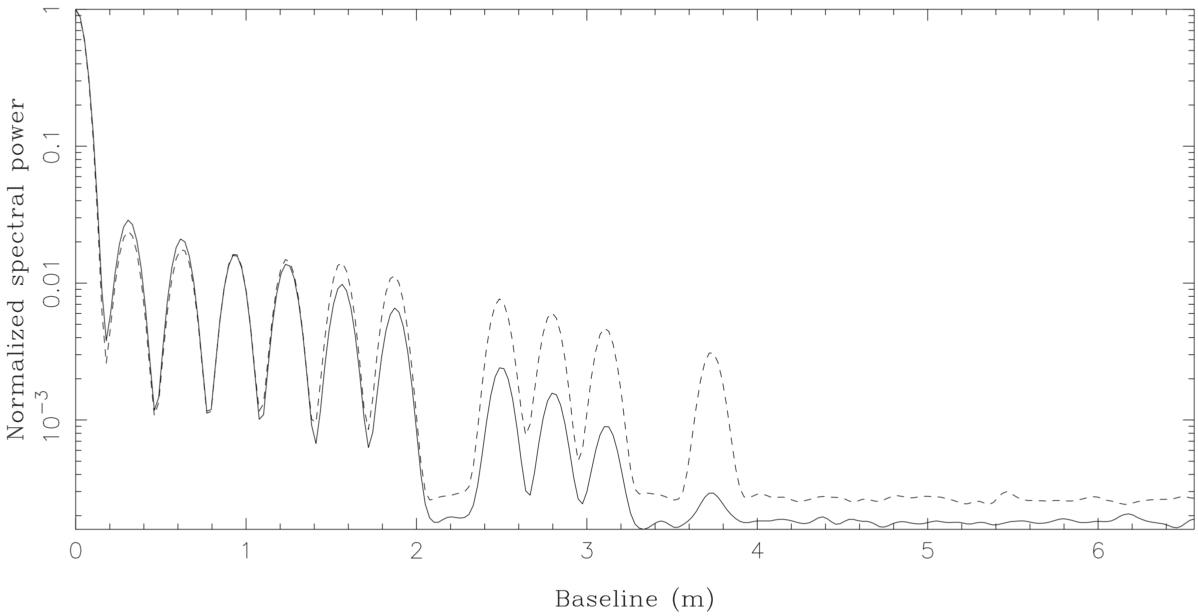

Figure 2.4: Power spectra of five-hole mask data at 710nm observing α Her (solid line) and α Oph (broken line). The flat noise floor beyond the tenth peak is due to a combination of readout and photon noise.

The ten peaks evident in the power spectra of Figure 2.4 correspond to the spatial frequencies in the fringe pattern arising from each pair of holes in the mask (see Figure 2.9 for a diagram of the mask). In this case, five holes yield 10 such baselines. The heights of the peaks in the power spectrum of α Oph exhibit a gradual decline at longer baselines due to the combined effects of atmospheric fluctuations and other coherence losses. The more rapid decline in power for α Her indicates that, in this case, sufficiently long baselines are present to sample regions where the visibility function has diminished, *i.e.* this star has been *resolved.* Visibilities were extracted from power spectra with the use of the formula:

$$V_f \;=\; N_h \left(\frac{P_f \;-\; P_{noise}}{P_0 \;-\; P_{noise}} \right)^{\frac{1}{2}} \tag{2.4}$$

where V_f is the visibility on the baseline yielding a peak of power P_f at spatial frequency f. The number of holes in the mask is N_h, whilst P_0 and P_{noise} are the values of the power spectrum at the origin and at the 'noise floor' (beyond the last baseline) respectively. This formula accounts for the systematic bias in the visibility estimates due to the (assumed flat or 'white') photon and readout noise processes.

Given that the point-source object was truly unresolved on even the longest baselines, its loss in visibility could be taken as a measurement of the coherence loss inherent in the atmosphere-telescope combination. Thus, it was possible to calibrate the 'target star' data by using the 'point source' data to provide an estimate of the mean system transfer function. A number of factors affected the fidelity of this calibration, most notably changes in the seeing due to the time lag and elevation difference when slewing from the 'target' to the 'point source'. Further factors associated with the change in optical trajectory and pupil geometry which occur when the telescope pointing is changed will be discussed in more detail in Section 2.7.

Closure phases were found by taking the arguments of the triple products of complex amplitudes. As for the visibilities, these were averaged over all the one-dimensional exposures to reduce the contribution from atmospheric noise. The theoretical treatment of Wirnitzer (1985) has been used to correct for the bias terms that are important at low photon rates. Usually the closure phases determined from observations of the 'point source' were, to within their errors, zero, as would be expected from an unresolved (or any other symmetrical) flux distribution. Thus it was not necessary to calibrate the 'target' closure phases. However on a few occasions the 'point source' closure phases were large, probably due to interference affecting the CCD electronics or to problems with the pupil geometry (Section 2.7).

Having reduced the raw data to a set of visibilities and closure phases, there were a number of ways of extracting astrophysically useful information. Diffraction-limited images could be produced by simple Fourier inversion of the visibility data; however, there are a number of highly developed algorithms to perform this mapping in such a way as to minimize spurious artefacts such as sidelobes arising from the non-uniform and noisy sampling of the Fourier plane. One of the most popular of these, known as the 'Maximum Entropy Method' (MEM) was used (Gull & Skilling 1984). As the experiment measured only relative phases, the particular implementation of MEM involved an iterative procedure developed for radio astronomy VLBI (Sivia 1987). Briefly, the steps are outlined below:

1. start with a model map (usually a point-source);
2. assign phases to the Fourier amplitudes which are consistent with the closure phase measurements and simultaneously produce a best fit to the model map phases;
3. invert and implement MEM to produce a map;
4. use the output of step 3 as the model map for step 2. Iterate steps 2–4 until the resultant map has phases and amplitudes which agree with the measurements to within the experimental errors.

Figure 2.5 illustrates the results of this procedure (hereafter simply referred to as 'MEM') for the binary star β Del.

In addition to providing an important sanity check on the performance of the entire system, binary stars such as this also served an important function in the calibration of the data. The orientation and scale of maps were not known precisely, since they were sensitive to details which were hard to measure precisely, such as the focal lengths and positions of lenses. At least

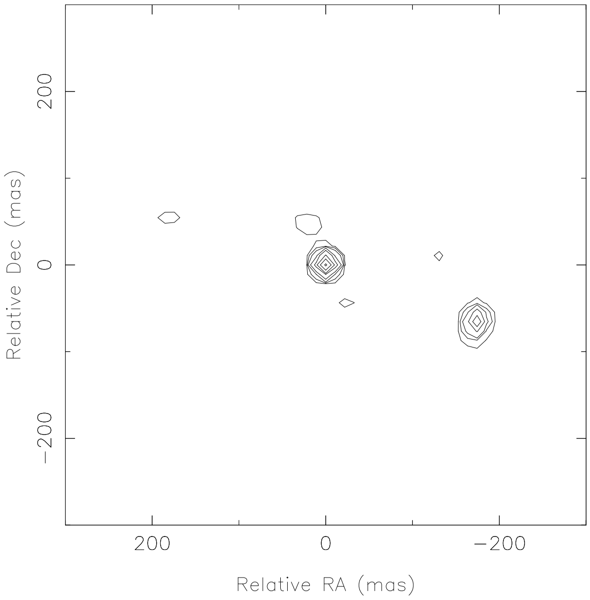

Figure 2.5: MEM reconstruction of the close binary β Del from aperture masking data at 710 nm. North is to the top, and East is to the left. The map has contour levels of 0.3, 1, 2, 5, 10, 20, 50 and 90%.

one binary star of known orbit was observed on each night. The result could then be compared with the expected position angle and separation computed from tabulated orbital parameters, thus enabling calibration of all maps from that night.

Although diffraction-limited maps produced by MEM were useful for qualitative interpretation, quantitative results were obtained by the fitting of models directly to the measured Fourier data. For example, Figure 2.6 illustrates the fitting of a radial profile to some visibility data. In addition to the uniform-disk model, Gaussian functions, limb darkened disks or other arbitrary model distributions could be fitted.

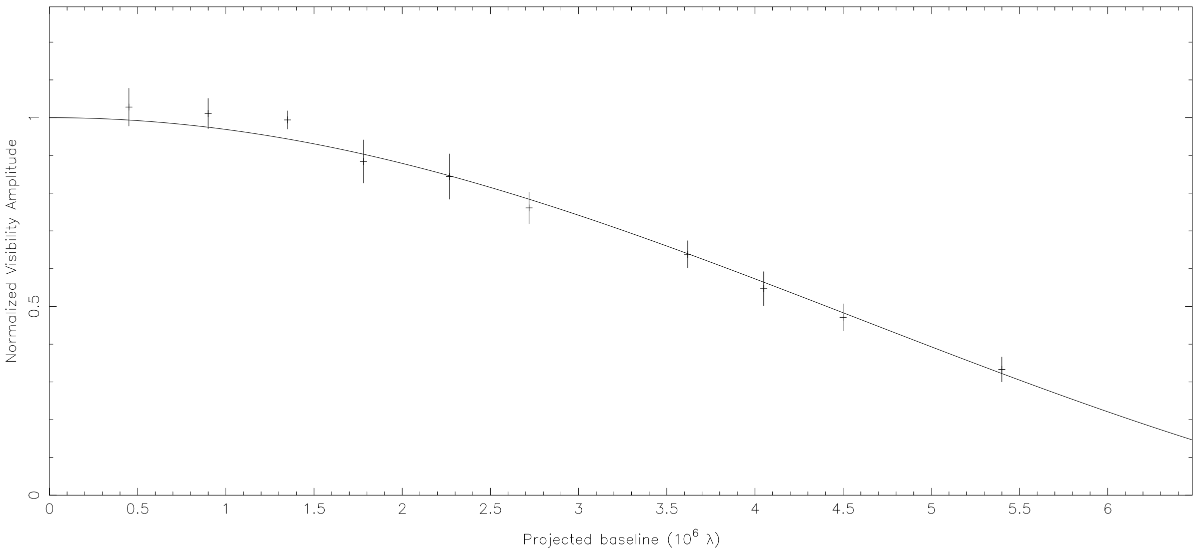

Figure 2.6: Visibility data for χ Cyg at 700 nm, averaged over all position angles. The solid line is the best-fitting uniform-disk model (diameter = 33 mas).

The fitting of models more complex than those with circular rotational symmetry was often suggested by examining the MEM-generated map as well as the bispectral data themselves. Asymmetries could by broadly classified into two groups: ellipticities and bright features. Elongation or ellipticity of the stellar disk was indicated in the data by modulation with position angle of the visibility at a fixed baseline length, whilst all the bispectral phases remained small. In those cases where the bispectral phases exhibited systematic departures from zero, more complex brightness distributions were indicated, for example: that produced by a bright feature located away from the center of an otherwise uniform-disk. Further discussion of modelling of the data will be given in Sections 3.2 and 4.2

2.4 Signal-To-Noise Considerations

To optimise the observing configuration, a series of trade-offs must be made. The diffraction limit of the telescope improves at shorter wavelengths, however both the detector sensitivity and the seeing deteriorate. More photons are collected as the bandwidth of the interference filter is increased, but narrow bands are desirable to investigate the behavior of the stellar atmospheres in various molecular transitions. In this section, we will be concerned with the signal-to-noise properties of measurements made with the CCD, particularly in relation to the pupil geometry.

For the accurate evaluation of system performance, it is vital to understand the sources of noise and their relative effect on the measurements. As Section 2.7 discusses some of the major sources of systematic error, for the present let us restrict our attention to random noise processes. The three most important of these are photon shot noise, detector readout noise and atmospheric noise. In order to weigh the benefits of various pupil geometries, it is helpful to make use of a simplified atmospheric model in which the telescope aperture is divided into a large number of sub-pupils, each of diameter $\lesssim r_0$. The distortions due to atmospheric turbulence are assumed to be constant in phase across each sub-pupil, but to vary randomly between sub-pupils and between exposures. Excellent introductions to this heuristic description may be found in the reviews of Roddier (1981) and Goodman (1985). Each pair of sub-pupils can be considered to be a Michelson interferometer generating fringes at that spatial frequency defined by the vector separation of the apertures. If more than one pair of sub-pupils contribute to the same spatial frequency in the image (*i.e.* if the sub-pupils have the same vector separation), then the pupil is said to be *redundant*. The redundancy R of the baseline is given by the number of times it is repeated.

Considering two noise processes, atmospheric and readout noise, the signal-to-noise ratio (SNR) for power spectrum measurements is given by (Roddier 1987; Nightingale 1991):

$$SNR \; = \; \frac{N_0^2 R}{N_0^2 R \; + \; \sqrt{2}\sigma^2 N_{pix}} \tag{2.5}$$

where the readout noise is assumed to give σ electrons per pixel over the array of N_{pix} pixels, and N_0 is the number of photons per sub-pupil per exposure. In the case where readout noise dominates (*e.g.* at low light levels), this reduces to:

$$SNR = \frac{N_0^2 R}{\sqrt{2}\sigma^2 N_{pix}} \tag{2.6}$$

The expression for the SNR, where photon shot noise and atmospheric noise constitute the important noise processes, is given below for a pupil with A sub-apertures (Buscher & Haniff 1993):

$$SNR = \frac{N_0 R/A}{1 + N_0 R/A} \tag{2.7}$$

For faint sources we neglect the contribution due to atmospheric noise so that the equation simplifies to:

$$SNR = \frac{N_0 R}{A} \tag{2.8}$$

It is important to bear in mind that these equations represent the signal-to-noise of a single power spectrum measurement and do not take into account a number of factors influencing the quality of the reconstructed image, such as the coverage of the Fourier plane afforded, or the quality of the bispectral phase information. Given that the flux per coherent patch N_0 is fixed for a given star, the SNR in the read-noise limited case is simply proportional to R. The more redundancy a given baseline has, the higher will be its signal-to-noise. Equation 2.8 yields a slightly different result for the photon noise limited case – the SNR will still improve in proportion to the redundancy, but *only* if this extra redundancy does not come at the cost of extra area in the pupil. Under these conditions, the best configurations are those that maximize the ratio of redundancy to total area.

In order to understand the implications of these ideas for the design of the pupil, consider the diagrams of Figure 2.7 (adapted from Buscher & Haniff 1993). In extending the mask from the non-redundant (a) to the redundant (b) configuration, the increased redundancy would be beneficial in a readout-noise limited system, however the area has increased with the redundancy and the SNR would not improve in the photon-noise limited case. The way to increase the redundancy more quickly than the area and thus improve the shot-noise limited SNR is demonstrated in (d), however the slit configuration is only beneficial in cases where the baseline is intermediate or short with respect to the slit length. When the baseline is long as in (c) the slit is worse than (a) or (b). Chevron masks (or the 'VI' encountered later) as in (e) perform poorly, especially with respect to photon noise. Buscher and Haniff (1993) also present signal-to-noise arguments similar to those above, but applied to closure phase measurement, which support these general conclusions as to the relative merits of the various pupil geometries.

It was important to determine into which of the noise regimes, readout noise or photon noise limited, the imaging experiment fell. Measurements of the noise properties of the apparatus,

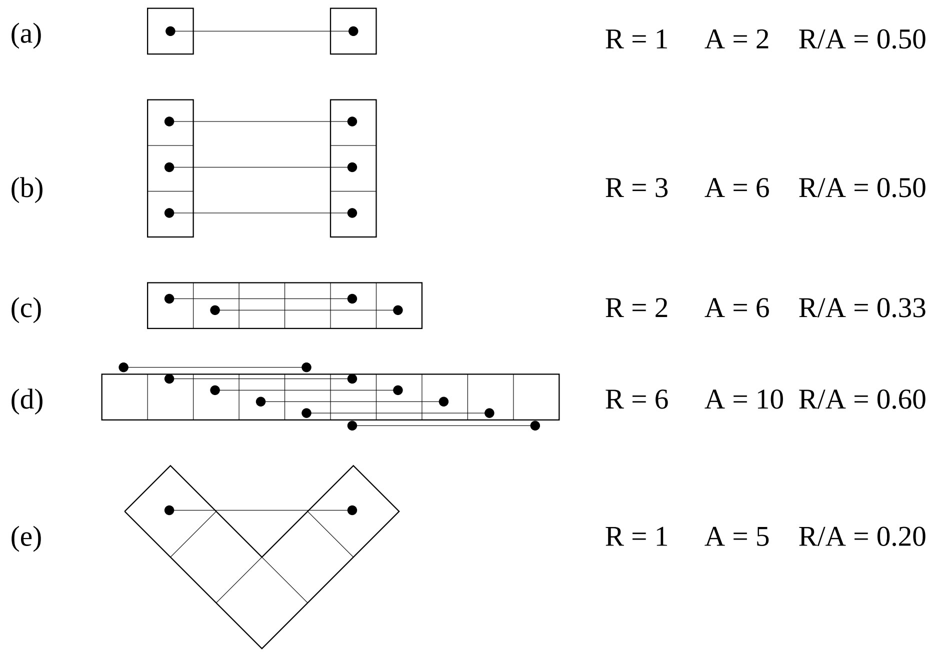

Figure 2.7: Schematic diagrams of some pupil geometries. Multiple copies of a given baseline are represented by joined dots. The baseline redundancy R and the pupil area A are given, along with the ratio R/A.

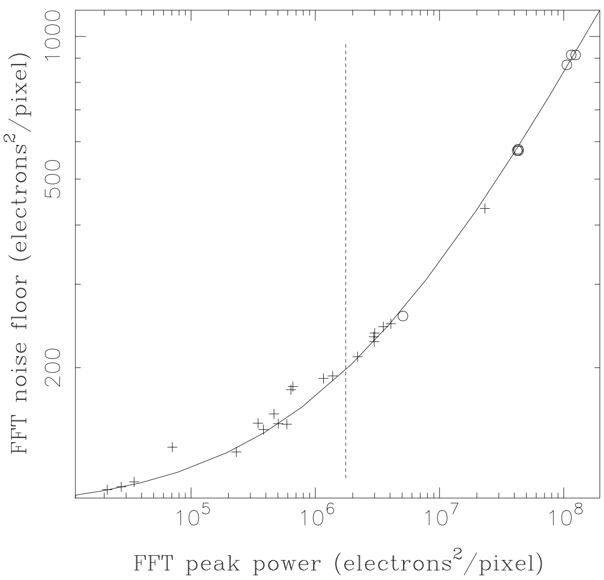

Figure 2.8: Noise floor plotted against peak for power spectra of datasets taken with non-redundant (crosses) and slit (circles) pupils. The fitting curve is of the form $Noise = A + B\sqrt{Pwr}$ where A is the dark noise associated with the CCD electronics and the $\sqrt{Pwr}$ term arises from photon noise. The constant of proportionality B is not equal to one if there are departures from uniformity in the detector sensitivity. To the left of the vertical dashed line readout noise dominates, whilst to the right statistical photon fluctuations are more important.

based on observational data, are shown in Figure 2.8. It is interesting to note that the fitted noise curve in Figure 2.8 not only yielded an estimate of the CCD readout noise ($A = 2.55 \times 10^4$ corresponding to about 10 electrons per pixel), but also a measure of uniformity of the detector. A uniform detector would give $B = 1$, however $B = 1.19$, gave a superior fit in this case. This indicates the presence of extra power in the specklegrams which may arise from sensitivity variations in the chip's active surface, or from aberrations in the instrumental optical path. It is common astronomical practice to divide this out using a uniformly illuminated test image. In this case, however, such 'flat fielding' is unnecessary as it is, in essence, performed in the process of calibration with an unresolved reference star.

It is clear from Figure 2.8 that our observations spanned a range over which the readout amplifier noise was dominant (for low count rates) through to a regime where photon fluctuations dominated the noise. For many of the observations, contributions from these two processes were roughly equal, and it should be noted that most observations which fell well into the shot-noise dominated regime were made with a slit pupil which allowed many more photons to pass than if non-redundant masks (NRM) were used.

2.5 Choice of Aperture Mask

Using the results from the previous section, a discussion of the appropriate choice of a practical pupil geometry for making various astrophysical observations is now given. A number of different masks used are depicted in Figure 2.9. There were a number of considerations related to the design of the 4- and 5-hole masks. In order to be truly non-redundant, the length of the shortest baseline had to be twice the diameter of the holes (*i.e.* the edges of the closest holes had to be separated by one diameter). This led to the diameter of the holes in the 5-hole mask being half that of the 4-hole mask. Additional aims in order to optimise the Fourier coverage were the measurement of the longest possible baselines passed by the pupil and the sampling at nearly even intervals out to that value.

The WHT pupil does not allow complete freedom in the design of an aperture mask (see Figure 2.9). There is a relatively large central obstruction due to the secondary mirror, and also the silhouette of the support struts known as the 'spider'. The secondary shadow makes the 4- and 5-hole non-redundant masks difficult to fit along the central axis of the pupil whilst maintaining even sampling and non-redundancy; for this reason the 'off-axis' versions were created.

Bearing in mind the noise limitations of the detector and the SNR Equations 2.6 and 2.8, we are now in a position to discuss the relative merits of the pupil geometries presented in Figure 2.9. Firstly we consider the off-axis versions of the non-redundant masks. Although they were designed for easier fitting into the pupil, the location of the holes proved to cause further problems with the pupil geometry (detailed later in Section 2.7) and they were dropped from use. The axial version of the 4-hole mask was also not favoured as it did not sample the longest baselines and was difficult to position accurately enough to avoid clipping of the

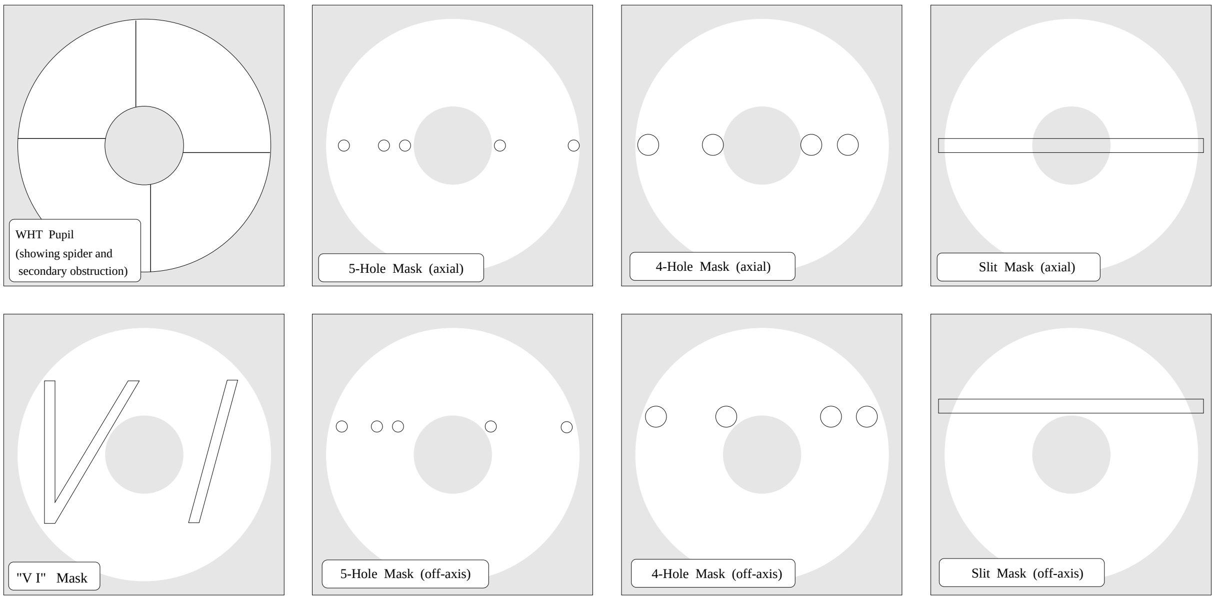

Figure 2.9: Aperture masks, shown slightly (20%) larger than life size.

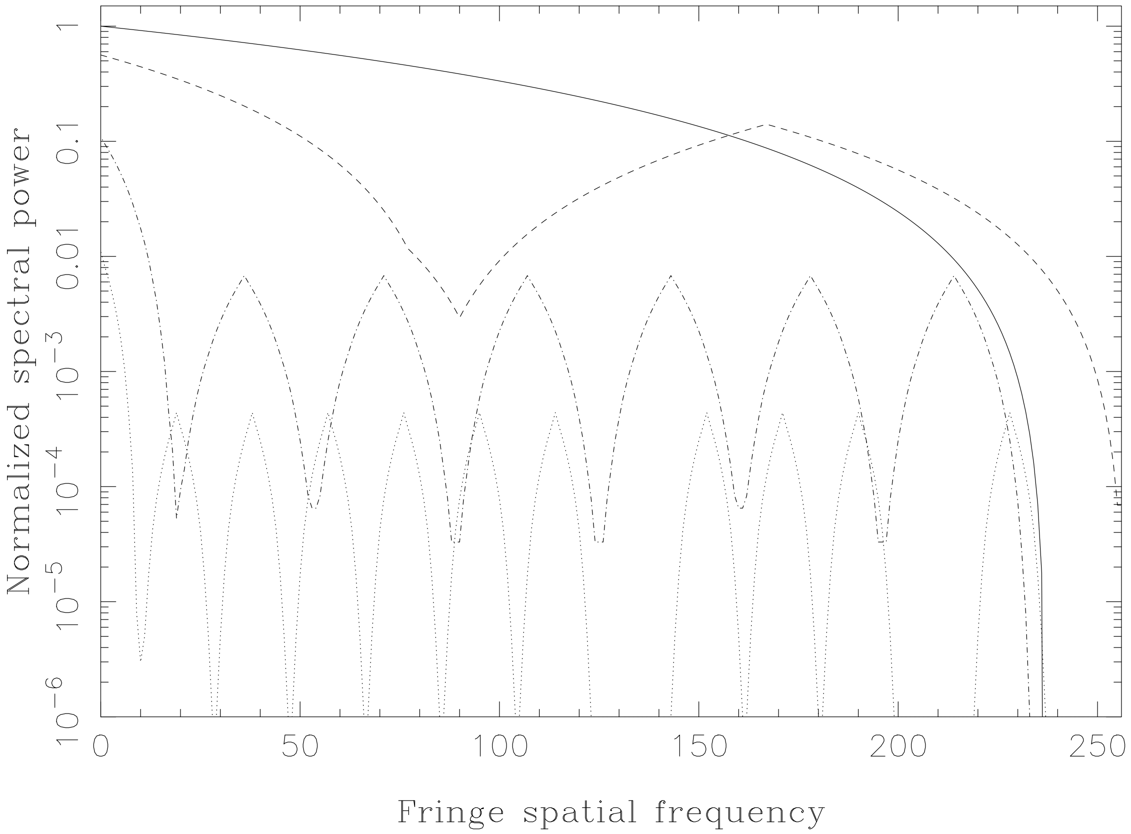

Figure 2.10: Simulated power spectra of various pupil geometries, normalized relative to the zero-spacing of the off-axis slit. The spectra are: slit (off-axis) – solid line, slit (axial) – dashed line, 4-hole (off axis) – dot-dashed line and 5-hole (axial) – dotted line. The cutoff of the aperture (4.2 m in the case of the WHT) is at a spatial frequency of 256 pix^{-1}.

edges of the holes. On the other hand, the 5-hole axial mask was found to be less sensitive to changes in the seeing and pupil geometry (Section 2.7) and to give good sampling out to long baselines (Figure 2.10). This mask also exhibited superior SNR properties against atmospheric and photon noise, especially at the important high spatial frequencies. For those objects which were bright, this was therefore the mask of choice. However, in practice, only a handful of Supergiants and the brightest LPV's at maximum light gave sufficient flux to overcome the limitations imposed by the CCD readout noise.

The 'VI' mask presents an instructive example for SNR analysis. It can be thought of as a chevron or 'V' folded so as to generate closure phases, with sub-apertures in each arm of the 'V' combining with a sub-aperture in the 'I' to form a closed triangle. It samples baselines continuously and has good resistance to atmospheric noise (as it is non-redundant) and readout noise (as it passes a large area of the pupil). A binary star has been successfully mapped using this geometry, however it has not been widely used for two reasons. Firstly, high fluxes combined with low redundancy led to poor performance in terms of photon noise (Equation 2.8). Secondly and more importantly, it was seriously affected by the systematic errors associated with changes in pupil geometry described in Section 2.7.

We now turn our attention to the linear slit configuration. Earlier it was found that, for short to intermediate baselines, this geometry should be competitive with a NRM in the read-noise limited regime and demonstrate superior SNR when shot noise is important.

Of the two slit masks, Figure 2.10 demonstrates that the axial slit has more signal for long baselines and samples the outer 10% of available baselines not passed by other masks. However this comes at the price of a large notch in coverage at intermediate baselines which can cause problems with visibility, and particularly closure phase measurements. The only triangles which form closing sets are those with three short baselines or those with two long and one short, which are least sensitive to source morphology. Nevertheless, the axial slit was useful in cases where the target object was not highly resolved, and as a consequence, measuring the visibility on the longest baselines was of primary importance.

The off-axis slit is closer to the idealized slit geometries presented in Figure 2.7. An experimental investigation of the SNR properties of this mask in comparison to non-redundant masks has been made. These results verified the conclusions given in Section 2.4 in finding that the slit's higher redundancy yielded enhanced performance against shot-noise for certain visibility measurements. For short to intermediate baselines, the improvement in SNR offered by the slit was found to be from 3 to 10-fold or greater, depending on the brightness of the object. For longer baselines ($> 80\%$ of the maximum), however, SNR of visibility data declined sharply to around or below that offered by non-redundant masks.

One of the most serious problems encountered with the use of slit masks was the poor performance with respect to closure phase recovery. Under similar conditions whilst observing the same (bright) object, the 5-hole non-redundant mask produced closure phases with $0.5 \sim 1.5°$ errors, whilst the off-axis slit gave errors of $10 \sim 20°$. This order-of-magnitude poorer performance was almost certainly due to atmospheric noise. The results of Buscher & Haniff

(1993) predict comparable SNR's for the two masks, but only in the photon-starved regime. For observations of M-giants and supergiants, it has been found that atmospheric noise more often provides the limiting factor on the measurements. No methods for circumventing this problem were found, and consequently, most of the data taken with slit masks yielded phase information of very poor quality.

On the other hand, one major advantage of configurations such as the slit (and 'VI'), which sampled many baselines simultaneously was the ability to choose, post hoc, which subset of Fourier data contributed to the final analysis. This has proved useful for a variety of reasons. Some objects, such as relatively wide (~500 mas) binary stars, exhibited modulations in visibility which could be undersampled by the non-redundant masks – thus necessitating the use of the slit. Others were so large that the visibility fell to very small values on relatively short baselines and the longer baselines had to be discarded due to lack of signal-to-noise. This was easy to do for the slit as the data could be re-sampled using a smaller maximum baseline. In addition, many observations were plagued with electronic interference which produced large spurious spikes in the power spectra. When post-observation Fourier sampling was possible, it was straightforward to simply avoid those spatial frequencies affected when performing the data analysis.

In addition to the pros and cons for the use of the slit mask presented above, there was one overwhelming argument which led to its extensive use: it passed a relatively large fraction of the total starlight gathered by the telescope. By far the most important single noise process for faint sources was readout noise and so the signal level (and hence the pupil area) had to be increased to overcome this. Slit masks brought a great many fainter sources within range of the experimental technique which could not have been observed at all with the 5-hole NRM. What was not established, however, was whether the slit mask was the best way to go about adding extra area to the pupil. Experience with 4-hole NRM's, and a number of theoretical arguments, suggest that a 5-hole mask with enlarged holes (making it partially-redundant) might give better phase recovery performance for fainter objects than a slit.

2.6 The Recovery of Atmospherically Degraded Data

Changes in the seeing over short or long timescales could have a detrimental effect upon the measurements, particularly when partially-redundant masks were used. A number of schemes for recovery of data corrupted in this way were evolved, and are described below.

Seeing changes over timescales of a few minutes could lead to apparent variations in visibility as the star was observed at different position angles. It was found that this could be as large as 50% and usually affected all baselines equally. A typical example illustrated in Figure 2.11. As the excursions introduced by the atmosphere were generally many times larger than any signal due to the morphology of the star, data were useless for all but the finding of approximate diameters.

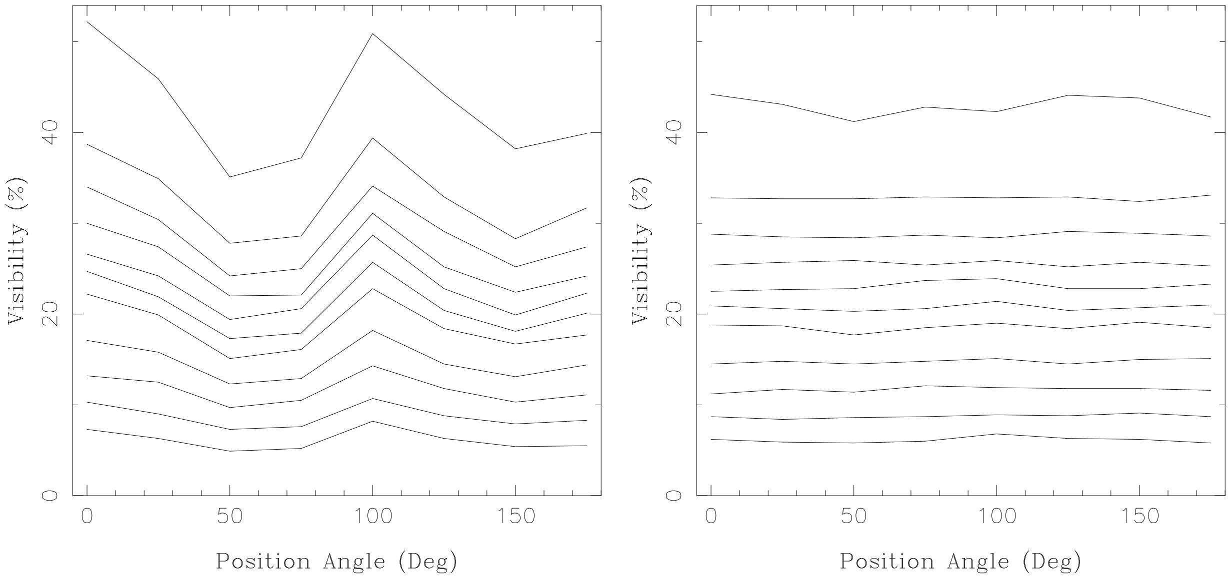

Figure 2.11: Plots of visibility vs. position angle for 12 different baselines within an off-axis slit mask. Successively longer baselines have lower visibilities. The data was taken observing the point-source β Cnc at a wavelength of 902 nm. The dataset to the left shows the excursions in visibility due to seeing changes, whilst that to the right is the same data after application of the 'self calibration' process (see text).

The scheme developed to calibrate for variable seeing relied on two assumptions. Firstly, it was assumed that when the seeing changed, the fractional change in visibility would be the same for all baselines. This was to be expected if the visibility changes were associated with changes in phase across the sub-pupils, and was shown to be valid with the use of slit data of unresolved stars. The second assumption was that sources were not significantly resolved on some of the shortest baselines, and that these should therefore contain no intrinsic visibility signal. As these baseline lengths were much shorter than one metre, this condition was equivalent to insisting that the targets had no structure on scales larger than about one quarter of an arcsecond. This was certainly *not* the case for many of the binary stars observed, but for all giant stars, it was a safe assumption over the wavelength range of interest. The scheme to account for seeing changes had two steps: (1) determination of the magnitude of the visibility change from the short baselines; and (2) correction the visibilities taken concurrently on *all* baselines by this same factor. This 'self calibration' process has been demonstrated to recover full visibility information from atmospherically corrupted data taken with a partially redundant mask. This was verified by ensuring that data taken on the same star but at different times and with different aperture masks yielded consistent results after processing.

This recovery scheme became a vital part of the analysis software since many stars were too faint to be observed with a mask which would have been less susceptible to atmospheric noise (*i.e.* a non-redundant mask). One strong incentive to observe such faint stars was the desire to follow Mira variables through a full pulsation cycle, including minimum light.

One further method for enhancing the data analysis procedure was the implementation of data selection. This approach has found widespread application in high-resolution astronomy.

The basic idea is to reject some, or even most of the data, basing the results on only those measurements where the atmosphere was at its best (see *e.g.* Devaney *et al.* 1989). Programs were written to implement this idea, defining the 'best' exposures to be those where the spectral power at selected baselines was at its highest. The fraction of the data discarded could be varied with optimal results being obtained by retaining only 5 to 10%. For datasets taken under highly variable seeing, this program was successful and helped generate a number of the results presented later. Despite this, it was not widely used, due in part to the fact that short-timescale ($\lesssim$10 sec) seeing fluctuations did not seem to be a major cause of error.

It was found to be worthwhile to record a 'sky background' dataset interleaved once every five observations. This was vital in those cases mentioned earlier where the CCD was affected by electronic interference. It was possible, given the 'dark' exposures, to simply subtract spurious features from the power spectra. Dark exposures were also used to help calibrate the black level of the detector, and were especially valuable in cases where there was a non-uniform background (due to detector imperfections or skylight contamination).

2.7 Pupil Geometry

One of the most serious sources of systematic error encountered was that visibilities could undergo drastic changes whilst observing at certain position angles. One such event, which came to be termed a visibility 'dropout', is illustrated in Figure 2.12. The nature of this problem, along with strategies to minimize its effect, forms the topic for this section.

For the moment, discussion will be restricted to the case of the off-axis 5-hole mask depicted in Figure 2.12. The first thing to be noted about the problem was that certain patterns of four baselines were always affected simultaneously. As each hole in the mask forms one end of four separate baselines, it was easy to verify that whatever was causing the dropouts was affecting a single hole at a time. The most likely candidates for causing blockages in the pupil were the shadows from the edges of the secondary and primary mirrors, and the silhouette of support struts (*i.e.* the spider) which appear to rotate as the telescope is moved. At first the edges of the mirrors were blamed as the spiders were thought to be too thin to create such a large effect. However, although clipping from the mirror edges could occur, it was established that most of the problems *were* arising from the spider. Firstly the hole labeled 'B' in Figure 2.12 could be affected without holes 'A' or 'C'. It was difficult to imagine how this could occur by blockage from the secondary or primary mirror's edge. Secondly, after analyzing a number of dropouts, it was found that they occurred at position angles consistent with the spider geometry.

The loss in visibility for baselines affected could be large – up to 50%. This presented a further puzzle: as the spider was 17 mm thick and the projected diameter of the holes on the primary mirror was 150 mm, then the loss of visibility when the spider centrally blocks the hole should be $\sim$1%. The obvious inference was that the spider was casting a larger shadow upon the pupil than anticipated. The thickness of this shadow was measured in three different ways: using the visibility losses, using the drop in total flux and by direct imaging of the pupil.

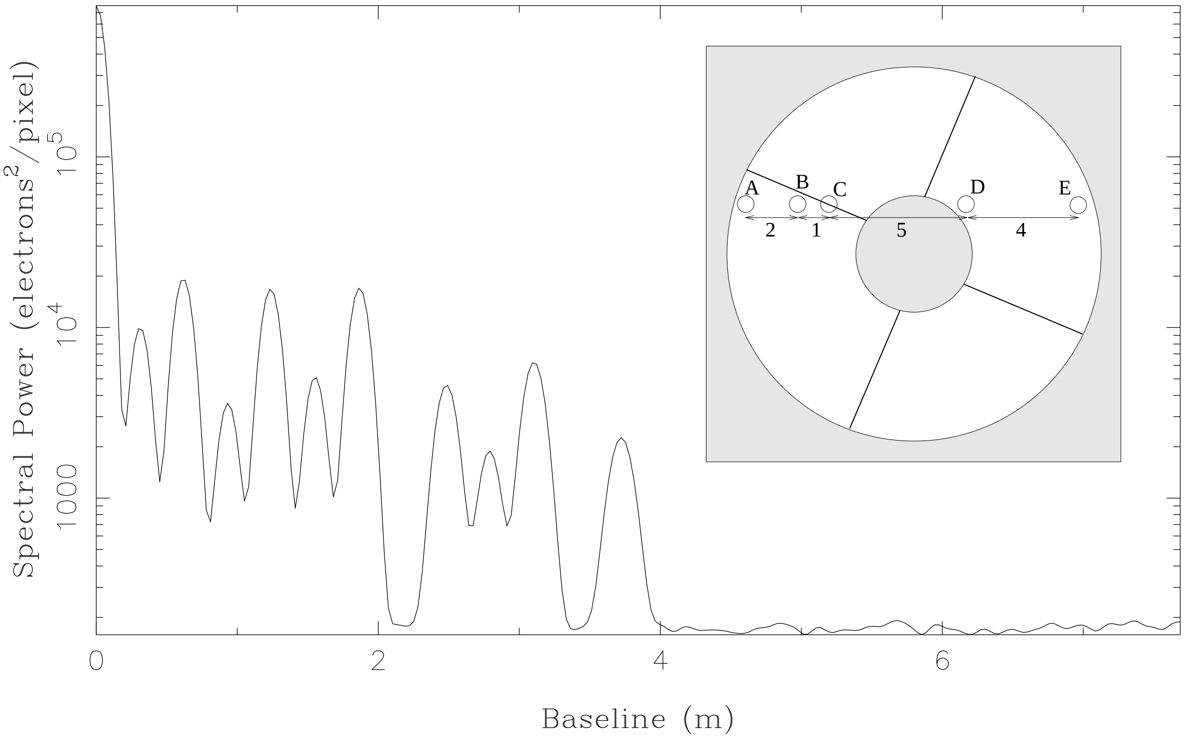

Figure 2.12: Power spectrum of a dataset taken whilst observing the unresolved star α Oph at 833 nm. Note the anomalously low power for baselines with 1, 3, 5 and 9 times the shortest baseline spacing. One possible explanation for this is illustrated to the right where the spider is depicted partially blocking one of the holes in the mask – see text for more details.

Firstly, the measured visibility losses were used to infer the size of the blockage responsible. If a measured visibility loss of 50% is to be attributed to obstruction of one of the pair of holes forming the baseline, then 73% of the flux must have been lost from that hole. Assuming the spider shadow crossed the centre of the 15 cm hole causing maximum extinction, it can be found, after some simple geometry, that the spider shadow was 9.6 cm wide.

Secondly, it was possible to measure the drop in total flux received at the detector due to the partial occultation of the hole. This was found to correspond to 75 to 80% of the flux through a single hole for the most severe dropouts. Again, this requires a shadow 10 cm in width.

The third and most direct measurement of the spider's silhouette was obtained by taking images of the pupil with a CCD, some of which are presented in Figure 2.13. Estimates of the width from measurements of these fell in the range from 9 to 13 cm. A number of additional interesting features were noted in these images. The concentric circular patterning is probably due to figuring inaccuracies in the mirror and indicates that the pupil must be slightly defocused. The bright bands near to some dark edges are probably due to Fresnel diffraction and small ring-patterns are due to diffraction around dust or condensation on the camera optics. Bright regions such as that in the lower left of the 902 nm image were found to be relatively long-lived ($\sim$minutes) and may be due to plumes of hot air in the dome.

Summarizing these measurements, it seems reasonable to take a value of about 10 cm for the

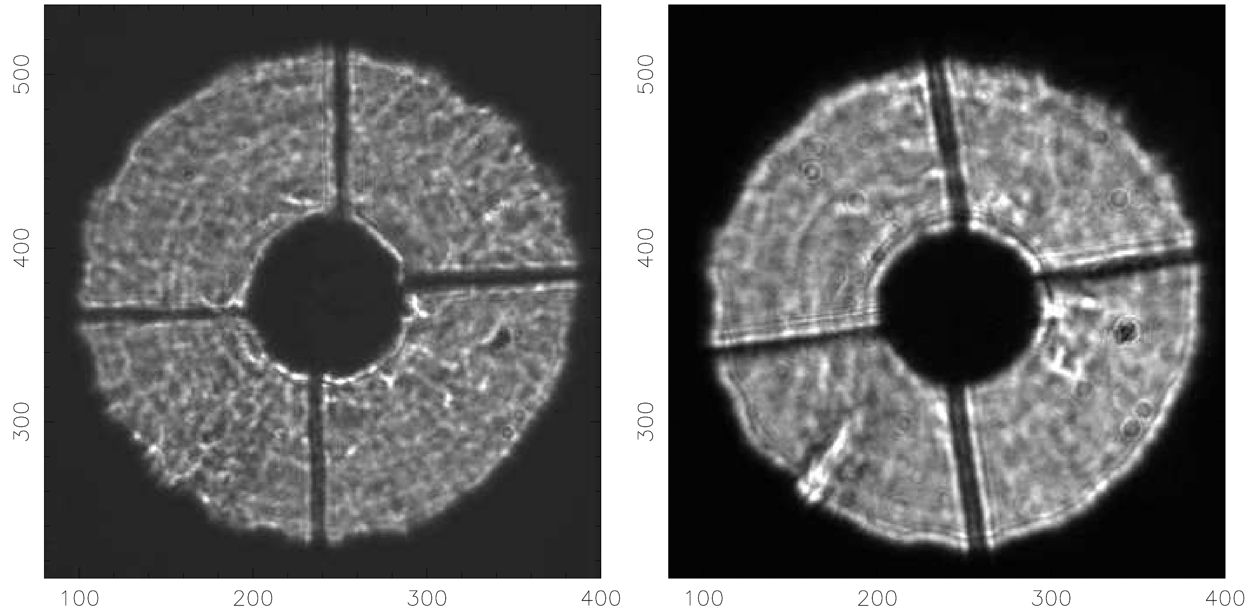

Figure 2.13: One second exposures of the WHT pupil illuminated by Vega (α Lyr) at 546 nm (left) and 902 nm (right). The secondary mirror cell and spider silhouettes can be seen.

width of the optical obstruction due to the spider. In order to investigate the cause for this unexpectedly wide shadow, the optical and mechanical design of the telescope is examined in more detail.

Figure 2.14 presents a mechanical drawing of the WHT showing that there are a number of complex structures obstructing parts of the pupil. In addition to the secondary mirror and its spider, there is a lower spider supporting the Nasmyth turret and mirror. Each spider consists of four sets of two vanes. These vanes are not aligned radially from the primary mirror's centre, but are offset from the centre line by 10 cm (this is visible in Figures 2.13 and 2.12). For the lower vanes, this fact has important consequences for the width of the shadow. Starlight passes the lower spider twice – once as a parallel beam on its way to the primary mirror, then again as a beam converging towards the secondary. As there are non-radial obstructions in the converging beam which are deep with respect to the light path, then the lower spider will be illuminated from one side, and its shadow will thus be enlarged. With the use of engineering drawings supplied by the RGO, the silhouette produced by the lower spider structure was computed. This is sketched in Figure 2.14, and can be seen to magnify the shadow cast by the vanes upon the pupil from 1.7 cm to about 5 cm. This explains some – but not all – of the effect seen.

One possibility is that the remaining additional 5 cm or so of obscuration might originate from further mechanical obstruction. If the vanes of the upper spider are misaligned with respect to each other and/or with respect to the lower spider, in a worst case a further 3 cm of width might be added to the shadow. At the time of these observations there were known problems with the positioning of the Nasmyth mirror and also changes made to the secondary ring, so the possibility that optical misalignments are responsible for the extra broadening cannot be ruled out. This idea was supported by the finding that the apparent widths of spiders could

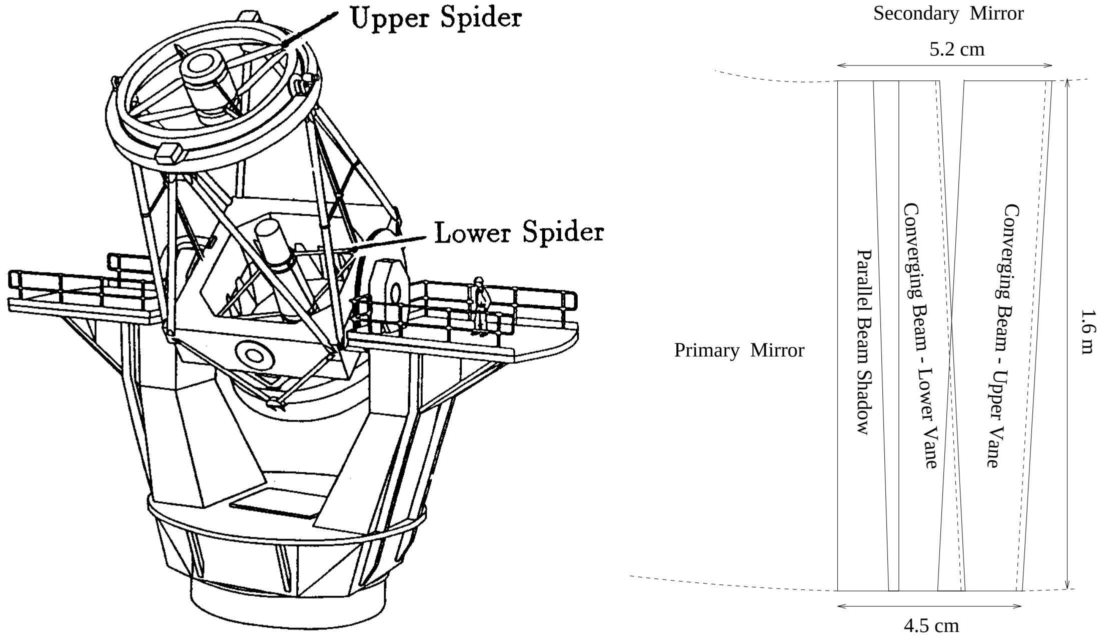

Figure 2.14: Perspective view of the William Herschel Telescope (left) showing mechanical supports. The computed silhouette generated by the lower spider structure is given (right) diagrammatically. The two extra shadows are formed after the starlight has reflected off the primary mirror and is converging to the secondary.

sometimes appear different as the pointing or rotation angle was changed (*e.g.* the left-hand leg of the spider shadow in the 902 nm image of Figure 2.14 appears thinner than the others).

One further hypothesis was developed in order to explain the extra broadening of the shadow cast by the spiders. This was based on the possibility that if the mechanical structure of the telescope was not at the ambient air temperature, then some local (or 'dome') seeing effects might be produced. More specifically, the upper structure of the telescope (upper spider and secondary ring) is exposed to a large solid angle of night sky whilst observing. In this thermal environment, the structure will radiate heat to the sky and thus its temperature will usually fall below ambient air temperature. Under such conditions a cool layer of air would form near to the surfaces. Light passing close to the spider would then undergo some deflection of its path due to the higher refractive index of the cooler, more dense air. If we assume a simple linear temperature gradient of $1°C$ over 10 cm, the gradient-index prism produced in the air around the spiders would deviate light by $2''$. As the field-of-view of our apparatus is only $3''$, this light would not be detected. Having established that not unreasonable conditions are required for this model, further experimental investigation was undertaken.

Figure 2.15 shows results from two different experiments investigating thermal lensing around telescope spiders. The photograph taken with the 36 inch telescope (Willstrop 1993) shows three separate images of the same star with increasing exposure times. In addition to the normal metal spider which was producing the vertical and horizontal diffraction rays, there was stretched across the pupil a cloth 'spider' of equivalent thickness but aligned at 45° to the real spider. It can be seen that the diagonal diffraction rays from this cloth spider exhibit

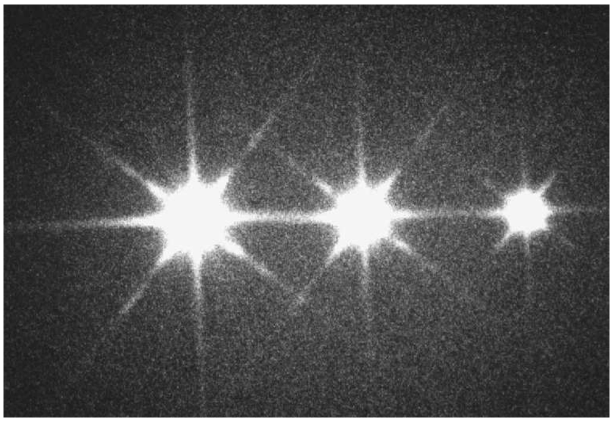

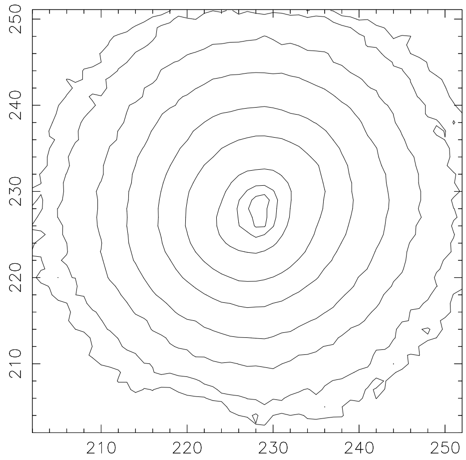

Figure 2.15: Long-exposure images taken with the 36 inch telescope in Cambridge (Left) and a contour plot of a 15 second exposure taken at the WHT. The image scale is $6'' \times 6''$ for the WHT image, whilst the contours are at 0.1, 0.2, 0.4, 0.6, 1, 5, 15, 50 and 95%

secondary maxima and minima, as one would expect from diffraction. The metal spider, on the other hand, produced rays with a more uniform profile radially along the spike as might be expected if thermal lensing, and not diffraction, was scattering the light. A similar experiment was undertaken at the WHT. It was thought that if lensing was responsible for the spider shadows, then the outer contours of a long-exposure image might show some evidence of this. No 'lensing rays' or square distortion at the edges of the field from Figure 2.15 was noted.

One further test of the 'cold air lensing' model was simply to measure the temperature of the air. Sensors were mounted on the telescope monitoring the temperatures of the upper spider, the incoming air and the gradient as the air passed the vanes. This was done continuously whilst observations were being made. The results (Breare 1993) showed that whilst the upper structure does indeed cool to below the ambient air temperature, any gradient in the air near the struts is small ($< 0.1°C$ in 10 cm). In conclusion, it seems unlikely that the anomalous thickness of the spider's silhouette can be due to thermal effects in the surrounding air, and that a mechanical origin is indicated.

We now turn our attention from the origins of the dropouts to dealing with their effects on the data. Despite the fact that the loss of visibility could be severe, with an ideal system, the dropouts still should not have affected the final calibrated Fourier amplitudes. This is because the process of calibration with the point source data should compensate for the altered pupil geometry automatically; provided the object and the point-source suffered *identical* obscurations. Unfortunately, in practice, this was not the case. The difficulty lay in ensuring that the pupil geometry did not change whilst the telescope was moved from the target to the calibration object. Although this is straightforward in principle, it required control of the image rotator to less than 1° in a fashion not envisaged in the telescope drive software. A more serious problem was caused by the repeated misalignment of the optical axis into the GHRIL due to a mechanical fault with the Nasmyth mirror mounting. The optical axis of the image rotator did not coincide with that of the telescope and so pointing offsets had to be introduced in order to keep the focus position fixed as the position angle was changed. This caused the pupil to move, so even if the orientation of the pupil was carefully controlled, there was no way to ensure that it did not undergo displacements in the mask plane. For these reasons, strategies were evolved to try to minimize the effects of problems generated by variable pupil geometry.

Firstly, we consider the recovery of 5-hole mask data corrupted by dropouts. Events which caused large changes in visibility were relatively easy to find, yet those where only a small fraction of one hole was obscured could still have a highly detrimental effect on the results. What was needed was a sensitive test to indicate the state of the pupil during each observation. Figure 2.12 depicts hole 'C' being occulted centrally by the spider, but more commonly the spider clipped the hole to one side or the other. Suppose, for the present it had blocked the right-hand side of hole 'C'. Baselines 'AC' and 'BC' would both then appear somewhat shorter (in addition to losing visibility) and baselines 'CD' and 'CE' would appear longer. By careful measurement of the precise positions of the peaks in the power spectrum, it was possible to measure the baseline lengths and thus monitor small changes in the pupil geometry. Patterns of length change for all the baselines could be combined with the visibility measurements to yield a picture of which holes were occulted and by how much.

In cases where dropouts were identified, the visibilities of the shortest affected baselines could be corrected so as to agree with the visibilities (at the same baseline length) of their nearest-neighbour position angles (given that these position angles did not also have occulted holes). Longer affected baselines were then corrected by the same factor computed for the short baselines. Although this recovery process was time-consuming, it was found that recovered data was internally consistent enough to give sensible maps and models, and externally consistent with other observations of the same object.

Attention has so far been focused on the 5-hole off axis mask, however looking back at Figure 2.9 it can be seen that both of the off axis non-redundant masks present a relatively large angular target for occultation by the spider. Indeed, about half of all data taken with these masks was affected. The adoption of one of the axial configurations certainly alleviates the problem, with generally only one position angle per observation suffering dropouts.

The off axis slit was *always* crossed by at least one and often two legs of the spider, whilst the 'VI' could be crossed by all four. For the off-axis slit, it was very much more difficult to determine from the data where the spider shadows were cutting the slit and to what extent each baseline was affected. Using the geometry of the spider's shadow as determined earlier in this section, numerical simulations have been performed in order to assess how the performance of the off-axis slit might be affected. Excursions in visibility due to the shadow crossing different parts of the slit at appropriate angles are commonly in the $10 \sim 30\%$ range and can, for some baselines, be up to 60%. The best hope of overcoming this source of systematic error is to ensure that the pupil geometries whilst observing the target and point-source objects are as nearly identical as possible. The process of dividing the target by the point-source visibilities will then compensate the calibrated Fourier amplitudes for the obstruction. The simulations indicated that even mismatches of one degree of rotation in the pupil could introduce errors of over 10% into the final visibilities.

2.8 Further Improvements

The observations presented here have been compromised by a number of problems in the optical and mechanical system. Many of these have been discussed in previous sections, including the variable pupil geometry caused by obstructions and shifts in pupil position. This was partially due to poor alignment of the image rotator with respect to the the optical axis. In addition, further problems occurred with the focus of the system. One of these was manifested as a sudden lurch in focus which occurred on timescales of an hour or so. It was simple to adjust the focus by a small amount to correct this, but often more difficult to know when it was necessary. This problem was probably caused by an automated compensation system intended to hold the focus fixed through changes in temperature of the telescope structure. A second difficulty with the focus was traced to the field rotator. Images would become gradually defocused as the rotator was moved to different position angles. This provided clear evidence that the rotator optics suffered from astigmatism. Further problems could arise due to the lack of any atmospheric dispersion correction in the optical system. For this reason, stars which did not transit at high elevations could be difficult to observe reliably.

With past experimental difficulties in mind, a new optical arrangement has been devised in an attempt to circumvent some of them. The camera has been placed on a rotating table, thus removing the need for a separate field rotator. It is hoped that the alignment of the rotation axis of this table with respect to the telescope's axis can be achieved more successfully than has been done for the field rotator in the past. This scheme also avoids a lossy and possibly imperfect element in the optical train, and opens the way for observations further into the infra-red (the path-length through glass using the existing optics would have incurred prohibitive losses). A second important innovation is the simultaneous monitoring of the telescope pupil. Rather than waste the light not passing through the holes in the aperture mask, it is reflected into a second camera which can then provide an image of the pupil during the observation. It should then be a simple matter to avoid dropouts by recording data only at those position angles where there are no obstructions.

And all about the cosmic sky,
The black that lies beyond our blue,
Dead stars innumerable lie,
And stars of red and angry hue
Not dead but doomed to die.

Julian Huxley
from 'Cosmic Death'

Chapter 3

Mira-Type Variables

3.1 M Giant Stars

Asymptotic Giant Branch (AGB) stars are ideal candidates for interferometric study due to their extended atmospheres and high fluxes in the red and IR. They also exhibit a range of poorly understood phenomena, including variability, mass loss, and maser emission. In this chapter we focus on stars of very late spectral type (M, C or S) and of luminosity class III – the Giants.

One of the characteristics of stars on the asymptotic giant branch is variability, with most (or perhaps even all) exhibiting it to a greater or lesser extent. According to the form which the light curve of each object takes, variability can be assigned into categories such as Irregular, Semi-Regular and Mira-type variable (see Kholopov 1987 for further details). Those with a large-amplitude regular pulsation cycles, known as Mira-type variables (named after their prototype object, Mira or o Ceti) have periods of 80 to 1000 days and light amplitudes in the visible ranging from 2.5 to 11 magnitudes. The majority of the M Giants we have imaged at the WHT fall into this category. The periodic nature and large amplitude of the light-curve for o Ceti is illustrated in Figure 3.1.

The presence of an extended complex atmosphere containing many atomic and molecular species in which dynamical effects, such as pulsation and convection, play significant roles has ensured that, despite detailed spectroscopic and photometric studies (see *e.g.* Habing 1990), there is still no consensus as to the physical processes which drive M-giant stars. As the majority of main sequence stars are expected to go through a giant phase, our lack of knowledge represents an important gap and has a large bearing on topics such as the enrichment of the inter-stellar medium by stellar winds, the formation of planetary nebulae and the final fate of stars. The advent of high-resolution imaging holds the promise of settling some of the long-debated ques-

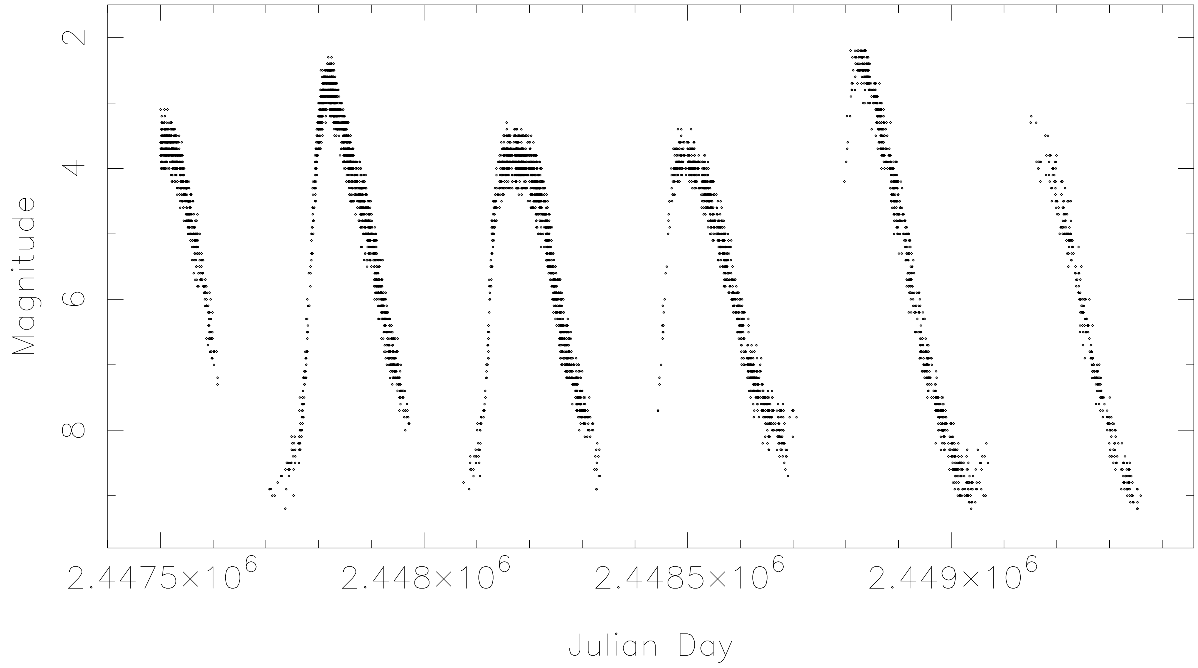

Figure 3.1: Visual light curve of o Ceti covering the period from 1989 to 1994. Data comes from the American Association of Variable Star Observers (AAVSO) archives (Mattei 1994), and each point represents an estimate of the magnitude of the star by one observer. The periodic gaps in coverage occur as o Ceti is not always observable.

tions and establishing the fundamental characteristics of these objects – such as their diameters, masses, effective temperatures (defined as the temperature of a blackbody which emits the same amount of energy per unit surface area as does the star) and modes of pulsation.

The definition of some of the basic parameters, such as the stellar diameter is not straightforward for stars with highly extended atmospheres. Although no stars possess a sharply defined surface, often there is a thin layer over which the density falls steeply to practically zero, and the escape probability of a photon quickly approaches one. Such stars are said to have a *compact* atmosphere (for a quantitative definition see Baschek *et al.* 1991). Red giants, on the other hand, have no such clearly defined region and are said to have *geometrically extended* atmospheres. There are five different types of definition of a stellar radius used in the literature, each based on various quantities, and for stars with extended atmospheres they do not necessarily agree. These are based on: the density, the mass, the optical depth, the intensity and the temperature. The *mass radius*, for example, is the radius at which the mass fraction inside falls below some small (pre-chosen) value whilst the *temperature radius* is the radius at which the local kinetic temperature is equal to the effective temperature. We will be concerned with the most commonly used definition, the *optical depth radius*, which is the distance at which the radial optical depth τ reaches some pre-chosen value of order unity, *i.e.* :

$$\tau(r) \;=\; -\int_{R_0}^{r} k(r')\rho(r')dr' \;\approx\; 1$$

where k = extinction coefficient per unit mass, ρ = density, and the integration starts at R_0, the upper boundary of the photosphere (or infinity in the case where there is no appreciable circumstellar extinction). Definitions based on both monochromatic and wavelength-averaged extinction coefficients have been used. In particular the Rosseland radius R_{ross}, based on the Rosseland mean extinction coefficient $\overline{k}$, is common in the literature.

We now turn to a brief discussion of the spectral characteristics of Mira variables. The strength and complexity of the absorption features in the spectrum of the Mira variable T Cep, as shown in Figure 3.2, are a reflection of the large number of atomic and molecular species present in the stellar and circumstellar environment. The deep absorption feature around 710 nm makes

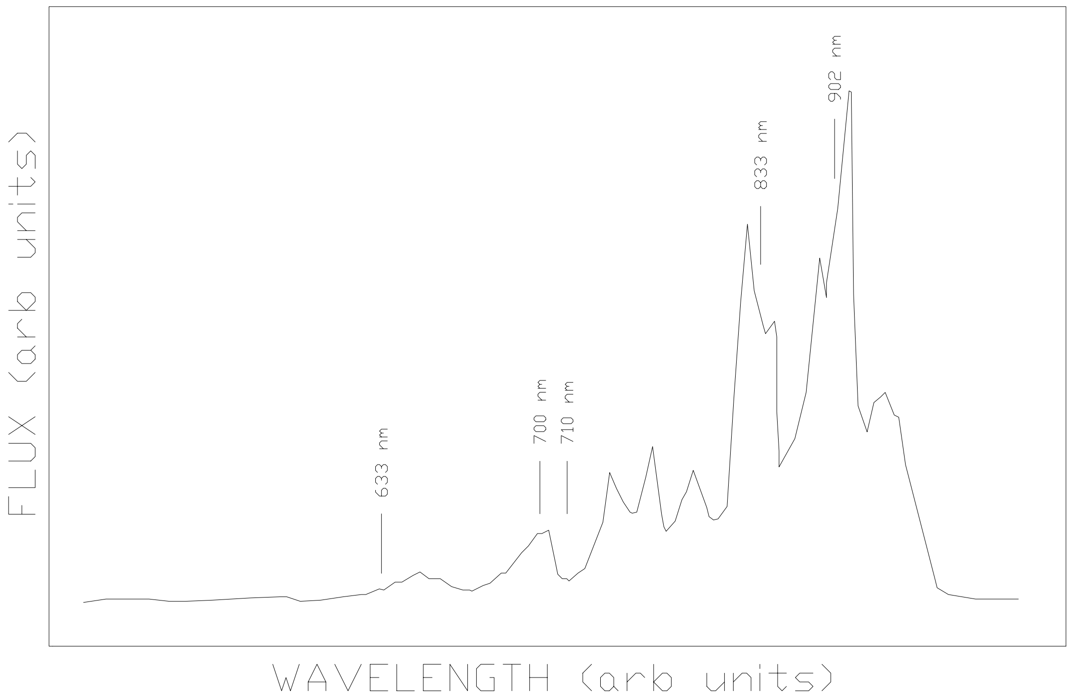

Figure 3.2: Spectrum of T Cep taken by placing a grating in the optical path to the CCD detector, and removing the high-resolution optics (mask and interference filter) in the setup described in Chapter 2. A number of AGB stars were observed in order to ensure that the interference filters isolated the appropriate regions of the spectrum. The data presented here were not corrected for the sensitivity of the detector, and the attenuation of signal at the extremes of the range (particularly towards one micron) is due to the CCD.

700/710 nm a useful pair of wavelengths for comparative observations, as the 710 nm measurement samples the outermost regions of the stellar emission, whilst at 700 nm the atmosphere is optically thinner and emission arises from deeper layers. Unfortunately, although 710 nm is a reasonably good 'absorption band' wavelength, there is no uncontaminated 'continuum' wavelength within the sensitivity range of the CCD detector. Thus, all the wavelengths within the detector's range of sensitivity sampled spectral regions containing contributions from both the underlying continuum emission and the outer layers. The variation of the diameter with wavelength has been used by previous authors (Labyerie *et al.* 1977; Bonneau *et al.* 1982; Quirrenbach *et al.* 1993) to study the atmospheric structure.

3.2 The Observations

The observations presented in this work were taken during eight sessions over a period from January 1991 to December 1993. Over this course of time, techniques evolved considerably (see Chapter 2) leading to some difficulties in the comparison of data taken at different epochs. Astrophysically useful information could be extracted from the measurements according to the following hierarchy:

1. the drop in visibility with baseline (averaged over all position angles) yielded an estimate of the diameter of the object;
2. the details of the form of the visibility curve with baseline gave information about the stellar intensity profile;
3. the variation of the visibilities with position angle yielded information about any deviations from circular symmetry in the image;
4. non-zero closure phases were indicative of a non-symmetric brightness distribution, such as that produced by a bright feature located away from the center of an otherwise symmetric disk.

The ordering of items in the list above is indicative of the depth of analysis obtainable for data of increasing quality. Under ideal conditions (*i.e.* observing a bright, resolved source during good seeing) the SNR of the visibility and closure phase data made a full investigation involving all the categories possible. However, under poorer conditions or for smaller objects, often only analysis described in the earlier items was possible. Further discussion of each of these points is given below.

1) Although the diffraction limit of a 4 m aperture at 700 nm is about 36 mas, it was possible to measure the diameters of stars much smaller than this. For a star with a diameter of only 20 mas, the visibility amplitude would drop to 65 % of the unresolved point-source value at the longest baselines. This could be measured and models of disks or other distributions fitted to the data. For stars which were as large or larger than the diffraction limit, problems could arise with the estimation of the diameter as the simple profiles used did not reflect the actual stellar intensity distribution. In these cases, Gaussian or other limb darkened model profiles usually gave better fits than uniform-disks.

2) For most of the stars observed, the measured Fourier data did not extend to sufficiently long baselines to enter that region beyond the first null in the visibility function where different limb darkening profiles are most easily distinguished. Thus both uniform-disk and Gaussian functions could produce satisfactory fits to the visibility data. For a few of the most resolved stars, the longest baselines were sufficient to measure beyond the first null and a more detailed investigation of the form of the stellar intensity profile was possible.

3) In a number of cases, good Fourier amplitude data were obtained for each position angle, but unfortunately the errors on the closure phases were too large to be useful in constraining

the fitting of models. This usually arose as a result of observations made with a slit pupil (see Section 2.5).

Even in the absence of phase information, it was possible to determine whether an object was distorted from circular symmetry by checking the visibilities for any systematic variation with position angle. For example, an elongation of the source along one axis (*e.g.* an ellipticity of the photosphere or a bright non-central feature) would result in a sinusoidal visibility variation at a given baseline length. As most stellar structures were not well resolved (with the exception of some binary stars), this signature was only pronounced at the longer baselines. An example of such a visibility signal can be found in Figure 3.12. However it was *not* possible to discriminate between centro-symmetric (*e.g.* ellipse) and non-centro-symmetric (*e.g.* disk with a spot) brightness distributions without the use of *phase* information.

4) For objects with both visibility and phase data of high quality, a detailed investigation of the brightness distribution could be attempted. Much could be learned by simple inspection of the data. The fall-off in visibility with increasing baseline gives the diameter and profile (steps 1 and 2 above) whilst the behaviour of the visibility with position angle yields some information about deviations from circular symmetry in the source (step 3). We now go on to consider the closure phases. If an object has a centro-symmetric brightness distribution, its closure phases will be zero for all triangles. Significant asymmetries, such as bright off-centre spots, can generate systematic closure phase signals. This is illustrated with data taken from the (centro-symmetric) point-source star α Oph and the (non-centro-symmetric) α Her in Figure 3.3. Thus,

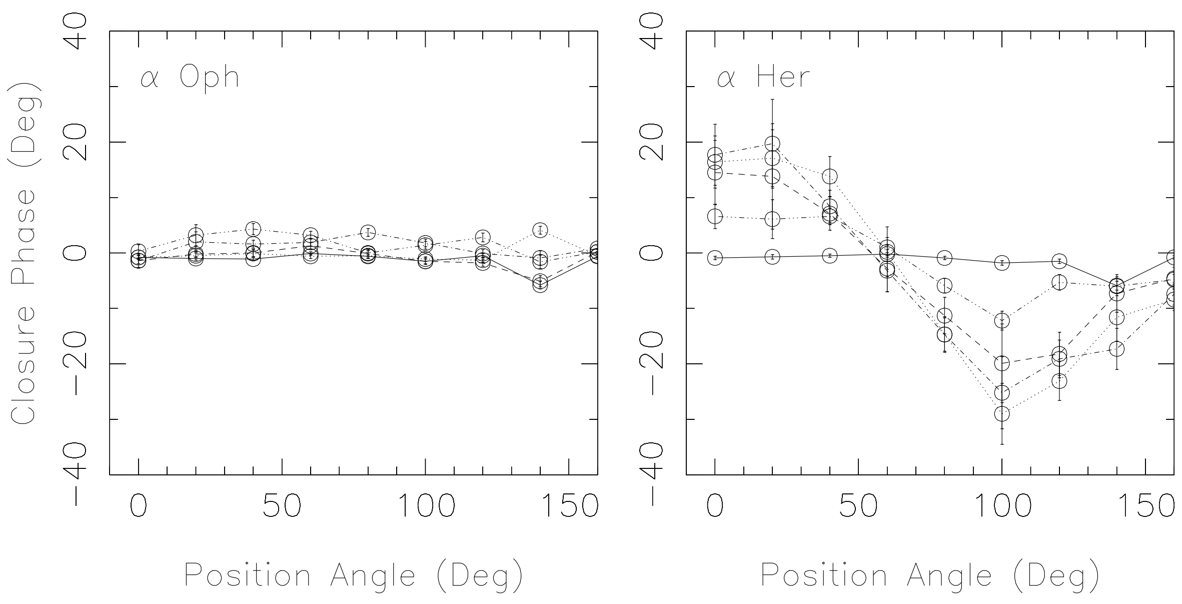

Figure 3.3: Closure phases plotted against position angle for data were taken with a 5-hole mask whilst observing α Oph (left panel) and α Her (right panel). Five closure phases corresponding to 5 triangles of baselines are shown. The point-source α Oph can be seen to produce closure phases close to zero, whilst the non-centro-symmetric α Her gives clear systematic excursions.

phase information makes it possible to distinguish between elliptical distortions and disks with bright features, since the former are centro-symmetric whilst the latter are not. For further interpretation of the data, the brightness distribution could be reconstructed with the use of the MEM algorithm (as described in Section 2.3). Although this gave some insight into the nature of the image, quantitative interpretation relied upon the fitting of models directly to the measured Fourier data. In most cases this was straightforward and a simple combination of a disk with a bright feature or elliptical distortion sufficed to produce a good fit to the data. More complex models with three or more components were sometimes required. However, the large number of free parameters often led to difficulties of convergence and uniqueness. For example, a model consisting of a disk with two spots has eight variable parameters and it was not possible to ensure that the fitting routine had found a globally optimal solution. In addition, a number of other models, (*e.g.* an elliptical disk with one spot: seven free parameters) could produce equally good fits. Further details of the model-fitting procedure are given in Section 4.2.

A summary of all observations (including giants and supergiants) of single stars is given in Appendix A, along with best-fitting uniform-disk and Gaussian diameters.

3.3 Simple Angular Diameters

This section is concerned with obtaining measurements of the stellar diameter for a selection of LPV's. Structure detected upon the stellar surface is discussed in greater detail later in Section 3.8, but for the present, information as to non-circular-symmetries is considered only in the context of any error it may introduce into the diameter estimates. As we shall see, a number of important questions about the behaviour of Miras can be addressed with the use of estimates of their angular sizes and brightness profiles alone.

The diameter fitting process is illustrated for a typical dataset in Figure 3.4. Three uniform-disk model visibility curves are overplotted on a full set of calibrated visibility measurements for the star χ Cyg. The median curve, corresponding to a disk of diameter 33.7 mas, can be seen to produce a good fit to the data. The outlying curves give an estimate of the range of excursion of the diameter permissible from the data, and hence an estimate of the error associated with the best-fit model.

Although the uniform-disk model was found to fit well to the data presented in Figure 3.4, for stars which were more highly resolved than this, it was not able to match the measurements. In particular, the nulls and secondary maxima expected from a uniformly illuminated and hard-edged disk were not seen in those cases where sufficiently long baselines were measured to sample the outer regions of the visibility function. An example of this is shown in Figure 3.5 for the star W Hya. Here both uniform-disk (solid line) and Gaussian (dashed line) models are shown. At long baselines the uniform-disk cannot reproduce the gradual flattening-off of the visibility curve, and so using such a model to parameterize the star would be likely to lead to systematic errors. This does not, however, prove that the profiles of such stars are actually more 'Gaussian-like'. The addition of bright unresolved features, such as have been shown to exist on many occasions on LPV's (Section 3.8) and all supergiants studied (Chapter 4),

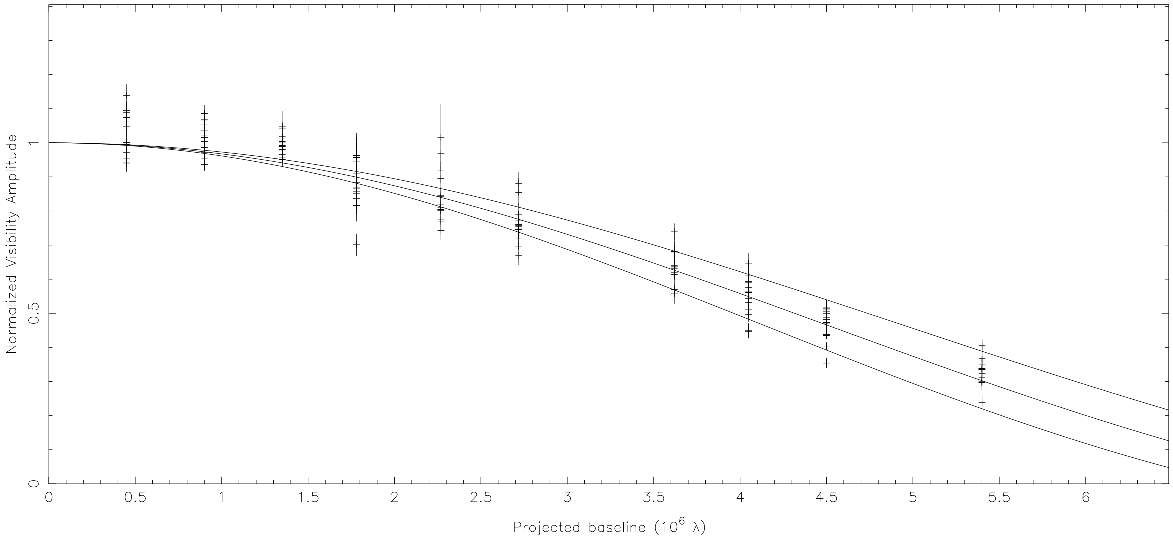

Figure 3.4: Normalized visibility data for χ Cyg plotted against baseline length. Observations were made with a 5-hole mask and data from all position angles are shown. The solid lines are the predicted visibility curves produced by three uniform-disks with diameters of 30.7, 33.7 and 36.7 mas. The central curve (33.7 mas) is the best-fitting disk diameter, whilst the other two cures (30.7 & 36.7 mas) illustrate the process of estimating σ, the error, from the scatter in the data.

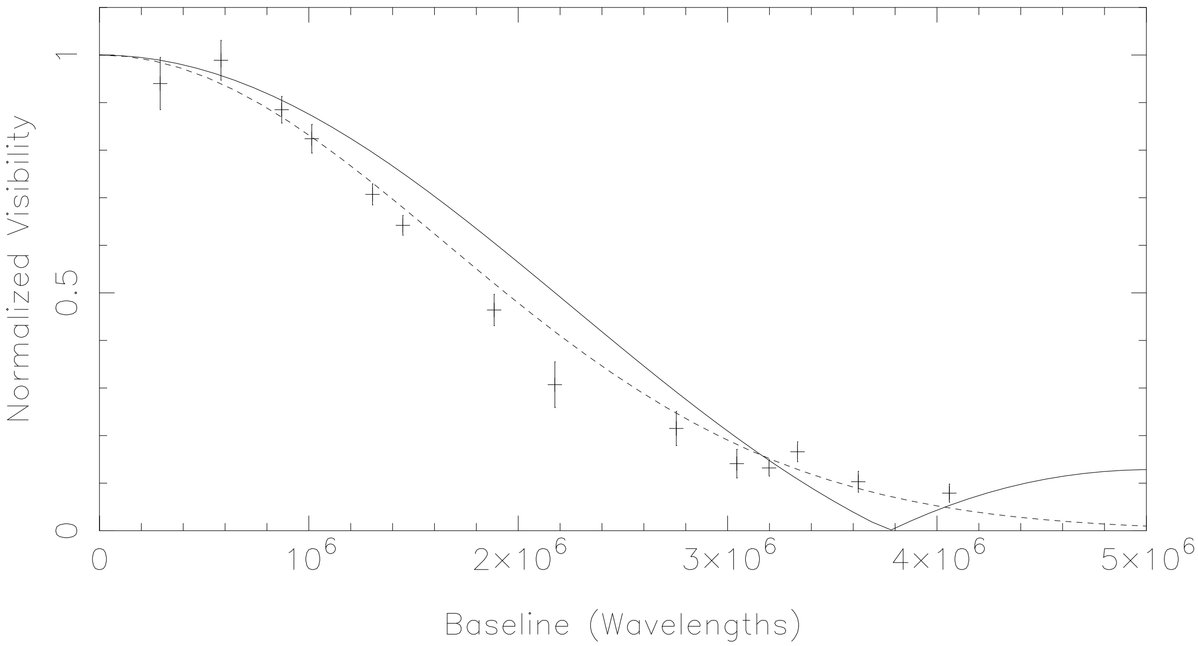

Figure 3.5: Normalized visibility data for R Hya plotted against baseline length from observations taken with a slit mask. The data shown have been averaged over all position angles to produce a single point at each baseline. The solid line is the predicted visibility curve for a uniform-disk of diameter 66.55 mas, whilst the dashed curve is the anticipated visibility function from a Gaussian disk of FWHM 47.58 mas. It is clear that the Gaussian model is better able to match the observations.

can also have the effect of holding the visibility up at long baselines and thus suppressing the nulls. However it has been found for LPV's that when the known features have been taken into account in the models (Appendix B), the underlying profile is still better matched by a Gaussian than a uniform-disk. The converse was found to hold for supergiants (Appendix C) where models consisting of uniform-disks upon which bright features were superimposed were preferred. Further discussion of the radial brightness profiles is given in Section 3.4 in relation to a set of model photospheres.

Appendix A contains the results of the fitting of circularly-symmetric uniform and Gaussian profiles to the visibility data for all the Miras and supergiants observed. A drawback with the use of simple one-parameter models is that the known departures from circular symmetry cannot be accounted for. Asymmetries can thus cause a number of problems for the fitting of such models. Changes to the radially-averaged profile due to bright features have already been mentioned above. However, in addition to these, the diameter of the star appears different as the position angle of the measurement changes. It is important to note that the mean fit to data at *all* position angles measured is given in Appendix A – ignoring any departures from circular symmetry. The advantages of this simple, first-pass approach are two-fold. Firstly, the models are not very prone to ambiguity, such as convergence which is sensitive to the initial conditions, and secondly, this facilitates comparison with results from the literature which are often presented in this way. By a comparison of the results of the simple one-parameter fitting with those from more complex 'disk + spot(s)' fits, it was found that in most cases the discrepancy between the diameters was under 10%. Thus an extra contribution of about 10% should be added to the errors on the diameters given in Appendix A to account for the effects of the asymmetries.

Diameter measurements at optical wavelengths of the Miras from Appendix A have been located in the literature only for a few stars, the two most studied of which are o Ceti and R Leo. o Ceti has been a favourite target for studies using speckle interferometry (Labeyrie *et al.* 1977; Welter & Worden 1980; Bonneau *et al.* 1982; Karovska *et al.* 1991), aperture masking (Haniff *et al.* 1992; Wilson *et al.* 1992) and separated-element interferometry (Ridgway *et al.* 1992; Quirrenbach *et al.* 1992). Although R Leo has not been quite so extensively studied using speckle techniques (Labeyrie *et al.* 1977; Blazit *et al.* 1977), it is fortunate that it lies close to the plane of the ecliptic and thus can be observed with lunar occultations (Di Giacomo *et al.* 1991 and references therein). Of those LPV's that remain, only a few references to optical diameter measurements have been found (*e.g.* χ Cyg in Christou & Worden 1980; R Lyr in Quirrenbach *et al.* 1993). Thus the measurements presented here, and published in Tuthill *et al.* (1994a; 1994b) and Tuthill & Haniff (1994) represent the first high-resolution imaging results for the bulk of the LPV's. Although the measurements are in good agreement with most of the more recent literature values, we do not pursue a detailed comparison here for a number of reasons. The diameters of LPV's have been found to be highly variable, both at different colours and at different epochs. Comparisons which attempt to take such factors into account are made later in Section 3.4.

The tenuous outer layers of M-giants and supergiants become opaque at substantially larger radii in TiO bands than in the continuum. Given the strong and complex nature of this absorption band structure over the region from 500 to 1000 nm for which the CCD was sensitive, it was not surprising that significant changes in stellar diameter were observed using the various filters. Such measurements can be used to obtain information about the atmospheres of these stars, and present a novel method for testing models of cool stars. The diameter ratios for a number of stars are given in Table 3.1 where the diameter at 700 nm has been used as the 'reference' diameter. Stars were selected from those tabulated in Appendix A on the basis of observational coverage and data quality. For the Miras, the ratio given is that of the FWHM's of Gaussian models, whilst for the supergiants, a uniform-disk fit has been utilized.

The first question to be addressed is whether the changes in diameter are due to true extension of the stellar photosphere, or whether differences in limb darkening for the different colours might account for the observations. Even for the extreme case of none to full limb darkening, the expected diameter correction is only 13%. As many of the ratios from the table are larger than this ($30 \sim 40\%$ being common for *o* Cet and R Cas – see also Figure 3.8) we conclude that the variation of diameter with wavelength is real and intrinsic to the stellar atmosphere.

Furthermore, it can be seen from Table 3.1 that the ratios are not the same for a given star at different epochs. This is particularly well illustrated for the case of *o* Ceti, where the ratios 710/700 nm and 833/700 nm are seen to exhibit dramatic changes at the Sep 93 and Dec 93 epochs with respect to earlier measurements. This is believed to result from real changes in the atmospheric extension or opacity of the stellar atmosphere with time and is discussed in detail later in Section 3.11.

We consider the 710/700 nm diameter ratio which can be seen to take values from 1.05 for α Ori to around 1.3 to 1.4 for R Cas and *o* Cet. As the spectra for late-type stars have a strong TiO absorption feature located near 710 nm (Figure 3.2), it is not surprising that all stars have a larger diameter here than at the contaminated continuum wavelength of 700 nm. It appears that the smaller values of 710/700 nm extension of around 5 to 10% are appropriate to the supergiants which have an earlier spectral type of M1$\sim$2, whilst the larger values of 10 to 40% apply to the later-spectrum Miras. This confirms the results of Quirrenbach *et al.* (1993) who found greater extensions for cooler stars in a study involving objects of spectral types from late K to early M. Furthermore, we extend this conclusion to cover objects of still later spectral type, and confirm the general results of previous studies (Labeyrie *et al.* 1977; Bonneau *et al.* 1982; Di Giacomo *et al.* 1991) in finding large diameter variations in LPV's. These results will be discussed quantitatively in relation to some recent atmospheric models of Miras (Scholz 1994) in the following section.

3.4 Photospheric Angular Diameters

Whilst being convenient for parameterizing the angular extent of stars, the simple uniform and Gaussian diameters presented in Appendix A are of limited value. To be of use in an astrophysical context it is necessary to convert these into estimates of the 'true' photospheric

Table 3.1: Diameter ratios for the wavelengths 633, 710, 833 and 902 nm with respect to the 700 nm diameter. The stars in the upper part of the table are LPV's, whilst the supergiants are given in the lower part. As only a limited number of observations could be taken during any observing session, not all colours were covered at each epoch. Blank entries occur where the diameter ratios are unknown.

Star	Epoch	D_{633}/D_{700}	D_{710}/D_{700}	D_{833}/D_{700}	D_{902}/D_{700}
o Cet	Jan 92		1.18	1.00⋆	0.77
	Jul 92	1.00	1.17	1.01	0.82
	Jan 93				0.83
	Sep 93		1.26	0.74	
	Dec 93		1.43	0.75	
R Leo	Jun 93		1.12		
R Hya	Jun 93			0.97	0.89
W Hya	Jun 93		1.16		
χ Cyg	Jul 92			0.85	0.80
	Jun 93	1.13	1.30		
T Cep	Jul 92				0.92
R Cas	Jul 92		1.32	0.69	
	Sep 93		1.29	0.76	
α Ori	Jan 92		1.06		0.98
	Jan 93		1.05		
	Sep 93	1.10			
	Dec 93	1.03			
α Her	Jul 92	1.09	1.16	1.06	
	Jun 93	1.05	1.12		
μ Cep	Sep 93	1.10	1.10		

$\star\ \lambda = 800\,\mathrm{nm}$

diameters. For cool stars, such a procedure has to accomodate both the variation of radius with pulsation phase and the strong wavelength-dependent opacity of the stellar atmosphere. Indeed, for cool variable stars even the notion of a photospheric diameter can lead to difficulties as mentioned in Section 3.1. Here we follow Ridgway *et al.* (1992) in adopting a definition based on optical depth in which the photospheric radius is defined as the radius at which the Rosseland mean opacity equals unity.

Ten stars were chosen for further analysis from those tabulated in Appendix A on the criterion that reliable diameter estimates could be extracted from observations at a minimum of two different colours. The sample (shown in Table 3.2) is thus in no way a statistically complete representation of Miras and is biassed towards nearer, brighter stars. The results presented in Sections 3.4, 3.5 3.6, and 3.7 appear in Tuthill *et al.* (1994b) for the case of R Leo, and for the whole sample of stars in Tuthill & Haniff (1994).

In order to correct for the effects of limb darkening, atmospheric extension and variability phase, a set of theoretical center-to-limb surface brightness distributions have been kindly supplied by Scholz (1994). These were based on a sequence of unpublished photospheric models that have been developed in combination with the self-excited pulsation models of Wood (1990a). Brightness profiles were computed for two models: a star driven to pulsate in its fundamental mode – the 'D' model, and a star pulsating in the first overtone mode – the 'E' model. Both of these models were sampled at four different stages through the simulated pulsation cycle, each providing a snapshot of the behaviour of the stellar atmosphere. These spanned ranges of effective temperature $T_{\rm eff}$ (by which we mean T evaluated at the radius R_{ross}) of 2710 – 3050 K for the D model and 2330 – 2760 K for the E model. Finally, in order to make use of these models in terms of our high-resolution imaging measurements, it was necessary to obtain predicted brightness profiles computed specifically for each of the filter bandpasses used during the observations. Thus for the eight snapshots – four of the D and four of the E model – and for each of the filters used, radial brightness distributions were calculated.

Some examples of these profiles are given in Figure 3.6. The profiles can be seen to be somewhere between the uniform-disk and the Gaussian (also shown for comparison) in shape, *i.e.* more 'sharp edged' than a Gaussian but smoother than a uniform-disk. It is interesting to note from the figure that the D and E model profiles do produce nulls and side-lobes in their visibility functions, as would be expected from a uniform-disk, but that they are not as pronounced. Although only profiles covering one wavelength (833 nm) and one point in the cycle of variability (0.0) are shown, these are more or less representative of the general form. Although most of the profiles were similar in shape, the relative *sizes* of the disks with respect to R_{ross} did undergo changes. For example, it can be seen from the figure that the expected profile for the first overtone pulsator has emission arising from a very much more extended region above R_{ross} than does the fundamental pulsator.

When using such model profiles, previous authors (Ridgway *et al.* 1992) have followed a two-step procedure involving the fitting of a uniform-disk model to their data and subsequently applied a 'scaling factor' derived from the models to correct for limb darkening and atmospheric extension. This was deemed inadequate here because, as noted in the previous section, the uniform-disk

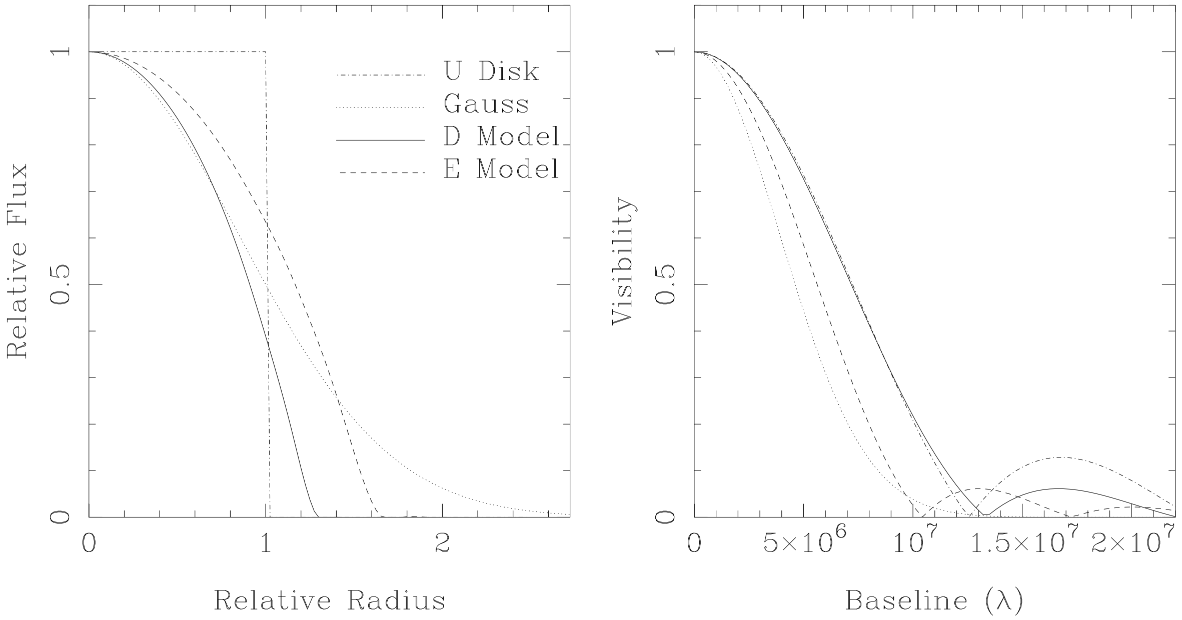

Figure 3.6: Brightness distributions and their Fourier transforms. The left-hand panel shows four model profiles, two of which are the familiar uniform-disk and Gaussian profiles. The other two are computed from numerical models of a fundamental mode pulsator (D model, solid line) and a first overtone pulsator (E model, dashed line) – both at a variability phase of 0.0. The profiles shown were computed for the 833 nm filter and are plotted against the radial coordinate where a value of 1 represents R_{ross}. The visibility function for each profile is given in the right-hand panel identified in the same line-type as that used to the left. Each assumes a 20 mas disk (*i.e.* R_{ross} = 20 mas) and λ = 833 nm.

model often produced a poor fit to the visibility data. This problem was avoided by Fourier transforming the model intensity profiles, yielding predicted visibility curves (as in Figure 3.6), and then performing least-squares fits directly to the measured visibility data. This gave direct estimates of the photospheric radii.

An additional advantage of the procedure of directly fitting the models to the data was that checks could be made on the extent to which the predicted profiles matched those measured experimentally. It was found that the profiles generally provided good fits to the visibility data, however the interferometer baselines were usually not sufficiently long to measure the regions near the nulls and secondary maxima where different models are most easily distinguished. In such cases, all models (including the uniform-disk and Gaussian) could match well to the data. Despite this, a significant fraction of observations did measure the outer regions of the visibility function. This occurred when observing the stars with the largest apparent diameters (o Cet, R Leo, W Hya and R Cas) at one of the shorter wavelengths (*e.g.* 700 or 710 nm) for which the spatial resolution was higher. Two examples of such datasets are given in Figure 3.7 for the stars o Cet and W Hya which clearly demonstrate that the model visibility curves exhibited departures from the measurements. Most notably, there do not appear to be the nulls and secondary maxima predicted by the atmospheric models, with the smooth fall-off in visibility being well matched by the Gaussian function. Thus we can conclude that our measurements

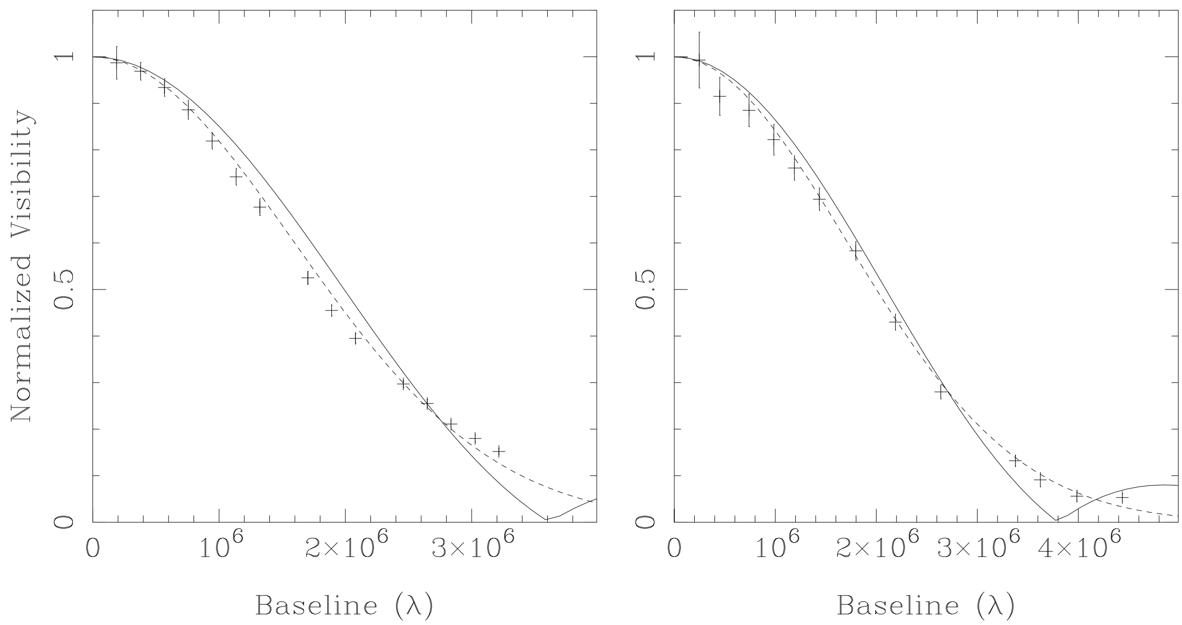

Figure 3.7: Model-fits to visibility data taken on *o* Ceti at 710 nm in September 1993 (left panel), and on W Hya at 700 nm in July 1992 (right panel). Both data sets have been averaged over all position angles yielding a single visibility point at each baseline length. Two different model-fits are shown: the solid line corresponds to an E model at phase 0.0, and the dashed line corresponds to a Gaussian profile. In both cases it can be seen that the Gaussian function provides a closer match to the observed data.

suggest a brightness distribution which is significantly less sharp-edged than those of the D and E models.

In explaining this discrepancy, a number of factors should be taken into account. Firstly, it is important to bear in mind that stars were only sufficiently resolved at the wavelengths of 700 and 710 nm to make meaningful comparisons between various profiles. However, in this complex region of the spectrum, the apparent size of the stellar disk can be critically dependent upon the detailed opacity behaviour of a number of molecular species and it has been acknowledged (Scholz 1994) that the models are probably not accurate at these wavelengths. Furthermore, the models are spherically symmetric whereas it has been demonstrated (Section 3.8; Appendix B) that the stellar morphologies are more complicated than this. The compact bright features which have been detected on the stellar surface should also contribute to holding up the visibility function on the longest baselines, thus suppressing any nulls which may otherwise have been present. Finally, an additional effect which may help account for the smooth shape of the measured visibility curves is scattering off a circumstellar envelope.

The results of the model-fitting for the ten stars comprising the sample are given in Table 3.2. Fits were generally made to data which had been azimuthally averaged over all position angles, however in cases where large systematic departures from circular symmetry were noted (see *e.g.* Section 3.8) a different strategy was adopted. Considering for the moment that the excursions in visibility with position angle represent an elliptical distortion, two separate diameters were

Table 3.2: Photospheric apparent diameters inferred by fitting theoretical centre-to-limb brightness profiles for long-period variables to the visibility data. The periods, dates, pulsation phases and filter information are all the same as those given in Appendix A (*q.v.*). The D and E notation refers to fundamental and first overtone models respectively. For further details see the text.

Star & period (d)	Date (d/m/y)	Variability phase	Filter $\lambda/\Delta\lambda$	D Model (mas)	E Model (mas)
o Cet	18/01/92	0.58	700/10	40.6 ± 5.1	36.5 ± 2.1
332	18/01/92	0.58	710/10	47.1 ± 5.4	42.0 ± 2.3
	18/01/92	0.58	902/50	37.4 ± 2.5	32.6 ± 1.6
	11/07/92	0.05	700/10	34.8 ± 4.3	31.2 ± 1.8
	13/07/92	0.05	700/10	37.4 ± 4.6	33.6 ± 2.0
	13/07/92	0.05	710/10	43.5 ± 5.2	38.9 ± 2.1
	11/07/92	0.05	833/41	42.3 ± 4.4	36.3 ± 1.7
	13/07/92	0.05	833/41	39.5 ± 4.3	34.0 ± 1.6
	12/07/92	0.05	902/50	36.4 ± 2.4	31.7 ± 1.6
	03/01/93	0.48	700/10	37.8 ± 4.6	33.9 ± 2.0
	04/01/93	0.48	902/50	38.6 ± 2.6	33.7 ± 1.7
U Ori	06/12/93	0.04	700/10	24.7 ± 3.0	22.2 ± 1.3
368	07/12/93	0.04	833/41	21.3 ± 2.4	18.5 ± 0.9
R Cnc	02/01/93	0.14	700/10	27.7 ± 3.4	24.9 ± 1.4
362	03/01/93	0.14	902/50	19.7 ± 1.4	17.9 ± 1.6
R Leo	20/01/92	0.27	833/41	43.0 ± 4.5	36.9 ± 1.8
310	20/07/92	0.27	902/50	43.6 ± 2.6	38.0 ± 1.9
	10/06/93	0.88	700/10	55.6 ± 6.7	49.7 ± 2.8
	10/06/93	0.88	710/10	60.9 ± 7.0	53.9 ± 3.0
R Hya	07/06/93	0.28	700/10	32.7 ± 4.0	29.4 ± 1.7
389	09/06/93	0.28	833/41	33.2 ± 3.7	28.7 ± 1.4
	08/06/93	0.28	902/50	32.9 ± 2.2	28.7 ± 1.4
W Hya	08/06/93	0.04	700/10	58.6 ± 7.1	52.4 ± 3.0
361	09/06/93	0.04	700/10	60.9 ± 7.3	54.4 ± 3.2
	09/06/93	0.04	710/10	71.4 ± 8.6	63.9 ± 3.5
R Aql	11/07/92	0.06	700/10	24.0 ± 3.0	21.5 ± 1.2
284	12/07/92	0.06	710/10	26.0 ± 3.0	23.3 ± 1.3

Table 3.2: – *Continued*

Star & period (d)	Date (d/m/y)	Variability phase	Filter $\lambda/\Delta\lambda$	D Model (mas)	E Model (mas)
χ Cyg	13/07/92	0.32	700/10	34.2 ± 4.2	30.7 ± 1.8
408	13/07/92	0.32	833/41	34.5 ± 3.8	29.8 ± 1.5
	13/07/92	0.32	902/50	32.2 ± 2.2	28.1 ± 1.4
	07/06/93	0.14	700/10	28.2 ± 3.5	25.3 ± 1.4
	08/06/93	0.14	710/10	37.0 ± 4.3	33.2 ± 1.6
	07/09/93	0.35	700/10	40.7 ± 5.0	36.6 ± 2.1
T Cep	12/07/92	0.72	700/10	31.0 ± 3.8	27.8 ± 1.6
388	12/07/92	0.72	905/50	28.4 ± 2.0	24.8 ± 1.2
	07/06/93	0.56	830/41	27.6 ± 3.1	23.9 ± 1.2
R Cas	13/07/92	0.05	700/10	34.6 ± 4.2	31.1 ± 1.8
430	13/07/92	0.05	700/10	34.1 ± 4.2	30.6 ± 1.8
	13/07/92	0.05	710/10	45.0 ± 5.3	40.1 ± 2.2
	13/07/92	0.05	710/10	47.8 ± 5.6	42.7 ± 2.4
	13/07/92	0.05	833/41	28.2 ± 3.2	24.5 ± 1.2
	08/06/93	0.82	700/10	36.0 ± 4.4	32.2 ± 1.9
	07/09/93	0.03	700/10	33.5 ± 4.1	30.0 ± 1.7
	08/09/93	0.03	710/10	47.2 ± 5.5	42.1 ± 2.3
	08/09/93	0.03	833/41	29.1 ± 3.3	25.2 ± 1.2

obtained: one for the major and one for the minor axis. The diameter given is then that of a sphere of equal volume to a prolate spheroid having major and minor axes as measured. In this way, the final result is heavily biassed to the minor axis. For both types of model (*i.e.* D and E), the average diameter obtained by fitting each of the four time-resolved 'snapshot' brightness profiles to the data is given. The errors quoted in Table 3.2 arise only from the scatter between the fits from the four different profiles. In particular, no error contribution has yet been included to account for the scatter of diameter values allowed from the visibility data, or from systematic effects arising from misfits between the model and measured brightness profiles. As expected for measurements taken over spectral regions containing molecular absorption features, the process of obtaining a photospheric diameter almost always resulted in a smaller estimate than those obtained by fitting a simple uniform-disk.

As mentioned above, the apparent photospheric diameters given in Table 3.2 were obtained by averaging the results of four fits – one from each 'snapshot'– rather than using only that one for which the model phase was closest to the (known) variability phase of the star. There were a number of reasons for this. Ideally, models should have been tailored for each star to take account of differing temperatures and atmospheric conditions; however, only two generic models (fundamental and overtone) were available. The variation of effective temperature of these models with phase goes some way towards representing the likely range of temperatures in our sample of stars.

The use of a single model phase appropriate to each observational phase should correct the measured photospheric diameter for any variations due to pulsation. However, before using the models to perform this correction, their predictions as to the variations in diameter with pulsation phase were compared with those actually observed. The models give quite different excursions in diameter dependent upon whether the star is a fundamental mode or a first overtone pulsator. Taking for example the 700 nm filter, the D model profiles varied by a total of 43% of the mean diameter, whilst the E model variations were only 7%. Sufficiently large diameter variations have certainly been observed over time to be consistent even with the D model predictions: for example, the large extension for the 700 and 710 nm diameters for *o* Ceti in September and December 1993 as compared with previous measurements. However these have been shown not to be periodic with the variability of the star, and have not been found at longer wavelengths as the D model profiles predict. In the case of *o* Ceti, the changes have been tentatively identified with an aperiodic dynamic instability in the upper atmospheres of Miras (see Section 3.11 for further details). For this reason, the September and December 1993 data for this star have not been used further in this analysis. If we instead consider the 833 nm filter, which should hopefully sample deeper photospheric layers and not be so affected by the outermost regions of the atmosphere, then the D model predicts diameter variations of 28% whilst the E model predicts 13% variations. For *o* Ceti, the only star for which a number of 833 nm observations at separate epochs exist, the diameter variations were no larger than about 10% between epochs – about the same size as the errors on the measurements. Thus the large changes in size predicted by the D model would seem to be ruled out in this case. In the light of these uncertainties as to the validity of the pulsation-phase corrections inherent in the models, it was decided to follow the course outlined above: *i.e.* to simply average the results from models at all phases.

In addition to predicting changes in the quasi-monochromatic diameters (as discussed above), the models of Scholz (1994) also predict changes in the *photospheric* diameter. These changes are, however, more modest with expected values of 20% for the D models and 10% for the E models. These are in rough agreement with the models of Bessell *et al.* (1989), which suggest that the star should be smaller (by $\sim 20\%$) at maximum than at minimum. On the other hand, Feast *et al.* (1989) found that the diameter of R Leo varied by no more than $\pm 5\%$ about its mean value. This result was based on the assumption that the blackbody temperature (found from fitting to near infrared $JHKL$ photometry) was equal to the effective temperature, thus allowing a computation of the stellar angular diameter. As there still seems to be active debate on the magnitude of the expected changes of photospheric diameter with pulsation phase, it seemed prudent not to apply any further explicit corrections to the data for this effect. In what follows, it should be borne in mind that such a correction could be as large as 10%.

In addition to the radial profiles and the variations with phase, the third and most stringent requirement for the models to match the observations is that they predict a *single* photospheric diameter from observations using different filter bandpasses. The large variations in angular diameter which could occur, particularly associated with the titanium oxide absorption features near 700 and 710 nm have been mentioned in Section 3.3.

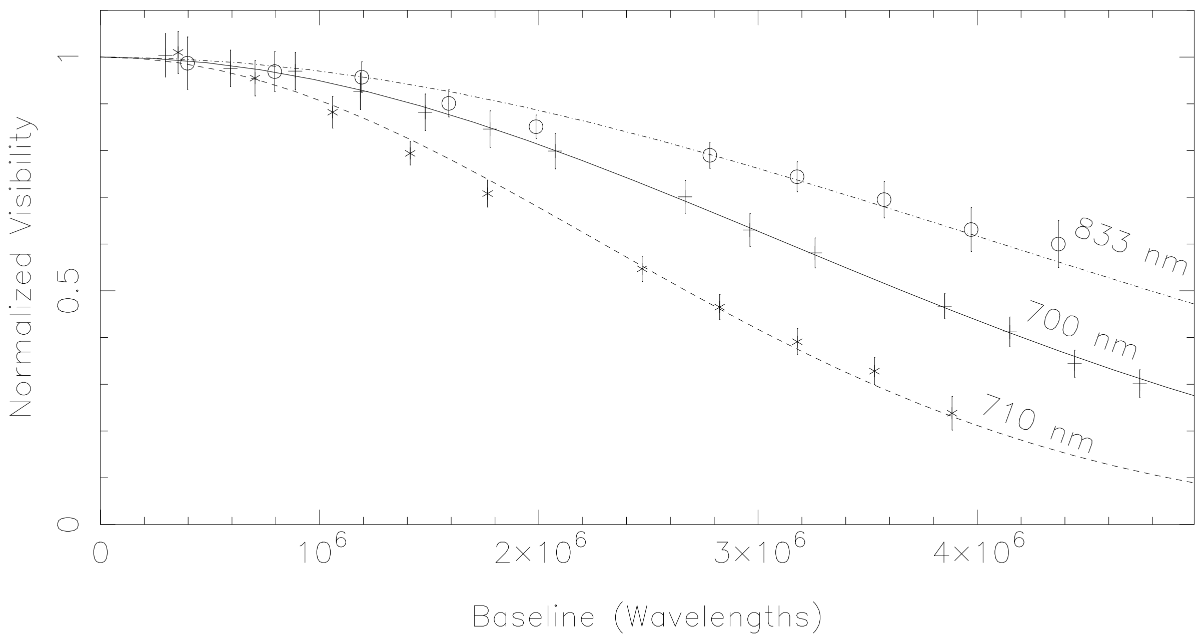

Figure 3.8: Visibility data taken whilst observing R Cas in September 1993. Three different filter bandpasses are shown: 700/10, 710/10 and 833/41 nm with the three curves giving Gaussian profiles of FWHM 26.7, 34.4 and 20.3 mas respectively.

Visibility data illustrating the changes in size with wavelength are given for R Cas in Figure 3.8. Observations were made during a single session in September 1993 and it was found that the star was 41% smaller at 833 than at 710 nm. The important question here is then: do the model profiles correct these widely differing datasets to yield similar photospheric diameters? Unfortunately, upon examination of Table 3.2, it is clear that this is *not* the case. For example, taking again the results for R Leo in September 1993, we see from Table 3.2 that the (ostensibly wavelength-independent) photospheric angular diameters predicted using the results from various filters differ by large amounts: for example, the 710 and 833 nm wavelengths give diameters of 47.2 and 29.1 mas. R Leo is thus predicted to be 38% smaller using the 833 nm as compared to the 710 nm measurements.

Generally, the atmospheric models predict relatively modest diameter variations of around a few per cent, and certainly in most cases less than 10%, for observations in the different filter bandpasses. In stark contrast to this, the observations uncovered variations in angular diameter which could be as large as a factor of two (see *e.g.* Table 3.1). However, such dramatic changes in size were associated with the shorter wavelength filters, particularly the 710 nm, with respect to the longer wavelength (833 & 902 nm) filters. It has been mentioned earlier that the atmospheric models are not expected to be particularly reliable at the shorter filter bandpasses. This problem is likely to be alleviated by giving further attention to the treatment of molecular opacities, and the tailoring of the models specifically for each star.

For the present, however, our main interest is in obtaining unbiased estimates of the photospheric angular diameters. In order to do this, an empirical approach was adopted. Photospheric angular diameters were found with the use of the D and E models (as given in Table 3.2). The ratios of these derived diameters for the different filter wavelengths used were then computed. Although there were found to be some variations between ratios for different stars and epochs, it was found that all obeyed the general rule that stars gave the largest deduced photospheric diameters at 710 nm and the smallest at 833 or 902 nm. It was possible to quantify this by taking the average of diameter ratios for a number of different stars – with the result that mean scaling factors, which could bring all the measurements into approximate agreement, were found. The mean ratios, computed with respect to the 902 nm diameter, are given as follows:

Filter	700	710	833	902
Ratio	1.14 ± 0.15	1.41 ± 0.14	1.05 ± 0.13	1.0 (defin.).

This information as to the discrepancy between the diameter ratios predicted by the models and those observed should be of interest in the context of improving the atmospheric simulations. For the present, however, we use them pragmatically to provide scaling factors to correct the various diameters at different wavelengths to yield a single photospheric diameter. The strategy adopted for doing this was as follows:

1. It was first assumed that the 833 and 902 nm bandpasses yielded results close to the 'true' photospheric diameter. The justification for this assumption was that these filters isolated windows closer to the infrared continuum and where molecular features were less prominent, and that the stellar atmospheric models were expected to perform more reliably there. It is important to note that the selection of these wavelengths led to the photospheric angular diameters chosen being the *smallest* of those derived.
2. Photospheric diameters derived from the models using data at 833 and 902 nm were not

significantly different from each other (to within the scatter in the data). Thus, for stars where one diameter measurement at either of these wavelengths was made, the diameter of the fitted model was taken to be equal to the photospheric diameter. In cases where a number of 833 and/or 902 nm observations existed, results were averaged to give the photospheric diameter.

3. Only in cases where no 833 or 902 nm measurement existed (this applied only to two stars: W Hya and R Aql) were the 700 or 710 nm observations used. The diameters of the fitting model profiles were divided by the scaling factors given above before the results were used as estimates of the photospheric diameter.

The photospheric angular diameters computed according to the recipe above using data from Table 3.2 are given in Table 3.3 for each of the ten stars in the sample. The quoted error now includes the term from the uncertainty in the appropriate model profile (as given in Table 3.2) and also the contribution calculated from the scatter in the visibility data themselves. In addition, in those cases (W Hya and R Aql) where the diameters were scaled using the correction factors, an extra 10% error was added in quadrature to account for the uncertainties in these.

Although a number of determinations of angular diameter have been found in the literature (see Section 3.3), we are particularly interested here in those which give an independent estimate of the true photospheric diameter. In particular, observations further into the infrared (*e.g.* at around $2\,\mu$m) sample regions which are much less troubled by molecular absorption and thus yield a clearer view of the underlying photospheric continuum. Such measurements exist for two stars: *o* Cet and R Leo. The angular diameter of *o* Cet has been measured in the infrared K-band by the Infrared Michelson Array (Ridgway *et al.* 1992). The models of Scholz (1994) suggest that the angular diameter measured at this wavelength should be close to the true (Rosseland) photospheric diameter; thus any correction factor for atmospheric extension and limb darkening should be small. They found a uniform-disk diameter of 36.1 ± 1.4 mas, which compares well with the value of 33.6 ± 3.5 mas from the E model-fit of Table 3.3 (for reasons explained later, we prefer to use the E rather than the D model fits).

The angular diameter measurement of R Leo was made with the lunar occultation technique at $2.16\,\mu$m by Di Giacomo *et al.* (1991). Their value of 33 ± 1.3 mas is somewhat smaller than the value of 37.4 ± 2.3 mas from Table 3.3. Again, any correction for limb darkening or photospheric extension should be small at this wavelength according to the models of Scholz (1994). However, Di Giacomo *et al.* state that least-squares fitting led to uniform-disk diameters in the range $30 - 35$ mas and it therefore seems possible that their quoted error estimate is optimistic. The small remaining discrepancy between the two results may be due either to the extra uncertainty associated with the stellar pulsation or possibly to cycle-to-cycle variability of the star.

3.5 Effective Temperatures

Estimates of the mean effective temperatures of the stars in the sample were derived by combining the photospheric angular diameters with bolometric fluxes using the relation:

$$T_{\text{eff}} = 2341(F_{\text{bol}}/\phi^2)^{1/4}, \tag{3.1}$$

where F_{bol} is the mean apparent bolometric flux in units of $10^{-8}\,\text{erg}\,\text{cm}^{-2}\,\text{s}^{-1}$ and ϕ is the apparent angular diameter in mas. For cool stars such as Miras where most of the energy is emitted at near infrared wavelengths, a convenient method for calculating bolometric magnitudes is to use a blackbody function to interpolate between measured JHKL photometry (Robertson & Feast 1981; Glass & Feast 1982; Feast *et al.* 1989). Here we follow a similar procedure but include additional photometry at 1.04 μm (Lockwood 1971) together with IRAS data (Beichman *et al.* 1994). For most of the sample, mean JHKL magnitudes were taken from the compilation of Catchpole *et al.* (1979), although for a few of the more northern sources, further measurements from the literature were included (Gillett *et al.* 1968; Wilson *et al.* 1972; Dyck *et al.* 1974; Kenyon & Gallagher 1983; Heske 1990). Because of the stars' close proximity, no corrections for extinction have been applied. Similarly we have made no corrections to account for H_2O opacity within the near infrared bandpasses. Because these two correction factors act in different senses, it is unlikely that they will have conspired to introduce any errors comparable to those arising from uncertainties in the mean near infrared magnitudes due to, for example, uneven sampling of the light-curves.

To accommodate the wide wavelength range of the photometry, a two-component blackbody fit was used as an interpolation device, although a single blackbody gave an adequate computation of the bolometric flux for the majority of the sample. One case where a single blackbody curve did not provide a good fit to all the photometric data is illustrated in Figure 3.9. The excess of mid- and far-infrared radiation accounted for by the cooler of the two components originates from a circumstellar dust shell surrounding the star. Such warm ($\lesssim$ 1000 K) dust envelopes result from mass loss and are known to be ubiquitous to LPV stars. These were noted to some extent in the infrared fluxes of all the stars in the sample. Bolometric magnitudes were integrated from the two-blackbody curves, thus compensating for some circumstellar dust extinction. The errors were estimated to be $\lesssim$ 0.15 magnitudes.

The values of T_{eff} evaluated from Equation 3.1 are summarized in Table 3.3, where for each star, effective temperatures have been computed on the basis of both the E- and D-model diameter estimates. As an alternative to this procedure, we have also included in Table 3.3 the blackbody temperatures. These have been obtained by fitting a single blackbody function to the mean near infrared fluxes between 1.04 and 3.45 μm. In the past there has been some controversy concerning the use of infrared blackbody temperatures as indicators of T_{eff}, with Feast and co-workers (Robertson & Feast 1981; Glass & Feast 1982) arguing for approximate equality between T_{eff} and T_{bb}, but Bessell *et al.* (1989) explaining this as a fortuitous coincidence. Our data show reasonable agreement between T_{eff} and T_{bb}, although there is marginal evidence that

Table 3.3: Angular diameters and temperature measures of the sample of stars. Columns 2 and 3 contain the mean bolometric magnitude and the fitted blackbody temperature, both obtained from infrared photometry (see text). The photospheric angular diameter is given in Column 5 (see previous section) whilst the effective temperature derived from Equation 3.1 is given in the last column.

Star	$m_{\rm bol}$ (mag)	$T_{\rm bb}$ (K)	Model	Ang. Diam. (mas)	$T_{\rm eff}$ (K)
o Cet	0.1 ± 0.2	2770 ± 190	D	38.0 ± 4.0	2629 ± 184
			E	33.6 ± 3.5	2796 ± 194
U Ori	2.2 ± 0.2	2410 ± 130	D	21.3 ± 3.7	2166 ± 213
			E	18.5 ± 2.6	2324 ± 195
R Cnc	2.2 ± 0.1	2550 ± 70	D	19.7 ± 3.8	2252 ± 223
			E	17.9 ± 3.6	2362 ± 244
R Leo	0.5 ± 0.2	2610 ± 110	D	43.4 ± 3.2	2244 ± 132
			E	37.4 ± 2.3	2417 ± 134
R Hya	0.5 ± 0.1	2680 ± 70	D	33.0 ± 4.1	2573 ± 170
			E	28.7 ± 3.3	2759 ± 171
W Hya	-0.1 ± 0.2	2460 ± 110	D	51.8 ± 7.3	2358 ± 199
			E	46.2 ± 5.8	2497 ± 194
R Aql	2.2 ± 0.2	2550 ± 150	D	19.5 ± 4.4	2263 ± 276
			E	17.5 ± 3.7	2389 ± 275
χ Cyg	0.8 ± 0.2	2190 ± 100	D	32.8 ± 4.1	2409 ± 187
			E	28.9 ± 3.0	2566 ± 178
T Cep	1.3 ± 0.2	2520 ± 120	D	28.2 ± 5.4	2315 ± 246
			E	24.3 ± 4.4	2494 ± 253
R Cas	1.1 ± 0.2	2210 ± 130	D	28.6 ± 3.9	2408 ± 198
			E	24.9 ± 2.9	2580 ± 192

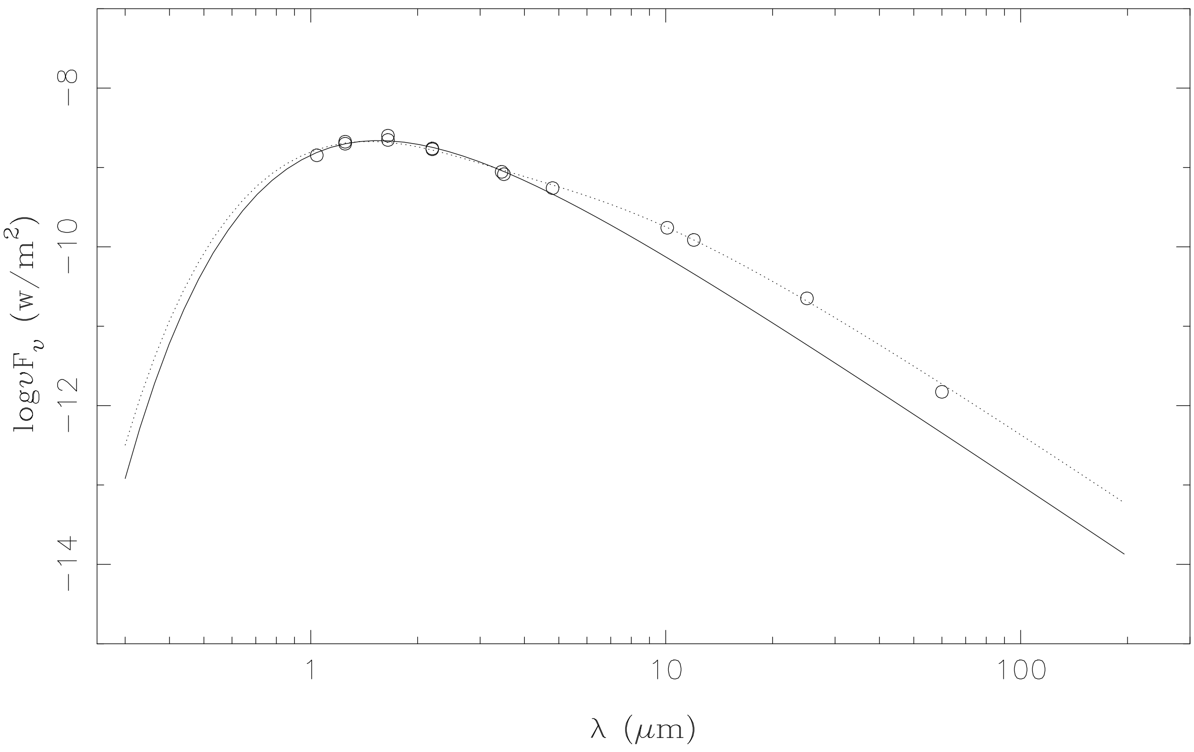

Figure 3.9: Photometry data (circles) and fitted blackbody curves for U Ori. The solid line is a single-blackbody fit to the 1.04 μm + JHKL fluxes only, whilst the dotted line is a two-component blackbody fit to all the data (including the IRAS photometry).

the blackbody temperatures are somewhat higher than the more direct measurements of $T_{\rm eff}$ derived from the photospheric diameters and bolometric magnitudes.

Although data from Table 3.3 are probably too inaccurate to draw any definitive conclusions concerning the effective temperature scale for Miras, the very low effective temperatures inferred under the assumption of fundamental mode pulsation cast doubt on whether such a hypothesis can be entertained. In particular, where independent and reliable measurements of $T_{\rm eff}$ exist in the literature, they agree well with our results based on first overtone pulsation. For example, Di Giacomo *et al.* (1991) have derived a value of 2450 K for the effective temperature of R Leonis on the basis of an infrared occultation measurement made in a relatively uncontaminated region of the spectrum. This can be compared with our first overtone measurement of 2417 ± 134 K. Similarly, the interferometric measurement of o Ceti by Ridgway *et al.* (1992), when corrected for their error in applying a limb darkening scaling factor, gives a value for $T_{\rm eff}$ of 2720 K: quite similar to our first overtone temperature of 2796 ± 194 K.

3.6 Stellar Distances

In order to convert an angular diameter measured interferometrically into a linear diameter, it is necessary to know the distance to the star. Unfortunately, there are no examples of Miras within the effective range of conventional photographic astrometry, thus hampering efforts to calibrate the distance scale for these objects. Despite this, a number of methods for computing distances have been proposed. Most approaches have been based upon establishing relationships between the spectral type and the luminosity (Rowan-Robinson & Harris 1983; Celis 1984), the mass and luminosity (Wyatt and Cahn 1983) or the period and luminosity. Of the latter type, a number of workers have concentrated on visible period-luminosity (PL) relations (Foy *et al.* 1975) and period-luminosity-colour (PLC) relationships (Celis 1980; 1981), whilst Feast *et al.* (1989) gives both PL and PLC relationships for the infrared. Of these, the most reliable are those of Feast *et al.* (1989), which are based upon studies of Miras in the Large Magellanic Cloud (LMC). We give both their PL and PLC relations (solutions 5 and 21 respectively) for the absolute K magnitude, M_K, in the case of oxygen-rich miras:

$$\text{(Period-Luminosity)} \qquad M_k = -3.47 \log P + 1.01 \tag{3.2}$$

$$\text{(Period-Luminosity-Colour)} \qquad M_k = -4.58 \log P + 2.00(J - K) + 1.24 \tag{3.3}$$

where P is the period, J and K the magnitudes in those infrared bands. The estimated uncertainty on the derived distance modulus, σ_M, was given by Feast *et al.* (1989) as $\sigma_M = 0.13$. We have also followed the authors in adopting a distance modulus of 18.47 to the LMC.

Wood (1990a) has suggested a correction to the PL and PLC relationships of Feast *et al.* (1989) to account for differences in metallicity between galactic and LMC Miras. This has the effect of making the predicted stellar distances 12% closer. However, since this is based entirely upon theoretical considerations and there has so far been no convincing supporting observational evidence, this result has not been adopted here. With the use of periods from Kholopov (1987) plus J and K photometry obtained as described in the previous section, the absolute K magnitude for each star could be derived with the PL and PLC relations. It was then straightforward to compare these with the apparent magnitudes, thus yielding estimates of the distance which are given in Table 3.4.

The errors on the distances given in Table 3.4 have been computed taking into account the scatter from the PL and PLC relations of $\sigma_M = 0.13$, plus the uncertainty in the mean J and K magnitudes of 0.1 mag. This gave relative errors in the quoted PL distances of 8%, whilst those for the PLC relationship were 15%. This larger uncertainty for the PLC based distances originates from the fact that the uncertainty in the J and K magnitudes represents the major contribution to the error, and the PLC relationship is more strongly dependent upon these values. Thus, despite the fact that Feast *et al.* (1989) found that their data for LMC Miras were significantly better represented by a PLC than a simple PL relation, the PLC relation has

Table 3.4: Stellar distances from the PC and PLC relations of Feast *et al.* (1989). The J and K magnitudes were obtained as described in the previous section. The relations then yielded the absolute K magnitude, which could be compared with the apparent K magnitude to give the distance.

Star	Period	m_J	m_K	PL law		PLC law	
				M_K	Dist.	M_K	Dist.
	(d)	(mag)	(mag)	(mag)	(pc)	(mag)	(pc)
o Cet	332	-1.30	-2.56	-7.74	110	-7.78	110
U Ori	368	0.65	-0.78	-7.89	265	-7.65	235
R Cnc	362	0.49	-0.85	-7.87	255	-7.80	245
R Leo	310	-1.30	-2.42	-7.63	110	-7.93	125
R Hya	389	-1.20	-2.50	-7.98	125	-8.02	125
W Hya	361	-1.50	-3.00	-7.86	95	-7.47	80
R Aql	284	0.65	-0.80	-7.50	220	-7.10	180
χ Cyg	408	-0.86	-2.42	-8.05	135	-7.60	110
T Cep	388	-0.48	-1.70	-7.97	180	-8.18	200
R Cas	430	-0.40	-2.10	-8.13	160	-7.42	115

not been used further here as our photometry is not sufficiently precise to take full advantage of this.

Unfortunately, although for many of these stars distance estimates have been published, the results of different methods can disagree by factors as large as three. It is worth pointing out, however, that the distances given in Table 3.4 generally lie amongst the nearest of the literature values. Thus the linear stellar diameters which are estimated from these distances in the following section will be *smaller* than would otherwise result from using many published distances. For the star R Leo, the trigonometric parallax has recently been determined to high precision (Gatewood 1992) with the use of the Alegheny Multichannel Astrometric Photometer. The distance of 120 ± 15 pc is in good agreement with the result of both the PL and the PLC relationships given in Table 3.4. With the expected availability of high-quality parallax measurements from the *HIPPARCOS* satellite, it should be possible to further verify and improve the work presented here.

3.7 Physical Diameters and Stellar Dynamics

By combining the estimates of the photospheric angular diameters from Table 3.3 with the distances from Table 3.4, the linear radii of the stars could be found. Two estimates of the radius derived in this fashion are given in Table 3.5, one originating from the D and one from the E model profiles. As we shall see, these measurements of the stellar radii permit a study of the dynamical behaviour of the stars, and the resolution of the contentious question as to the pulsation mode of LPV's.

The first mode identification was made for old disk miras by Wood (1975) who identified first overtone pulsation from theoretical modelling studies. This was subsequently supported observationally (Robertson & Feast 1981; Glass & Feast 1982) using effective temperatures inferred from infrared photometry together with luminosities from PL relationships. Further confirmation came from studies of metal-rich Miras and semi-regular variables in globular clusters (Whitelock 1986; Perl & Tuchman 1990). However, dynamical models of Mira atmospheres, which predict shock-front speeds in good agreement with observed CO velocities have strongly favoured fundamental-mode pulsation (Hill & Willson 1979; Willson 1983). Until recently, there seemed to be some consensus that overtone pulsation could not be made to account for the observed line velocities (Wood 1990a; 1990b). In contrast, however, Tuchman (1991) has modelled the pulsation acceleration and finds that the observations are inconsistent with fundamental pulsation, and that Miras are pulsating in the first overtone.

The linear stellar radii derived in this work can be used to determine the mode of pulsation unambiguously (see *e.g.* Hughes 1993). This relies upon obtaining a measurement of the *pulsation constant* Q given by:

$$Q \;=\; P\left(\frac{M}{M_\odot}\right)^{\frac{1}{2}}\left(\frac{R}{R_\odot}\right)^{\frac{-3}{2}} \tag{3.4}$$

where P is the period in days, whilst M and R are the stellar mass and radius respectively. As the period P is easily measured, and the mass M is thought to be reasonably well constrained to $\sim 1\ M_\odot$, then the determination of the stellar radius leads to an estimate of Q – which is directly related to the dynamical state of the star. An alternative parameterization of the pulsation equation for the fundamental mode is given by the following equation (Wood 1990a):

$$\log(P) \;=\; -2.07 \;+\; 1.94\log(R/R_\odot) \;-\; 0.9\log(M/M_\odot) \tag{3.5}$$

Although no similar recent parameterization exists in the literature for first-overtone pulsation, Fox & Wood (1982) have tabulated Q values for a range of different stellar pulsators, including those in the first-overtone. The expected stellar diameters for fundamental and first-overtone pulsators, computed from Equations 3.5 and 3.4, and based upon the assumption that stars are of mass $1M_\odot$, are given in Table 3.5 for all stars in the sample.

Although the masses of Miras are still uncertain, primarily due to the effects of mass loss, they are expected to be low-mass objects, and a mass of $\sim 1M_\odot$ seems most likely for the stars in the sample. In this case, the diameter measurements clearly rule out fundamental-mode pulsation in *all* ten stars. This conclusion is graphically illustrated in Figure 3.10 which gives a plot of both measured and theoretically expected radii for a number of stars. It can be seen that the radii of most stars in the sample are too large to admit the possibility of fundamental-mode pulsation, even if the masses are as large as $1.5M_\odot$. On the other hand, the radii are seen to lie within a band for which stellar models of $1 - 1.5M_\odot$ overtone pulsators predict values which *are* consistent with the measurements. It is also interesting to note from the figure that the

Table 3.5: Linear Radii – predicted and measured. Columns 2 and 3 give the predicted radii for a $1M_\odot$ star pulsating in the fundamental and first overtone modes. The distances and angular diameters are from previous sections, and have been used to derive the linear stellar radius for both the D and E models given in the last column.

Star & Period (d)	Fundamental Radius ($R_\odot$)	1st Overtone Radius ($R_\odot$)	Dist. (pc)	Model	Ang. Diam. (mas)	Stellar Radius ($R_\odot$)
o Cet	233	365	110	D	38.0 ± 4.0	443 ± 59
332				E	33.6 ± 3.5	392 ± 51
U Ori	245	380	265	D	21.3 ± 3.7	606 ± 116
368				E	18.5 ± 2.6	526 ± 85
R Cnc	243	377	255	D	19.7 ± 3.8	536 ± 112
362				E	17.9 ± 3.6	487 ± 105
R Leo	224	355	110	D	43.4 ± 3.2	515 ± 56
310				E	37.4 ± 2.3	444 ± 45
R Hya	252	387	125	D	33.0 ± 4.1	442 ± 65
389				E	28.7 ± 3.3	384 ± 54
W Hya	243	377	95	D	51.8 ± 7.3	523 ± 85
361				E	46.2 ± 5.8	467 ± 70
R Aql	215	343	220	D	19.5 ± 4.4	459 ± 110
284				E	17.5 ± 3.7	412 ± 93
χ Cyg	259	394	135	D	32.8 ± 4.1	471 ± 70
408				E	28.9 ± 3.0	415 ± 54
T Cep	252	387	180	D	28.2 ± 5.4	545 ± 113
388				E	24.3 ± 4.4	470 ± 93
R Cas	266	401	160	D	28.6 ± 3.9	494 ± 78
430				E	24.9 ± 2.9	430 ± 61

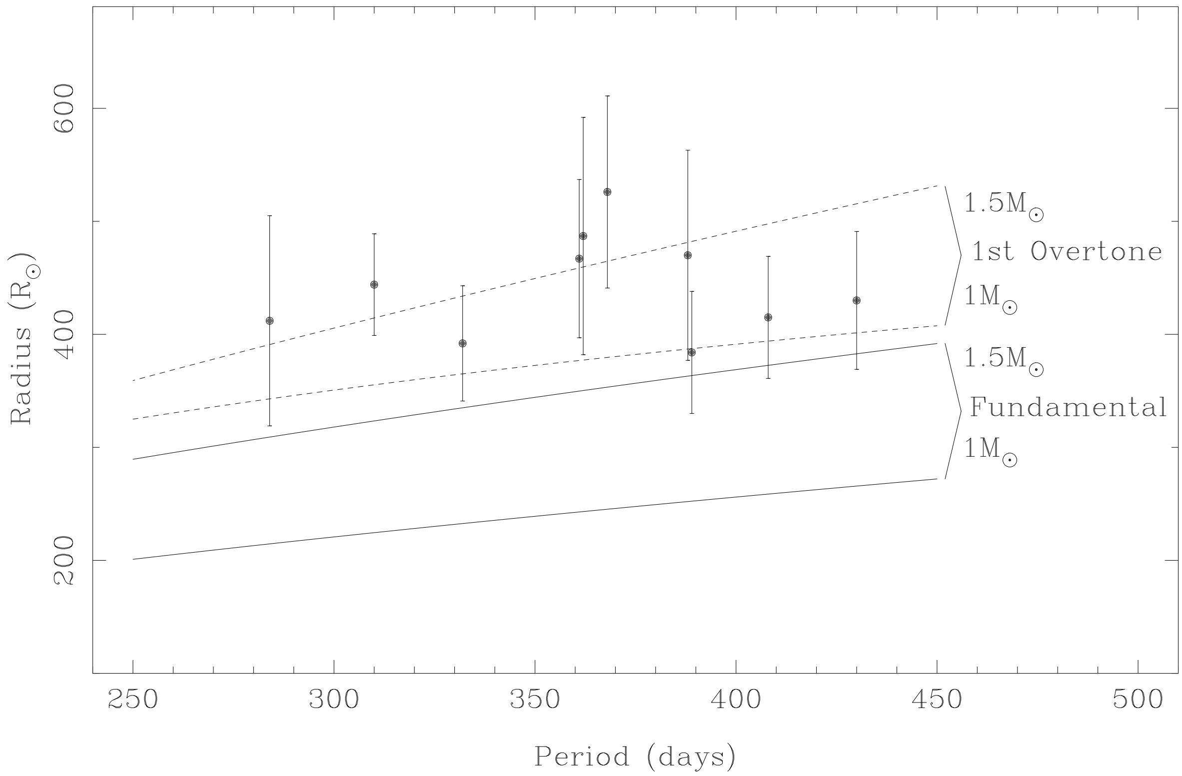

Figure 3.10: Stellar radii plotted against pulsation period for the 10 Miras in our sample. Also shown are theoretical curves for a 1 and a 1.5 $M_\odot$ mass star pulsating in the fundamental mode (solid line) and in the first overtone (dashed line).

radii of all the stars seem to lie in a band from about 400 to 500 $R_\odot$, and (given the errors) are consistent with an even narrower spread. This supports Feast *et al.* (1989) who suggest that Miras are a physically well-defined class of object occupying an instability strip of finite width in the HR diagram.

Before the final conclusions are drawn, it is necessary to reassess critically a number of aspects of the development of the argument, highlighting any potential uncertainties or further possibilities. Although the quasi-monochromatic diameters themselves are well constrained by the data, the process of conversion of these into photospheric diameters bears examination. This was achieved with the models of Scholz (1994) and in the process of doing so, a number of deficiencies were identified in the model brightness profiles (see Section 3.4). These problems were, however, only manifested at the shorter (700 & 710 nm) wavelengths which generally did not contribute to the final analysis, and more importantly, the derived photospheric diameters were in good agreement with independent measurements obtained in the near-infrared (Di Giacomo *et al.* 1991; Ridgway *et al.* 1992). This provides strong evidence that the corrections for photospheric extension and limb darkening cannot be wrong by large factors, and in addition, rules out the possibility that some further effect (*e.g.* dust scattering) is causing the stellar disks to appear greatly extended.

Turning now to the stellar distances, although modifications to the PL relationship at the $\sim 10\%$

level have been suggested (Wood 1990a), it seems unlikely that larger departures could exist. This is borne out by the close agreement found in the case of R Leo between the derived PL distance and the directly determined trigonometric parallax of Gatewood (1992). Furthermore, where estimates of the distance to stars in the sample have been found to have conflicting values given in the literature, these are almost always further away which has the effect of making the stellar radius larger; thus precluding fundamental pulsation even more strongly.

Finally, some comment needs to be made on the masses of Mira variables. It seems to be generally accepted that the main-sequence progenitors to Miras are $\lesssim 2M_{\odot}$ stars, with those heavier than this evolving through the AGB without penetrating the instability region occupied by Miras (Wood & Cahn 1977; Cahn & Wyatt 1978). These results are based upon modelling of late stellar evolution, where relationships have been derived linking the mass to observables such as the luminosity and the pulsation period. With the use of these, Wyatt & Cahn (1983) give the main-sequence masses of 9 of the 10 stars in our sample: all are found to lie between 1 and $1.35M_{\odot}$. Note that stars are likely to be substantially lighter than their main-sequence progenitors because of their individual mass-loss histories. Unfortunately, observational verification of these theoretical results is scanty. Although a handful of Miras are in known binary systems, very few instances of direct determination of their masses have been made. Fernie (1959) used visual orbital information for X Oph combined with velocity data to estimate the mass of this star as $1M_{\odot}$. However since observations covered only one-tenth of a complete orbit, this value is probably not accurate to a factor better than two. Thus it does not seem possible observationally to rule out substantially higher mass ($\gtrsim 1.5M_{\odot}$) stars for which fundamental-mode pulsation could be occurring.

Unless such a radical revision of the generally accepted masses of Miras can be entertained, it seems highly unlikely that stars with periods falling in the range from 280 to 430 days can be pulsating in the fundamental-mode. This conclusion is consistent with many earlier studies (*e.g.* Wood 1975; Robertson & Feast 1981; Glass & Feast 1982; Whitelock 1986; Balmforth *et al.* 1990; Perl & Tuchman 1990; Barthès & Tuchman 1994) and it is to be hoped that the discrepancy between the observed and predicted pulsational velocities for overtone pulsators found by workers such as Wood and Willson (see *e.g.* Wood 1990b for further discussion) can be resolved – for example by the nonlinear modeling of accelerations (Tuchman 1991).

Although we appear to have ruled out fundamental-mode pulsation for the sample stars, a number of interesting questions remain. It is important to note that first-overtone pulsation has *not* been definitely established, and that stars could be pulsating in still higher (*e.g.* second-overtone) modes. In addition to predicting overtone pulsation in Miras with periods greater than 150 days, Robertson & Feast (1981) suggest that those with shorter periods are anomalous and may be fundamental pulsators. High-precision parallax measurements from the *HIPPARCOS* mission, together with monochromatic angular diameter measurements, obtained at the new 10 m class telescopes or at dedicated astronomical imaging interferometers such as the COAST array, should provide answers to these questions.

3.8 Stellar Morphologies

Useful morphology information could not be extracted for the majority of observations of LPV's presented in Appendix A. Only in cases where the angular size of the target was large enough to permit good sampling of the visibility function was it possible to go beyond the investigations of angular size and limb darkening presented in the preceding sections. These conditions were easier to attain at the shorter wavelengths (633, 700 and 710 nm), since the system resolution was somewhat higher, and the stellar atmospheres were apparently more extended. Those observations for which stars were sufficiently resolved, and for which the seeing, received flux and system performance combined to give data of sufficient quality are presented in Appendix B. For all stars listed in this appendix, diffraction-limited images were reconstructed with the use of the MEM algorithm and extensive model-fitting to the data was performed.

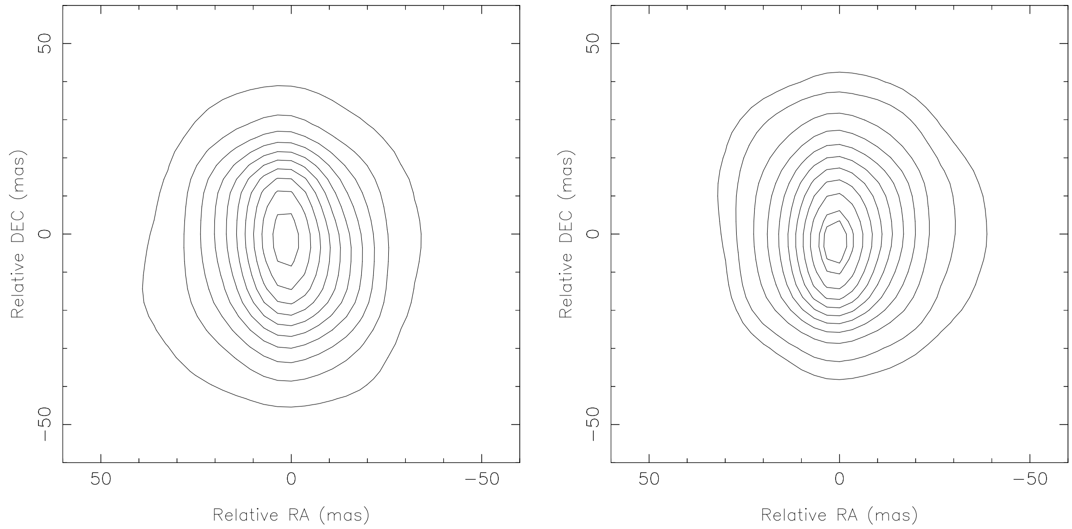

Figure 3.11: MEM-reconstructed maps of R Cas at 710 nm from data taken in July 1992 (left) and September 1993 (right). North is to the top and east to the left. The contour levels are from 5 to 95% in increments of 10%.

Examples of stellar images are presented in the contour maps of Figure 3.11 which shows R Cas to be highly distorted over two separate epochs. We follow the case of R Cas for the moment in order to illustrate the procedure by which morphology information for the Miras was extracted from the data. The question arises as to whether the elongation was due to an elliptical distortion or to bright asymmetric features. Although some non-centro-symmetry is visible in the MEM maps, these do not provide conclusive evidence either way, and we must refer back to the raw Fourier data. These are presented, for the July observation, in Figure 3.12. The sinusoidal wave in visibility on the longer baselines shows that some strong distortion must be present. However, in this case the systematic and non-zero nature of the closure phase signals indicates that the brightness distribution is non-centro-symmetric. Thus the 'disk + 2 bright spots' model has been fitted to the data, and can be seen from Figure 3.12 to give a close approximation to the observed visibility and closure phase signals.

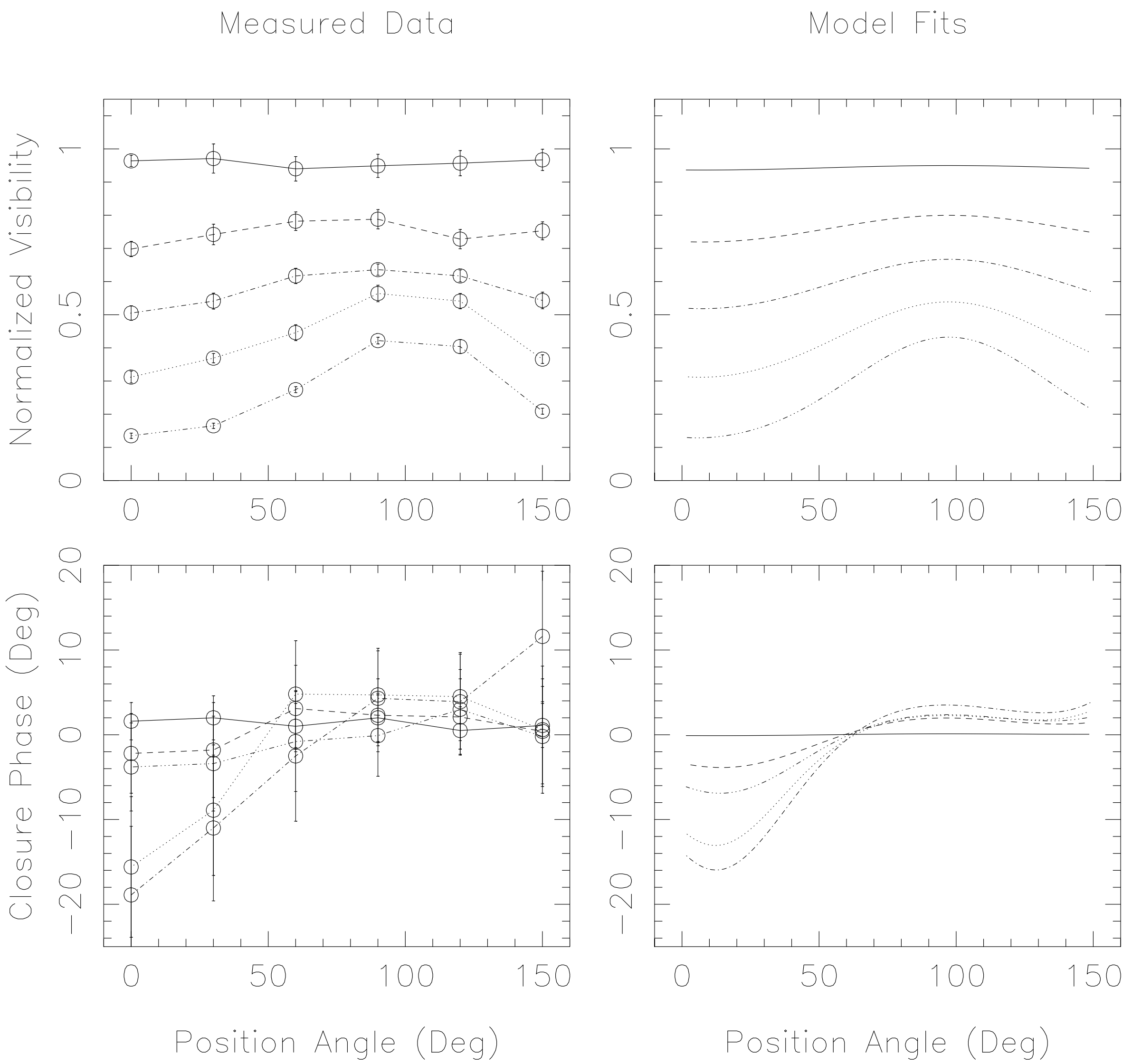

Figure 3.12: Measured Fourier data (left) and the corresponding fitted model curves (right) for R Cas at 710 nm in July 1992. Visibilities for various baselines sampled by the slit mask are presented in the upper panel, whilst closure phases for five different triangles are given in the lower panel. The model producing the smooth curves consisted of a circular Gaussian profile with two bright spots.

Table 3.6: Morphology information for selected Mira-type variables.

Object	Epoch	Morphology	Symmetry	Confidence
o Cet	Jan 92	Elongation at 60°.	Unknown	high
	Jul 92	Disk with (3?) bright features.	Asymmetric	fair
	Jan 93	Elongation at 25°.	Unknown	low
	Sep 93	Disk with 1 bright feature at 50°.	Asymmetric	high
	Dec 93	Disk with 1 bright feature at 120°.	Asymmetric	fair
R Leo	Jan 92	Disk with 1 bright feature at 115°.	Asymmetric	high
	Jun 93	Elongation at approx. 0 to −30°.	Unknown	low
W Hya	Jun 93	Elongation, PA 100°.	Unknown	fair
χ Cyg	Jul 92	Elongation at 5°.	Unknown	low
	Jun 93	Disk with 1 bright feature at 160°.	Asymmetric	high
	Sep 93	Elongation at 80°.	Unknown	low
R Cas	Jul 92	Disk with 2 bright features at 0° & − 160°.	Asymmetric	high
	Jun 93	Elongation at 20°.	Unknown	high
	Sep 93	Disk with 1 bright feature at 180°.	Asymmetric	high

We now proceed to summarize the morphology results for Miras presented in Appendix B. Initially, only visibility information was considered in order to determine if any distortion from circular symmetry existed. This was done by fitting elliptical Gaussian disks to the data, the results for which are presented in Table B.1 (in Appendix B). In cases where the closure phase signals had adequate signal-to-noise (this was less likely when the slit mask was used), further interpretation in terms of asymmetric features was possible. Details of models and raw data for each star individually are then given in Appendix B. Table 3.6 briefly summarizes these results – giving an outline of the stellar morphology and level of confidence in the result for each star and at each epoch.

One of the most interesting results of the morphology analysis is that there seemed to be no cases where a star was clearly identified as being *symmetrically* distorted. That is to say, in all cases where the closure phases had a small error, they demonstrated some excursion from zero and it was possible to identify the non-symmetric model (disk + spot) as being favoured over the symmetric (elliptical) model. It thus seems probable that in *all* cases where departures from circular symmetry exist, bright features on the surface of the star were responsible. Proof of this conjecture requires further observational study with a strong emphasis placed upon recovery of phase information.

In addition to the standard quasi-monochromatic imaging experiments already described, one further experiment was performed in order to test whether there were any detectable differences in morphology when a star was observed in the light of two orthogonal polarizations. o Ceti was observed at 830 nm, firstly with a linear polarizer set to pass light with an electric vector parallel to the expected axis of elongation, then with the electric vector perpendicular. This experiment yielded the result that there was no significant difference in morphology detected for light of the two polarizations. However, further measurements are necessary to confirm this since the observations were made under conditions of poor seeing. Future observations would benefit from the use of a shorter shorter wavelength filter, since the star is likely to be more resolved, and thus changes in the brightness distribution easier to detect.

3.9 Time Evolution

The only LPV's for which good observations covering a number of epochs exist were o Ceti, χ Cyg and R Cas, and it is upon the temporal behaviour of these stars that we will focus in this section. Data taken over number of different observing sessions was inherently difficult to compare since equipment, techniques and conditions could vary between observations. Discussion in this section relies upon results presented in more detail in Appendices A and B.

One example of an object for which comparisons between observations at different epochs could not be made with a high degree of confidence was χ Cyg. For two of the epochs, July 1992 and September 1993, this star was too faint to yield high-quality Fourier data and it was only in June 1993 that the morphology could be clearly established. Despite this, measurements of the angular diameter from Appendix A at 700 nm, did seem to indicate changes in size which were larger than the errors on the measurements. The star was smallest in June 1993 near the optical maximum, and larger by some 10 – 20 % at the other two epochs. The existence of a bright feature at about 165° during the June 1993 observations does seem reliable, however the data alluding to further changes at the other epochs in Appendix B was not of high quality.

Data was taken at three epochs for R Cas: July 1992, June 1993 and September of 1993. A remarkable consistency was observed, both in terms of angular size and morphology over this period. Diameters at all wavelengths were found to be the same to within 5 %, and also the dramatic elongation along a position angle of approximately 0° was observed to persist with an observed axial ratio of 0.7 for July 1992 and 0.8 for June and September 1993. Bright asymmetric features were found to be responsible for these distortions.

Observations of o Ceti over five epochs have shown this star to exhibit complex behaviour, with marked changes in size and morphology. Figure 3.13 summarizes the FWHM of Gaussian models fitted to visibility data at various epochs and colours. The two epochs of data at JD 2448260 and 2448523 were obtained from re-analysis of data taken by Wilson (1992). It can be seen from the figure that whilst the 833 and 902 nm diameters were not found to suffer large excursions, the angular sizes at 700 and 710 nm did undergo marked changes. Particularly dramatic are the last two epochs beyond JD 2449000 corresponding to September and December 1993, where the 700 nm diameter was seen to increase by 35 % and the 710 diameter by 40 – 60 %. It is interesting to note that these changes do not seem to be correlated with the variability phase.

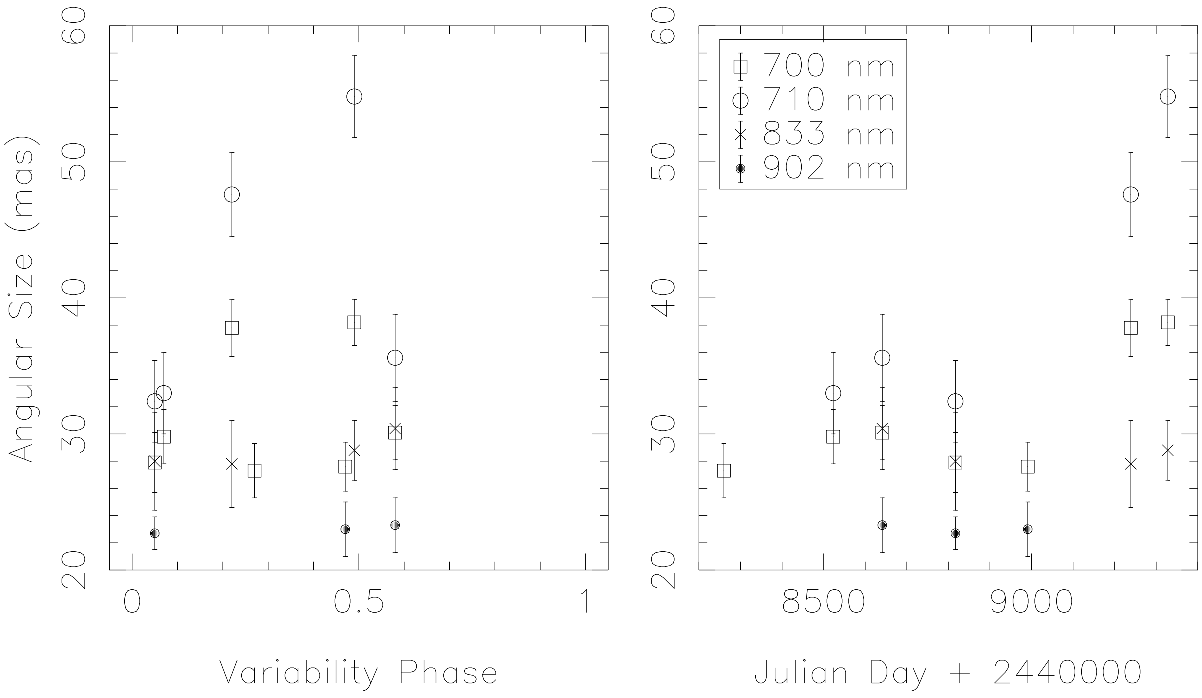

Figure 3.13: Full-width half maxima of Gaussian models fitted to visibility data on *o* Ceti taken through different filters and at a number of epochs. The panel to the left shows angular size data plotted as a function of the variability phase, whilst to the right the same data is plotted against Julian Date.

When plotted against this (left panel Figure 3.13) the data show little clear structure, with a number of different observations, all at almost identical phases, giving very different diameter estimates. Thus the large increase in size at 700 and 710 nm would not seem to be simply related to the pulsation cycle.

The morphology of *o* Ceti over the period of observation seems to have been dominated by the presence of bright features distorting the disk. Although it is possible that consecutive observations did show similarities due to some long-lived feature, there were no clear cases of this noted. There was, however, strong evidence of significant changes in the numbers, locations and fluxes of bright regions upon the surface of *o* Ceti. Some of the features of *o* Ceti's morphology and behaviour are summarized in the time-sequence of MEM maps shown in Figure 3.14. In particular the first four maps correspond approximately to light maximum, minimum, maximum and minimum of two full pulsation cycles. The final two epochs show the increase in angular size already described, although for these and the other maps, it can be difficult to see underlying asymmetries which are apparent in the raw Fourier data.

3.10 The Origin of Asymmetries

Although a number of early speckle interferometry programs concentrated upon objects such as *o* Ceti and R Leo (Labeyrie *et al.* 1977; Bonneau *et al.* 1982), only recently have authors noted

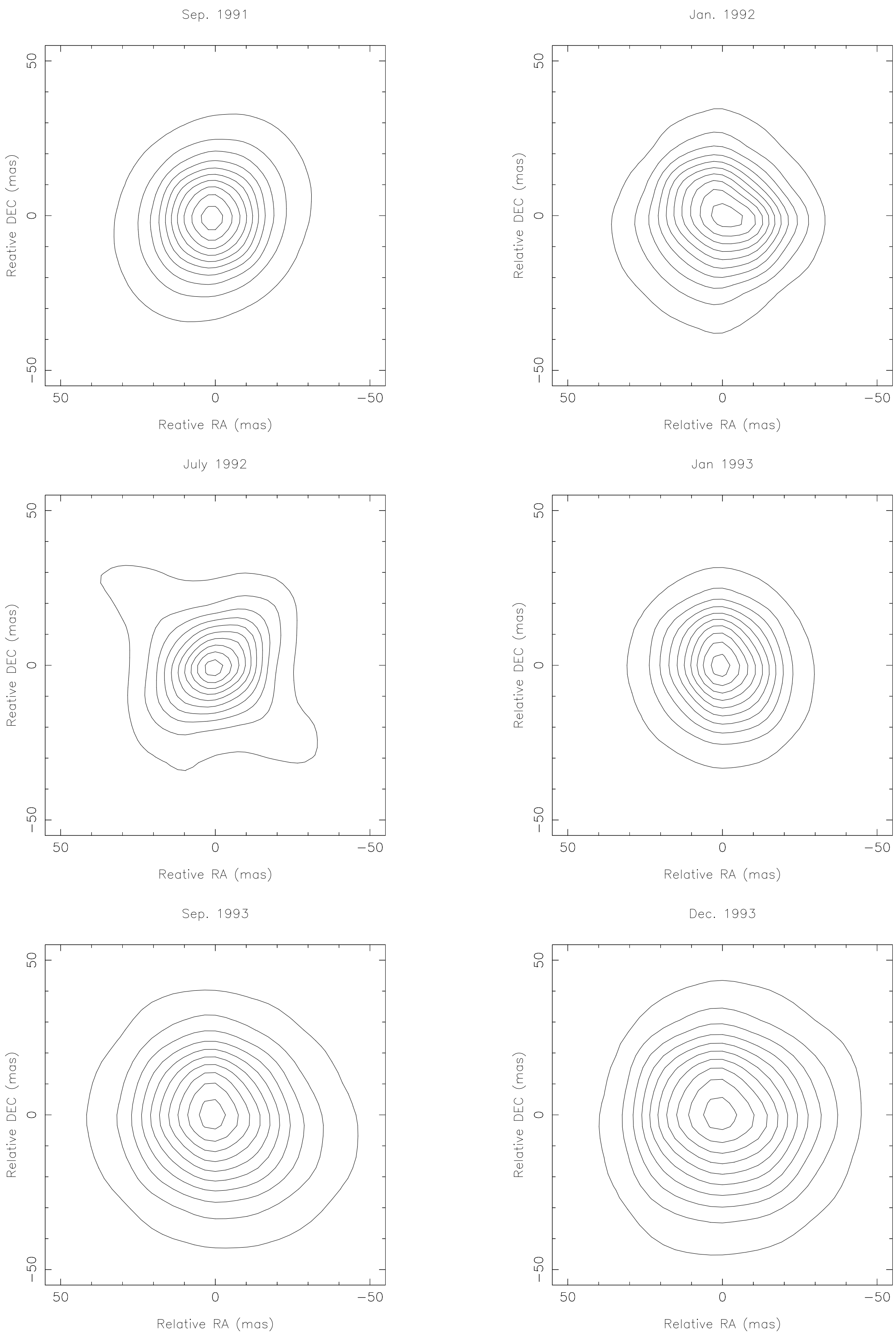

Figure 3.14: MEM maps of o Ceti at 700 nm from data taken at 6 separate epochs. Maps have contour levels from 5% to 95% in increments of 10%. North is to the top and East to the left.

departures from circular rotational symmetry. The first such detection at optical wavelengths (Karovska *et al.* 1991) showed *o* Ceti to exhibit distortions which were interpreted as an ellipticity of the photosphere. Data from four sets of observations over a period from November 1983 to November 1988 were presented, and it was concluded by the authors that large changes in the position angle of the elongation had occurred. The non-circularly symmetric nature of *o* Ceti's atmosphere was verified by Haniff *et al.* (1992) and Wilson *et al.* (1992) with NRM observations in September 1990 and January 1991 respectively, and also by Quirrenbach *et al.* (1992) from a number of observations made with a separated-element Michelson interferometer towards the end of 1990. These authors all interpret their data in terms of an ellipticity of the photosphere. Wilson *et al.* claimed that their observations combined with those of Karovska *et al.* (1991) demonstrate that the position angle and axial ratio remained fairly constant at 120° and 0.85 over at least 4 pulsation periods of the star from 1987. Quirrenbach *et al.* (1992) however, suggest to the contrary, that their data show large variations from cycle to cycle over the same period.

Interferometric studies at optical wavelengths presenting detailed morphology information for LPV's other than *o* Ceti have not been found in the literature. In explaining the cause of asymmetries in the brightness distribution of Miras a number of possibilities present themselves. These are discussed in some detail below.

(I) *o* Ceti has long been known to be a member of a close binary system and the star's upper atmosphere could be affected by this orbital motion. However, recent speckle observations (Karovska 1993) suggesting a period much longer than 400 years renders the possibility of strong tidal or other gravitational interactions unlikely. Two further arguments count against this scenario. Firstly, there were large changes in morphology, evident from previous studies and in this work, occurring on very much shorter timescales than the orbital period. Secondly, there were also distortions detected in other stars (such as R Cas) which have no known companion. It is worth pointing out that *o* Ceti's companion was not detected at the wavelengths used here, and was probably too faint to affect the imaging results for that star.

(II) A somewhat speculative scenario envisages the presence of a very close companion at an earlier period of the star's history. As the star evolves onto the giant branch and the stellar envelope swells, this companion star would be engulfed. Although considerable asymmetry could be generated on the surface under such circumstances, this common-envelope phase is unlikely to last long with the companion spiraling rapidly into the core. This process could spin up the stellar envelope (which under normal circumstances would have a very small amount of angular momentum) thus the asymmetries are explained as the equatorial bulge of a rotating body. Rapid spin, however, would generate a fixed elongation and is not consistent with the observed changes of morphology. Moreover, this model should produce a smooth elliptical distortion whilst closure phase data presented in Section 3.8 clearly identifies asymmetric bright regions as being responsible for many deviations from circularity.

(III) The presence of asymmetric shocks, probably related to the pulsation of the star have been suggested as a possible origin for the observed distortions. Firstly, it is not clear whether flux from such regions could contribute significantly in the red and near IR spectral regions. Shock-induced local heating seems more plausible, and also avoids the problem that the observed weak wavelength-dependence of the surface structure is not consistent with emitting regions which are very much hotter than the underlying photosphere.

(IV) It has been suggested (Danchi *et al.* 1994) that the asymmetries at optical wavelengths may not result from distortions in the photosphere, but rather arise from scattering in an anisotropic circumstellar environment. Mass loss is particularly significant for AGB stars, and it has been well established that the circumstellar environments are often significantly anisotropic. In the case of o Ceti, an extended bipolar outflow has been detected in CO $J = 2 \rightarrow 1$ and $J = 1 \rightarrow 0$ emission (Planesas *et al.* 1990). Dyck *et al.* (1984) have found deviations from circular symmetry for the dust shells around number of AGB stars in the near-IR (1.65 – 4.8 μm), including a north-south elongation for χ Cyg. Further evidence that the mass-loss process is not spherically symmetric comes from a number of sources including studies of planetary nebulae (*e.g.* Zuckerman & Aller 1986) and polarimetric investigations of stars undergoing mass loss (Johnson & Jones 1991). A number of questions need to be addressed to make this model more credible; namely whether the scattering process can be efficient and anisotropic enough to account for the large amount of flux (over 10%) observed in the spots, and secondly how the large radii of the dust shells ($\sim$ 100 mas for χ Cyg) is consistent with the smaller ($\sim$ 20 mas) displacements of the bright regions. Further questions could be raised as to the whether the observed timescale ($\sim$ months) for morphology changes fits with the likely evolution of the circumstellar shell. As scattered light should be highly polarized, further testing of this conjecture could be made by observing a star in different polarizations. Section 3.8 has mentioned the results of one such experiment which indicate that there were no large differences in morphology for the different polarizations, contrary to expectations if the asymmetries are related to dust scattering. Finally, the agreement between our visible diameters and those obtained at around two microns (Di Giacomo *et al.* 1991; Ridgway *et al.* 1992) argues against significant dust scattering.

(V) The presence of non-spherical pulsations in o Ceti was suggested by Shawl (1974) in order to explain polarimetry and photometric data. Haniff *et al.* (1992) and Wilson *et al.* (1992) point out that observations at three separate maxima in the light curve from 1987 (Karovska *et al.* 1991) to 1990 exhibit an elongation at a constant position angle of approximately 120°. This, they argue, is suggestive of a causal link between the pulsation of the star and the apparent photospheric distortion. Further weight is added to this argument by noting that the elongation near maximum in June 1992 from Appendix B is again close to 120° (however, note the doubts as to data quality at this epoch). Additional observations of o Ceti near the maximum in 1993 do not, however, follow this trend. Evidence from observations of other stars is marginal. Although this hypothesis is attractive, it does not seem the most straightforward way to explain one further aspect of the observations: the fact that when good phase data was obtained objects were found to have bright asymmetric features rather than elongations.

(VI) Although Karovska *et al.* (1991), Haniff *et al.* (1992) and Quirrenbach *et al.* (1992) interpret their imaging data in terms of a simple elliptical elongation, they make no claim to have recovered phase data of sufficient quality to determine whether the flux distribution is centro-symmetric or asymmetric. That is to say: was it best fit by an elliptical distortion or a disk with a bright spot? Wilson *et al.* (1992) claim that closure phase data gave evidence that there was no compact bright feature on the stellar surface, thus vindicating their choice of the elliptically distorted model. However, examination of their published phase data showed that there *were* significant and systematic departures from zero as might be expected from a bright spot. The fitting of such models to their data yielded a model of a disk with an asymmetric feature contributing about 14% of the flux, which was preferred over the elliptical model-fit given by the authors. For the observations presented here, it has been noted in Section 3.8 that in all cases where good closure phases were obtained, 'disk + spot' models were found to be superior to elliptical models. If it is true that all cases of departure from circular symmetry can be explained by the presence of compact bright features located away from the centre of the stellar disk, then one likely explanation for these is the presence of large convective cells. The dominance of a small number of such convective instabilities or supergranules in M-giant stars was suggested by Schwarzschild (1975), and seems to be the favoured model in explaining similar bright features detected on the surface of Betelgeuse (Chapter 4; Buscher *et al.* 1990; Wilson *et al.* 1992).

The most likely possibility of those given above seems to be that asymmetries are due to the hot tops of convective zones, as this is consistent with the measured visibilities, phases and timescales for change. In addition, the existence of the phenomenon has been predicted theoretically and also probably identified in observations of similar class of object: the M-supergiants (see Chapter 4). For imaging data which are partially resolved and often have poor or no phase information, such features could appear to present an elliptical distortion. In addition to further imaging observations, this scenario could be verified by combining imaging with polarimetry. The presence of Schwarzschild-type convective cells has been suggested as the origin of the time-variable polarizations noted for LPV's (Boyle *et al.* 1986), and an initial attempt to correlate the position angles of the observed distortion and of the polarization vector was made by Karovska *et al.* (1991). This process is complicated by the detailed behaviour of the polarization with wavelength and is further discussed for the case of Supergiants in Section 4.7.

3.11 The Diameter Variation of o Ceti

One further aspect of the stellar morphology and its time-evolution warrants discussion: the observed changes in size over different epochs. The simplest models of the atmospheres of LPV's would simply link the angular diameter to the pulsation cycle, with the star executing regular changes in size according to the phase. Although Quirrenbach *et al.* (1992) have performed an analysis of the the diameter variation of o Ceti with the use of data from 3 epochs near to the light maximum of late 1990, their results are difficult to compare directly with ours since they have used a model consisting of two large overlapping elliptical disks to interpret the measurements. They report significant changes in size at a wavelength of 800 nm between observations only one month apart. They attribute these variations to infalling material at velocities around 15 km/sec, and also to changing opacities in the outer atmosphere.

Although there are not enough observations presented here to follow the stars χ Cyg and R Cas closely through their pulsation cycles, it is worth briefly recalling the results from them. The size of χ Cyg at 700 nm was seen to vary, with the FWHM of Gaussian functions fitted to the data changing by 10 to 20% between epochs. On the other hand, variable behaviour was not noted for R Cas where observations at three different phases gave diameters which agreed with each other to within 7% (within the errors of the measurement). It does not appear that clear periodic behaviour with pulsation cycle as suggested by the atmospheric models of Scholz (1994) was observed, although the sampling of the variability cycle was too sparse for both stars to draw strong conclusions.

The only object for which measurements were taken at a significant number of epochs was o Ceti. It was seen in Figure 3.13 that the diameter variations in o Ceti did *not* seem to be correlated in a simple way with the pulsation phase. Unlike R Cas however, o Ceti did exhibit significant changes in size: notably an extreme enlargement at the wavelengths of 700 and 710 nm towards the end of 1993 (Section 3.9). Behaviour similar to this has not been reported in the literature, and is perhaps one of the most novel and interesting findings of the high-resolution imaging program.

One possible interpretation of these results relies upon a physical instability which has been found in hydrodynamical models of the atmospheres of Mira variables (Wood 1979; Willson & Hill 1979; Hill & Willson 1979; Drinkwater & Wood 1985). This is manifested as a tendency for pulsation generated shocks injected from the deep photosphere into the intermediate layers to slow down due to the presence of regions of infalling material generated by the passage of previous shocks. After a number of pulsation cycles, complex behaviours such as semi-regular modulation of the amplitudes of shocks were observed. In particular Wood (1979) and Drinkwater & Wood (1985) found that a number of shocks eventually coalesce into a single large shock capable of exceeding the escape velocity and driving through the outer atmosphere. Such aperiodic behaviour was not, however, reported in the more recent detailed numerical models of Bowen (1988).

The existence of irregular pulsation in the layers above the photosphere helps to explain a number of earlier observations. The velocities of metallic absorption lines have long been known not to show any strong correlation with pulsation phase (Joy 1954). This has been interpreted as indicating aperiodic behaviour in the shocks at upper atmospheric levels (Hill & Willson 1979). In addition, circumstellar absorption lines indicative of multiple discrete expanding shells around mass-losing stars (Bernat 1981; Ridgeway 1981) are consistent with the picture of mass driving by occasional coalesced shocks.

The presence of a non-periodic shocks is an attractive explanation for the observed enlargement of o Ceti for a number of reasons. Firstly, the models of Drinkwater & Wood (1985) predict that a shock sufficiently strong to escape altogether only occurs occasionally: about once in 10 or 20 pulsation cycles. This is in keeping with the prior behaviour of this star, which has not been seen to exhibit such large fluctuations at any time over the decade prior to the outburst of late

1993 (see Wilson *et al.* 1992; Karovska *et al.* 1991). Secondly, the enlargement was seen to be highly pronounced in the titanium oxide band around 710 nm, less so where more continuum light is observed at 700 nm, and not detected at all to within the errors of measurement at 833 nm in a polluted continuum spectral region. This is consistent with a relatively diffuse shell of material scattering only those wavelengths for which the stellar atmosphere has a very high optical thickness – *i.e.* in the metal oxide bands (which are also known to show aperiodic line velocities as mentioned above). Thirdly and finally, using angular diameter measurements taken from Appendix A and a distance to o Ceti of 110 pc (from Section 3.3), it was possible to compute that the observed changes in angular size correspond to linear velocities at the star in the region of $10 \sim 15$ km/sec. These are of the right magnitude to be atmospheric shocks as described in the models of workers such as Wood or Willson. However, it is important to point out that the observed diameter variations might not be entirely due to physical motion of the emitting material. Changes of opacity such as might be expected from heating or cooling of regions of the stellar atmosphere may also play a role in the apparent changes in angular size.

Away high high in the East swung Remmirath, the Netted Stars, and slowly above the mists red Borgil rose, glowing like a jewel of fire. Then by some shift of airs all the mist was drawn away like a veil, and there leaned up, as he climbed over the rim of the world, the Swordsman of the sky, Menelvagor with his shining belt.

J.R.R. Tolkien
from 'The Fellowship of the ring'

Chapter 4

Supergiants

4.1 M-Supergiants

M stars of luminosity class I comprise some of the largest and most powerful stars known. They are generally believed to arise from more massive progenitors than the Mira-type variables discussed in the previous chapter, and have been found to exhibit quite different behaviour. Although they do often vary in brightness, cycles are often far less regular – falling into the semiregular and irregular categories. Light amplitudes are much shallower than for Mira-type variables. In common with Miras, however, they possess extended and complex atmospheres in which both convection and pulsation are thought to play significant roles.

The spectra of supergiants exhibit similar features to those discussed for LPV's (Section 3.1), however whilst most of the LPV's had a spectral type of M6 or later, the supergiants presented in this chapter are all of types M1 or M2 with the exception of Rasalgethi with a spectral type of M5. Thus many of the dominant features in the spectra of LPV's, such as the TiO absorption bands, were much less pronounced for these stars. The wavelength dependence of the diameter of the molecular atmosphere was correspondingly less extreme (Quirrenbach *et al.* 1993).

With the use of the high angular resolution imaging techniques, it was possible to address a number of important questions relating to stellar atmospheres and their behaviour.

4.2 Interpreting the Observations

The extraction of information from data taken with the imaging apparatus of Chapter 2 has already been described in some detail for the case of LPV's in Section 3.2. Those remarks are equally relevant to results presented in this chapter, however there was some shift in emphasis for a combination of experimental and astrophysical reasons. Since most of these stars were brighter and less variable than the Miras, data were generally of a higher quality and masks which passed a smaller amount of flux, such as the 5-hole non-redundant mask, could be used. The superiority of closure-phase signals recovered from such non-redundant (as compared to partially redundant) pupils has been mentioned in Section 2.5, and for many of the objects discussed in this chapter, recovery of full Fourier amplitude and phase information was possible. This was fortunate since the study of the detailed surface morphology was particularly relevant to understanding the processes within the supergiant atmospheres.

Diffraction-limited images were reconstructed from the data with the use of the MEM algorithm (Section 2.3) and a number of maps produced in this way are presented later in this chapter. These have been found to be particularly useful in yielding qualitative insight, and as a guide to assist in the process of fitting of models. Quantitative analysis has relied on the fitting of model distributions to the Fourier data, however this process was not straightforward. A more detailed description is given in the following steps:

1) Choosing a model.
Model distributions could be built up from a number of components including uniform-disks, Gaussian disks, unresolved spots, lines or shells. These could be varied in intensity, moved about or distorted (*e.g.* circles could become ellipses) in order to match the observed data. As there were no instances where strong variations in visibility with position angle coincided with closure phases clustered about zero, it was safe to assume that distortions were due to non-central bright features rather than smooth elliptical distortions. This assumption was vindicated by the use of the MEM algorithm which gave maps with bright spots superimposed on approximately round underlying disks. The next question in choosing a model was whether to use a uniform or limb darkened (Gaussian) profile for the underlying disk component. Although the Gaussians used in the case of LPV's were found to work well, the supergiants were not expected to have quite such extended molecular atmospheres and they should thus not be as highly limb darkened. The question was settled experimentally, with the attempted fitting of both types of underlying profile to a large number of datasets. In almost all cases, the uniform-disks produced a better fit and were adopted, although it should be pointed out that some limb darkening would certainly be expected for these stars. Thus, results are usually presented in terms of fits of a model consisting of a uniformly-illuminated circular disk with some number (from zero up) of unresolved bright features.

2) Fitting the model.
The model-fitting program attempted to reduce the mismatch between the observed visibilities and closure phases, and those predicted from the model's flux distribution. This was achieved with simple optimisation algorithms (*e.g.* 'hill-climbing') working on the free parameters in the model. For example, a uniform-disk with one bright spot would normally have a variable flux and diameter for the disk component, and variable flux, radius (displacement from origin) and position angle (from North) for the spot – yielding a total of 5 free parameters. Unfortunately, it would have been too slow and inefficient to simply search this entire parameter space for an optimal solution and the algorithm was restricted to hill-climbing and limited grid searches. It

was not possible to ensure that solutions obtained by these methods were globally optimum. Partial alleviation of this problem was made by starting the optimisation at a number of different points in the parameter space and ensuring that they converged to the same, or at least to an inferior solution. Luckily, in most instances, simple models converged to a single solution which was superior to all others, and the difficulties with uniqueness and reliability were only endemic for models with a large number of free parameters.

3) Testing the reliability of the model
Initially, data were always interpreted in terms of the *simplest* model *i.e.* a uniform-disk. More complex models were only used in those cases where the best fit from a simpler model was clearly not reproducing all the systematic behaviour evident in the data. An illustration is given in Figure 4.1. Although the best fitting 'uniform-disk + 1 spot' model does reproduce the broad sweep of the phase signal, there was still in this case a clear systematic residual. The addition of the extra spot for the 'uniform-disk + 2 spot' model can be seen to rectify this problem since these curves match well to most of the significant excursions in the measured data. Although it is more difficult to tell from the figure, the visibilities on the longer baselines were also more accurately reproduced. Thus in this case, the two-spot model was highly preferred over the one-spot. However the attempted fitting of a three-spot model is *not* indicated as the simpler two-spot was found to match well leaving little systematic residual. By this process, the final model chosen was always the *simplest* which could fit the observations well.

Observations of all supergiants studied – Betelgeuse, Antares, Rasalgethi and μ Cep – are listed in Appendix A, whilst a detailed presentation of bispectral data and the results of model-fitting is given in Appendix C. The remaining sections of this chapter discuss the target objects in more detail, with reference to the results contained in the appendices.

4.3 Betelgeuse

As one of the largest and brightest stars in the visible and near infra-red sky, Betelgeuse (α Orionis) has been a popular target for high resolution imaging experiments since the first stellar angular diameter measurement of Michelson and Pease (1921). Indeed, this star is the most thoroughly studied of all red giants, with research published using data from spectral regions from the radio to X-rays and encompassing a wide range of observational techniques. This wealth of information makes Betelgeuse an ideal test-case in the study of phenomena such as mass loss and variability which are ubiquitous to stars in the M-giant phase.

The details of observations of Betelgeuse over four epochs (Jan 92, Jan 93, Sep 93 & Dec 93) are given in Appendix A. As α Ori is very bright, high SNR measurements were made with the 5-hole non-redundant mask yielding good quality visibility and particularly phase information. These data are discussed in detail in Appendix C, where results from the fitting of model distributions are also given. Diffraction-limited images were also produced with the use of the MEM algorithm for a number of observations. These are given in Figure 4.2.

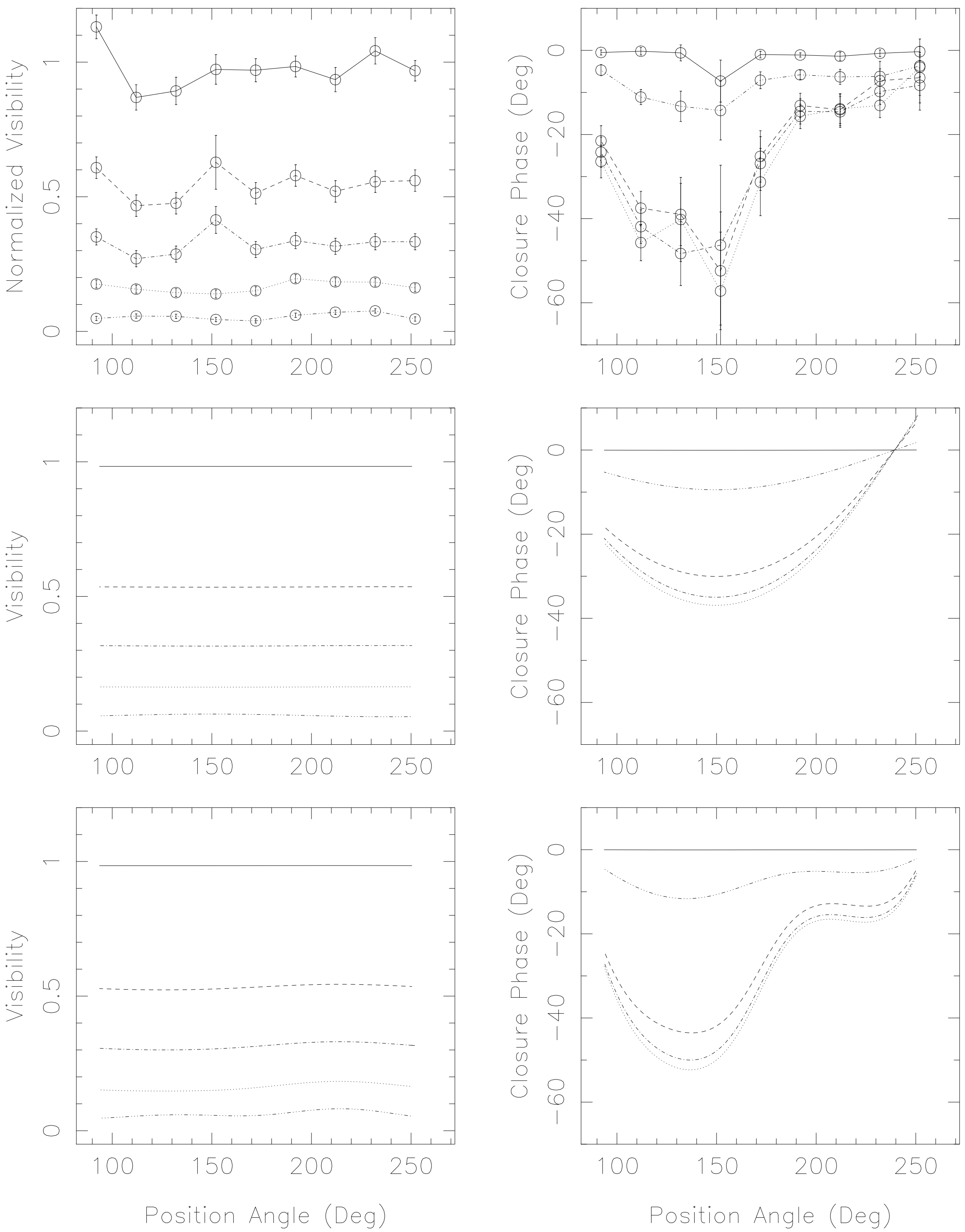

Figure 4.1: The upper panels show visibility and closure phase signals from December 1993 observations of Betelgeuse at 700 nm. The central panels show the fits obtained by the best 'uniform-disk + 1 spot' model, whilst the lower panels show fits from a 'uniform-disk + 2 spots' model.

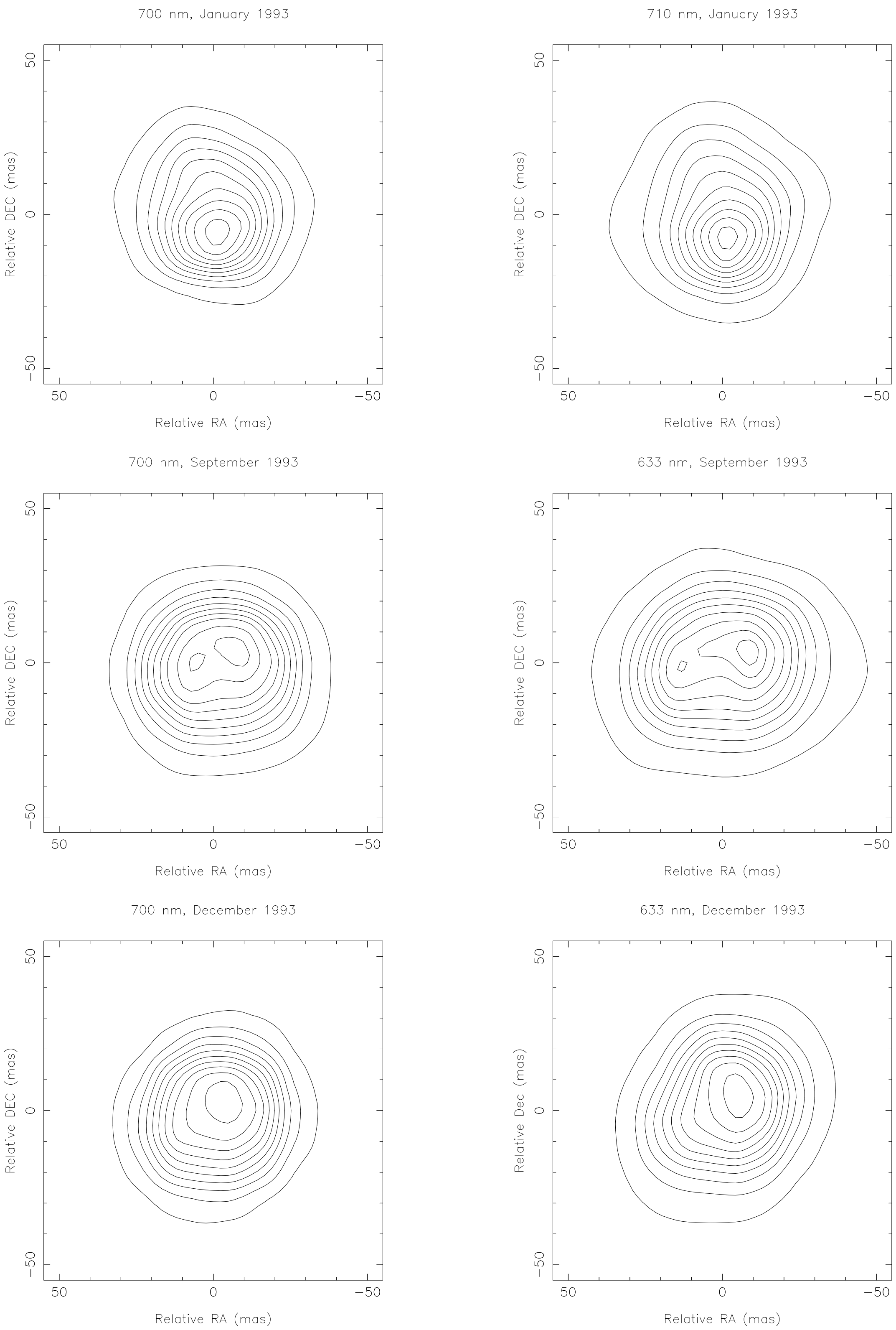

Figure 4.2: MEM maps of Betelgeuse at various wavelengths from data taken at 3 separate epochs in 1993. The topmost pair of images are from January, the middle pair from September and the lower pair from December. Maps have contour levels from 5% to 95% in increments of 10%.

The large excursions in the closure phase signal with position angle noted in data from *all* epochs confirm the existence of asymmetries in the brightness distribution of this object. It was found that good fits to these data could be obtained with the use of a model consisting of a uniformly-illuminated disk with 1 – 3 bright features contributing from 14 to 29% of the total flux. The results of this model-fitting were found to be qualitatively consistent with the diffraction limited maps produced by the MEM algorithm (Figure 4.2). This confirms previously reported detections of surface structure on this star (Buscher *et al.* 1990; Wilson *et al.* 1992 and references therein). NRM observations by these authors revealed bright features placed asymmetrically on the stellar disk which contributed between 10 and 25% of the flux. Earlier work with a shearing interferometer (Roddier & Roddier 1983) found a deviation from circular symmetry which could be explained by a feature contributing about 10% of the flux. Although observations from different epochs (both within this work and from previously published results) showed good consistency of general form, they differed markedly in detail. These changes were noted when bright spots were detected with different fluxes and at different locations upon the stellar disk for observations only months apart. On the other hand, the derived diameters were consistent with those found by previous authors (*e.g.* Balega *et al.* 1982; Cheng *et al.* 1986 Buscher *et al.* 1990; Wilson *et al.* 1992;).

At first sight it might appear from Appendix C that there was also variability of the morphology between observations at different colours but at the *same* epoch. Evidence for this is, however, weak since any apparent changes can be attributed to one of two effects. Firstly, if the data were noisy and/or the model not well constrained, the fitting routine could converge to somewhat different solutions, although the data themselves were quite similar. A common example of two morphologies which are inherently difficult to distinguish is (1) a bright spot at a small radius and (2) a fainter spot at a larger radius. Secondly, some differences can be ascribed to the differing angular resolution available at different wavelengths. Examples of this were the Sep. and Dec. 1993 observations where the extra resolution afforded at 633 nm (as opposed to 700 nm) was sufficient to result in the phase signals recorded being very much more complicated. Thus, more complex (3 spot) models were needed to fit the 633 nm data than the (2 spot) fits for the 700 nm data, and although the fits at the two wavelengths exhibited strong similarities, there were differences of detail.

The fact that there was no strong wavelength dependence of the amount of flux in the spots can be used to set limits on the minimum size of the bright regions. We begin by assuming that the bright spots are due to areas of higher temperature on the stellar disk. In order that there is no change in the ratio of the spot : disk flux at the level of a few per cent over 67 nm (the difference in wavelength between the 700 and the 633 nm filters), then the hotspots cannot be at a very much higher temperature than the disk. Combining this information with the fact that the spots contribute a significant fraction of the total flux, then the conclusion is that they must then be *large*. It can be shown (*e.g.* Wilson 1992) from constraints such as these that the bright features are no more than 400 K above the ($\sim$ 3500 K) effective temperature and occupy at least 5% of the area of the stellar disk.

It is interesting to note from the model-fits of Appendix C that fainter ($\lesssim$ 6%) spots almost invariably occur at larger ($\gtrsim$ 10 mas) radii. There are two possible reasons for this. One is that hotspots further from the centre of the disk will appear increasingly foreshortened from the viewpoint of the observer, and will thus appear less bright. Furthermore, limb darkening will cause objects which are close to the edge of the disk to be more obscured than those in the middle. It might be surmised that *all* hotspots in fact have similar intrinsic brightnesses (in the 10 – 20% range) and that most observed differences arise due to these two effects. If this is the case, hotspots might provide a 'standard candle' for directly probing the limb darkening function through a statistical analysis of a number of spot fluxes and radii.

We now turn to the question of the physical cause of the surface features on Betelgeuse. A number of scenarios have been suggested, including a companion passing in front of the stellar disk, effects related to stellar rotation, magnetic activity and large convective zones. The first of these can be ruled out by noting that the features do not exhibit regular orbits as might be expected from stellar companions. It is possible that magnetically controlled surface activity complexes exist on the surfaces of supergiant stars. However, in other magnetically active stars and in the sun, large scale magnetic features suppress convection and are therefore accompanied by a temperature decrease causing a local *dark* spot (Baliunas and Dupree 1982). An investigation as to whether the high-resolution imaging data are consistent with the presence of dark spots rather than the bright spots discussed until now was made. This consisted of the fitting of models comprising a uniform-disk with a number of features containing negative flux. The features were allowed to vary in position and intensity as with previous model-fitting. It was found in all cases that the data could only be adequately matched with the use of a 'dark spot' model containing very many more degrees of freedom than an equivalent 'bright spot' (this result was also found to hold for the other supergiants in this chapter). Thus, whilst it was not possible to rule out the presence of dark spots, adequate fits were much more contrived. Although it may be possible that in M-giant stars, magnetic activity is responsible for upwellings of hot matter, the low X-ray flux from Betelgeuse has been interpreted as indicating that magnetic fields are relatively weak (Belvedere, Chiuderi & Paterno 1982).

The most favoured model to explain the surface features is that of large scale convective cells on the stellar surface (Schwarzschild 1975). A small number of such regions are expected to dominate the surfaces of cool variable stars, and their presence has been invoked in explaining the observed irregular variations in magnitude and polarization (see Section 4.7) for these stars. It should, however, be borne in mind that magnetic fields and convection are intimately related and that both might feature in the dynamics of the hotspots.

One of the most exciting aspects of the results for Betelgeuse is that a single, proven high resolution technique has been in use from February 1989 to December 1993 and has collected data at seven separate epochs. It has thus been possible to begin the examination of one of the most hotly-debated aspects of the behaviour of this star: the time evolution of its surface. In particular, the characteristic timescale for the growth and decay of the surface hotspots has been investigated. Wilson (1992) set an upper limit of 9 months by noting that the pattern of hotspots had changed significantly from January to September of 1991. We now have access to two sets of epochs at smaller temporal intervals than this: September 1991

– January 1992, and September 1993 – December 1993. It was not possible to identify the same bright feature unambiguously in maps from September 1991 (Wilson 1992) and January 1992 (this work). Unfortunately, the poor quality of the January 1992 data (see Appendix C) made it impossible to be certain that no correlation existed. From the September 1993 and December 1993 observations, however, the brightest feature at both epochs exhibited almost identical parameters. Taking an average over the two colours, the data from September 1993 yielded a spot with $flux = 12\%$, $r = 4$ mas and $\theta = 38°$, whilst that from December 1993 yielded $flux = 13\%$, $r = 4$ mas and $\theta = 33°$. Thus the fluxes, radii and position angles of the features are almost identical and it appears highly likely that the same feature was present at both epochs. This is the first reported identification of the same feature appearing in maps taken at different (> few days) times, and the characteristic timescale for evolution of the hotspots has been found to lie between 3 and 9 months.

Although the measured linewidths of features in α Ori's spectrum would permit the interpretation that the changes are due to stellar rotation, angular momentum considerations would seem to preclude this. If the star started out on the main sequence with an average value of specific angular momentum (for $10M_{\odot}$ this is 2×10^{13} m^2/sec) its change of moment of inertia upon entering the giant-branch would result in a rotational period of 1 200 yr (Smith *et al.* 1989). As this is very much slower than the observed timescale for change, it seems likely that motions intrinsic to the surface structure are responsible for the observed evolution.

As we have placed limits on both the sizes and evolution times of the hotspots, it is possible to proceed to a discussion of the velocities of motion associated with the changes. A spot covering 5% of the disk's area will have a diameter of about one fifth that of the whole disk. Taking the distance to Betelgeuse as 110 pc (Danchi *et al.* 1994) and a typical angular diameter at 700 nm of 52 mas yields a linear diameter in this waveband of 1 200 $R_{\odot}$ (corresponding to a diameter of $\sim$ 5 AU). The velocities involved for spots of diameter 240 $R_{\odot}$ to change in 3 to 9 months are then in the range 5 – 20 km/sec. These velocities are large when compared with the photospheric sound speed of 3 – 4 km/sec (Smith *et al.* 1989) and even constitute a considerable fraction of the escape velocity ($\sim$ 42 km/sec assuming a mass for α Ori of $10M_{\odot}$). Such supersonic motions are suggestive of the presence of associated shocks in the stellar atmosphere. Furthermore, the hotspots could play a significant role in mass loss as material could be moving at sufficient velocities to carry it large distances above the stellar surface. Since observations of circumstellar dust around Betelgeuse suggest that material is non-isotropic (Sloan *et al.* 1993; Danchi *et al.* 1994 and references therein), some link may exist between mass loss and photospheric irregularities. One such model has been proposed (Goldberg 1986) in which matter is lifted by convective processes into a region where it cools sufficiently for the formation of dust grains. These are then accelerated away from the star by radiation pressure, possibly also carrying gas along through viscous processes.

We now proceed to investigate the relationship between the imaging data and one of the longest-studied aspects of α Ori's behaviour – its light curve. Photometry presented in Figure 4.3 covers a period concurrent with the high-resolution observations, and comes from two sources. One light curve is based on visual estimates compiled by the AAVSO (Mattei 1994) whose records

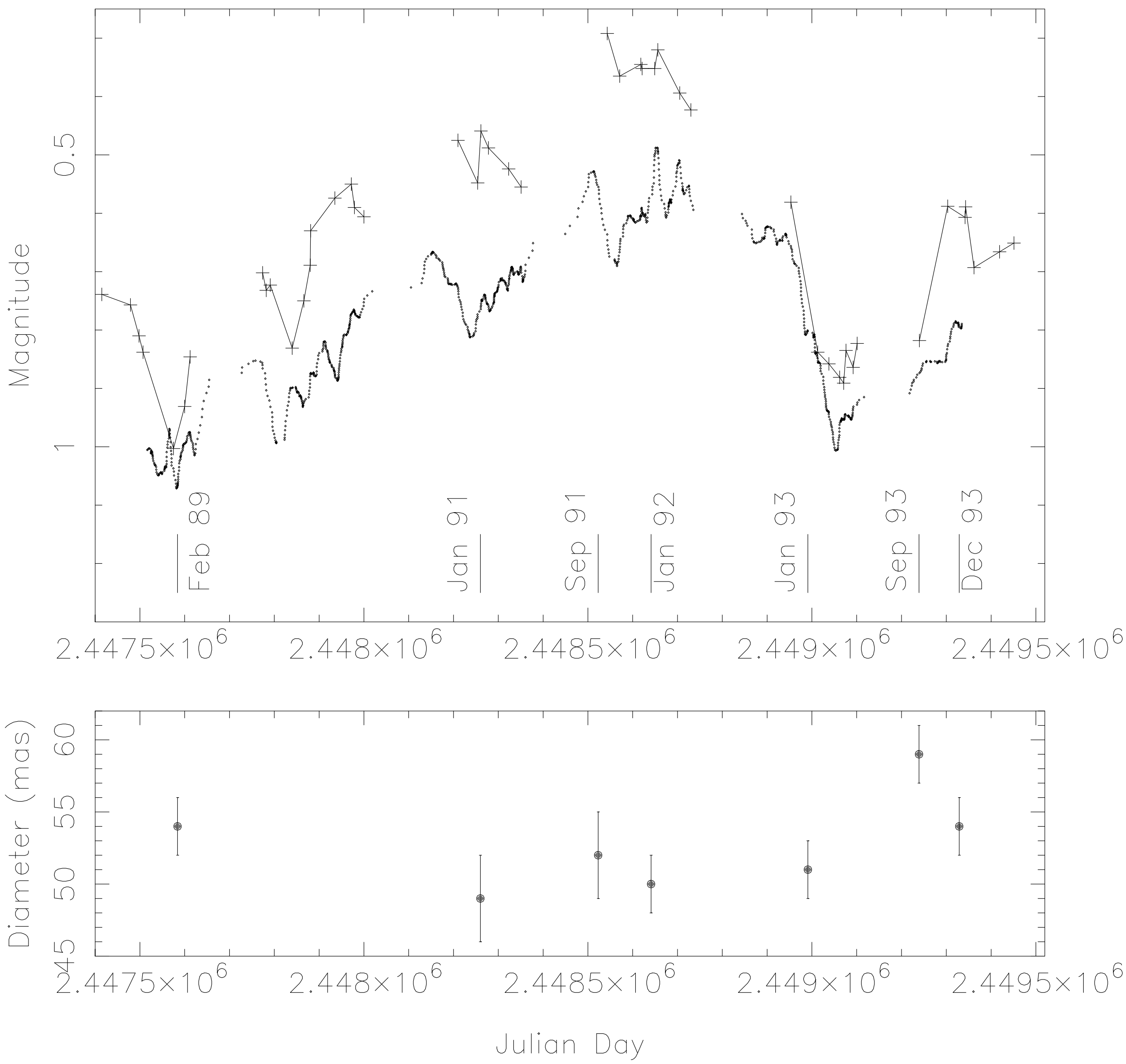

Figure 4.3: Photometry and diameter measurements for Betelgeuse. The upper panel contains visual estimates of the magnitude from the AAVSO which have been smoothed (dotted line), and also published (Krisciunas 1990; 1992; 1994) V-band photometry (crosses connected by line segments). The lower panel gives the diameter of α Ori at 700 nm. See text for more details.

stretch back over 70 years. V-band photometry data from Krisciunas (1990; 1992; 1994) is also shown. Considering the latter photometry for the present, it can be seen that from early 1992 to early 1993 the star seems to have grown dimmer by over 0.5 mag – corresponding to a drop in flux of around 40%. This variation is probably too large to be entirely accounted for from the observed variations in the bright surface features. It is conceivable that the contribution from these could cause variability at the 5 to 10% level, or perhaps up to 20% if all the spots were to disappear altogether, however other phenomena probably also contribute to the variations in flux. The foremost of these is pulsation. The question of the extent of periodicity in the light curve of Betelgeuse has been debated since the turn of the century. Recent monitoring of metallic spectral lines in the region of Hα, in addition to Hα itself, seems to have settled the question in favour of a 400 $\pm$ 20 day period (Dupree *et al.* 1987; Smith *et al.* 1989). These authors find cyclic radial velocity variations with a semi-amplitude of $\sim$ 2 km/sec. From these data, the expected amplitude of pulsation observable in the stellar disk (assuming a distance of 110 pc) should correspond to $\sim$ 4 mas – which should be within range of detection given that the errors on the diameter measurements are typically around 2 or 3 mas.

We now return to the diameter measurements presented in the lower panel of Figure 4.3 which were obtained from the underlying disk component of 'disk + bright spot(s)' models fitted to the data at 700 nm. The 1989 point is from Buscher *et al.* (1990), the two 1991 points are from Wilson (1992) and the remainder are from Appendix C. It can be seen that the general form of behaviour exhibited by the diameter is consistent with pulsation – the size is largest when the star is dimmest (Sep 93 and also Dec 93 & Feb 89). Although the observed $\sim$ 8 mas change in angular diameter is somewhat larger than that predicted assuming a velocity of 2 km/sec, the actual radial velocities measured by Smith *et al.* (1989) exhibited irregularities and excursions from the periodic behaviour which could account for this. In addition, some diameter changes could result from changes in opacity rather than the bulk motion of material. The tentative conclusion here is that stellar pulsations in α Ori have been directly observed as changes in the apparent diameter. If this result can be confirmed, it represents an important step in the understanding of the atmospheres of Betelgeuse and other M-supergiants. Further precise determinations of the diameter changes could be combined with the radial velocity information to yield an independent measurement of the distance to this star.

Finally, no evidence for either of the stellar companions reported by Karovska *et al.* (1986; 1989) has been found. Maps generated with the MEM algorithm show no features with a peak brightness of more than a few per cent outside the stellar disk.

Additional discussion of the observational results from Betelgeuse is given in Section 4.7 (correlations with polarimetry) and Section 3.3 (quasi-monochromatic diameters over various spectral features).

4.4 Rasalgethi

Rasalgethi (α Herculis) is a multiple star system identified in most catalogues as having two components, α Her A and α Her B separated by $5''$. This separation is enough to put α Her B – itself a spectroscopic binary consisting of a G5 II giant and an F2–F8 dwarf – out of the field of view during observations of α Her A. α Her A (hereafter referred to simply as Rasalgethi or α Her) is an M5 Ib–II supergiant and has a somewhat later spectral type than the other (M1-2) supergiants discussed in this chapter. It has recently been suggested that this star is also a close binary with a separation of 192 mas and a period of hundreds of years (McAlister *et al.* 1989), however no magnitude difference was given. No evidence for this companion was found over the wavelength range spanned by our observations (633 to 833 nm) and an upper limit of five per cent or so can be placed on the relative flux from any such component.

Observations of Rasalgethi yielded high-quality visibility and phase data for observations in July 1992 and June 1993. Bright asymmetric features on the stellar disk were clearly identified at both epochs, with a high degree of consistency being noted for all colours from a given observing session. A single feature contributing 15 – 17% of the flux was noted in July 1992, with the possibility of an additional feature at the 3% level. In June 1993, two features contributed 18 – 21% of the total flux. Further details are given in Appendix C, whilst diffraction-limited images reconstructed from data at 633 nm taken at both epochs are given in Figure 4.4. These were published in Tuthill *et al.* (1994a) and show the first reported detections of asymmetries on the surface of this star.

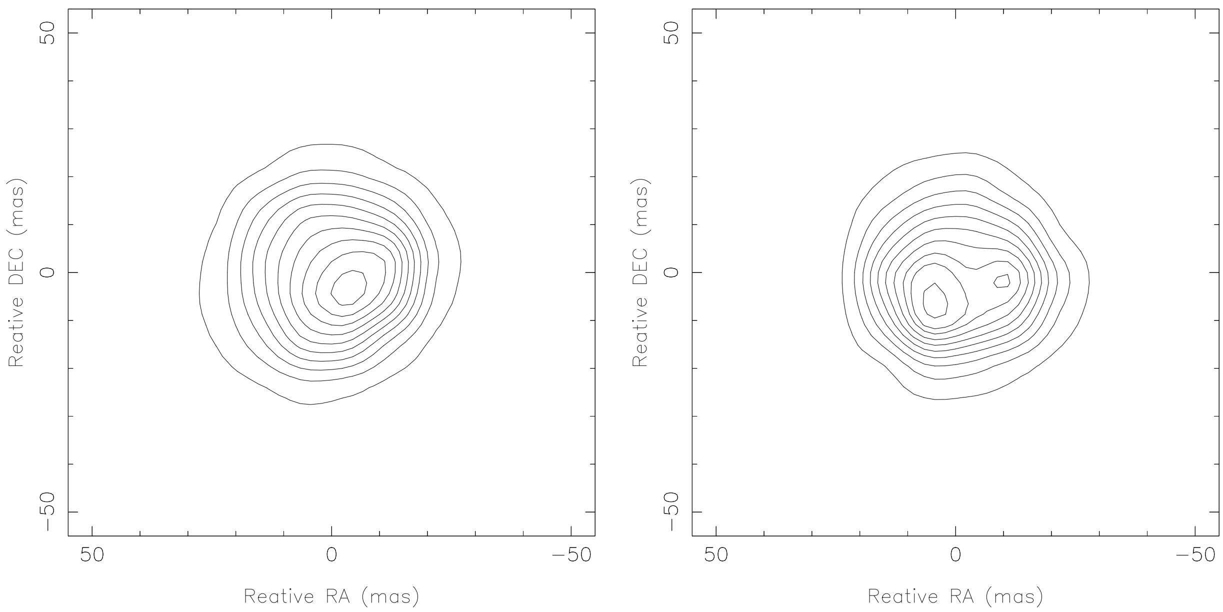

Figure 4.4: MEM reconstructions of Rasalgethi at 633 nm from data taken in July 1992 (left panel) and June 1993 (right panel). North is to the top and east to the left whilst the contour levels are from 5 to 95% in 10% increments.

Although the morphologies from the two epochs exhibited close similarities of general form (*i.e.*

a uniform-disk with hotspots contributing some 20% of the flux), they did differ markedly in the locations of the spots. Thus we may place an approximate upper limit to the evolution timescale of the hotspots as one year. Although Smith *et al.* (1989) found tentative evidence for a companion with a period of a few years in their radial velocity data, this is not an attractive explanation for the observed features. In order to fit the observations there would need to be two such companions, both of similar spectral type.

As was the case for Betelgeuse, by far the most favoured scenario is the existence of hot regions at the tops of large convective zones. It is worth pointing out the strong similarities between the results for Rasalgethi and Betelgeuse. The approximate fractional brightness ($\sim$ 20%), wavelength dependence ($<$ few per cent change from 633 to 710) and also timescale for change of the hotspots all appear to be remarkably consistent for these two stars. Thus, much of the previous discussion for Betelgeuse is also highly relevant here and the reader is referred to Section 4.3 for further details and arguments. The observations of Rasalgethi are also examined in the context of their relationship to polarimetry later in Section 4.7.

Although the diameters of the underlying disk component from the 'disk + spot' models did seem to be somewhat larger in July 1992 than June 1993, this could be the result of insufficiently well constrained model-fitting, since these differences were not noted in the fitting of simple disks from Table A.1. Such uniform-disk fits from Table A.1 give diameters in the range from about 35 mas in the quasi-continuum at 700 nm to 40 mas in the TiO band at 710nm. This behaviour is discussed further in Section 3.3. The angular diameter of Rasalgethi has been measured in the infrared at 2.2 μm using a two-telescope Michelson interferometer (Benson *et al.* 1991) as 32.2 $\pm$ 0.8 mas. These authors correct their results for limb darkening using the models of Scholz & Takeda (1987) to find a photospheric diameter of 34.0 $\pm$ 0.8 mas and go on to derive an effective temperature of 3120 $\pm$ 40 K for this star. This diameter appears to be in good agreement with our measurements, however appropriate corrections for the expected brightness profile would have to be computed and applied before a detailed comparison could be made.

The light-curve for Rasalgethi has been found from AAVSO visual photometry records to exhibit both lower amplitude and less regular variations than Betelgeuse. Fluctuations are often no larger than $\pm$ 0.1 mag and only occasionally exceed $\pm$ 0.2 mag, usually with no preferred timescale or periodicity (Smith *et al.* 1989). These figures imply changes in flux at the 20 – 30% level. Further monitoring of the stellar surface is required to establish whether the evolution of the bright regions alone is sufficient to provide this variability. If this is not the case, additional effects such as pulsation or dust obscuration may also play some role.

4.5 Antares

The M1.5 Iab supergiant Antares (α Scorpii) is one of the brightest stars in the sky and has been extensively studied in the past. Antares has a known companion, however with a separation of $3''$ and a Δm of 4 magnitudes, this should not affect our interferometric observations. Hereafter we refer to α Sco A as simply 'Antares' or 'α Sco'.

Antares is the only star whose diameter has been measured independently by all four major techniques: intensity, amplitude and speckle interferometry, plus lunar occultation. It thus presents a valuable opportunity to cross-check the results from the different methods. Summaries of previous diameter measurements may be found in Richichi & Lisi (1990) and White (1980), whilst some more recent results are given in Wilson *et al.* (1992) and Bedding (1992). Despite the problems with dispersion encountered in the analysis of the data on Antares (see Appendix C) our diameters of around 37 mas at 633 and 700 nm (Table A.1) are in excellent agreement with those at similar wavelengths in the literature. We adopt a correction factor for limb darkening based on the models of Manducka *et al.* (1977) of $D_{phot} = 1.1\ D_\lambda$ where D_{phot} is the photospheric diameter and D_λ is that measured at wavelength λ. Thus we obtain an angular diameter of 41 ± 3 mas, which is in close agreement with infrared occultation diameters for which a less contaminated measurement of the continuum diameter would be expected.

The detection of a bright feature on the surface of Antares contributing 5% of the total flux (Appendix C) confirms the identification of asymmetries in the stellar profile from lunar occultation measurements (Evans 1957; Richichi & Lisi 1990). Observational coverage is not extensive enough nor of high enough quality to warrant detailed discussion in this case. It is interesting to point out, however, that this detection in Antares leads to the remarkable conclusion that for all the supergiants that have been observed, and at all wavelengths and epochs, asymmetric structure *was* detected on the stellar surface. Thus it appears likely that such hotspots are ubiquitous to M-supergiants, and it is proposed that the convective mechanism of Schwarzschild (1975) is responsible. The light curve of Antares is highly irregular and its optical flux can vary by a factor of 2 (0.75 mag). Although the detected level of hotspot activity does not seem sufficient to cause such a large variation, further observations are needed to confirm this. For further discussion, the reader is referred to the preceeding sections on Betelgeuse and Rasalgethi.

4.6 μ Cep

Even more luminous than Betelgeuse, the M2 Ia supergiant μ Cephei offers the chance to study one of the most extreme of the red supergiants. Although its distance (of $\sim$ 800 pc) is poorly known, estimates of M_v range from -6.6 to -8 making it one of the most luminous stars in its class – and consequently one of the most luminous known. Many of its characteristics lend support to the view that it lies near the upper limit of stability for such stars.

Since the nature of the high-resolution data taken on μ Cep led to some fairly remarkable conclusions regarding its morphology, we proceed by describing the extraction of image information in some detail. In order to illustrate the discussion which follows, bispectral data from μ Cep and the unresolved reference star ζ Cep is given in Figure 4.5. Morphology information may be extracted by inspection of such data as follows:

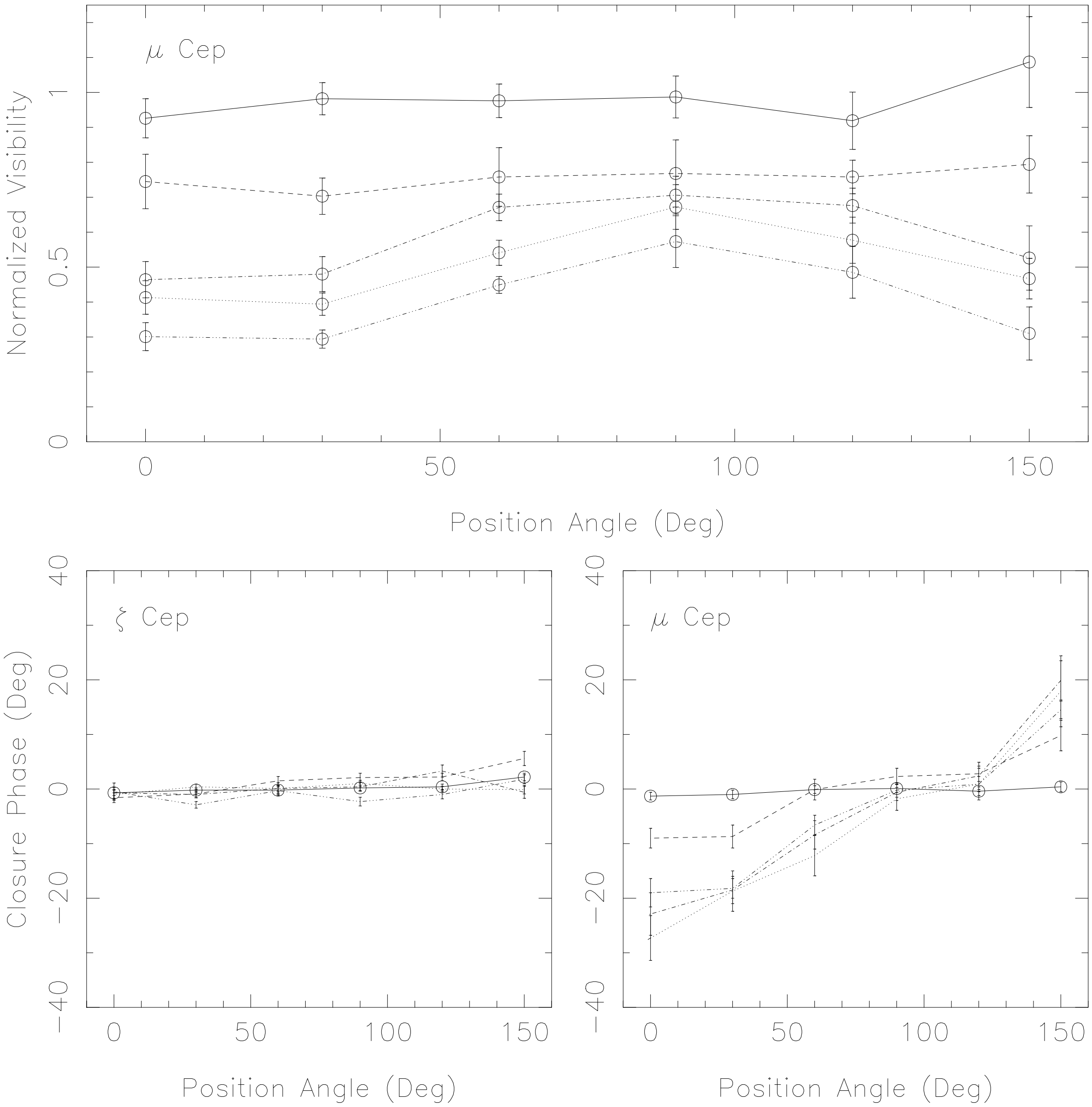

Figure 4.5: Visibility and phase information for μ Cep at 633 nm plus phase signals from unresolved reference star ζ Cep. Data is from June 1993. The upper panel shows visibility data for baselines 1, 5, 8, 9 and 10 passed by the 5-hole mask, plotted against position angle on μ Cep. The lower panel to the left shows closure phase data from the point-source star ζ Cep, whilst to the right are phases from μ Cep.

1) The general fall-off in visibility with increasing baseline at all position angles indicated that the object was resolved, with an angular diameter in the region of 30 mas. Thus μ Cep was not highly resolved and even on the longest baselines available ($\sim$3.8 m) the visibility had only dropped to $\sim$ 40%.

2) The large, systematic variation of visibility with position angle on the longer baselines gave clear evidence of departures from circular symmetry. In the simplest interpretation, these could be either an ellipticity of the stellar disk (with an axial ratio of $\sim$ 0.7) or a bright feature located away from the centre of a circular disk. In the latter case, the strength of the visibility excursion implied a spot with a minimum of 10% of the total flux.

3) Centro-symmetric brightness distributions give closure-phases which are 0 or 180°. The fact that there were no large systematic errors in the recorded phase signals is verified by the fact that the (centro-symmetric) point-source star ζ Cep did yield closure phases which were zero to within their errors. Thus the fact μ Cep's closure phases showed clear non-zero signals ruled out the elliptical model and required the brightness distribution to be non centro-symmetric.

4) Closure phases from all triangles lay near to zero at the position angle 90° indicating an axis of symmetry at right angles to this direction. Furthermore, the visibilities on the longest baselines were highest also at 90°, indicating that the object was least elongated in this direction. Taken together these two facts make an extremely strong case for the existence of a bright feature (or features) somewhere along an axis of symmetry at approximately 0° (north-south). The high level of internal consistency between the phase and visibility data encourage further confidence that the signals are real and not the artifact of some systematic error.

5) We consider for the moment the simple model consisting of a uniformly illuminated disk plus a single bright unresolved spot. Two different solutions when fitting this model could be found which were consistent with the magnitude of both the visibility and phase signals. For one (denoted the 'A' model in Appendix C) the spot was very bright ($\gtrsim$ 30 % flux) and located just on the northern limb of the stellar disk. For the other (the 'B' model in Appendix C), the spot was fainter ($\sim$ 10 % flux) but located a long way from the center of the disk – so far that it was actually one full radius *beyond* the limb to the south. These two models produce broadly similar visibility and phase signals, with the most notable difference between them being that the 'A' model phases are quite smoothly varying, whilst the 'B' model's exhibit a kink (see Appendix C). As this kink in closure phase signal *was* observed for both the 633 and 710 nm data in of June 1993, and also the 700 nm data of July 1992, then it would seem that the 'B' type models are closer to the truth. However, how far can we trust the finer details of the phase signals? One way of assessing the errors on the phase data is to inspect the resultant phases whilst observing an object with known morphology – such as the unresolved ζ Cep. As the closure-phases recorded were very close to 0° (see Figure 4.5) then a correspondingly high confidence should be placed in the results for μ Cep.

6) Finally, a still better fit could be obtained by allowing the unresolved bright feature of the 'B' model to become resolved, giving the 'C' model. This model was only a significantly better fit for the highest-quality (*i.e.* June 1993) data.

Although the discussion above used the June 1993 data as an example, results from other colours and epochs were highly consistent, lending further weight to support the general conclusions as to the brightness distribution of μ Cep. Thus the 'A', 'B' and 'C' models seem capable of producing increasingly close fits to the observations.

We now turn to investigation of the asymmetry by estimating the temperature difference of the bright region from that of the disk. There was tentative evidence from the observations that the bright region contributed a slightly higher proportion of the flux at 633 nm than at 710 nm, both from the July 1992 and June 1993 data. Typical values for this increase (from Appendix C) were around 3% so that, for example, the flux in the feature changed from 21 to 24% as the wavelength decreased from 710 to 633 nm. We assume that the underlying disk component had an effective temperature of 3500 K, and also that the size of the emitting region did not change between 710 and 633 nm. It can then be shown from the blackbody radiation law that the temperature of the bright region must be higher than the disk by $\sim$ 800 K. It should be borne in mind that this figure is extremely sensitive to the quantitative details of the fitted model – which are not tightly constrained by the data. Thus if the brightening from 710 to 633 nm is taken to be anywhere in the range from 0 to 5%, which is permissible from the uncertainties in the data, then the temperature increase for the spot could lie anywhere from 0 to 1500 K.

One possible explanation for the asymmetry in the stellar brightness distribution is the existence of a companion star in a close orbit. For this scenario, the 'B' or 'C' models provide the best interpretation of the observations, with a bright feature located some 20 mas to the south of the main disk. Assuming reasonable values for the distance and mass of the system, the orbital period is likely to be a few tens of years. Furthermore, the companion star must also be of late K or M spectral type. This is demonstrated by the temperature calculation above, and even more strictly by the fact that μ Cep has not been observed to be a spectroscopic binary. Furthermore, in order to provide 10 $\sim$ 20% of the flux, the companion must be extremely luminous itself: $\lesssim$ 2 mag fainter than 'μ Cep A'. Thus any such companion must be a cool red supergiant. That there could be two such objects orbiting each other at a radius which is about the same size as the diameter of the stars – so that the outer regions of their atmospheres are overlapping – begins to sound somewhat contrived. If the changing flux in the asymmetric component (dimmest in July 1992 and brightest in June 1993) is believed to be real, this provides an additional argument against this scenario. Orbital motion was not detected in the observations since the position of the bright feature was similar at all three epochs – covering a total timespan of 14 months. Further suggestions are that the stars are actually well separated and that their apparent proximity is due to the projection from the viewpoint of the earth; or alternatively that the companion is heavily obscured by an envelope of material drawn off from the primary and thus represents an intermediate stage between a separate binary and a common-envelope phase. However, it is hard to believe that a binary with such extreme characteristics would not have been found in earlier work such as spectroscopy, photometry or studies of line velocities.

The next scenario for the cause of the asymmetry to be discussed is the presence of Schwarzschild (1975) type convective zones. The nature of these hotspots was discussed in more detail in the preceding sections, where it was suggested that they are responsible for bright features on the surface of Betelgeuse, Rasalgethi and Antares. It is simplest to envisage the convective hotspots on μ Cep with the use of the 'A' models. For these a feature contributing $\sim$ 30% of the flux was found to be located close to the northern edge of the disk. Such a single, bright hotspot is consistent with the suggestion of De Jager and Vermue (1978) that the larger and more luminous the supergiant, the larger the relative size of the turbulent zones. Unfortunately however, the 'A' models, along with other models in which the bright feature is restricted lie within the stellar disk, were shown not to be capable of adequately reproducing all the systematic trends in the data. Those models which did produce good fits to the data – the 'B' and especially the 'C' model – had significant contributions to the flux coming from regions which were *beyond* the stellar disk. Certainly, this has not been observed in previous cases where convective zones have been suggested and it is not obvious how a convective zone could cause emission from regions far above the photosphere.

Thus neither of the explanations given above – a stellar companion or convective zones – seems entirely satisfactory, although it is difficult to rule them out entirely with the current data. One speculative suggestion might be that the disk of μ Cep is actually rather larger ($\gtrsim$ 40mas) but is obscured by patchy circumstellar material. This author favours a different picture in which the star is dominated by a very few – perhaps only 1 or 2 – extremely powerful convective zones which are responsible for effectively all the heat transport from the stellar interior. The observations may be explained if such zones are capable of distorting the photosphere or even of elevating matter above the stellar surface. Certainly such a scenario is consistent with the picture of extensive and anisotropic mass loss built up from studies of resonant scattering in NaI and KI (Mauron & Qureci 1990) and CO (Le Borgne & Mauron 1989). Further progress in unravelling the puzzle posed by μ Cep's morphology is likely to be made with observations at higher resolution, either from separated-element interferometers or from the new generation of 10 m-class telescopes.

4.7 Polarization Correlations

It has been known for some time that cool luminous variable stars exhibit intrinsic linear polarization (see *e.g.* Zappala 1967; Dyck 1968; Kruszewski *et al.* 1968; Serkowski 1971). With the refinement from earlier broadband observational technique to narrowband measurements, then more recently to full spectropolarimetry, an increasingly complex picture has emerged. Most authors attribute the origin of the continuum polarization to some scattering process, either Rayleigh scattering by H_2 at a photospheric layer, molecular coherent scattering by titanium oxide in an intermediate layer, or scattering from dust grains in a circumstellar shell. Saar and Huovelin (1993) on the other hand, suggest the magnetic intensification effect (Leroy 1962) could produce a net linear polarization from optically thick spectral lines in a magnetic field (Mullan & Bell 1976). Their models of stars with temperatures down to 4000 K suggest this mechanism should dominate; however for cooler giants with a low surface gravity, a smaller contribution to the polarization should result. A number of additional mechanisms have been advanced to explain polarizations in certain atomic emission and absorption bands (see *e.g.* Boyle *et al.* 1986).

Irrespective of the physical process which polarizes the radiation, there must, of course, be an overall departure from spherical symmetry which allows a net polarization to appear in the integrated starlight. A variety of sources for such asymmetries have been proposed including nonspherical circumstellar dust shells (Shawl 1975), clouds of aligned grains (Svatoš & Šloc 1981; Polyakova 1984), equator-to-pole temperature gradients (Harrington 1969), giant convection cells (Schwarzschild 1975), localized hot spots (Schwarz and Clarke 1984), non-radial pulsation of the star (Serkowski 1970), magnetic activity (Mullman & Bell 1976) and stellar obscuration by patchy dust (Nordsieck 1994). A number of these can be discounted on account of the time-dependence of the observed polarization. The asymmetry must vary on a timescale of months to years and be capable of radical change to any angle in a random or quasi-periodic fashion. Thus a some global models may be ruled out as too slow (*e.g.* temperature gradients). Furthermore, the enhancements and decreases in polarization relative to the continuum values across atomic lines and molecular bands are not readily explained by models which rely entirely upon anisotropic dust scattering (nonspherical dust shells, aligned grains). For M-supergiants, one of the only mechanisms not discountable a priori is that of convection cells.

A model whereby the polarization is produced by the action of the asymmetric radiation field generated by a hotspot on an (assumed isotropic) scattering region above the photosphere has been developed by Schwarz and Clarke (1984). With a small number of hotspots present at various locations on the model disk, they found it was possible to reproduce the chief features of both observed broadband (Schwarz & Clarke 1984) and narrowband (Clarke & Schwarz 1984) polarimetric behaviour of Betelgeuse. If such a non-uniform photosphere is the origin of the polarization behaviour, then the features on high resolution images should correlate with polarimetry data taken concurrently (Boyle *et al.* 1986). In the simplest case where the image contains a single bright feature located away from the centre of the disk at a position angle ϕ, then the polarization angle θ would be expected to be at $\theta = \phi \pm 90°$. All further interpretation of imaging and polarimetry in this section is based on this model. In the case of Mira, such a simple relationship between the observed photospheric distortion and the angle of the polarization was not reported by Karovska *et al.* (1991) who ascribe their lack of correlation to a change in size of the scattering particles with pulsation phase in this star. As there is still no consensus as to the origin of intrinsic polarization in late-type variables, the application of the relatively recent capability to produce images of stellar photospheres should cast new light onto this problem.

In order to investigate the relationship between the results of high-resolution imaging and polarimetry, data obtained from an experiment at the Pine Bluff Observatory of the University of Wisconsin were kindly supplied by Nordsieck (1994). These gave measurements of the angle and intensity of the polarization for the stars Betelgeuse, Rasalgethi and μ Cep over a period concurrent with the observations from the high-resolution program. Most of the imaging was done using fairly narrow filters ($\sim$10 nm) and in a region around $\sim$700 nm where spectral features such as titanium oxide absorption bands were extremely strong. Unfortunately, the polarimetry data gave only the average polarization over a wide range of wavelengths from 400 to 750 nm, with the effective mean for the stars probably lying around 550 nm. This was less than ideal, since the intensity and angle of the polarization has been shown to exhibit both rapid fluctuations in and out of spectral features such as absorption bands, and also slower trends from the blue to the red. These can be extremely large, for example Boyle *et al.* found that the blue to red rotation for R Leo was 60° over a wavelength of only 150 nm, whilst the rotations associated with the titanium oxide bands for a number of LPV's including R Leo and Mira could easily exceed 90° as compared to nearby continuum θ. Further discussion of the possible extent to which correlations might be affected by this is given for each object.

A further complication to the process of correlating the positions of bright features with the directions of polarization occurs in those cases where more than one bright feature was identified. For such stars it was generally found that a brighter feature was found close to the centre of the disk, whilst fainter one(s) were located at larger radii. This was not surprising considering that a spot closer to the limb would suffer both from foreshortening and stronger limb darkening. Even if it were assumed that all hotspots emit approximately the same flux, they would still not contribute equally to the net polarization. Indeed, a spot exactly at the centre of the disk would not generate any polarization, whilst the largest contribution comes from those features near to the limb. This highlights an inherent difficulty with this sort of comparison – the polarimetric measurements were most sensitive to those features which were further from the centre and thus fainter and more difficult to detect in the images.

In the absence of detailed atmospheric models of the transfer of polarized light in the extended atmospheres of luminous late-type variables, we will limit ourselves to a qualitative comparison. Much of the discussion which follows centres around the Figures 4.6, 4.7 and 4.8 for Betelgeuse, Rasalgethi and μ Cep respectively. These give the polarization intensity and angle from Nordsieck (1994) are plotted over time, along with the expected $\phi \pm 90°$ angle of the contribution due to each spot from the observations summarized in Appendix C. Light curves from the AAVSO (Mattei 1994) are also shown. It should be borne in mind that the significance of the correlation of a given spot's predicted polarization θ with that actually measured is dependent upon the strength and radius of the feature, which may be obtained from Appendix C. Further details and characteristics for each star are discussed in turn below.

Betelgeuse

Due to its high apparent brightness, Betelgeuse has been a prime candidate for polarimetric study both observationally and theoretically, and was one of the first late-type stars found to have intrinsic polarization. As the polarization exhibited by α Ori is relatively low, with all measured values being less than one per cent, any polarization added by the interstellar medium could seriously affect the observations. Clarke & Schwarz (1984), however, using measurements of nearby field stars, conclude that this contribution is very small ($< 0.03\%$). A characteristic timescale of one to several months for significant polarization changes to take place is evident from extended datasets (Hayes 1980, 1981; Nordsieck 1994). This ties in extremely well with both the theoretical (Schwarzschild 1975) and observed (Section 4.3) evolution time of the convective cells, lending further support to the idea that hotspots are involved in the polarization process. Spectropolarimetric data taken in 1979 (Clarke & Schwarz 1984) show a steady decrease in polarization with wavelength from about 0.5% at 500 nm to 0.1% at 750 nm. Although there was no significant general trend in θ indicated over this region, rotations of around 20° between the continuum and the absorption bands were noted.

Figure 4.6 presents the variations in visual magnitude as well as polarization percentage and angle over a period during which a number of high angular resolution images were obtained. With reference to this figure, further comments on each epoch of data are given in turn below.

February 1989: Data at this epoch is taken from Buscher *et al.* (1990), who found clear evidence for a bright feature at a position angle ϕ of around 277° and a radius of ~6 mas at 633, 700 and 710 nm. The expected θ produced by such a feature is clearly not consistent with the polarimetry observations. Buscher *et al.* do not, however, state whether the fit to the 'disk + single spot' model left any residual signal in the data as would arise if an additional (fainter) feature were also to exist.

January 1991: The positions of hotspots at this epoch were obtained from Wilson *et al.* (1992) who found two features of approximately equal brightness (~8%) and radius (~10 mas) at $\phi \simeq 100°$ and 300° using wavelengths of 546, 633, 700 and 710 nm. These two features both produced polarizations which were close to the observed θ, although it was perhaps somewhat surprising that given two bright hotspots both contributing to polarization at roughly the same angle, the polarized intensity suffered a local dip to 0.1%.

September 1991: Results presented for this epoch were obtained from a re-analysis of data taken by Wilson (1992). Unfortunately, no known binary was mapped concurrently with these data for calibration purposes and so the orientations are somewhat uncertain. Although a bright spot was clearly detected at $\phi \simeq 144°$ at both 700 and 710 nm, evidence for the second dimmer feature at 57° came only from the 710 nm observation and was only marginally well constrained. Although this fainter feature did seem to match well to the θ given by polarimetry, for the reasons given above, this apparent correlation should be treated with caution.

January 1992: The serious limitations in data quality from this epoch have been described in Appendix C. Although it is seen from Figure 4.6 that the brighter feature should produce a θ closely matching that of the observations, this is surprising given that this hotspot is very nearly in the centre of the disk (1 ~ 2 mas) and should thus contribute little to the net polarization. The (fainter) non-central feature at this epoch, however, produced a polarization at a very different angle from the measurements.

January 1993: High-quality data at this epoch yielded two hotspots on approximately opposite sides of the disk. These both produced a model polarization in nearly the same direction, and were both fairly close to the measured polarimetry value.

September 1993: As there were two different wavelengths of data both of high quality, the 633 nm were selected since they were closer to the λ of the polarimetry and also as they yielded slightly higher system resolution. Three spots were identified from fitting to this data, with one fairly central (3 mas) and bright, and two fainter ones at radii over 20 mas. One of these

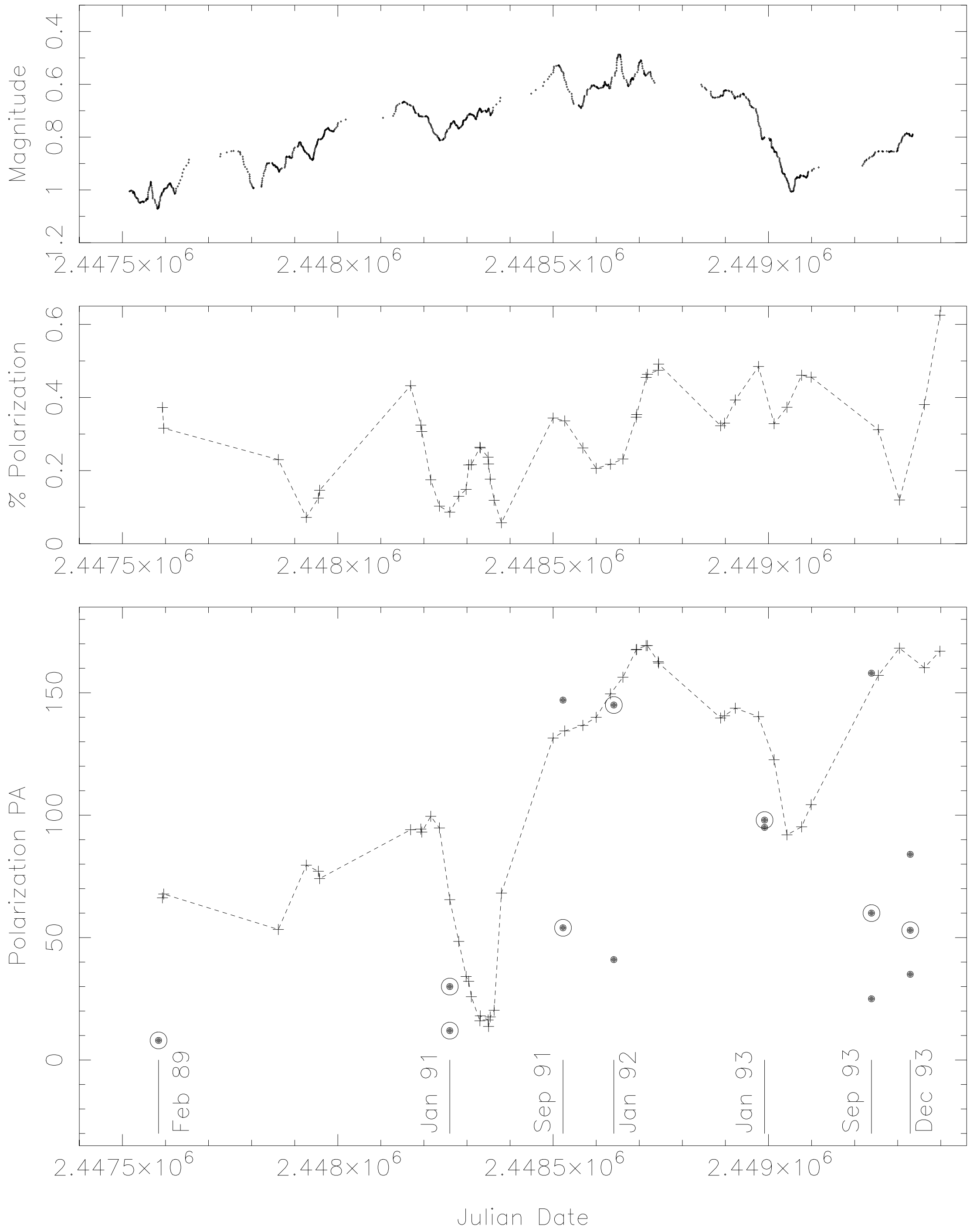

Figure 4.6: The topmost trace is a visible light curve for Betelgeuse over the period 1989 – 1994, obtained by smoothing data from the AAVSO (Mattei 1994). Crosses (connected by dashed line segments) presented in the lower traces originate from spectropolarimetry data obtained from Nordsieck (1994). The bottom trace gives the position angle of the electric vector of the mean polarization, whilst the middle panel gives the polarization strength. Also plotted on the lower trace are black dots denoting the expected position angle of the polarization, given a simple scattering model and the observations from Appendix C. Simple dots are from weaker ($\lesssim$ 6%) spots, whilst circled dots represent stronger features.

dimmer features produced a polarization which was very close to the observations, whilst the other was some 45° away.

December 1993: As for September 1993, the 633 nm results have been chosen in preference over those at 700 nm. One bright and one dim feature were located relatively close (5 mas) to the disk's centre, whilst an additional faint feature was identified at a radius of 26 mas and an angle $\phi \simeq 125°$. All three features including the more distant spot produced model polarizations which were clearly not in agreement with the observed polarization, which at this epoch, suffered a dip in intensity to 0.1%.

Summary: Betelgeuse
Correlations have been made between the results of high resolution imaging and polarimetry with a simple working assumption of a polarization angle θ produced at 90° from the orientation of the hotspot ϕ. Two cases of fairly good agreement were found (January 1991 and January 1993). Three further cases exhibited some tentative positive correlation (in decreasing order, September 1993, September 1991 and January 1992). The remaining two cases showed no correlation (February 1989 and September 1993). Although these results could hardly be described as unequivocal, they do perhaps lend some further weight to the identification of bright photospheric regions as being involved in the processes which generate the net linearly polarized light from Betelgeuse.

There have been no published attempts to correlate images of the stellar photosphere with polarimetry for Betelgeuse. From this study, a number of difficulties have been pinpointed, and the results are certainly positive enough to encourage further efforts. Some improvements might include using polarimetry data which has been integrated over a relatively narrow spectral region similar to that used for the imaging, and the optimisation of the observing configuration to obtain greater dynamic range in the images and thus enhance the detection of features near the stellar limb. In addition, Clarke and Schwarz (1984) show that a more detailed model to predict the resultant polarization is needed when a disk is allowed to contain more than one bright feature. Certainly, Betelgeuse has been found to exhibit a number of hotspots and this complexity makes the prediction of its polarization behaviour more difficult. Indeed, it may be the case that bright features which are extremely difficult to detect, such as those on or even behind stellar limb, can play an important role in determining the polarization properties of the star.

Rasalgethi

As for Betelgeuse, Rasalgethi does not exhibit particularly strong linear polarization and is also thought not to be seriously affected by polarization originating in the interstellar medium (Nordsieck 1994). Detailed spectropolarimetry of this object has not been located, and thus it was not possible to estimate the likely changes (in intensity and rotation) for the polarization with wavelength. As Rasalgethi is of a later spectral type than both Betelgeuse and μ Cep, it is probably safe to assume that excursions will be more severe, especially where titanium oxide bands complicate the spectra. Comparison of Nordsieck (1994) polarimetry data and morphology information from high-resolution observations (Appendix C) is summarized in Figure 4.7,

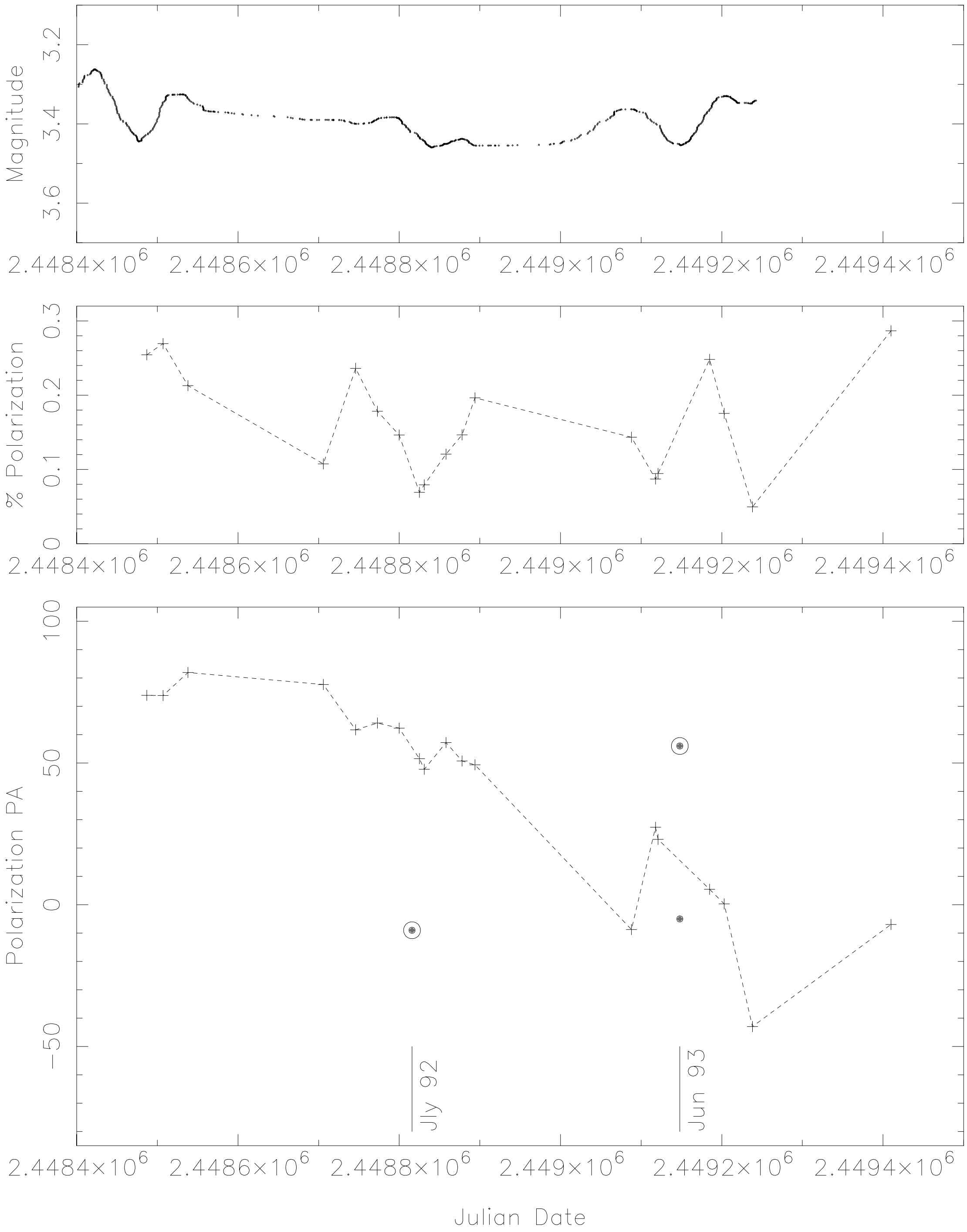

Figure 4.7: The topmost trace is a visible light curve for Rasalgethi over the period 1991 – 1994, obtained by smoothing data from the AAVSO (Mattei 1994). Crosses (connected by dashed line segments) presented in the lower traces originate from spectropolarimetry data obtained from Nordsieck (1994). The bottom trace gives the position angle of the electric vector of the mean polarization, whilst the middle panel gives the polarization strength. Also plotted on the lower trace are black dots denoting the expected position angle of the polarization, given a simple scattering model and the observations from Appendix C. Simple dots are from weaker ($\lesssim$ 6%) spots, whilst circled dots represent stronger features.

and discussed further below.

July 1992: The principal bright feature detected at this epoch was not located far from the centre of the disk ($\sim$ 5 mas) at $\phi \simeq -100°$. It can be seen from Figure 4.7 that the expected θ from this feature falls a long way from the measured value. Although data presented in Appendix C did indicate that an additional feature at a greater radius might exist, the resolution was not great enough to adequately constrain its position.

June 1993: The three wavelengths of observation at this epoch (633, 700 & 710 nm) gave fairly consistent results; one bright feature quite close to the disk's centre and an additional feature at a radius of 20 mas and $\phi \simeq -95°$. In this case, a close match is found in the θ predicted from the feature near the limb, and that measured with the polarimeter.

Summary: Rasalgethi
For this object we find one case where a quite good correlation between the imaging and the polarimetry exists (June 1993), and one case where uncertainty in ϕ of the more important distant spot made it impossible to tell (July 1992). Again, this is encouraging for the 'hot convective zone plus scattering' model of polarization in late-type variables, although obviously in this case the imaging results are too sparse to draw strong conclusions. This is the first known comparison of concurrent polarimetry and imaging for this star, and further discussion of these results would follow along similar lines to that given previously for Betelgeuse (*q.v.*).

μ Cep

The broadband optical polarization of μ Cep is known be variable with maximum values of 4%, and with θ lying anywhere between 0° and 180°. This star is at a low galactic latitude (+4°) and in a field direction where interstellar polarization is thought to be significant. Values of 1 $\sim$ 2% at an angle of 40° $\sim$ 50° for this interstellar component have been found, based upon observations of field stars (Polyakova 1974; McLean 1979). When the measured polarization from μ Cep is low, it can be difficult to disentangle the intrinsic from the interstellar contributions.

It is interesting to point out that the more extreme asymmetries detected in the images of this object (Section 4.6; Appendix C) as compared to other supergiants correspond to larger intrinsic polarizations – 4% as compared to 1% for α Ori – from polarization measurements. Extrapolating this relationship to the case of V CVn, one can only surmise as to the extent of the photospheric asymmetry necessary in order to give rise to a polarization which can be as large as 7% ! Narrowband spectropolarimetry data for μ Cep from Boyle *et al.* (1986) showed that the polarization intensity and angle did not show a strong dependence upon wavelength. In particular, rotations in θ associated with TiO bands were no more than $\sim$ 10°. As the net polarization at the time of Boyle's measurements was relatively low at around 1%, it was not clear whether the results were an indicator of the behaviour of the intrinsic, or of the interstellar, component of the polarization.

For the remainder of this section, we assume that surface hotspots are the cause of the asymmetries in μ Cep, ignoring the contention as to this identification discussed in Section 4.6. As both the morphology and the polarimetry data were simpler than those recorded for the other stars, it has been found profitable to discuss both the intensity and angle of the polarization from Figure 4.8.

Using the polarimetry data and the imaging observations over the three epochs, it has been possible to find a single constant vector for the interstellar polarization which brings all these results into agreement. This 'interstellar' contribution was found to have a magnitude of 1.4% and to be at an angle of $-35°$. The polarization intrinsic to the star could then be found by subtracting off this vector from the polarimetry measurements, and is shown as a dotted line in Figure 4.8. Further discussion of results at each epoch is given below.

July 1992: Having subtracted the 'interstellar' term, the 'intrinsic' polarization can be seen to be at an angle which is very close to the expected θ from the bright feature detected at $\phi = 195°$. In addition, the polarization intensity can be seen to be relatively low at around 1.5%. This is in keeping with the fact that the asymmetric feature at this epoch was found to be only half as bright as it was later in June 1993 *i.e.* the lower proportion of flux in the spot corresponds to a lower level of polarization.

June 1993: At this epoch, the high resolution observations from Appendix C have shown that the flux in the asymmetric component has increased significantly – by a factor of about 2 – since July 1992. This is consistent with the raw polarization intensity recorded on this occasion, which exhibited an increase to over 2 % from values under 1% at the previous epoch. Correcting with our 'interstellar' value we find close agreement between the 'intrinsic' polarization θ and that predicted from the known location of the hotspot. Furthermore, the 'intrinsic' polarization intensity is now about 3% which is a factor of 2 larger than that at the previous epoch. This is as one would expect if the doubling in brightness of the hotspot is linearly related to the fractional polarization.

September 1993: Both the asymmetries detected from interferometry and the polarization measurements (angle and intensity) did not change much since the June 1993 observations. The interpretation is then the same as that given above. The polarimetry data and the imaging data are found to be qualitatively and quantitatively consistent with the addition of the constant 'interstellar' polarization at $-35°$.

Summary: μ Cep
With the use of a slightly more complex model consisting of a static interstellar component along with polarization arising from scattering in the stellar atmosphere above a bright photospheric region, it has been possible to construct a quantitative explanation describing all the main features of the polarimetry and imaging data. It is important to note that the interstellar polarization *was* a free parameter for this model.

However, it should be pointed out that an alternative qualitative interpretation of the polarimetry results could be made based on the interstellar polarization found by Polyakova (1974) and McLean (1979): *i.e.* at an angle of $40° \sim 50°$. The July 1992 observations are explained by assuming that the star does not have a strong intrinsic polarization, so that the intensity and angle of the measured polarization have therefore relaxed to their interstellar values. The June and September 1993 observations are then consistent with a stellar contribution of $\sim 2\%$ at

$\sim 100^\circ$ from polarization above the hotspot. Such a scenario has the drawback that it does not explain two things; why was there no 'intrinsic' component detected in July 1992 despite there being detected asymmetries, and why was the increase in intrinsic polarization not linearly related to the increase in brightness of the hotspot?

This is the first known attempt to correlate polarimetry and imaging for this star. Further work is necessary in establishing the contribution from interstellar polarization. Until this can be done, the positive connection between bright photospheric features and net polarization should be viewed as tentative. Despite this, the general behaviour of the data looks encouraging and the evidence seems to weigh in favour of the hotspot model of Schwarz and Clarke (1984) as the origin of light polarization in μ Cep. This star is an ideal candidate for further study since it is bright, can produce high levels of polarization and its morphology (at least on three occasions) showed high levels of distortion. In addition, the asymmetry has been of a fairly simple nature with a single dominant non-central feature, thus making the job of interpretation of the expected polarization much simpler than for Betelgeuse or Rasalgethi.

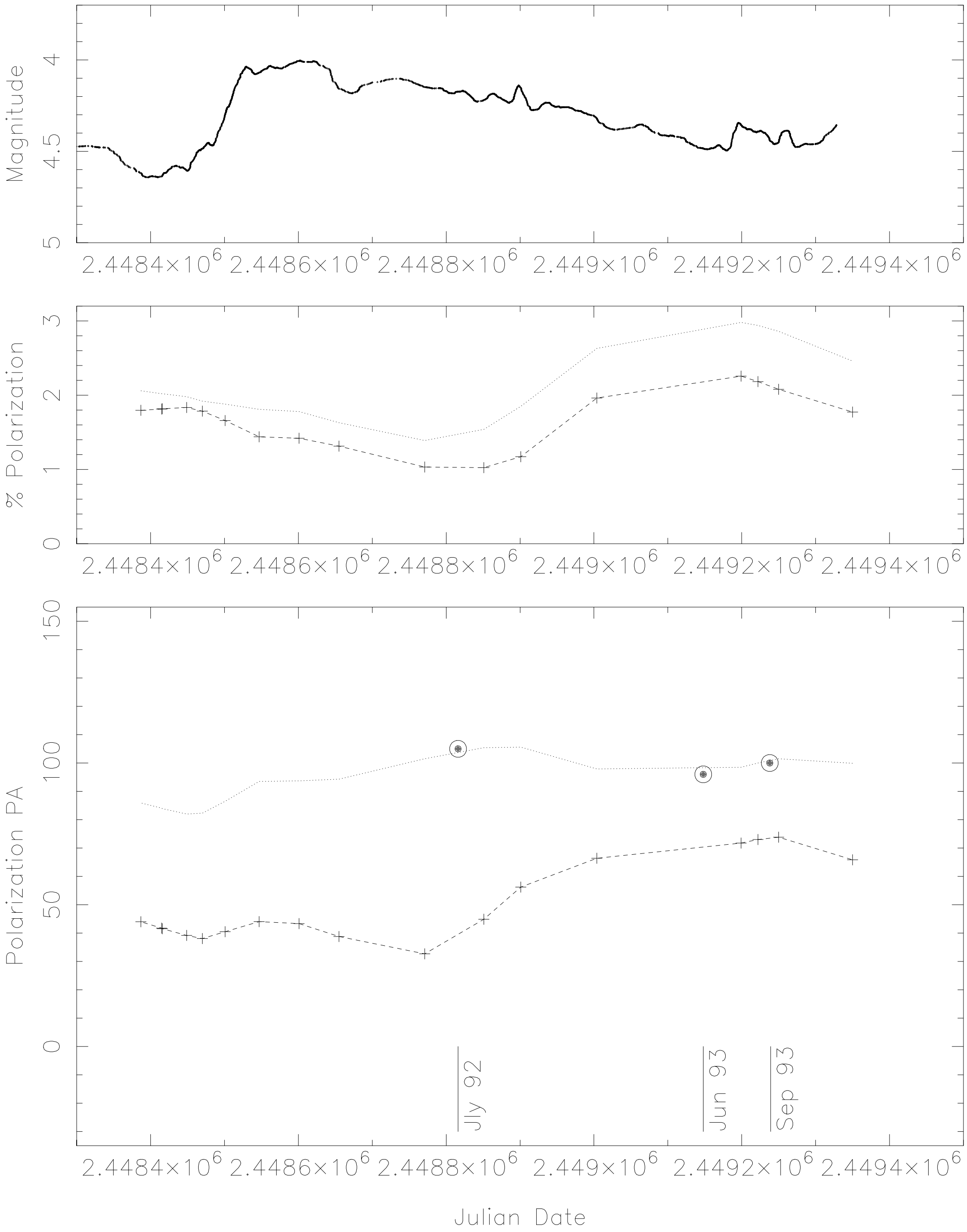

Figure 4.8: The topmost trace is a visible light curve for μ Cep over the period 1991 – 1994, obtained by smoothing data from the AAVSO (Mattei 1994). Curves presented in the lower traces originate from spectropolarimetry data obtained from Nordsieck (1994). As before, the crosses joined by the dashed line give the measured polarization fraction and angle in the middle and lower panels respectively. The dotted curve was obtained by subtracting off a constant 'interstellar' polarization term as described in the text. The circled black dots denote expected position angle of the polarization, given a simple scattering model and the observations from Appendix C.

Over it the Star of Evening
Melts and trembles through the purple,
Hangs suspended in the twilight.

Henry Longfellow
from 'The Song of Hiawatha'

Chapter 5

Seeing

The refinement of our understanding of the detailed properties of the atmospheric phase screen and its effect on starlight is vital for ground-based high resolution imaging. This chapter presents results from a number of different studies in this area.

5.1 Seeing Theory

The standard mathematical model of seeing is based on the theory of atmospheric turbulence developed by Kolmogorov (1941). In this theory, energy is continuously injected into the atmosphere by large scale motions and subsequently cascades down to smaller spatial scales. The characteristic length scale at the top of this cascade is known as the *outer scale*, $L_{\circ}$, and corresponds to the largest turbulent cells. Energy is eventually lost to viscous dissipation which becomes important below the so-called *inner scale*, $l_{\circ}$, which takes a value of a few millimetres near the ground and about 1 cm at the tropopause. The range of spatial frequencies between the outer and inner scales is known as the *inertial subrange* since viscosity plays no significant part in determining the flow. As was realized by Tatarski (1961), refractive-index fluctuations are caused by the mixing of air at different temperatures. He described the statistics of the phase screen with the use of the refractive-index *structure function*, $D_n(\underline{r})$:

$$D_n(\underline{r}) \;=\; < |n(\underline{r}') - n(\underline{r}' - \underline{r})|^2 >$$

where $D_n(\underline{r})$ is the variance of the refractive-index $n(\underline{r}')$ between points with vector separation $\underline{r}$. Under conditions of Kolmogorov turbulence, the structure function can be written as:

$$D_n(\underline{r}) \;=\; C_n^2 \; |\underline{r}|^{2/3}$$

where C_n^2 is a constant of proportionality known as the refractive-index structure constant. Following Tatarski (1961), the phase structure function can be derived by integration of the phase perturbations due to refractive index fluctuations along the light path:

$$D_\phi(\underline{r}) \equiv < |\phi(\underline{r}') - \phi(\underline{r}' - \underline{r})|^2 >$$

$$= [2.91k^2 \int_0^h C_n^2(s)\ ds]\ \underline{r}^{5/3}$$

Here $\phi(\underline{r})$ is the wavefront phase at position $\underline{r}$, k denotes the optical wave-number and the integral is taken over the atmosphere of height h. This expression is more conveniently expressed with the use of the parameter r_0 introduced by Fried (1966) as:

$$D_\phi(\underline{r}) = 6.88 \left(\frac{|\underline{r}|}{r_0}\right)^{5/3} \tag{5.1}$$

where

$$r_0 = [0.423\ k^2 \int_0^h C_n^2(s)\ ds]^{-3/5}$$

Equation 5.1 forms the starting point for many theoretical investigations of atmospheric seeing and its effect upon ground-based telescopes. Of particular interest here are the phase tilts induced by turbulence at various scales within the inertial range. The mean phase excursions are given by:

$$\Delta\phi_{rms} = \sqrt{D_\phi(\underline{r})} \propto (|\underline{r}|)^{5/6}$$

The phase tilts are then found to be:

$$\frac{\Delta\phi_{rms}}{|\underline{r}|} \propto (|\underline{r}|)^{-1/6} \tag{5.2}$$

Thus we arrive at the result that the magnitudes of the phase tilts will be only *weakly* dependent on the characteristic scale sizes of the wavefront distortions.

In describing the temporal behaviour of incoming starlight, some of the simplest models rest upon an assumption known as 'frozen turbulence'. Refractive-index variations are assumed to behave as if fixed to a rigid screen which is blown along by the wind at a uniform velocity $\underline{v}$. In its simplest form, a single such screen moving across the pupil in a set direction is used. It is possible to define a temporal structure function analogous to the spatial one given earlier, and under conditions of frozen turbulence it can be shown that (Buscher 1988):

$$D_\phi(t) \equiv < |\phi(t') - \phi(t'-t)|^2 > = \left(\frac{t}{t_0}\right)^{5/3} \tag{5.3}$$

For a wind of velocity $\underline{v}$, the parameter $t_0 = 0.314 r_0/|\underline{v}|$ represents the characteristic timescale for phase fluctuations. Further discussion of the mathematical ramifications of the frozen turbulence approximation in the context of imaging can be found in Goodman (1985).

5.2 Measurements at the WHT

Data obtained for the purposes of high-resolution imaging using the setup described in Chapter 2 could also be used to gather information about the local seeing and the performance of the telescope and optical system. One easily measured diagnostic was the motion of the centroid of the image on the CCD detector, which gave the mean wavefront tilt across the pupil due to the combined effects of seeing and telescope tracking errors. This section discusses a number of studies based on such centroid motions.

The centroids of one-dimensional images in the time-series datasets shown in Figure 5.1 clearly exhibit periodic motions. This type of motion was found to be common and was almost certainly due to imperfect telescope tracking. The oscillations depicted resulted from a motion of the telescope structure as a whole and were possibly excited by microseismic activity or vibrating equipment, or more likely, errors in the servo-control loop and/or human activity (note that (live) observers in the GHRIL were supported by the telescope). Motion of the stellar image could compromise the quality of high resolution imaging data. If the fringe pattern was not stable on the detector during the integration, visibility would be lost. The longest baselines, having the finest fringes on the detector, would be the most seriously affected. In those cases where telescope vibrations were prevalent it was not possible to recover this lost visibility.

A study of the seeing and telescope vibrations was made using data taken with a slit mask in January, June, September and December of 1993. This provided a useful yardstick against which to measure the performance of various imaging strategies, as well as being of more general interest.

Power spectra of the motion of the centroid are capable of revealing periodic oscillations, and are valuable in cases when these are not so obvious as those in Figure 5.1. A number of algorithms to find the centroid of exposures were tried, including first moment, Gaussian fit and fitting with a free-form symmetric template using Bayesian methods (Gull 1992). Despite the fact that Stone (1989) found the simpler moment routines to be inferior in an astronomical imaging context, they have been used to generate the results presented here since their implementation into a real-time working wavefront monitoring system should be simpler and require less computational time.

Figure 5.2 shows two examples of the power spectra of centroid motion. A large number of these were computed for observations of various stars on many different nights. It can be seen from

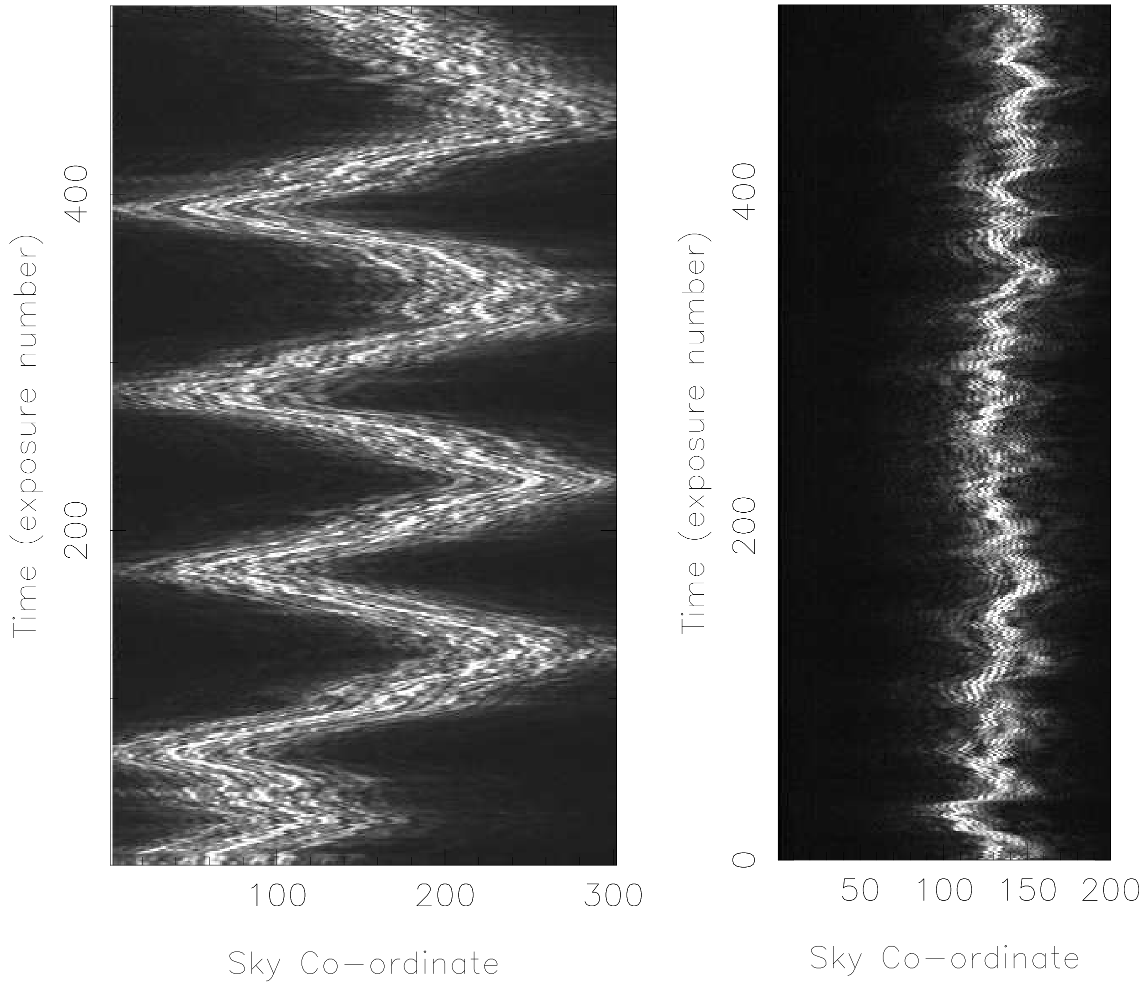

Figure 5.1: Time-series of 512 one-dimensional speckle frames taken whilst observing α Sco at 700 nm with a 5-hole mask (left) and ρ Her at 710 nm with an axial slit mask (right). The total durations of the time-series for α Sco and ρ Her are 8.7 and 4.6 seconds whilst the angular scales on the horizontal axes correspond to $3.3''$ and $2.2''$ respectively.

Figure 5.2 that the bulk of the power in centroid motion was in the low frequency components. In this critical region (below 5 Hz or so), strong peaks, such as is depicted for ρ Her, could dominate the spectra. When this was the case, most of the image motion was occurring as periodic motions, presumably of instrumental rather than atmospheric origin. This regime, where the telescope was found to be responsible for most of the overall wavefront tilts, was found to be common, encompassing, for example, almost all the data from the January and June 1993 runs. The region below 3 Hz was particularly prone to oscillations, and this is also where most of the rigid-body mechanical resonances of the telescope are located.

Centroid motions were found at much higher frequencies than those mentioned above, most notably around 14 Hz (evident in 80 per cent of the data) but also at other frequencies between 10 and 40 Hz. Although these motions were of small amplitude (at most a few pixels peak-to-peak) and would contribute little to the broadening of a long-exposure image, they could still

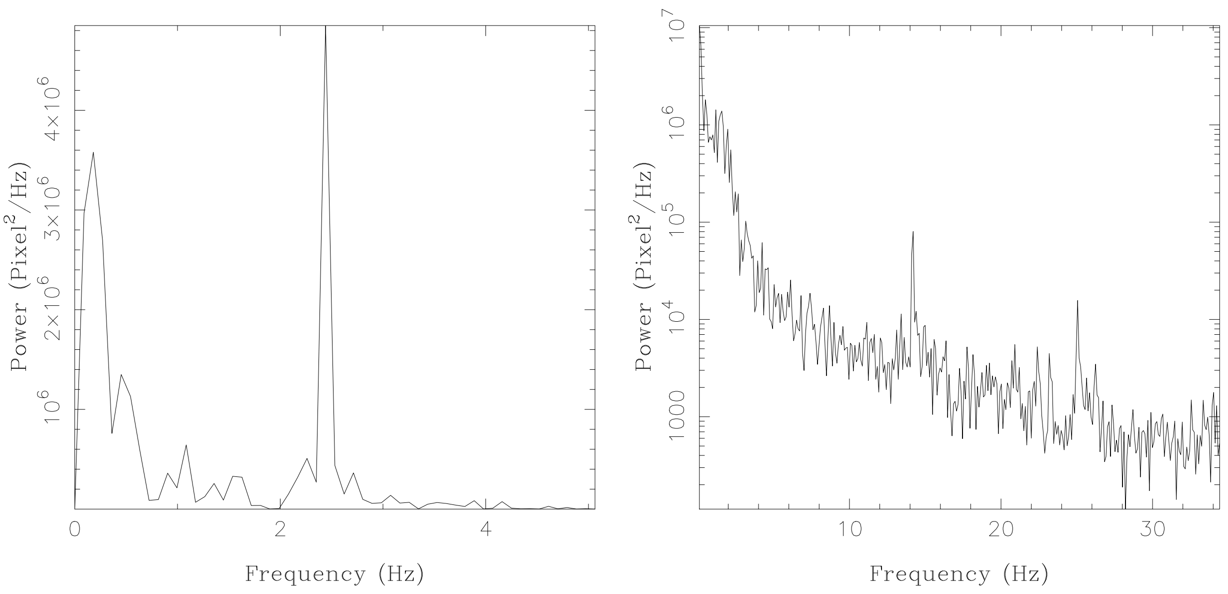

Figure 5.2: Two examples of power spectra of the centroid motion of 500 one-dimensional exposures taken over ~8 sec. To the left is the power spectrum of the centroid of data taken on ρ Her (illustrated in the previous figure) exhibiting a clear peak at about 2.4 Hz. The right-hand trace shows data from η Cyg displayed on a logarithmic scale and showing features at around 14 and 25 Hz.

cause sufficiently rapid motion to blur the fringe pattern thus lowering the visibilities. Likely candidates for exciting these oscillations were the large extractor fans which vent air from the dome.

An estimate of the seeing was provided by measuring the FWHM of the one-dimensional images in datasets such as those in Figure 5.1. One way to do this was to compress all the flux into a single line of pixels by vertically binning the entire time series. This yielded a 'long exposure' image where the length of exposure was equal to the total record length, *i.e.* some 5 to 10 sec. A second way to perform this compression was to first center the data according to the centroid of the flux received in each one-dimensional exposure before binning. This had the effect of removing the mean image motion introduced by the atmosphere and telescope, and when the tilts were dominated by the latter, yielded an estimator dependent only upon the intrinsic seeing. More importantly, it provided information on the likely improvement obtainable in image quality at a large telescope when an active tip-tilt correction system with a response time of around 10 milliseconds is employed.

Estimates of both the 'long exposure' and 'tilt corrected' seeing as described above are given in Table 5.1. The mean and error for each datum was determined from at least 30 datasets taken over intervals of approximately 45 minutes, and thus these values are fairly representative of the mean prevailing conditions. Also shown are estimates of the seeing made as a part of a long-term monitoring program by the staff at the observatory. These Royal Greenwich Observatory (RGO) seeing estimates are broadband, whilst those compiled from our slit data taken with the CCD system described in Section 2.2 (Columns 3 and 4 of the table) utilized a wavelength of 700 nm.

Table 5.1: Estimates of the seeing at the WHT. The calendar date and approximate time of night of the observations is given. The three estimates of the seeing are discussed further in the text, with the relative improvement gained from the 'long exposure' to the 'tilt corrected' given in the last column.

Date (1993)	RGO Estimate (arc-seconds)	'Long Exposure' (arc-seconds)	'Tilt Corrected' (arc-seconds)	Improv. (%)
Jan 2 (mid)	2.0	$2.23 \pm .19$	$2.00 \pm .19$	11
Jan 3 (mid)	1.7	$1.50 \pm .06$	$1.29 \pm .06$	14
Jun 7 (early)	1.1	$0.85 \pm .14$	$0.78 \pm .14$	8
Jun 7 (late)	1.2	$0.83 \pm .14$	$0.71 \pm .09$	15
Jun 8 (early)	1.1	$1.97 \pm .22$	$1.92 \pm .17$	2
Jun 8 (late)	1.4	$0.70 \pm .11$	$0.63 \pm .08$	10
Jun 9 (early)	1.4	$0.75 \pm .15$	$0.63 \pm .16$	16
Jun 9 (late)	1.1	$0.47 \pm .03$	$0.38 \pm .03$	19
Sep 7 (mid)	1.3	$1.19 \pm .12$	$1.14 \pm .12$	4
Sep 8 (mid)	1.1	$0.90 \pm .07$	$0.77 \pm .07$	14
Dec 6 (mid)	1.3	$0.86 \pm .14$	$0.73 \pm .11$	10
Dec 7 (mid)	2.3	$1.79 \pm .20$	$1.74 \pm .12$	3

Table 5.2: Theoretically predicted relative improvement in half-width for seeing-limited images from a 4.2 m telescope operating at 700 nm under various seeing conditions.

Seeing (arcsec)	r_0 (m)	ΔWidth (%)
0.5	.29	19
1.0	.15	15
1.5	.10	12
2.0	.07	10

In the majority of cases, the estimates of the width of the seeing disc provided by the RGO were larger than those measured with the aperture masking apparatus. Since most of the RGO estimates were made with the slit viewing camera at the Isaac Newton Telescope where the pixel scale is $0.55''$, it is doubtful if any sub-arcsecond seeing disc would be adequately sampled to enable reliable estimation of its width.

Although on some occasions the center-and-add routine reduced the measured half-width to under 50% of its initial value, the greatest mean improvements over the entire 45 minute datasets were around 20%. Working from the initial assumption of Kolmogorov turbulence, Fried (1978) has derived the expected improvement in imaging performance upon removal of the overall wavefront tilts. For the telescope size and wavelength appropriate here, Fried's results are given in Table 5.2.

A Comparison of Tables 5.1 and 5.2 shows a broad agreement between the theoretically expected and the measured improvement in image width, except in cases where the seeing was poor. When the seeing was worse than $\sim 1.5''$, however, the data became untrustworthy. This was because the image of the speckle pattern became too large to fit on the CCD detector, causing the wings of the distribution to be clipped. Although the agreement between the measurements and theory may at first sight appear reassuring, it is somewhat surprising in the light of the known tilts, induced by the telescope, present in the data. It has been established in a number of ways throughout this chapter that periodic oscillations contribute significantly to the motion of the image – often seeming to dominate over other sources of motion. Thus it might be expected that the improvement upon tilt correction would be *larger* than predicted from Kolmogorov theory, given this extra instrumental contribution to the motion. This leaves open the possibility that the theoretical predictions have over-estimated the importance of the tilts to the image width.

A realistic tilt compensator must work within the practical constraints imposed by real-time detection and non-zero response time from any mechanical corrector. With this in mind, an investigation of how quickly an active optical system needs to perform in order to gain the benefits demonstrated in Table 5.1 was performed. This was done by smoothing the centroid data, thus discarding the high frequency information. It was found that almost the full benefit was maintained whilst discarding all but the lowest frequencies. Only with an equivalent frequency of response below 2.5 Hz was there significant broadening from the fully tilt-corrected profiles of Table 5.1. This is consistent with the power spectra presented earlier, where it was concluded that most of the power in centroid motion was manifested at low frequencies.

5.3 The Shift-And-Add Algorithm

In addition to the Fourier methods of Chapter 2, there are a number of other procedures to obtain diffraction-limited images from short-exposures (see *e.g.* Roddier 1988). One of these, known as the shift-and-add (SAA) technique, was implemented and found to compare favourably with Fourier methods under some conditions. SAA is based on the empirical idea due to Lynds *et al.* (1976) that in a speckled image, each speckle can be regarded as a distorted image of the object. In the method originally described, the reconstructed image is obtained by averaging over many such distorted images, both as speckles within a single frame, and over a number of frames. In order to apply the technique to fainter and/or more extended sources, Cady & Bates (1980) restricted the algorithm to using only the brightest speckle in each frame. Independent frames were centred on the brightest speckle and added, with the diffraction-limited component forming on top of a large background. The technique was seen to work for a fairly large optical bandwidth, as long as the object had a bright point which produced the brightest feature in the speckle pattern (Bates & Cady 1980). Figure 5.3 shows SAA images of single point-source objects under conditions of good seeing. As the seeing deteriorates, the fraction of the flux in the diffraction-limited component lessens, with an increasing amount of light scattered into the surrounding halo.

Previous workers have recorded two-dimensional speckle patterns, with their attendant high

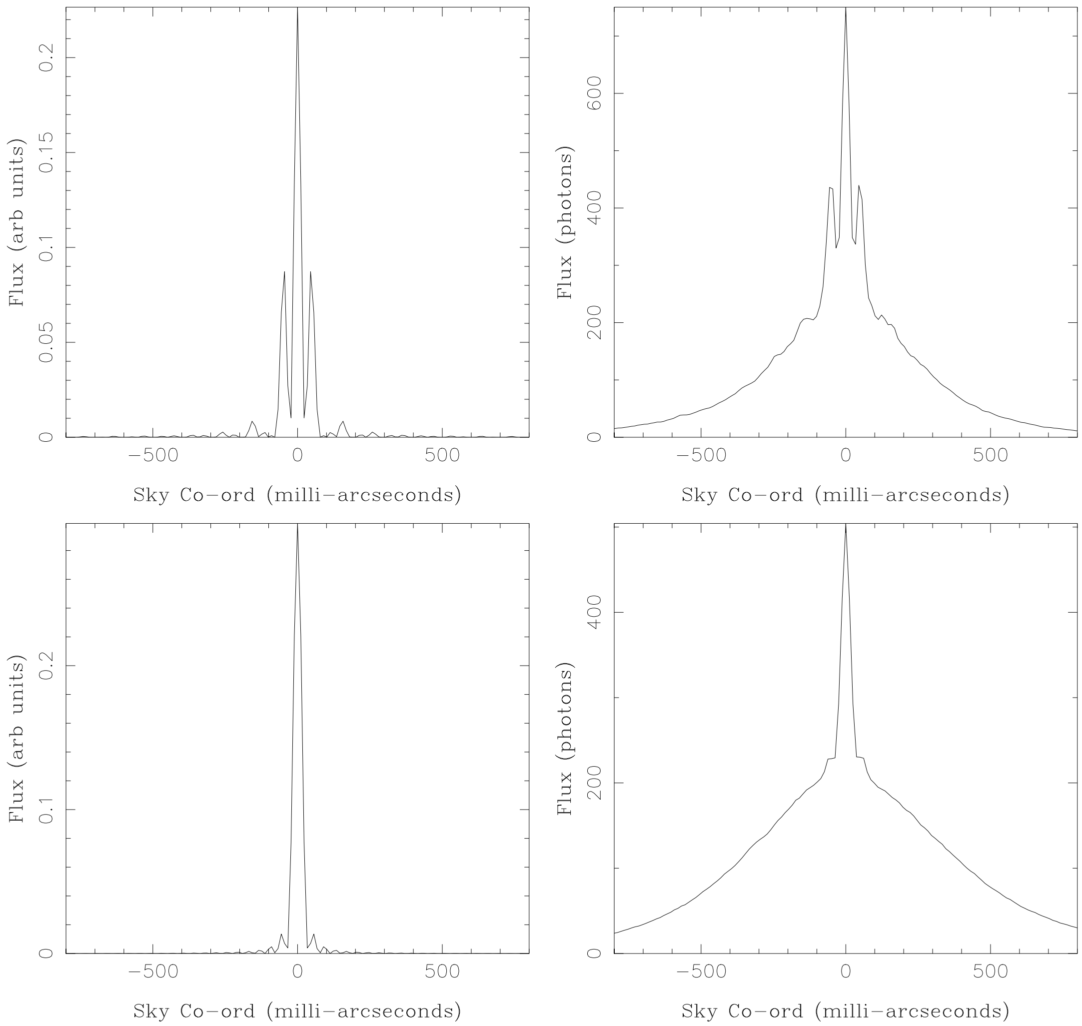

Figure 5.3: Theoretically computed diffraction-limited telescope images (left) using an axial slit with a central obstruction (top) and an unobstructed off-axis slit (bottom). Shift-and-add images recorded using each of these mask geometries whilst observing a point source star are shown to the right.

readout times and data storage requirements. The strengths of this particular implementation of SAA arise from the fast continuous one-dimensional readout technique discussed in Section 2.2. The main advantage is the ability to average over a very large number of speckle frames, with 20 000 being fairly typical for about 30 minutes observing. To obtain the same number of two-dimensional speckle frames from the CCD camera system would require over 20 hours of observing time. In addition to this extremely good statistical isolation from atmospheric noise, the one-dimensional data were also quick to process.

Binary stars make ideal candidates for SAA imaging due to the relatively simple structure and point-like behavior of the components. However, because of the duplicity of the speckles, the algorithm can produce 'ghost' images symmetrically placed about the brightest component. The problem is exacerbated when the magnitude difference between the two stars is small, since small random fluctuations will cause the algorithm to centre the pattern on speckles arising from

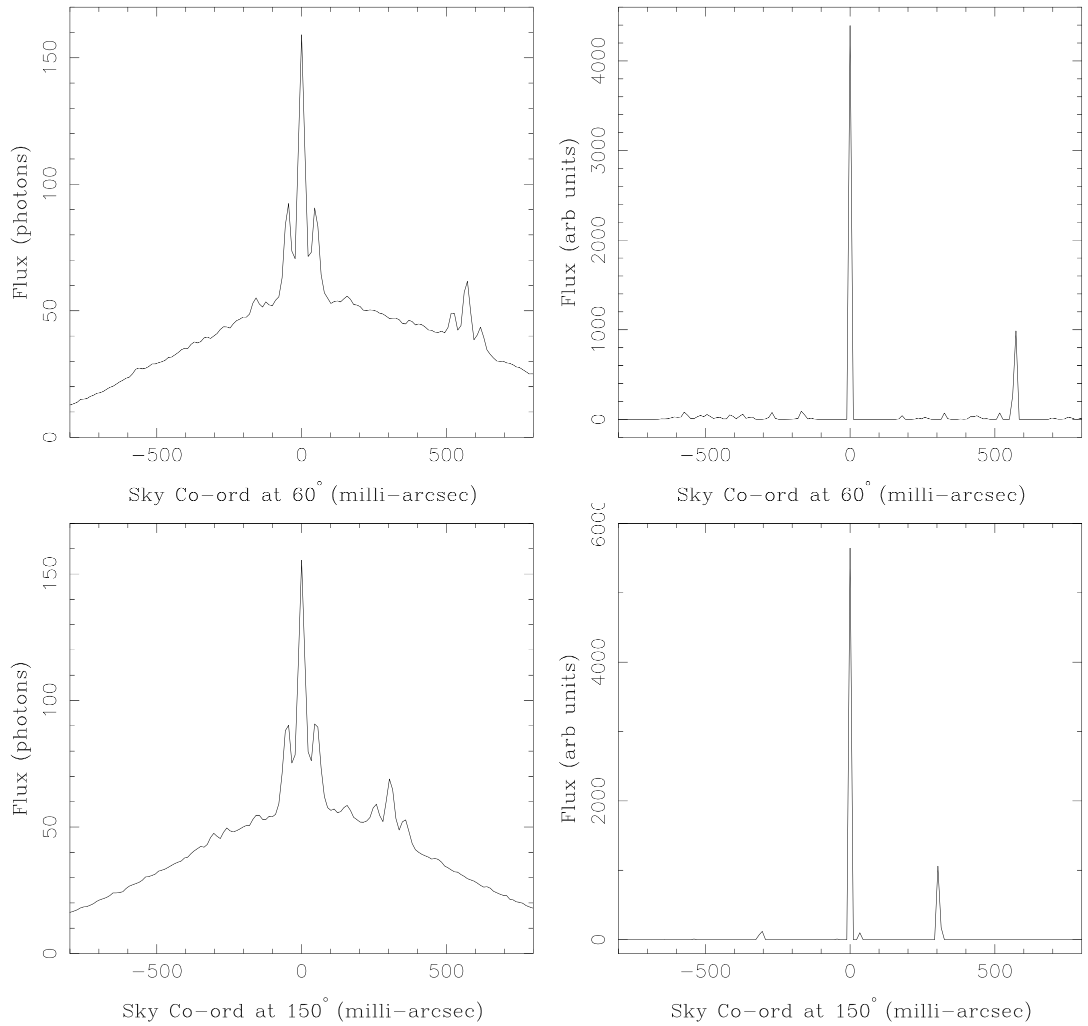

Figure 5.4: SAA images of γ CrB (left) at two position angles 60° (upper) and 150° (lower). Observations were made with an axial slit mask at a wavelength of 700 nm. One-dimensional maximum-entropy reconstructions are shown (right).

either component. Thus the pattern is not being centred on the same (object) point for each exposure.

SAA images of the well-known close binary, γ CrB are presented in Figure 5.4. Data were recorded with a slit mask in the usual way (Section 2.2) and interleaved with observations of a nearby unresolved star. It was then possible to treat the SAA image of the unresolved single star as a point-spread function to be deconvolved from the SAA image of the binary star. This deconvolution was performed using a one-dimensional implementation of the maximum entropy method (Gull & Skilling 1984). As can be seen from Figure 5.4, it was possible to restore a satisfactory one-dimensional image of the binary star for each position angle recorded. A faint ghost-image can be noted in the data at a position angle of 150°.

Even with only two position angles as in Figure 5.4, the orientation and separation of the double-star could be determined extremely well. This method provided a useful cross-check on the Fourier methods outlined in Chapter 2, and in all cases the two techniques produced consistent results. The SAA method proved successful at recovering data for which the previous methods did not prove adequate. One example of this was the $\Delta M_v = 2.6$ binary star τ Cyg, the data for which were taken under conditions of poor seeing. Despite repeated attempts, the Fourier reduction programs described in Chapter 2 would not yield a map with a clearly identifiable binary component. The SAA algorithm, on the other hand, yielded the separation and position angle of this star with an extremely high level of confidence. In addition, the time taken to perform this reduction, both in terms of computer usage and human input, was dramatically reduced. From signal-to-noise measurements it was estimated that in good (sub-arcsecond) seeing, the dynamic range should be sufficient to detect a companion at least 5 magnitudes fainter than the primary. One further advantage of this method is the ability to use a very much broader bandwidth than is possible with Fourier methods, thus collecting more flux and bringing fainter objects within reach (Bates & Cady 1980).

One star not known to be a binary was detected in this fashion. α Del does have a distant (one arcminute) faint ($\Delta m_v \sim 8\,\mathrm{mag}$) known companion – see *e.g. The Hipparcos Input Catalogue* (Turon *et al.* 1992). This puts the companion well outside our field of view, and so the brighter component ($m_v = 3.9$) should behave as an ideal point-source for our experiment. Since this star is near to the well-known close binary β Del, and is not indicated as being multiple in the catalogue of McAlister & Hartkopf (1984), it was used as an atmospheric calibration point-source. Upon implementing the SAA algorithm upon the data, however, it quickly became apparent that α Del(A) was itself a close binary system. α Del is then a triple system, where a distant faint companion orbits a close binary. This close double-star has an approximate Δm_v of 1.6 at 710 nm. The position angle was $-163.2^\circ \pm 5$ whilst the separation was $212.5 \pm 5\,\mathrm{mas}$ on 9 June 1993 (JD 2449149). Most of the error in these estimates comes not from the measurements themselves, but rather from the uncertainties of calibration of the plate scale and orientation.

Attempts were made to resolve further double stars. Data were taken on known spectroscopic binaries, of which one component was a K giant. Velocity curves for these systems were known, and the addition of orbital separation information would have allowed the determination of the masses. It was hoped, thereby, to improve the mass estimates of K giants as these are not well known. Unfortunately, it was not possible to identify any secondary components from the data. However, the observations were made prior to a successful demonstration of the SAA technique on data from the WHT experiment and consequently the setup was not optimised for this analysis procedure. Similar problems hampered the attempted detection of duplicity in the binary Mira systems X Oph and o Ceti.

The range of applicability of this simple implementation of the SAA technique was investigated by using data from extended sources as well as the multiple stars already discussed. As was expected, the lack of a bright, concentrated point enabling the algorithm to identify single speckles severly hampered the imaging of such objects. The iterative matched filter approach (Ribak *et al.* 1985, Ribak 1986) would help to circumvent this problem with the use of a digital filter to optimise the detection of individual speckles.

One further technique which has found application in the detection of binary stars from speckle exposures is to perform an auto-correlation on each image. Despite yielding no phase information, the phaseless symmetric map is sufficient for the separation and position angle of binaries to be determined (modulo 180°). This method was implemented by performing an average of the auto-correlation of each one-dimensional frame, over all the data taken at each position angle. Although it was possible to resolve many double-stars, this method proved inferior in signal-to-noise terms when compared with SAA using the same data.

5.4 A Simple Hartmann Seeing Monitor

In order to perform experiments on the nature of atmospheric seeing, a simple wavefront sensing device was designed, built and operated on a number of occasions and at different telescopes. Hartmann sensors are devices for measuring the phase across an incoming wavefront. The most popular form, known as a Hartmann-Shack sensor, employs a grid of small lenses to divide an input pupil into an array of sub-apertures. The light from each of these is focused separately upon a two-dimensional detector. The wavefront tilts across each sub-aperture cause displacements in the position of each image, and if the subsections are not larger than r_0, then the phase across the entire pupil may be derived. Measurements are normally made at least once each t_0 to follow the temporal evolution of the seeing fluctuations.

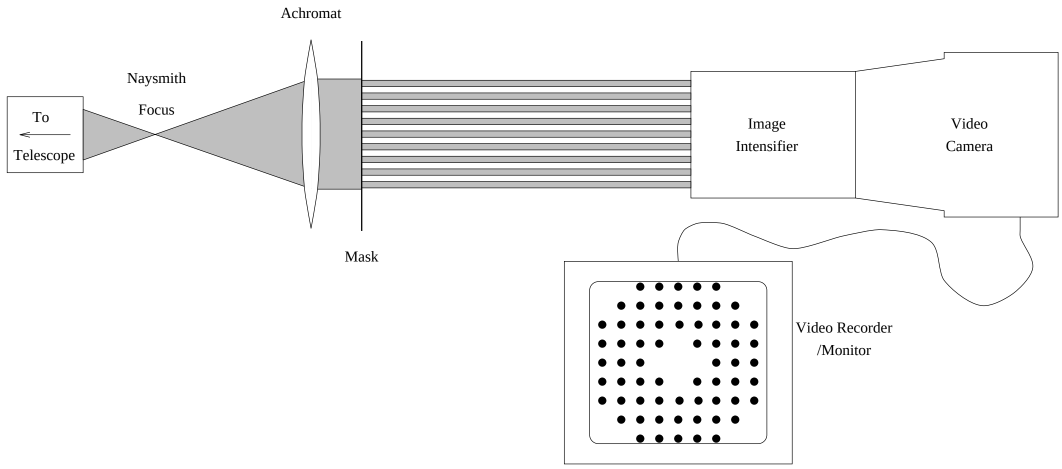

Figure 5.5: Hartmann apparatus for seeing measurements. Starlight was collimated using an achromatic lens, then passed through a mask consisting of an array of holes. It was then detected, after propagating for a certain length, by an intensified CCD camera and the data recorded on video tape. A typical pattern of spots from starlight passing through the mask is shown on the sketch of the monitor.

The apparatus constructed, which is depicted in Figure 5.5, did not meet these ideals of performance in a number of respects. Data were recorded at the standard video frame rate of 20 msec/exposure which is likely to be longer than t_0. A more serious limitation was imposed by the simple pupil-splitter which consisted of a sheet of aluminium foil, through which holes had been photochemically etched. Light from each hole formed a diffuse spot on the intensified camera, and despite the fact that they were not in focus (in contrast to the spots from a lenslet array), their centroids could still be used to yield a measurement of the wavefront phase tilts across each sub-aperture. Although the holes were scaled such that they corresponded to the expected value for r_0 ($\sim$20 cm at the WHT), each was separated by one diameter from its neighbours, so that only one quarter of all possible r_0 sized patches were sampled. These gaps in measurement precluded the full interpolation of the phase across the pupil. Despite these drawbacks, the device was simple and inexpensive to construct, and was adequate for the purposes of the intended experiments.

Data were taken both at the 36 inch telescope in Cambridge, and at the 4.2 m WHT under various seeing conditions. The most interesting data came from the WHT and we shall restrict our attention to these. Observations were made on the night of 20 January 1992. The $f/11$ beam from the telescope was collimated with a 63 mm focal length achromat, and then passed through an array of holes of diameter 0.3 mm and center-to-center spacing 0.6 mm. This resulted in the apparent diameters of the holes projected onto the primary mirror being 22 cm. The mask was 88 mm from the intensifier which gave sufficient throw for the phase tilts at the holes to cause measurable shifts in the positions of the spots. Caution had to be exercised in order not to have too much throw, or the motions of the spots would become so large that they would overlap with neighbouring spots and thus become extremely difficult to follow. The final scale used was such that a motion of 20 pixels on the detector represented a wavefront tilt of one arcsecond. Note that there was no specific wavelength-selective element in the system, thus the apparatus sensitivity depended upon the response curve of the image intensifier – which peaks in the blue.

Video tape data of the grid of sub-apertures fitting within the pupil and back-illuminated by light from the stellar source were recorded for approximately ten minute intervals. These raw data could be viewed on a video cassette player as a pattern of spots which was in rapid motion as the seeing fluctuations generated phase tilts across the holes. The information to be extracted from each frame was the location of the centroid of each of the spots in the array.

Data were analyzed as follows. Each video frame was captured using a frame-grabber card, and transferred into computer memory as an intensity map. A program then divided this map into square regions, with the spots from the sub-apertures occupying the approximate centre of each region. The flux within these squares was then binned in the horizontal and vertical directions separately, yielding the 'i' and the 'j' profile of intensity. Finding the centroid of these gave a measurement of the (i, j) co-ordinate of the bright spot due to (and hence the wavefront tilt across) each sub-aperture. Having performed this task for each of the $\sim$ 50 spots in the grid, the centroiding process above was repeated for the next frame of video data. In this fashion, it was possible to build up a time-sequence of the (i, j) positions of the spot from each sub-aperture, with a time resolution of 20 msec.

5.5 Seeing Studies with a Hartmann Sensor

The primary aim of the Hartmann experiment was to investigate the frozen turbulence assump-

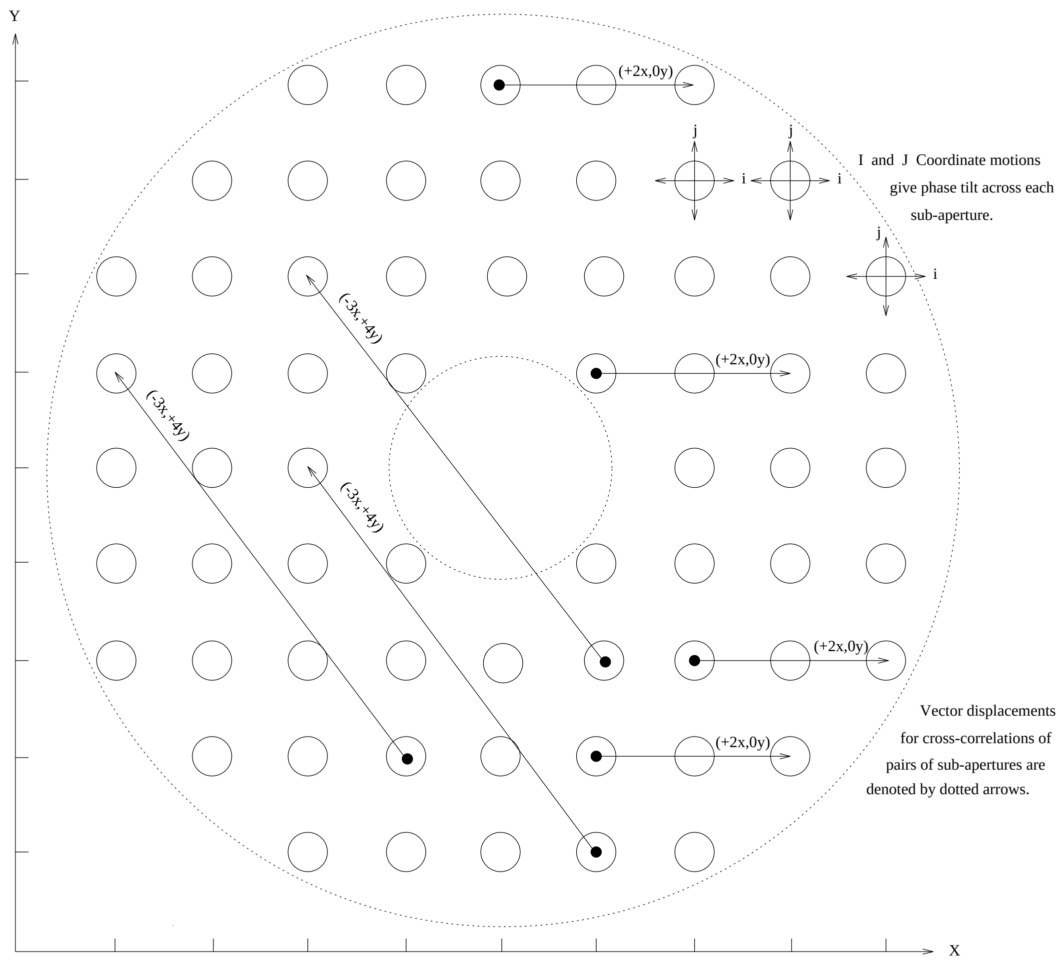

Figure 5.6: Diagram of a frame of Hartmann data. The large circles in a dotted line-type represent the shadows from the secondary and primary mirrors - thus in the absence of the grid of holes the region between these circles would be illuminated by starlight. The small circles represent the locations of the bright spots due to each sub-aperture. For consecutive frames, these all move in the i and j directions. Cross correlations of the spot motions were made for pairs of holes at certain vector displacements. The cross correlation function of the entire pupil was found by taking the mean of the motions of all pairs of spots separated by the same vector displacement. Two examples of these vectors for a few different pairs of spots are shown by the arrows: $(+2x,\ 0y)$ and $(-3x,\ +4y)$.

tion outlined in Section 5.1. In particular, it was hoped to address two questions. The first of these was to determine the number of turbulent layers with discrete wind velocities contributing to the seeing. The second related to testing the assumption underlying the frozen turbulence model: that the turbulent motion is slow enough so that the time for cells to cross the pupil is much shorter than their evolution time. Thus, the aim was to measure the extent to which fluctuations were truly 'frozen' as they blew across the telescope.

Having obtained time-sequences of the motion for each sub-aperture, the analysis proceeded by *cross-correlating* these data. The i co-ordinate data for one sub-aperture was cross-correlated with the i co-ordinate data for a second sub-aperture. This was done for all sub-apertures having the same vector separation as the original pair, each of which yielded a (time) cross-correlation function. The (time) cross correlation of the entire pupil was found by taking the mean of all these functions, and thus represented the pupil correlation at a given single vector displacement. A diagram illustrating this procedure is given in Figure 5.6.

Unfortunately, it was found that the seeing could not be studied with the use of data recovered in this way. Problems arose because these data were found to be dominated by a periodic motion of the whole pupil. This motion is shown in Figure 5.7 and was almost certainly

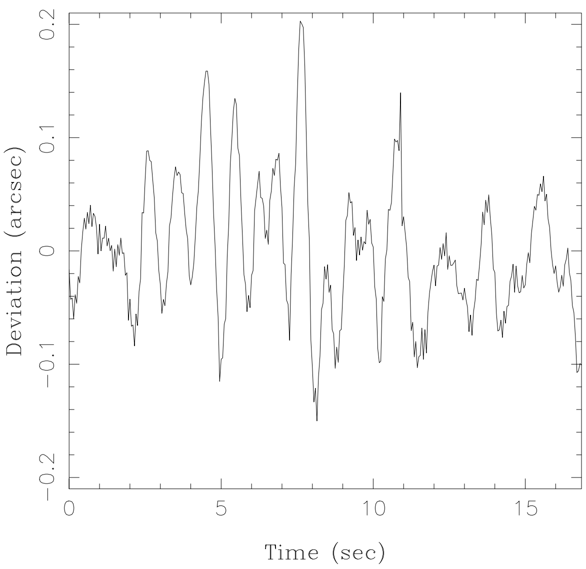

Figure 5.7: Mean i co-ordinate motion of all sub-apertures as a function of time. Note the dominance of the periodic motion with an amplitude of approximately $0.2''$ and a frequency of 2.6 Hz. Similar motions were observed for the j co-ordinate.

of instrumental origin since the oscillation frequency of 2.6 Hz agreed precisely with one of the commonest telescope mechanical resonances. The cross-correlation signal caused by this oscillation was large enough to dominate any effects due to the atmospheric phase screen – thus it was necessary to subtract the mean telescope motion from the motion of each sub-aperture before performing any cross-correlations. Note that in addition to removing the telescope vibration term, this process also removed any large-scale phase tilts due to the atmosphere.

Cross-correlations of the entire array of sub-apertures were then performed for various vector displacements, so that phase corrugations from different parts of the pupil and at different times could be compared. For large vector displacements of the pupil (*e.g.* $(-3x,\ +4y)$ in Figure 5.6), the number of pairs of sub-apertures which contributed to the mean pupil cross-correlation decreased, thus reducing the signal-to-noise.

Correlation functions of the measured phase tilts within the pupil for time delays of ± 10 sec were computed. This was performed for vector displacements of the pupil from 0 (auto-correlation) to $> 3\,\mathrm{m}$ in all directions. Two entire independent datasets of this type were generated, one correlating motions in the i co-ordinate and the other in the j co-ordinate. Examples for the i co-ordinate motion are displayed in Figure 5.8.

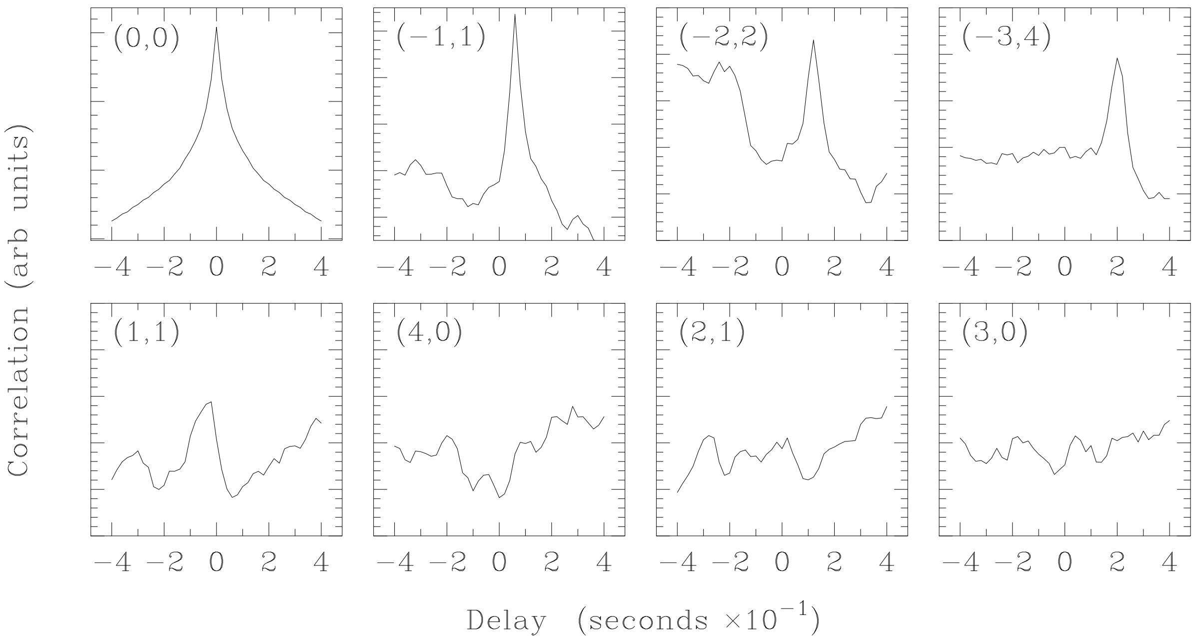

Figure 5.8: Observed cross-correlation functions (with the mean telescope motion subtracted). The upper left-most panel shows the mean auto-correlation of the motions of all spots within the pupil, which peaks at zero delay. Vector displacements (in units of hole spacings on the grid) are indicated in parentheses to the upper left of each panel. Three further boxes in the upper row show cross-correlations of the array of sub-apertures at increasing displacements. The direction of these displacements was chosen to be parallel with the wind, so that the three boxes show a peak at increasingly large delay in going from left to right – corresponding to the time-of-flight for wind-driven fluctuations. The lower panels show correlations of the pupil with displacements in directions not lying along the principal wind direction. For these data, some correlation was noted for small vector displacements (first panel) but this rapidly diminishes (later panels).

A great deal of information can be inferred about the seeing from the cross-correlation functions. In order to interpret these data more easily, two quantities were extracted from each mean correlation function. These were (1) the *strength* of the peak and (2) the *delay* of the peak – with both quantities being set to zero if there was no clear peak in the correlation function. These two quantities were recorded as a function of the pupil displacement vector. The results are shown graphically in the contour maps of Figure 5.9.

We now proceed to interpret these data in the context of the frozen turbulence model. The first conclusion which can be drawn is that there *was* one single dominant layer of turbulence moving with a discrete velocity at the time of these observations. This can be seen from Figure 5.9

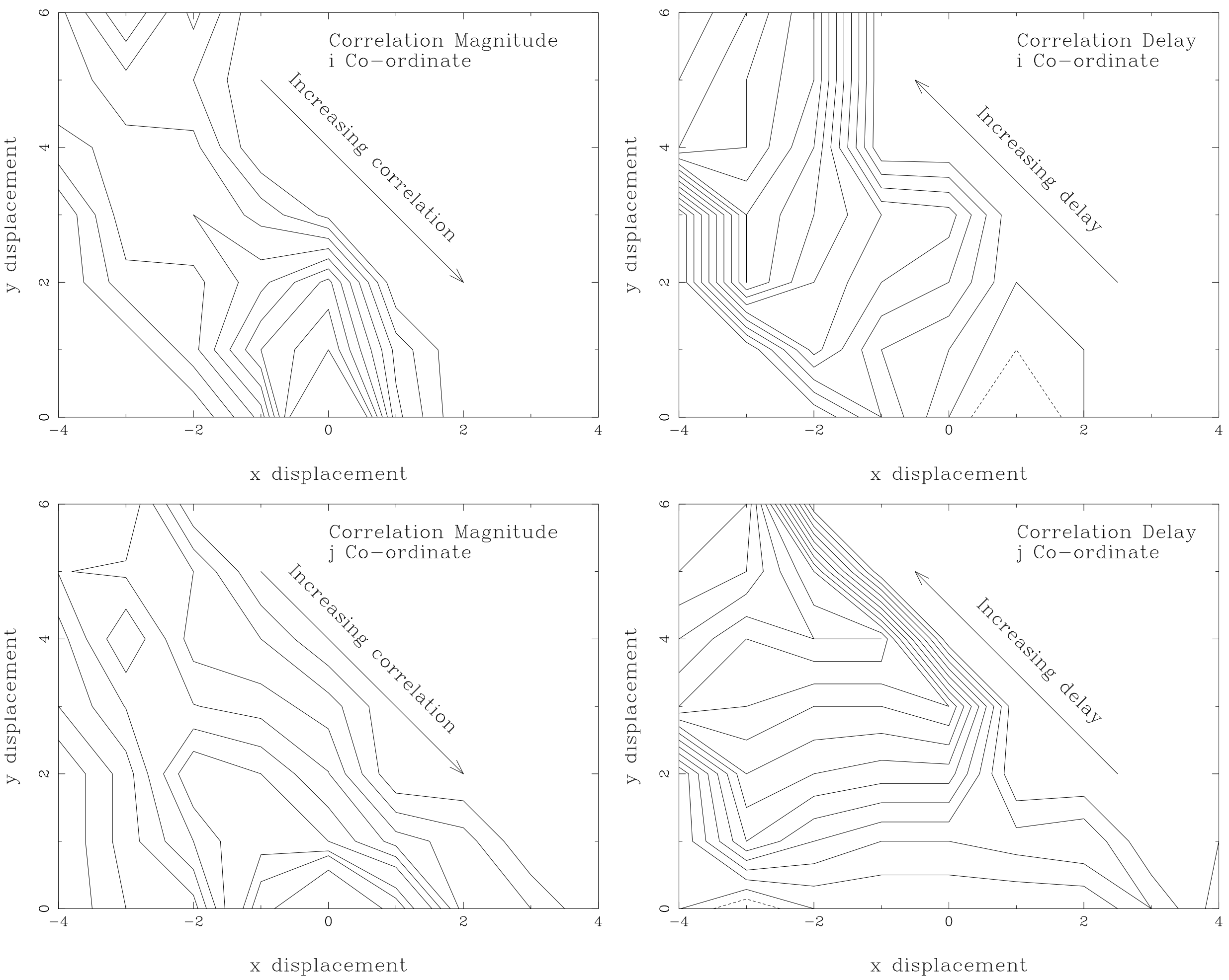

Figure 5.9: Contour maps of the cross-correlation strength and delay. The strengths of the peaks in the cross-correlation functions are displayed as contour maps (left), where the co-ordinates of the maps correspond to the displacement of the array of sub-apertures within the pupil. The maximum correlation is seen at position (0, 0), and this can be seen to decline rapidly in all directions except towards the upper left. This is interpreted as being the wind direction. The delays in the correlation peaks are given in the maps to the right. The maximum delay, corresponding to the longest time-of-flight downwind is in the upper left-hand corner. Data from the upper panels comes from analysis of motion in the i co-ordinate, whilst the lower panels have used the j co-ordinate motion. All maps have evenly-spaced contour levels.

where the correlation strength diminishes rapidly in all directions but one – *i.e.* downwind. The delay data are consistent with this and show an approximately linear increase in time lag – consistent with a time-of-flight – in the same direction. The wind was found to be blowing at 10.7 m/sec across the pupil at an angle of about 50° to the x axis. These conclusions are consistent for both the i and j correlations. If there was an additional wind direction affecting the phase screen, further correlations should have been noted in other directions. Even if a second turbulent layer happened to be moving in the same direction but at a different speed, this should have been noted as a broadening or splitting of the peaks in Figure 5.8. No such splittings were seen. The absence of such behaviour strengthened the case for the single layer.

We now turn to the question of the scale size of the fluctuations. Equation 5.2 shows that for Kolmogorov turbulence, approximately equal contributions to the phase tilts arise from all spatial scales. Thus there should have been no preferred scale size for the refractive-index fluctuations in the wavefront. However, the Hartmann experiment was only sensitive to phase perturbations on a limited range of spatial scales. This is because the larger scales causing tilts across the whole 4.2 m aperture were removed from the data (as it was not possible to distinguish them from telescope tracking errors). Furthermore, the wavefront sensor was not sensitive to the smallest scales (below ~ 0.2 m), since these would cause speckling in the spots from each sub-aperture, but would not alter the mean positions of the centroids. Thus the experimental procedure discarded information on scales smaller than the size of the holes, and larger than the size of the pupil.

The scale size of the fluctuations actually recorded was determined experimentally from measurements of the widths of the peaks in the correlation functions. This peak width gave the time-of-flight for fluctuations to cross one hole. Combining the widths taken from cross-correlation data (Figure 5.8) with the (known) wind velocity yielded scale sizes in the range 0.80 to 1.10 m. Little evidence was found for wavefront tilts on scales larger than this. It was not clear whether this deficit at larger scales was an artifact due to the subtraction of the mean motion, or was due to a true fall-off in turbulent power at larger scale sizes. If the latter was true, it would have a bearing on the question of the size of the outer scale L_o. The value of L_o appropriate to astronomical seeing has remained contentious for some time, with estimates varying from a few metres (Coulman *et al.* 1988, Nightingale & Buscher 1991) to a few kilometers (Colavita, Shao & Staelin 1987). Although the results presented here should be viewed as provisional until many details of the experimental procedure can be improved, they may point to the existence of an outer scale *smaller* than the 4 m telescope pupil.

Finally, we now discuss the time evolution of the phase screen. For frozen turbulence, the phase screen does not evolve at all as it crosses the pupil. This would imply that the strengths of the correlation peaks in Figure 5.8 should not fall off with longer vector displacements, *i.e.* perfect correlation would be expected in the down-wind direction. Figure 5.9, however, clearly shows that the correlation did diminish as the pupil was displaced successively further from the auto-correlation position. This is hardly surprising since the frozen turbulence assumption, although convenient, is a drastic over-simplification of the real dynamics of the atmosphere. It can be seen from Figure 5.9 that the correlation between apertures about 2 to 3 m apart diminished to approximately half the value for apertures separated by only 0.4 m (the minimum). Combining this with the conclusion that the scale size for phase tilts was of order ~ 1 m, it can be concluded that the evolution of fluctuations occurs over length scales of a few times their own characteristic size.

As might be expected, the temporal behaviour of astronomical seeing has been found to be neither fully static as in the frozen turbulence model, nor entirely random, but rather lies between these extremes. There is a strong need to quantify information of this nature for the field of adaptive optics. If it is possible to use the wavefront information from previous measurements to predict the future behaviour of the phase screen, albeit imperfectly, this should prove extremely valuable. Such 'limited predictability' to the seeing would enable the attainment of better performance from the correction system using guide-stars which are further away (increasing the isoplanatic patch size, especially downwind) or fainter (increasing the effective integration time).

Chapter 6

COAST

If the Theory of making Telescopes could at length be fully brought into practise, yet there would be certain Bounds beyond which Telescopes could not perform. For the Air through which we look upon the Stars, is in a perpetual Tremor; as may be seen by the tremulous Motion of the Shadows cast from high Towers, and by the twinkling of the fix'd Stars. Long Telescopes may cause Objects to appear brighter and larger than short ones do, but they cannot be so formed as to take away that confusion of the Rays which arises from the Tremors of the Atmosphere.

Sir Isaac Newton

Separated-element stellar interferometry offers the potential to attain extremely high resolutions using baselines measured in kilometers. This chapter describes one such instrument, known as the The Cambridge Optical Aperture Synthesis Telescope (COAST). This device was at a developmental stage throughout the course of the work described here. Research was performed upon a number of aspects of the COAST, mostly relating to practical aspects of the design and instrumentation.

6.1 Introduction

The COAST has been designed as a coherent array of four telescopes operating in the red and near infra-red with baselines of up to 100 m. The telescopes are arranged in a 'Y' configuration in order to make use of a radio-astronomical technique known as *earth-rotation synthesis*. This relies upon the rotation of the earth to sweep the telescopes – and thus the baselines – around with respect to the distant astronomical target. Sufficient UV coverage for imaging is built up as baselines within the 'Y' sweep out paths in the Fourier plane.

For the present, however, we shall restrict our attention to a subset of the completed design consisting of two telescopes separated by the relatively modest baseline of a few metres. In order to appreciate the design of the instrument, it is best considered as a set of dedicated subsystems responsible for different aspects of the performance. These are depicted in Figure 6.1 as: (1) the telescopes, (2) the optical path compensator, (3) the fast tip-tilt corrector and (4) the beam combiner & fringe detection systems.

Each telescope comprises a 50 cm siderostat flat feeding a fixed horizontal Cassegrain telescope with a magnification of $\times 16$. Precision rotary tables enable the siderostat to be accurately pointed for the acquisition and tracking of target objects. Telescopes are housed in dry weatherproof enclosures and the beams are fed through pipes into the optics laboratory using beam-

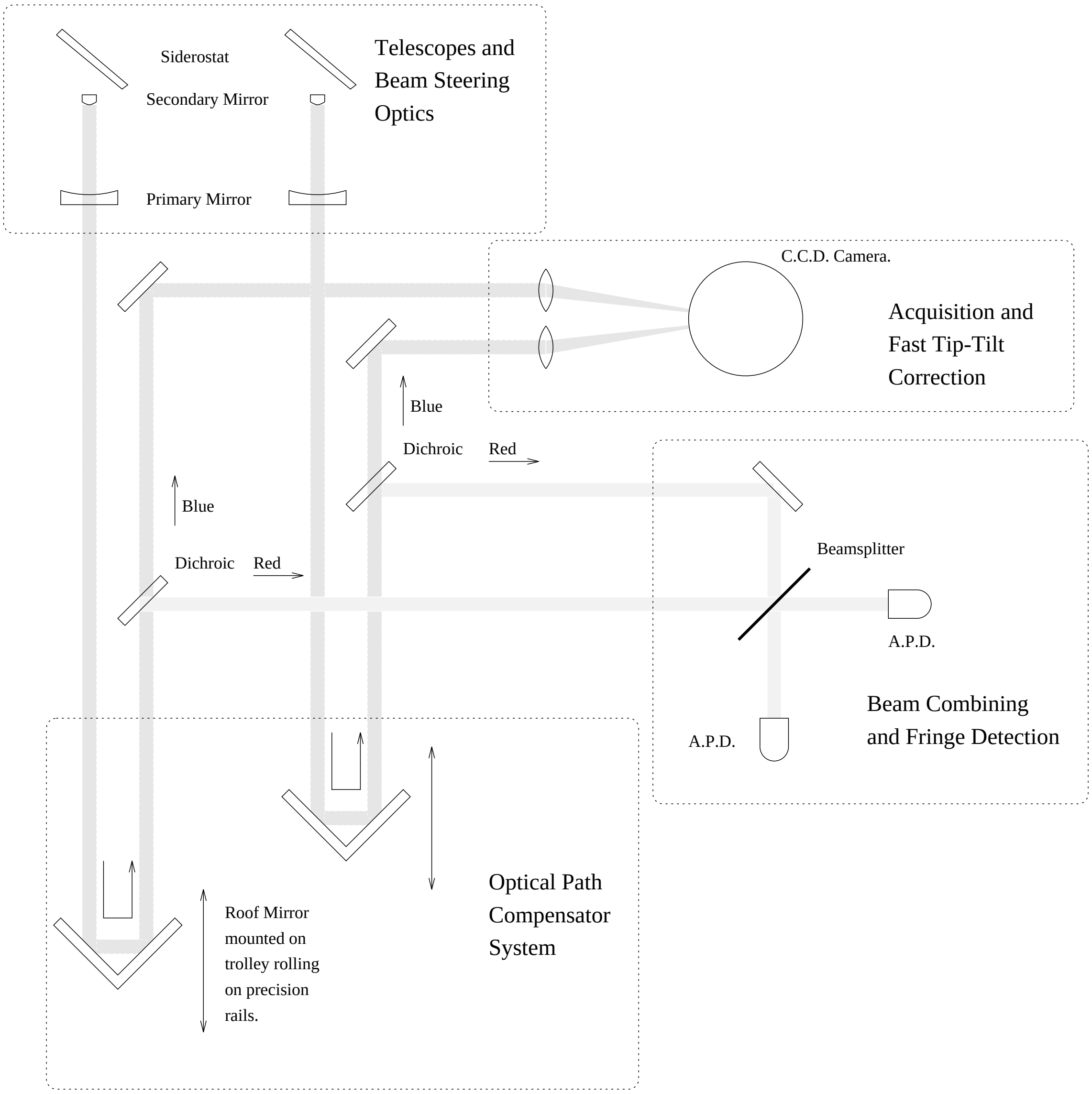

Figure 6.1: Schematic diagram of optical layout for COAST.

steering mirrors. The baselines can be changed by moving the telescopes to different stations where they locate upon kinematic mountings.

Upon entering the optics laboratory, starlight passes into the path compensation system whose function is to ensure the equalization of the optical paths to the source through each arm of the interferometer. This is achieved by reflection of the beam in a roof mirror carried by a trolley running on precisely aligned rails. The motion of this trolley is carefully controlled by a computer in combination with a servo loop and a laser metrology system. In addition to smooth motion which fixes the phase centre of the interference pattern whilst the array moves with respect to the source, it is also possible to superimpose sawtooth or other waveforms onto the optical path. This has the effect of sweeping through the interference envelope and enables the measurement of the fringe visibility and phase. Light emerging from the path compensator is split using a dichroic, so that wavelengths longer than 650 nm pass into the beam combining optics, whilst the shorter wavelength light is used for acquisition and fast tip-tilt correction.

The next subsystem to be discussed is responsible for star acquisition and guiding using the blue light passed through the dichroics. The CCD camera depicted in Figure 6.1 can be operated in two modes, the first of which reads out a large area for the purposes of finding and centering a new object in the field. When this is accomplished, a second mode can then be activated in which the camera reads out only a small area, binned so as to simulate a quadrant detector for each input beam. This provides rapid measurements ($\lesssim$5 ms) of the tilts in the incoming wavefronts. These are mainly due to the seeing, but also posses a contribution from mechanical vibrations and imperfections in the siderostat drives. In order that the beams from different telescopes overlap and so generate an interference pattern, it is important that these tilts are removed. This is achieved by feeding the error signals from the simulated quadrant detectors into a servo control system using a piezo-electrically driven two-axis mirror located at each telescope.

The final measurements of stellar visibilities and phases are obtained from the beam combining system. It is here that the interference pattern from starlight gathered from the different telescopes is recorded. For only two input beams, a relatively simple beam combiner can be used. This is depicted in Figure 6.1 and consists of a beam-splitter with an avalanche photodiode (APD) at each output port. Avalanche photodiodes are single-element detectors and were chosen for their low noise, fast response time and high quantum-efficiencies over a broad range of wavelengths. Since the APD's have only a single element, it is not possible to sample a spatial interference pattern and it is necessary that fringes are encoded temporally. This is done with the use of the path compensation system. The optical path in one arm of the interferometer is modulated, causing the phase centre of the array to sweep through the interference pattern. Fringes are then recorded as a time-modulation in intensity received at the APD's.

Over the course of the research described here, a number of aspects of the instrument were at early stages of development. There were only two functioning telescopes rather than four and the path compensation system was not automated and thus could not track the fringe envelope. Further details of the design and performance of the COAST array can be found in a number of conference proceedings dedicated to high resolution astronomical imaging (Beckers & Merkle 1992, Robertson & Tango 1994).

6.2 Experimental Work

Work performed on the COAST array fell into one of three categories; (1) design and construction of instrumentation, (2) evolution of alignment and observing strategies, and (3) testing of performance. This section details research on areas within each category.

A number of projects involved the construction of instrumentation for the COAST. One of these was a simple portable reflectometer for use in monitoring the degradation in surface quality of the mirrors, particularly those housed at the telescopes. The device constructed was battery operated and capable of measuring the reflectivity using light-emitting diodes of four colours – infrared, red, green and blue; each having an approximate center wavelength of 880, 650, 563 and 470 nm respectively. The photodiodes were mounted in a sensor head which could be placed on the mirror to be tested. Within this sensor head, light from the photodiodes was concentrated upon a small ground-glass plate and was subsequently collimated with a lens. Light then reflected off the test mirror and back through the lens, to arrive at a focus upon a pin photodiode. The device was calibrated with a number of test mirrors whose reflectivities had themselves been measured using a laboratory reflectometer. One reference mirror was kept with the portable refelctometer and measurements were taken of this reference every time a measurement of a mirror was made. Thus measurements of reflectivity were differential with respect to the reference mirror; an arrangement which calibrated for drifts such as changes in battery charge. The reflectivity of telescope mirrors was found to diminish rapidly, and it was for this reason that the telescope enclosures were sealed when not in use and had de-humidifiers installed to keep the air dry. This was found to alleviate the problem, greatly extending the working lifespan of the mirrors.

A second device was constructed and has since become an integral part of the COAST interferometer system. The purpose of the device is to convert the output of the APD's into an audible signal. This has been found to greatly assist in the finding of interference fringes. The signal from the APD's is amplified and sent to a loudspeaker, thus the sinusoidal modulation caused by the fringes is recognizable as a monotone burst. That this technique was found to be so successful at locating fringe envelopes is largely a tribute to the ability of the human auditory processing system to isolate an often weak signal amidst a strong background. However, in some instances the sources of noise such as atmospheric scintillation and photon noise on the APD signal could make fringes hard to identify. Some features were added in order to assist in this. One was that the signals from APD's at different output ports of the beamsplitter could be subtracted from each other before amplification. This had the effect of eliminating the atmospheric scintillation noise. Furthermore, variable cutoff lowpass and highpass digital filters were added so that if the expected frequency of fringes was known, it would be possible to amplify only signals of that frequency. The filters covered a frequency range from 20 Hz to 1 kHz – the expected region for transit fringes given the baselines in use.

Much of the process of alignment, optimisation and testing was possible using artificial sources of light such as lasers and lamps focussed on pinholes. Within this category were studies of the optical quality, throughput and mechanical stability of various parts of the instrument. A number of inadequate optical components were isolated in this way; for instance some dielectric mirrors in use on the path-compensator were not highly reflective ($< 50\%$) in the red, and the (ostensibly 50/50) beam-splitter being used reflected only 30% of the light, and did not treat vertical and horizontal polarizations equally. These difficulties were all rectified with the replacement of the offending components. Further problems were isolated with the sensitivities of the APD's. These were traced to the front surfaces of the fibers feeding the devices, which were simply cleaved by snapping the fiber and could contain cracks and irregularities. Better faces were achieved by gluing the fibers into commercial couplers, then polishing the faces flat. This has the added advantage that fibers can be precisely located with the use of the couplers and thus APD's could be interchanged or replaced without a lengthy alignment procedure.

One particularly useful technique in testing optical performance was the conversion of the device into a Michelson interferometer using an artificial light source (*e.g.* tungsten lamp or laser). This was achieved by introducing the collimated artificial light into one output of the beam-splitter, then arranging mirrors in each arm of the interferometer (*e.g.* at each telescope) to reflect the beam back. The interference generated when the path lengths through each arm were equalized could be used to measure a number of things. Coherence losses due to the poor surface quality of any optical components could be noted from an analysis of the visibility of the fringe pattern. The motion of the fringes was used to measure the stability of the optical path and contained contributions both from the atmosphere and from mechanical instabilities, both of which were examined. The former comprised a measurement of the degradation in performance of the array due to seeing effects between the telescopes and the optics building. Since temperature inhomogeneities at the earth's surface can be large, it is hoped to minimise this 'ground seeing' term by enclosing the beams from each telescope in pipes. The interferometer setup was also used to investigate the short-term mechanical stability of the apparatus. This was done by monitoring the fringe pattern whilst simultaneously placing a loudspeaker at different positions. The frequency of the loudspeaker was varied, and could excite mechanical resonances in components which were not adequately mounted. These vibrating components could then be detected by the modulation they induced in the fringe pattern.

When the stage where two telescopes could each acquire and track a star was reached, aspects of system performance not assessable in other ways were scrutinized. Although the computer control and electronics systems for the path compensator trolley were not then in place, the optical components could be moved manually. A search was made for stellar fringes, with two telescopes separated by a baseline of 2.8 m, by moving the path compensation carriage to fixed points. The earth's rotation then swept the position of the white light fringe (*i.e.* equal paths to the beam-splitter) past this point. As it did so, so-called 'transit fringes' would be generated as the object crossed the phase centre of the array. The initial search for fringes with a new interferometer is invariably difficult since the interferometer baseline is poorly determined. Fringes were first recorded in this way whilst observing Vega in June 1991. An example of a typical fringe envelope recorded at the passage of a transit event is given in Figure 6.2.

Data such as those given in Figure 6.2 were processed by subtracting the signals from the two output ports of the beam-splitter. The fringe signal will vary in antiphase for these two signals, whilst atmospheric scintillation noise will be the same for each (careful examination of the figure verifies this). Thus the subtraction of the signals this has the effect of removing the atmospheric noise whilst enhancing the fringe signal. However, differences in sensitivity between these two APD's made it necessary to scale the signals before subtraction. In addition, the (constant) mean total signal level was added back on to the difference signal in order to be able to compute the visibility as follows:

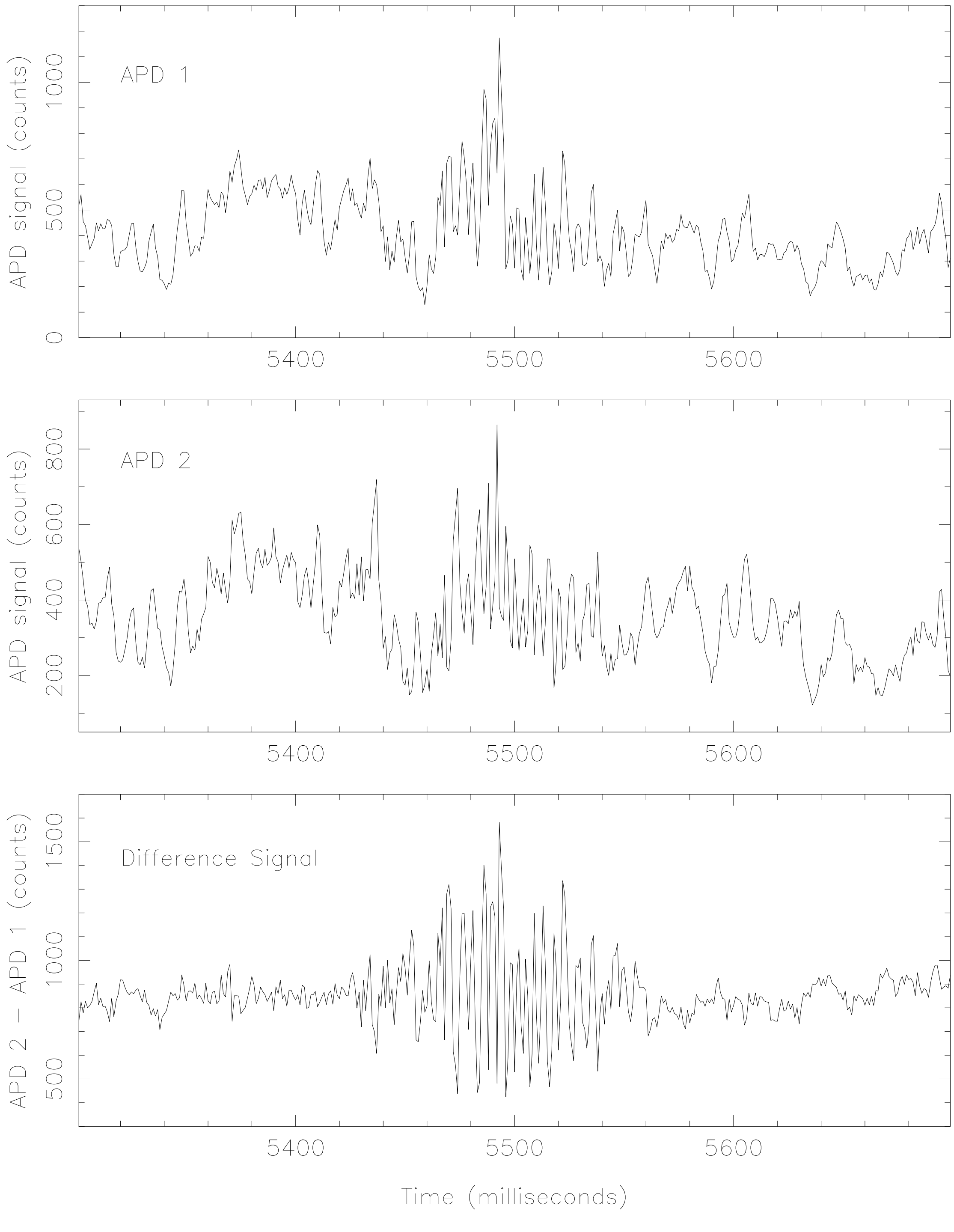

Figure 6.2: Fringes recorded whilst observing Aldebaran at 830 nm with a bandwidth of 40 nm on a baseline of 2.8 m. The two upper traces show the raw output from the two APD's, one at each output port of the beam-splitter. The difference signal in the lower panel was computed by subtracting a scaled version of the APD 2 signal from APD 1 then adding a constant level (see text). Fringes are 'transit fringes' where the path compensation trolley is stationary, allowing the rotation of the earth to sweep through the fringe packet.

$$F_{diff} \;=\; F1 - F2 \times \frac{\langle F1 \rangle}{\langle F2 \rangle} \;+\; 2\langle F1 \rangle$$

where $\langle Fi \rangle$ denotes the mean of the recorded flux Fi in detector i. The fringe packet can be seen clearly in the difference trace as a rapid variation at the centre, whilst the fluctuations at the edges are due to photon noise. The width and shape of the fringe envelope is determined by the bandpass of the filter used to select the wavelength. In this case the 40 nm 'tophat' filter should give rise to a *sinc* function, although in this case secondary maxima are not evident in the noise at the wings.

Observations of stars over a wide range of declinations and hour angles, including those with elevations as low as 20° all produced interference fringes. These observations were extremely useful in the process of surveying the precise baseline vectors. This was important when it came to the prediction of the location and trajectory of the fringe envelope on a newly acquired star. In addition, certain types of imperfection in the optical system (such as the rotational axis of the siderostats not coinciding with the reflective surface) could be found in this way. The survey of the relative telescope locations was made by combining the exact locus of the position of the white-light fringe (as measured by the laser metrology system in the path compensator) with the co-ordinates of the star and the sidereal time. This was particularly effective when data from stars at many different locations in the sky was included. Repeating this process at intervals allowed a check on the long-term mechanical stability of the array. No change at the level of about $\pm 40\,\mu$m was detected over a period of weeks.

The procedure for obtaining interference fringes on a star is illustrated in Figure 6.3. The upper trace shows the optical delay line being stepped ahead of the fringe pattern manually (by means of a micrometer screw). The earth's rotation would then sweep the phase centre of the array through the interference pattern, causing fringes to appear (and sound). The delay line could then be stepped forward again, and the process repeated. Also shown in the figure is a plot of the instantaneous visibility due to the fringes. It can be seen that this does not fall to zero between fringe transits. This contribution to the visibility does not arise from coherence, but rather from photon noise and should be calibrated before astronomical measurements are made.

It may also be noted from Figure 6.3 that the visibilities of the fringe packets varied (typically from 25 to 45%). Not only were there large fluctuations in visibility between successive transits, but within one fringe envelope (*e.g.* Figure 6.2) the visibility did not rise and fall smoothly following the expected *sinc* function. Measurements such as these were a stringent test of the performance of the fast tip-tilt correction system since these fluctuations in visibility were due to imperfect superposition of the Airy disks from the two telescopes. With a theoretical expectation of about 70% for the visibility given the sizes of the apertures used, further losses were also indicated. In addition to the fast guiding problems, these could be due to a polarization mismatch in the different arms of the interferometer, poor figuring of some optical surfaces or departures from ideal behavior in the beam-splitter or dichroics.

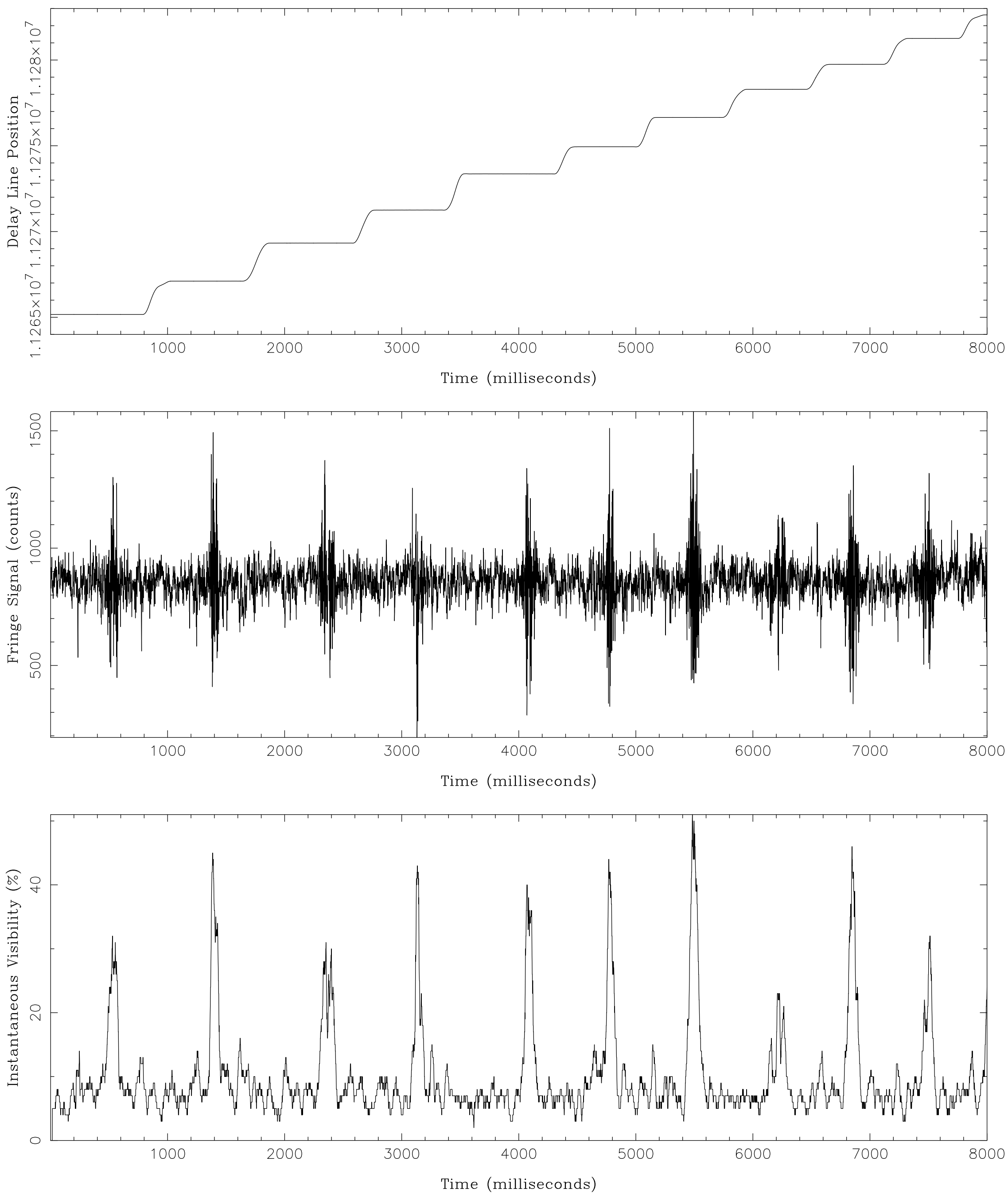

Figure 6.3: Data presented in this figure was taken whilst observing Aldebaran using two of the telescopes in the COAST array at a wavelength of 830 nm. A series of 'transit fringes' (see text) is given in the centre trace for each step in position of the optical delay line, given in the upper trace. The locus of the motion of the fringe centre is determined by the baseline and the apparent motion of the source. Processing of the fringe data yields the instantaneous visibility, as given in the lower trace.

6.3 Quadrant Cell Optics

The fast guider system initially deployed a CCD which was operated in such a manner as to simulate two quadrant detectors. Although this system proved successful for two telescopes, it was thought that attaining sufficiently fast readout rates for the four simulated quadrant detectors required in the final system might prove difficult – particularly if it was found that the fidelity of the guiding was limited by the integration time. This provided a strong incentive to develop a quadrant cell based on the photon counting APD detectors.

Initial proposals to do this involved focussing the incoming beam onto the point of a silvered pyramid. Light coming from the faces of the pyramid would then be gathered in a set of four lenses and sent to four separate APD detectors. Not only would this system be bulky and complex to align with its many optical surfaces, but attaining a sufficiently precise point to the silvered pyramid might prove difficult. Since the APD detectors come from the manufacturer already pigtailed with a multi-mode fiber, a very much more elegant system would involve polishing flat planes onto the sides of 4 fibers, then simply arranging them into the desired quadrant geometry.

Initially, it was thought that the 250 μm fibers themselves were too small for facets to be placed on the sides successfully, so some simple fiber 'horns' – long conical fibers were prepared. These were pure silica and tapered from a diameter of about 2 mm to 200 μm over a length of 10 cm. They were of one uniform refractive index (having no cladding) and were made from the rapid draw of molten material. It did prove possible to polish flat surfaces onto the wide end of these tapers, and to arrange two such fiber horns so that they formed a sharp interface (giving an active face of two semi-circles). However, this idea was not developed further for a number of reasons. The tapers were extremely delicate and difficult to work with, and as they had no cladding, light would leak out at any point where the surface was in contact with foreign matter. Thus they had to be kept scrupulously clean. The process of coupling them into the existing fibers was made almost impossible by the fact that they had extremely high numerical apertures and light would be lost upon entering clad fibers of lower numerical aperture.

The possibility of placing the facets directly onto the sides of the 250 μm fibers themselves was investigated. Firstly segments of fiber were glued into a groove cut into the corner of an aluminium block. This groove had to be precisely machined to a depth such that the amount of fiber which protruded above the surface of the metal when it was in place was the amount to be polished away. The overhanging material was ground away by hand using successively finer grits of diamond paste. Extreme caution had to be exercised not to bend or stress the fiber since this resulted in instant flaws or cracks. The final quadrant cell was built from four fibers, each of which had two flat planes polished into its sides. All four were assembled under a microscope, before polishing the front ends so that the final detector had a uniform flat face. Care had to be exercised in the final assembly to ensure that the fibers from the separate quadrants were not too tightly bolted together or else evanescent coupling between different cells resulted. The front face of one completed quadrant detector is depicted in Figure 6.4, with three of the four quadrants illuminated in each panel , illustrating the dead-space and cross-talk characteristics

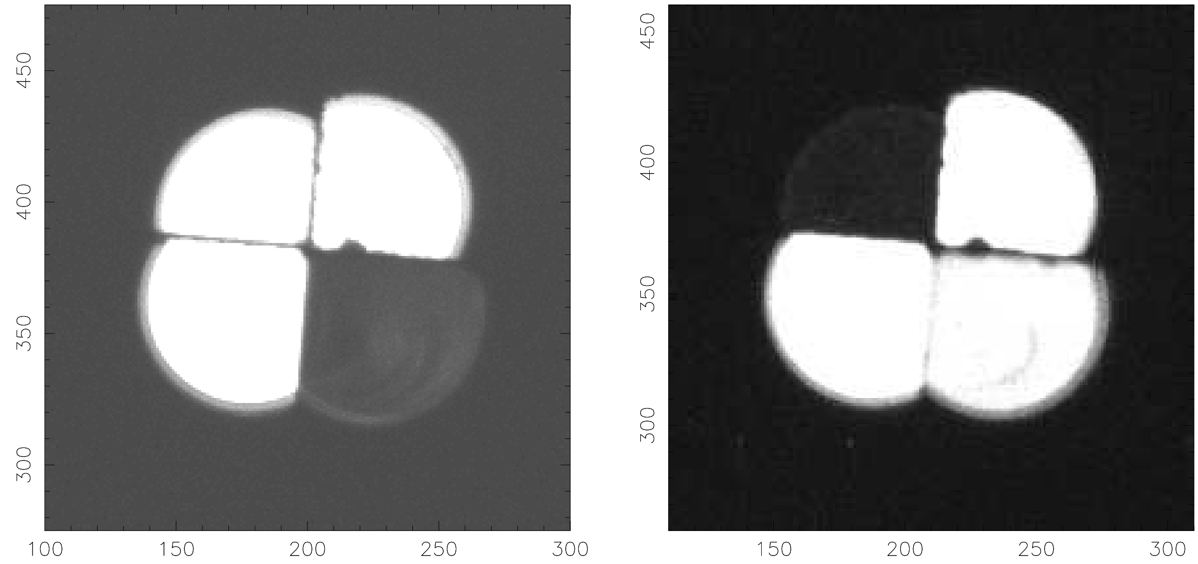

Figure 6.4: Two magnified images of a fiber quadrant cell. Various quadrants are illuminated in order to show dead space and isolation between quadrants. The enlargement is such that the square field is 570 microns on a side.

of these devices.

Measurements of completed quadrant cells were made by imaging the front face, with a large magnification, onto a CCD detector. Separate quadrants could then be illuminated by introducing light (*e.g.* from a laser or tungsten lamp) at the 'output' of each of the four fibers. By this method it was found that the detector face was 300 μm across, with a dead-space between quadrants of about 6 μm. The irregularities visible in the image were about 15 μm wide, and should be avoidable with further development of the fabrication process. Cross-talk between illuminated and non-illuminated quadrants was found to be less than 0.5% in all cases. Direct measurements of the optical throughput were extremely difficult to make, however a comparative measurement between one quadrant of the cell and a simple length of fiber was made. This was done by focussing a laser onto the entrance face of both the quadrant and the single fiber in turn, and measuring the throughput by butting the active surface of a large-area pin photodiode up to the exit faces. This procedure yielded identical transmission levels to within about 10%, the error being caused mainly by uncertainties in alignment. Thus it seems likely that the losses through the fiber quadrant were similar to those for the short length of silica fiber: a few per cent at each surface and certainly less than 10% in total.

In summary, the quadrant cells were small, fairly robust and straightforward to couple to the existing detectors. As a single device, they were easy to align and incorporate into the optical setup, and their performance was certainly satisfactory. The main drawback was the time and trouble needed in their fabrication. They have not, as yet, been incorporated into the COAST telescope and so their operation has not been studied *in situ*.

Could we employ the ocean as a lens, and force truth from the sky, even then I think there would be much more beyond.

Richard Jefferies
from 'The Storey of my Heart' (1883)

Chapter 7

Conclusions

In this chapter, a quick review the work presented in the body of this thesis is given, with some comments and suggestions for areas of future development. Research has proceeded in a number of areas associated with high angular resolution imaging of astronomical objects. Significant progress has been demonstrated in these fields, with interferometric methods being shown to be capable of routinely obtaining images whose resolution is limited only by the lengths of the interferometer baselines available. Methods involving both single monolithic telescopes and separated array-telescopes have been studied. The capability to resolve structure on very small angular scales has been found to be extremely valuable and it has been possible to successfully address a number of important astrophysical questions.

We start by discussing the single-telescope experimental techniques. Methods of aperture masking implemented at the 4.2 m WHT were found to be successful in imaging two classes of target: binary and red giant stars. Improvements and extensions have been described which help to alleviate problems such as atmospheric noise and imperfections in the optical system. Furthermore, the benefits and trade-offs in terms of signal-to-noise obtained with the use of various pupil geometries, particularly non-redundant and partially-redundant (slit) configurations have been investigated. With the use of the latter, it has been found to be possible to greatly extend the limiting magnitude of the technique enabling much fainter objects to be studied, but at the particular expense of poor recovery of phase information. A number of areas for future development present themselves. The new generation of 10 m class telescopes which are under construction at various observatories worldwide offer the chance to improve the resolution obtainable by a factor of two over the results presented here. Changing the observing wavelength also offers the chance for improved resolution in the case of moving towards the blue, or for the study of more and different classes of target in the case of wavelengths further into the infrared. The latter of these possibilities looks imminently possible with the development of high-efficiency array detectors capable of operation in the spectral region from one to a few microns. When incorporated into an aperture masking system at a large telescope, such a detector could facilitate the study of Active Galactic Nuclei (AGN) in addition to the cooler outer regions of M-giants and protostellar objects such as T Tauri stars.

The work presented relating to separated-element interferometers, and the COAST array in particular, was not at such an advanced stage: the capability to produce images with the COAST should be realized in the near future. In terms of the study of relatively large extended objects such as red giants, the high-resolution imaging techniques used in this work should be complemented rather than replaced by separated-element telescopes. The measurement of the relatively short baselines (out to four or five metres) will probably still be best accomplished at a monolithic telescope, with COAST supplying longer baseline information. The vastly longer baselines available to such array-telescopes, however, permit the study of a much wider range of astronomical targets. These encompass the diameters and morphologies of almost any bright stellar targets from normal main sequence stars to Cepheid variables and T Tauri stars. In addition, close binary stars, star clusters, supernovae, or even extragalactic objects such as AGN may be imaged. The capabilities of some optical array-telescopes (although not the COAST) allow extremely high precision astrometry measurements to be made – which could yield stellar distances and proper motions, possibly even revealing planets orbiting other stars.

The extensions to the capability of the aperture masking program mentioned above have resulted in an important shift in emphasis. It has been possible for the first time to study at high resolution a large number of stars and thus get some representation of the behaviour of the whole class of object, rather than performing individual case studies as have been done in the past for Betelgeuse and Mira. Furthermore, many of the objects (two of the four supergiants and almost all of the Miras) have not been studied at all using high resolution techniques previously, and these results thus represent an important resource for the astronomical community interested in M-giants.

Turning now to the results for Mira variables, it has been shown that high resolution imaging information can be extremely valuable in an astrophysical context. The measurement of radial profiles and angular diameters has enabled the stringent testing of models of M-giant atmospheres, and has yielded information on the wavelength and phase dependence of the atmospheric extension and limb darkening. In combination with the atmospheric models and distance estimates, the linear sizes and effective temperatures of a sample of stars were computed. These were found to be both larger and cooler than many previous workers in the field had suggested, with their effective temperatures being similar to their blackbody temperatures. These results have direct and clear implications for the mode of pulsation of Miras, and in the likely event of these stars being low mass objects ($\lesssim 1.5 M_{\odot}$), the possibility of fundamental mode pulsation has been clearly ruled out. The detailed morphology information was also able to discriminate amongst a number of competing theories which attempted to explain the distortions previously seen in images of Mira. It was found, with the advantage of phase information, that asymmetries in images arose from non-central bright features rather than from ellipticities of the photosphere. Thus it was possible to identify the model based upon bright convective hotspots in the stellar photosphere as being preferred. Furthermore, observations of Mira at a number of different epochs may have provided evidence for a theoretically predicted instability in the upper atmospheres of LPV's. An extreme enlargement of the apparent size of Mira at two epochs was tentatively identified as resulting from the aperiodic coalescence of shocks in the upper atmosphere. As such shocks are thought to be associated with motions which are at or above the escape velocity of the star, they may have important implications for the mass-loss rate and circumstellar environment of LPV's.

We now summarize the results for the supergiants studied. Observations confirmed previously-reported bright features on the surface of Betelgeuse, and extended these to three other supergiants: Rasalgethi, Antares and μ Cep. As bright features were also detected in the Mira variables, it appears likely that hotspots are not an isolated phenomena but are ubiquitous to most M-giants. The timescales for change of these features were pinned down for Betelgeuse to be around a few months. Analysis of the results points to the hypothesis that hot convective zones are responsible for the asymmetries. It seems unlikely, however, that all the variations in brightness observed in the light-curves of supergiants can be attributed to the growth and decay of such bright features. The presence of stellar pulsations has been suggested as a likely cause of additional variability, and tentative evidence for observed diameter changes in Betelgeuse – possibly constituting direct detection of pulsational motion – were presented. The observations of the star μ Cep were particularly remarkable for the extreme nature of the departures from circular symmetry. Although a number of proposals explaining these were put forward, none were seen to be entirely satisfactory. This star certainly warrants further study, preferably at higher resolutions where the ambiguities in possible morphologies can be resolved. Finally, a comparative study of the imaging results with polarimetry was made for Betelgeuse, Rasalgethi and μ Cep. A number of difficulties and potential improvements for this type of study were identified, and it was concluded that in many instances there did seem to be some relationship between the two different sets of data. This was certainly sufficient to encourage further attempts to understand the role of surface features in the generation of net polarizations in the emission from M-giant stars.

The advancement of capability in high-resolution imaging is dependent upon the detailed knowledge of the atmosphere and its effect upon incoming starlight. Progress was also reported in this area, and periodic vibrations, presumably of instrumental origin, were shown to be a significant factor in the broadening of long-exposure images taken at the WHT. Additional methods for obtaining diffraction-limited performance from short exposure images were investigated, with the shift-and-add algorithm being favoured under certain circumstances. Specifically, it was suggested that searches for and observation of binary stars might be particularly well accomplished using this technique. Finally, a pilot study using a Hartmann-type wavefront sensor was performed. This found that the atmospheric seeing on the night of observation could be well represented by a single layer of turbulence moving at a discrete velocity and in a specific direction. Furthermore, the timescale of evolution of the atmospheric phase screen was investigated, allowing a test of the extent of the validity of the 'frozen turbulence' model. The results suggest that there is some limited predictability to the form of the phase screen in the down-wind direction – thus holding out the hope that adaptive optical systems could be constructed so as to capitalize on this. This could result in relaxed design constraints and superior performance for such devices, and certainly deserves further attention in subsequent studies with more advanced equipment.

Appendix A

Observations

Table A.1 gives a summary of all high-resolution aperture masking observations analyzed for this dissertation, except those of binary stars (which were mostly used for calibration purposes). Explanatory notes describing the contents of each column follow:

Column 1 gives the name of each star observed, along with the (Kholopov 1987) designation of its type of variability. GCVS 'M' denotes a Mira-type variable, 'SRa', 'SRb' and 'SRc' denote classes of semi-regular variable and 'L' denotes a slow irregular variable. The variability of two further stars, CH Cyg and R Aqr is complicated by the presence of a close companion and they have been designated symbiotic (Symb.). For the Mira-type variables, the period of variability (in days) from Kholopov (1987) is also given. Stars are ordered according to right ascension (J2000).

Column 2 gives the calendar date at the beginning of the night when observations were made.

Column 3 gives the phase in the stars' variability cycle at the time of observation (if applicable).

Column 4 gives the centre wavelength and the bandwidth of the interference filter used for the observation.

Column 5 gives the type of pupil mask used in the observation.

Column 6 gives the diameter of a best fitting uniform-disc model to the data. The error quoted is based on the observed scatter in the data and represents a 1σ confidence limit. It does *not* include some sources of systematic error, for instance that produced by inaccuracies in the measurement of the detector image scale (which should be less than 2%). Further problems may arise because of the adoption of the simple brightness profile (uniform in this case). The late-type stars observed were not expected to exhibit such profiles, and indeed it was usually the case that even the best-fitting uniform disc model did not fit well to the measured visibility curve. This problem was only pronounced for stars with large angular diameters so that measurements of the outer regions of their visibility functions could be made. A related, although slightly distinct source of error arose due fact that, for some objects, asymmetric features were observed on the stellar surface (see Appendices B and C). This could cause problems for simple one-parameter models as they could not be made to reproduce the complex behaviour of the Fourier data. It is estimated that the typical extra contribution to the error for the fitted diameters due to the effects above could be as large as 10%.

Column 7 gives the full-width half-maximum of a best fitting Gaussian brightness profile to the visibility data. As for column 6, the error represents an estimation of σ based on the scatter in the data. The comments above about systematic errors are also applicable here. For the LPV stars, the misfit between observed visibility curves and the Gaussian models was invariably less severe than for a uniform-disc, and consequently the extra contribution from such sources of systematic error should be smaller – closer to 5% – in these cases. The extra contribution to the error on the FWHM for supergiants is probably similar to that for the uniform disk: *i.e.* $\lesssim$ 10%.

Column 8 contains comments about the observations. Instrumental problems during the July observations of 1992 meant that for some data the sky position angle could not be determined. This is denoted by 'PA Unknown'. 'Poor Data' was often the result of observations made under bad seeing conditions, however instrumental effects (such as the lack of atmospheric dispersion correction in the case of α Sco) could also contribute.

Table A.1: High angular resolution imaging observations from Jan 1992 to Dec 1994.

Object & Var. Type	Date (d/m/y)	Var. phase	Filter $\lambda/\Delta\lambda$	Pupil Mask	Uniform-disc Dia (mas)	Gaussian FWHM (mas)	Notes
o Cet	18/01/92	0.58	700/10	Slit	44.6 ± 3.0	30.1 ± 2.0	
M 332	18/01/92	0.58	710/10	Slit	53.0 ± 4.5	35.6 ± 3.2	
	20/01/92	0.58	800/10	Slit	47.0 ± 5.0	30.4 ± 3.0	
	18/01/92	0.58	902/50	Slit	37.9 ± 3.5	23.3 ± 2.0	
	13/07/92	0.05	633/10	4-H	40.1 ± 3.8	27.8 ± 2.0	
	11/07/92	0.05	700/10	5-H	39.4 ± 3.4	26.4 ± 3.4	PA Unknown
	13/07/92	0.05	700/10	5-H	42.0 ± 3.2	28.3 ± 2.2	
	13/07/92	0.05	710/10	5-H	45.8 ± 4.7	31.7 ± 3.0	
	11/07/92	0.05	833/41	5-H	44.0 ± 5.3	29.6 ± 3.6	PA Unknown
	13/07/92	0.05	833/41	4-H	40.7 ± 4.4	26.3 ± 3.1	
	12/07/92	0.05	902/50	4-H	36.4 ± 2.0	22.7 ± 1.2	PA Unknown
	03/01/93	0.48	700/10	Slit	43.4 ± 3.0	27.6 ± 1.8	
	04/01/93	0.48	902/50	Slit	37.2 ± 3.2	23.0 ± 2.0	
	07/09/93	0.22	700/10	Slit	55.7 ± 3.0	37.8 ± 2.1	
	08/09/93	0.22	710/10	Slit	70.0 ± 4.3	47.6 ± 3.1	
	08/09/93	0.22	833/41	Slit	43.4 ± 5.0	27.8 ± 3.2	
	06/12/93	0.49	700/10	Slit	58.2 ± 2.5	38.2 ± 1.7	
	06/12/93	0.49	710/10	Slit	85.8 ± 5.0	54.8 ± 3.0	
	07/12/93	0.49	833/41	Slit	45.4 ± 3.5	28.8 ± 2.2	
α Ori	19/01/92	–	700/10	5-H	43.5 ± 2.0	30.8 ± 1.4	
SRc	19/01/92	–	710/10	5-H	46.3 ± 2.5	34.0 ± 1.8	
	19/01/92	–	902/50	5-H	42.6 ± 3.0	27.2 ± 2.0	
	02/01/93	–	700/10	4-H	44.4 ± 1.7	30.1 ± 1.2	
	03/01/93	–	700/10	5-H	42.7 ± 2.2	29.4 ± 1.5	
	03/01/93	–	710/10	5-H	45.7 ± 3.0	31.8 ± 2.3	
	08/09/93	–	633/10	5-H	54.2 ± 4.0	39.9 ± 2.2	
	07/09/93	–	700/10	5-H	49.3 ± 3.0	36.7 ± 2.3	
	06/12/93	–	633/10	5-H	48.6 ± 2.0	34.3 ± 1.2	
	06/12/93	–	700/10	5-H	47.1 ± 2.5	33.1 ± 1.7	

Table A.1: *continued*

Object & Var. Type	Date (d/m/y)	Var. phase	Filter $\lambda/\Delta\lambda$	Pupil Mask	Uniform-disc Dia (mas)	Gaussian FWHM (mas)	Notes
U Ori	06/12/93	0.04	700/10	Slit	28.1 ± 2.0	17.3 ± 1.2	
M 368	07/12/93	0.04	833/41	Slit	22.9 ± 3.0	13.8 ± 2.0	
R Cnc	02/01/93	0.14	700/10	Slit	31.6 ± 3.4	19.8 ± 2.1	
M 362	03/01/93	0.14	902/50	Slit	22.5 ± 4.0	13.9 ± 3.0	
R Leo	20/01/92	0.27	833/41	4-H	44.9 ± 2.0	28.8 ± 1.5	
M 310	20/01/92	0.27	902/50	4-H	43.3 ± 2.0	27.8 ± 1.5	
	10/06/93	0.88	700/10	Slit	64.2 ± 5.7	40.8 ± 2.5	
	10/06/93	0.88	710/10	Slit	67.9 ± 7.0	45.8 ± 4.0	
SS Vir	03/01/93	0.06	833/41	Slit	19.5 ± 2.0	11.6 ± 1.2	
M 355							
V CVn	13/07/92	0.15	833/41	4-H	24.2 ± 3.0	14.6 ± 2.0	
M 192							
	02/01/93	0.10	700/10	Slit	29.4 ± 2.5	17.8 ± 1.6	
R Hya	07/06/93	0.28	700/10	Slit	37.2 ± 3.3	23.4 ± 2.0	
M 389	08/06/93	0.28	710/10	Slit	–	–	Too Faint
	09/06/93	0.28	833/41	Slit	36.0 ± 4.0	22.7 ± 2.5	
	08/06/93	0.28	902/50	Slit	34.1 ± 3.4	20.9 ± 2.2	
R CVn	13/07/92	0.06	833/41	4-H	–	–	Unresolved
M 328							
W Hya	08/06/93	0.04	700/10	Slit	65.9 ± 4.8	46.0 ± 3.4	
SRa	09/06/93	0.04	700/10	Slit	64.7 ± 5.2	46.7 ± 3.8	
(361)	09/06/93	0.04	710/10	Slit	79.5 ± 3.6	53.6 ± 2.4	
S CrB	13/07/92	0.19	833/41	Slit	21.7 ± 3.0	13.0 ± 1.8	
M 361							
V CrB	13/07/92	0.12	833/41	Slit	21.1 ± 2.0	12.9 ± 1.2	
M 358							
R Ser	13/07/92	0.27	700/10	Slit	16.0 ± 7.0	10.0 ± 4.0	Poor Data
M 357	13/07/92	0.27	833/41	4-H	15.0 ± 5.0	9.0 ± 3.0	Poor Data

Table A.1: *continued*

Object & Var. Type	Date (d/m/y)	Var. phase	Filter $\lambda/\Delta\lambda$	Pupil Mask	Uniform-disc Dia (mas)	Gaussian FWHM (mas)	Notes
U Her	09/06/93	0.02	700/10	Slit	33.6 ± 6.0	20.3 ± 3.6	Poor Data
M 406	09/06/93	0.02	710/10	Slit	35.4 ± 4.0	20.6 ± 2.5	Poor Data
	07/06/93	0.02	902/50	Slit	19.9 ± 3.0	11.9 ± 2.0	
30 Her	11/07/92	–	700/10	4-H	–	–	Unresolved
SRb	11/07/92	–	710/10	4-H	20.0 ± 3.0	12.1 ± 1.8	
α Sco	13/07/92	–	700/10	5-H	33.2 ± 3.0	20.7 ± 2.0	Poor Data
L							
	09/06/93	–	546/10	5-H	38.6 ± 4.0	27.1 ± 2.8	Poor Data
	08/06/93	–	700/10	5-H	36.7 ± 2.5	24.3 ± 1.6	
α Her	13/07/92	–	633/10	5-H	37.5 ± 1.8	24.8 ± 1.2	
SRc	11/07/92	–	700/10	5-H	34.5 ± 2.5	21.8 ± 1.6	PA Unknown
	12/07/92	–	710/10	4-H	39.5 ± 1.4	26.1 ± 1.0	PA Unknown
	13/07/92	–	710/10	5-H	40.7 ± 1.6	27.2 ± 1.1	
	13/07/92	–	833/41	5-H	36.4 ± 2.5	22.7 ± 1.6	
	09/06/93	–	633/10	5-H	36.6 ± 1.8	24.1 ± 1.2	
	07/06/93	–	700/10	5-H	34.7 ± 1.5	22.4 ± 1.0	
	08/06/93	–	710/10	5-H	39.1 ± 1.6	26.1 ± 1.1	
X Oph	13/07/92	0.27	833/41	4-H	21.8 ± 6.0	13.0 ± 4.0	Poor Data
M 334							
R Lyr	12/07/92	–	710/10	4-H	–	–	Unresolved
SRb							
R Aql	11/07/92	0.06	700/10	4-H	24.6 ± 6.0	15.0 ± 4.0	PA Unknown
M 284	12/07/92	0.06	710/10	4-H	30.4 ± 4.0	21.2 ± 3.0	PA Unknown
	13/07/92	0.06	833/41	4-H	–	–	Unresolved
CH Cyg	07/06/93	–	700/10	Slit	20.0 ± 4.0	10.8 ± 2.5	Poor Data
Symb.	09/06/93	–	710/10	Slit	24.2 ± 2.8	15.2 ± 1.8	
R Cyg	12/07/92	0.16	833/41	4-H	–	–	Unresolved
M 426							

Table A.1: *continued*

Object & Var. Type	Date (d/m/y)	Var. phase	Filter $\lambda/\Delta\lambda$	Pupil Mask	Uniform-disc Dia (mas)	Gaussian FWHM (mas)	Notes
χ Cyg	13/07/92	0.32	700/10	Slit	39.5 ± 4.0	24.4 ± 2.5	
M 408	13/07/92	0.32	833/41	4-H	33.3 ± 4.0	20.7 ± 3.0	
	13/07/92	0.32	902/50	4-H	32.9 ± 2.0	19.6 ± 1.5	
	09/06/93	0.14	633/10	Slit	36.6 ± 3.0	24.2 ± 1.9	
	07/06/93	0.14	700/10	5-H	34.0 ± 1.6	21.4 ± 1.0	
	08/06/93	0.14	710/10	Slit	41.2 ± 4.0	27.9 ± 2.5	
	07/09/93	0.35	700/10	Slit	43.5 ± 4.0	26.4 ± 2.5	
μ Cep	12/07/92	–	546/10	4-H	27.8 ± 3.5	17.5 ± 2.1	PA Unknown
SRc	12/07/92	–	633/10	5-H	27.0 ± 3.5	16.7 ± 2.1	PA Unknown
	11/07/92	–	700/10	4-H	31.4 ± 3.0	19.6 ± 2.0	
	12/07/92	–	710/10	4-H	29.3 ± 3.0	18.2 ± 1.8	PA Unknown
	08/06/93	–	633/10	5-H	30.5 ± 3.4	19.4 ± 2.2	
	09/06/93	–	710/10	5-H	33.4 ± 4.0	21.4 ± 2.7	
	08/09/93	–	633/10	Slit	32.0 ± 3.3	19.9 ± 2.0	
	07/09/93	–	700/10	Slit	29.2 ± 2.9	18.1 ± 1.9	
	08/09/93	–	710/10	Slit	32.0 ± 4.2	20.3 ± 2.7	
T Cep	12/07/92	0.72	700/10	4-H	33.9 ± 4.0	21.8 ± 2.6	PA Unknown
M 388	12/07/92	0.72	905/50	4-H	27.4 ± 6.0	20.0 ± 5.0	PA Unknown
	07/06/93	0.56	830/41	Slit	29.0 ± 4.0	18.6 ± 2.5	
R Aqr	13/07/92	–	830/41	4-H	23.4 ± 4.0	14.3 ± 2.5	Poor Data
Symb.							
R Cas	13/07/92	0.05	700/10	4-H	41.4 ± 4.0	26.8 ± 2.5	
M 430	13/07/92	0.05	700/10	Slit	42.9 ± 5.0	28.0 ± 3.2	
	13/07/92	0.05	710/10	4-H	51.0 ± 5.0	36.1 ± 3.4	
	13/07/92	0.05	710/10	Slit	55.5 ± 5.0	36.4 ± 3.4	
	13/07/92	0.05	833/41	5-H	30.8 ± 3.0	18.9 ± 2.0	
	08/06/93	0.82	700/10	Slit	42.5 ± 4.0	27.3 ± 3.0	
	09/06/93	0.82	710/10	Slit	–	–	Too Faint
	07/09/93	0.03	700/10	Slit	41.2 ± 2.5	26.7 ± 1.6	
	08/09/93	0.03	710/10	Slit	54.1 ± 3.4	34.4 ± 2.2	
	08/09/93	0.03	833/41	Slit	33.0 ± 4.0	20.3 ± 2.5	

Appendix B

Morphologies of Miras

An investigation of morphology was worthwhile in cases where the star was well resolved and data quality – preferably from a number of independent observations – was adequate. Table B.1 lists all LPV's falling into this category, and gives a first-pass estimate of distortion from circular symmetry based upon *visibility* information only. Each object is dealt with in more detail, with both Fourier phase and amplitude information being considered, in the notes which follow later in this appendix.

Columns 1 through **4** give respectively the star name, date, wavelength and pupil mask for each observation (see Appendix A for more details). **Columns 5, 6** and **7** present the results of the fitting of a model profile to the visibility data. In this case, the model consisted of a Gaussian intensity profile which was allowed to vary azimuthally, so that the initially circularly-symmetric disk could be distorted into an ellipse. It is important to note that at this stage, the fitting uses visibility information *only.* **Column 8** gives an estimate of the reliability of the fitted model, taking into account the quality of the data and the extent to which the model reproduces the observed visibilities. Finally, those cases where closure phase information was recovered are denoted by 'yes' in **Column 9**.

The recovery of closure phase information enabled a more detailed investigation of the source morphology to be made. For example, the visibility data from most stars in Table B.1 could be reproduced well by either an elliptical disk, or a disk with a bright feature (or features). The only way to distinguish these models was to examine the closure phases. If these were all small, the symmetrical (*i.e.* elliptical) model would be preferred, whilst if they were large and systematic, the presence of asymmetric bright features would be indicated. Unfortunately, for the most observations made with a slit pupil, recovered closure phases had prohibitively large errors (see Section 2.5) so that centro-symmetric and non-centro-symmetric models could not be distinguished. In these cases, 'disk + spot(s)' models are not given as it was not possible to adequately constrain the model parameters.

Table B.1: Morphology information for selected Mira-type variables.

Object	Date	λ	Mask	Gaussian Ellipse fwhm	ratio	ϕ	Fit	CLP signal
o Cet	18/01/92	700	Slit	31	0.92	59°	good	no
	18/01/92	710	Slit	38	0.83	58°	good	no
	13/07/92	633	4-H	29	0.80	118°	fair	yes
	13/07/92	700	5-H	30	0.84	134°	fair	yes
	13/07/92	710	5-H	35	0.85	119°	fair	yes
	03/01/93	700	Slit	29	0.87	24°	fair	no
	07/09/93	700	Slit	39	0.92	46°	good	yes
	08/09/93	710	Slit	49	0.96	58°	good	yes
	06/12/93	700	Slit	38	0.99	38°	good	no
	06/12/93	710	Slit	56	0.96	65°	good	yes
R Leo	20/01/92	833	4-H	30	0.89	129°	good	yes
	10/06/93	700	Slit	40	0.96	-2°	fair	no
	10/06/93	710	Slit	51	0.89	-33°	poor	no
W Hya	08/06/93	700	Slit	49	0.90	106°	good	no
	09/06/93	700	Slit	48	0.94	94°	good	no
	09/06/93	710	Slit	55	0.95	107°	good	no
χ Cyg	13/07/92	700	Slit	25	0.96	102°	poor	no
	09/06/93	633	Slit	25	0.89	-12°	good	no
	07/06/93	700	5-H	23	0.91	-20°	good	yes
	08/06/93	710	Slit	31	0.80	-16°	fair	no
	07/09/93	700	Slit	30	0.89	83°	fair	no
R Cas	13/07/92	700	Slit	32	0.69	7°	good	yes
	13/07/92	710	4-H	42	0.70	-5°	good	yes
	13/07/92	710	Slit	42	0.69	6°	good	yes
	08/06/93	700	Slit	29	0.79	20°	good	no
	07/09/93	700	Slit	29	0.80	1°	good	yes
	08/09/93	710	Slit	39	0.77	2°	good	yes

o **Ceti**

January 1992: Mira showed a clear elongation at a position angle of about 60° in both 700 and 710 nm data. Closure phase measurements were not good enough to distinguish between symmetric (elliptical) and non-symmetric ('disk + spot') models.

July 1992: In addition to a strong visibility signal, measured closure phases were clearly indicative of a non-symmetric light distribution. For the three colours at this epoch (633, 700 & 710 nm) the complex behaviour of the visibility and closure phase curves made the fitting with simple models very difficult. Adequate fits were only found using models with a large number of degrees of freedom, such as a Gaussian disk with three bright spots as given below:

	Gaussian Disk			Bright Features		
	Flux	fwhm		Flux	r	θ
633 nm	60 %	36 mas	(1)	14 %	15 mas	-57°
			(2)	17 %	3 mas	137°
			(3)	9 %	14 mas	-118°
700 nm	66 %	39 mas	(1)	16 %	8 mas	-56°
			(2)	13 %	9 mas	120°
			(3)	5 %	16 mas	-157°
710 nm	69 %	49 mas	(1)	8 %	15 mas	-48°
			(2)	12 %	3 mas	94°
			(3)	11 %	12 mas	-113°

Data and computed model curves for the 710 nm observation are given in Figure B.1. Raw visibility and closure phase data for other colours at this epoch exhibited a broad similarity to those presented for in the figure. Fitted models also had common features (for example the spot at a position angle of around 50°) but did differ in detail. One explanation for this could be that the data were not adequate to constrain models with such a large number of degrees of freedom properly. It was difficult to ensure, especially for such complex models, that the fitting algorithm had arrived at some globally optimum solution. The possibility of systematic errors introduced by clipping of the holes in the pupil mask (see Section 2.7) cast further doubts as to the reliability of results at this particular epoch. Flux distributions of a purely symmetric nature (*e.g.* elliptical) could, however, be ruled out by the closure phase data.

January 1993: Observations were made under poor seeing conditions with a slit pupil and did not yield usable phase information. In addition, the fact that only a single 700 nm observation contributed to the morphology analysis at this epoch meant that the results given in Table B.1 should be treated with caution.

September 1993: Observations at 700 and 710 nm using an off-axis slit yielded visibility curves without a particularly dramatic variation with position angle, but a systematic non-zero closure phase signal was measured. Modelling these data with a Gaussian disk with one bright spot yielded :

	Gaussian Disk			Bright Feature		
	Flux	fwhm		Flux	r	θ
700 nm	95 %	38 mas	(1)	5 %	17 mas	44°
710 nm	91 %	54 mas	(1)	9 %	11 mas	59°

In this case, both the data and the model-fits were in close agreement for the two wavelengths. (Note: it was difficult to distinguish between a bright spot close to the center of a disk, and a fainter spot further out). The data and model-fits for the 710 nm observations are given in Figure B.2. The clearly preferred morphology at this epoch was that of a circular disk superimposed on which is a single asymmetric bright feature.

December 1993: Observations of Mira were taken with an off-axis slit mask as the star was faint at this epoch. The 700 and 710 nm data yielded some morphology information. Closure phases had large errors but did exhibit a systematic trend. 'Gaussian disk + spot' model-fits are given, however it should be noted that, especially at 700 nm, the closure phase data do not have sufficiently small errors to rule out the symmetric (elliptical) models.

	Gaussian Disk			Bright Feature		
	Flux	fwhm		Flux	r	θ
700 nm	96 %	39 mas	(1)	4 %	15 mas	44°
710 nm	87 %	61 mas	(1)	13 %	15 mas	119°

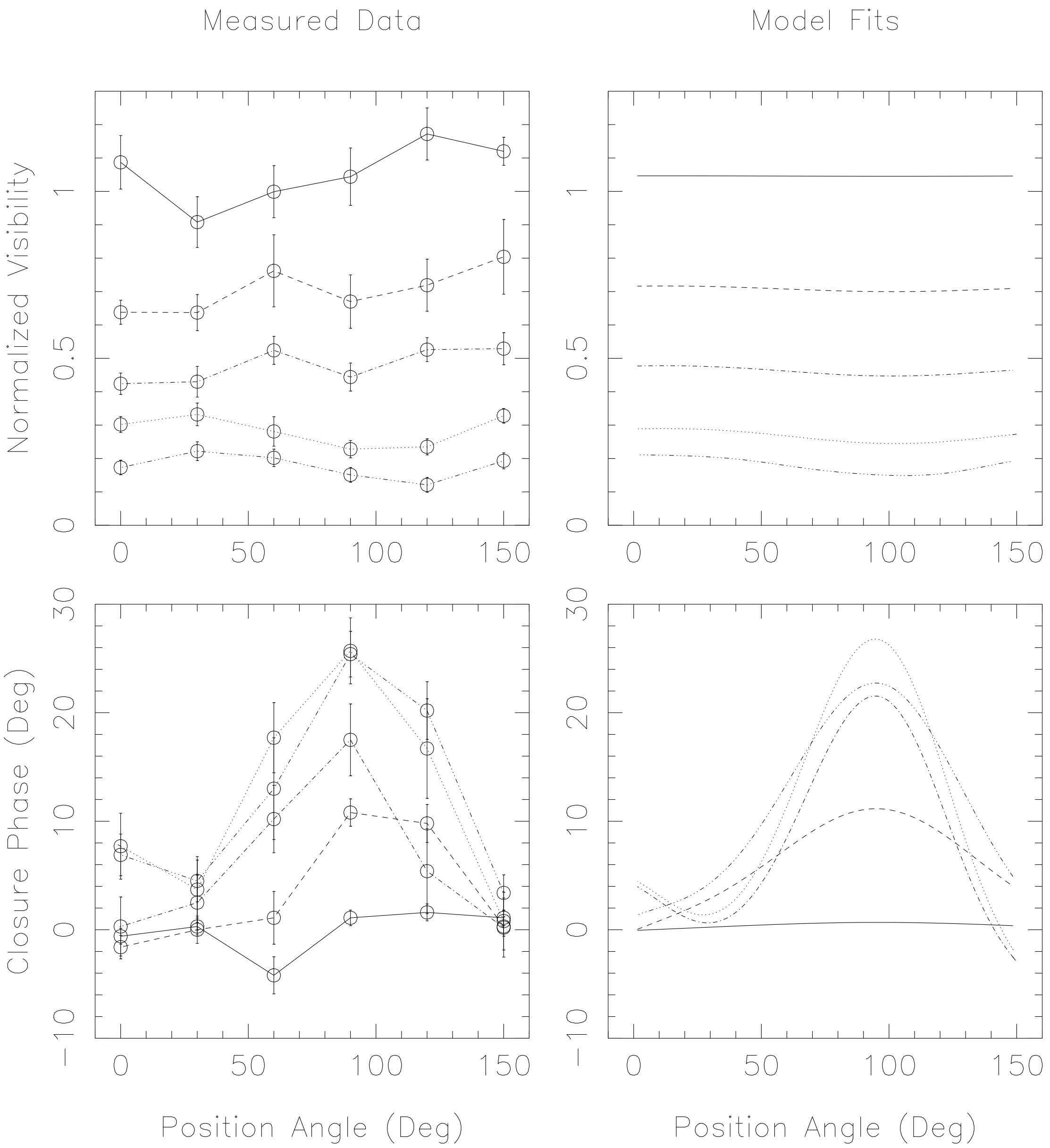

Figure B.1: Visibility data for baselines 1, 4, 6, 8 and 10 of a 5-hole mask taken on Mira at 710 nm in July 1992 are presented in the upper left panel. Closure phases for 5 different triangles are given in the lower left panel. The curves in the right-hand panels are the fits produced by the best 'Gaussian disk + three spot' model.

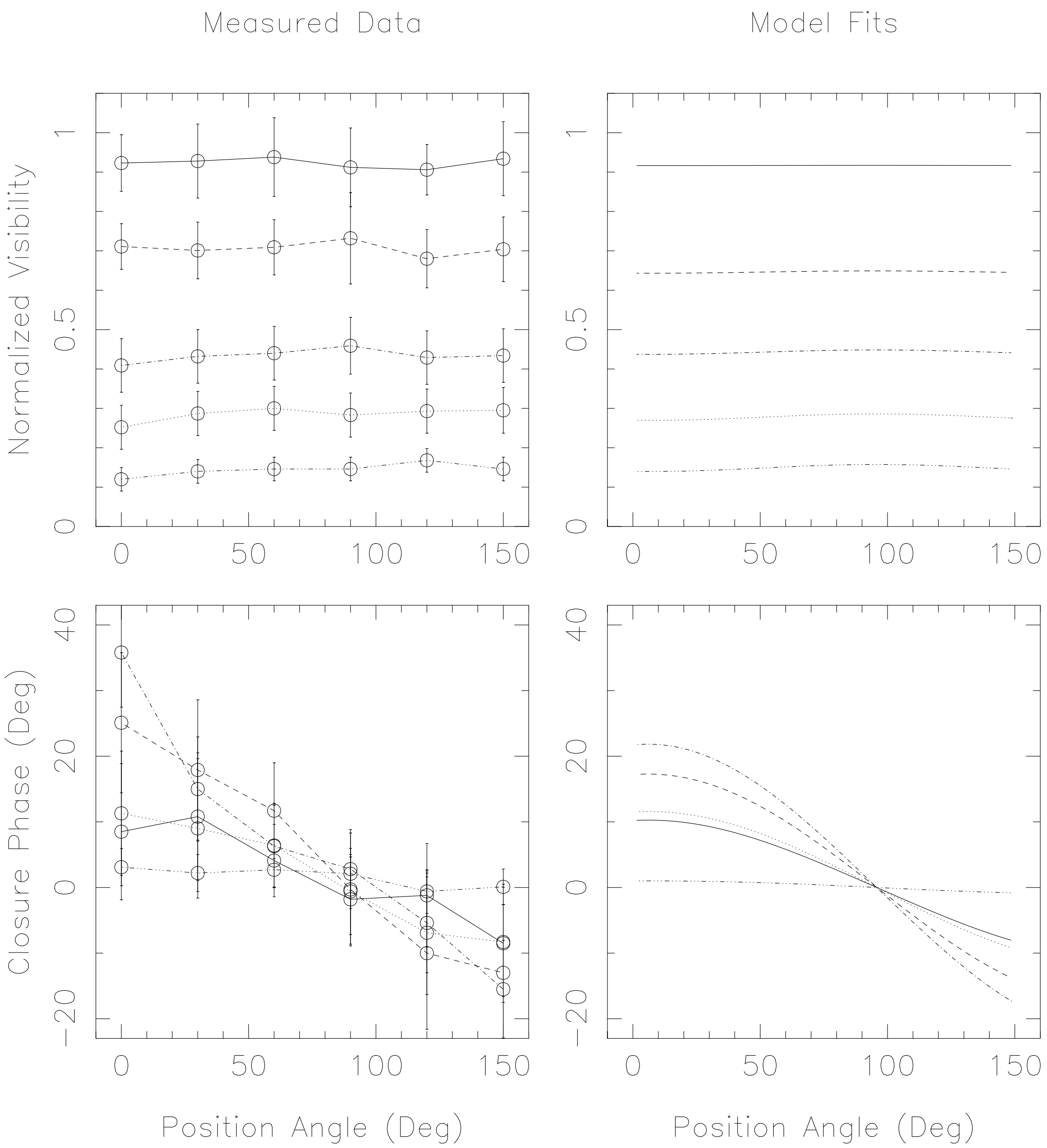

Figure B.2: Data and model-fits for Mira at 710 nm in September of 1993. Visibilities for various baselines sampled by the slit mask are presented in the upper left panel, whilst closure phases for 5 different triangles are given in the lower left panel. The curves in the right-hand panels are the fits produced by the best 'Gaussian disk + one spot' model.

R Leonis

January 1992: The 4-hole non-redundant mask data exhibited clear and systematic signals in both visibility and phase. The star was clearly identified as having a non-symmetric flux distribution by the closure phase signals, thus the elliptical models were ruled out. Data were well fitted with the 'Gaussian disk + one bright spot' model, as given below:

	Gaussian Disk			Bright Feature		
	Flux	fwhm		Flux	r	θ
833 nm	87 %	31 mas	(1)	13 %	10 mas	114°

June 1993: Slit data taken at this epoch yielded no usable phase information, thus it was not possible to investigate the morphology of R Leo at this epoch further. In addition, sparse position angle coverage made the estimates of symmetric distortion presented in Table B.1 unreliable.

W Hydrae

June 1993: Observations made using the axial slit mask yielded no usable phase information. The results presenting an elongation at around 100° presented in Table B.1 were consistent for the three datasets. Some caution over this result does need to be expressed as W Hya was at an elevation of only 32° when observed near transit. Although the filters had relatively narrow bandpasses, it could be difficult to ensure that there were no effects due to residual atmospheric dispersion present in the visibility data.

χ Cygni

July 1992: Closure phases were not recovered from slit mask observations of χ Cyg, thus the morphology at this epoch is not discussed further. In addition, the poor quality of the recovered visibility data makes the elongation from the sole 700 nm observation presented in Table B.1 unreliable.

June 1993: Although no closure phase information could be extracted from slit mask observations at 633 and 710 nm, the 700 nm 5-hole mask data from this epoch did exhibit a systematic signal. 'Gaussian disk + spot' models were fitted to all three datasets, but only for the 700 nm data was it possible to identify this as superior to the centro-symmetric elliptical model presented in Table B.1. The three fitted models were, however, highly consistent with each other lending confidence to the positive identification of an asymmetric bright feature at this epoch.

	Gaussian Disk			Bright Feature		
	Flux	fwhm		Flux	r	θ
633 nm	91 %	23 mas	(1)	9 %	14 mas	168°
700 nm	93 %	22 mas	(1)	7 %	12 mas	159°
710 nm	92 %	27 mas	(1)	8 %	17 mas	165°

September 1993: χ Cyg was faint at this epoch and the single 700 nm slit observation provided no useful phase data. As the Fourier amplitudes were also noisy, the star's morphology at this epoch has not been well established.

R Cassiopeiae

July 1992: A number of observations of R Cas were made through various filters and pupil masks. All visibility data showed a very strong and systematic excursion with position angle, clearly establishing the existence a large deviation from circular symmetry. The quality of the phase data, however, varied for the different observations. It was clear that the closure phases were non-zero so that some asymmetry was required to explain the data. However the measured phase signal in most cases was not large enough to support the proposition that the visibility excursions arose from a single asymmetric bright spot. Good fits could be obtained with two bright spots on almost opposite sides of the disk; an arrangement which produced a large wave in the visibility signal, but only moderate closure phases. Such fitting produced a consistent set of models for the three observations under consideration:

	Gaussian Disk			Bright Feature		
	Flux	fwhm		Flux	r	θ
700 nm	70 %	32 mas	(1)	20 %	14 mas	0°
(slit)			(2)	10 %	8 mas	-151°
710 nm	73 %	43 mas	(1)	14 %	13 mas	-15°
(4-H)			(2)	13 %	9 mas	-160°
710 nm	74 %	36 mas	(1)	14 %	15 mas	3°
(slit)			(2)	12 %	19 mas	-166°

June 1993: The single 700 nm observation was taken with the slit mask and did not yield usable phase data. The Fourier amplitude information, however, had small errors and showed a clear signal indicative of significant distortion present at this epoch. The fitting of 'disk + spot' models was not attempted in the absence of worthwhile closure phase data.

September 1993: Observations taken at 700 and 710 nm using the slit pupil yielded marginal phase information which had low signal-to-noise. Despite this, it was possible to fit 'Gaussian disk + spot' models and to identify these models as superior to the elliptical disk models presented in Table B.1. In addition, both colours produced highly consistent fits lending confidence to the positive identification of an asymmetric bright feature at this epoch.

	Gaussian Disk			Bright Feature		
	Flux	fwhm		Flux	r	θ
700 nm	91 %	24 mas	(1)	9 %	21 mas	-177°
710 nm	92 %	33 mas	(1)	17 %	21 mas	-181°

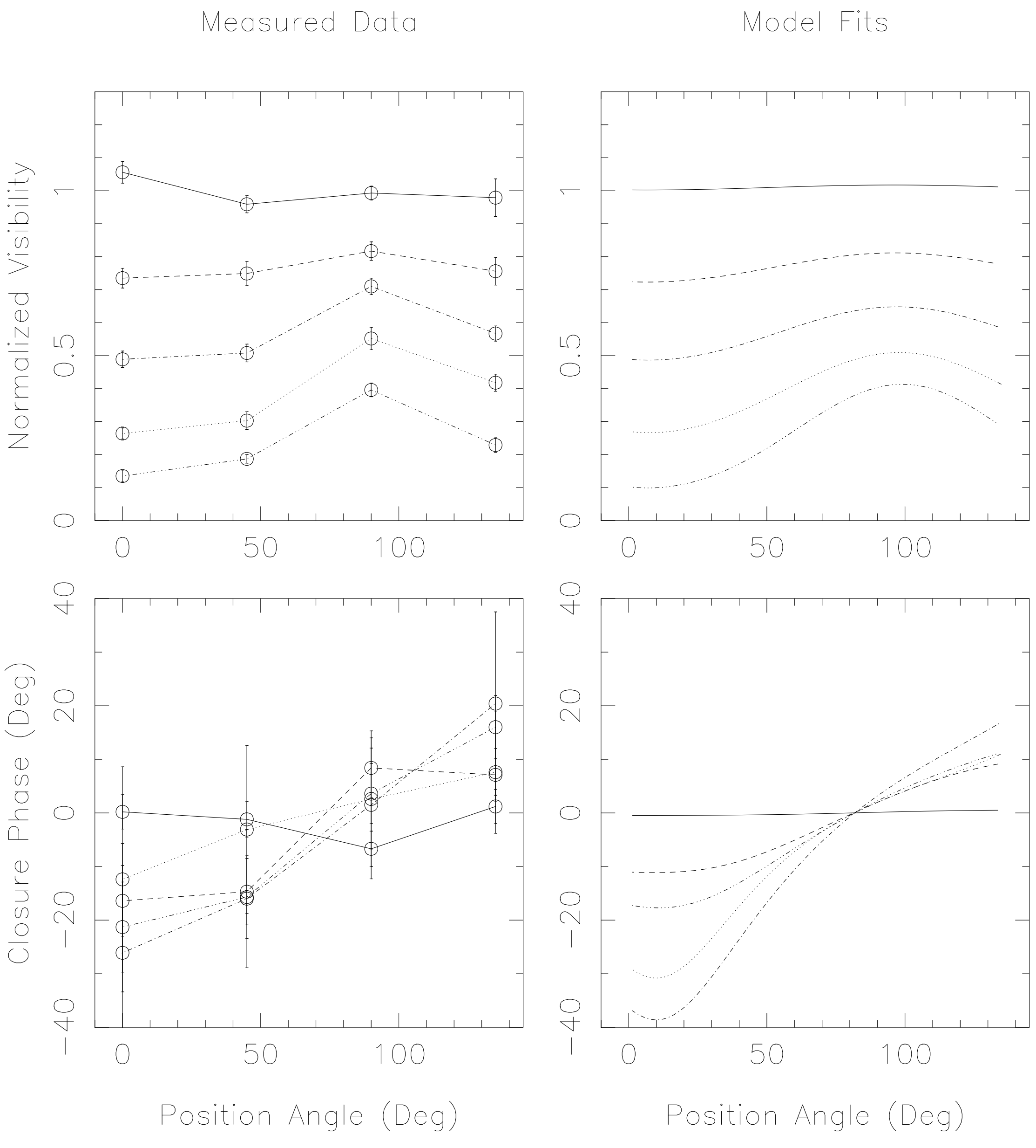

Figure B.3: Data (left) and model-fits (right) for R Cas at 700 nm in July of 1992. Visibilities for various baselines sampled by the slit mask are presented in the upper left panel, whilst closure phases for 5 different triangles are given in the lower left panel. The curves in the right-hand panels are the fits produced by the best 'Gaussian disk + two spot' model.

Appendix C

Morphologies of Supergiants

This appendix gives the morphologies of of all supergiants studied – α Ori, α Sco, α Her and μ Cep. In addition to the presentation and discussion of bispectral information, descriptions of simple model distributions which were able to reproduce these observed data are also given. These models were composed of a few simple elements: impulse functions, circular uniform-disks and Gaussian disks. In most cases, the model given is the *simplest* possible which was found to produce a satisfactory fit to the data.

C.1 Betelgeuse

Betelgeuse (α Ori) was one of the primary targets for any observing run during which it was visible in the night sky. This is because it is one of the largest and brightest stars within the operational range of the imaging instrument. Summaries of data taken over four epochs from January 1992 to December 1993 are presented below.

January 1992: A misalignment of the 5-hole pupil mask in the optical path caused one of the holes to be fully occulted by the shadow cast by the telescope's secondary mirror (see Section 2.7). The loss of this hole had serious consequences for the attempt to recover morphology information from the data. The six remaining baselines consisted of the three shortest and the three longest of the ten normally measured by the 5-hole mask. There was thus a large gap in Fourier coverage for intermediate baselines making it extremely difficult to interpolate the object visibility function. Even worse, the four (of ten) closure phases recovered consisted of three short or two long and one short baselines; which were the least sensitive to object morphology. Despite these problems, a clear phase signal was recorded indicating the presence of asymmetric distortions. These excursions were fitted with a model consisting of a uniform-disk and two unresolved features. Although the fits given below were found to reproduce the recorded phase signals well, caution over the results at this epoch should be expressed.

Wavelength	Uniform-Disk			Bright Features		
	Flux	Diam.		Flux	r	θ
700 nm	86 %	50 mas	(1)	12 %	1 mas	69°
			(2)	2 %	17 mas	-53°
710 nm	79 %	43 mas	(1)	17 %	2 mas	40°
			(2)	4 %	29 mas	-45°

January 1993: Although the seeing at this epoch was variable to poor, observations of Betelgeuse taken with the 5-hole mask were found to yield high quality bispectral information. The presence of asymmetric features was clearly established from an examination of the closure phases; which were non-zero and systematic. It was found that a model distribution consisting of a uniform-disk with two bright unresolved features could be made to produce a close fit to the observed Fourier data. Models are given below, whilst Figures C.1 and C.2 give the observed Fourier visibilities and closure phases at 700 nm and 710 nm, along with the fits produced by the models. MEM-generated image reconstructions are also given for both 700 and 710 nm observations in Figure 4.2.

Wavelength	Uniform-Disk			Bright Features		
	Flux	Diam.		Flux	r	θ
700 nm	79 %	51 mas	(1)	18 %	4 mas	187°
			(2)	3 %	27 mas	16°
710 nm	71 %	65 mas	(1)	23 %	6 mas	188°
			(2)	6 %	12 mas	-6°

September 1993: Successful observations were made with a 5-hole mask at wavelengths of 633 and 710 nm. Closure phase signals were extremely strong, even wrapping through 180° for some triangles as different position angles were measured. Fits of the 'uniform-disk + unresolved spots' model to the data are given below. Whilst it was possible to fit the 700 nm data using only 2 spots on the model disk, the more complex behaviour of the 633 nm phases required 3 spots to obtain an adequate fit. Figures C.3 and C.4 give bispectral data for the 700 nm and 633 nm observations, along with fits produced by the models. MEM-generated images of Betelgeuse at this epoch can be found in Figure 4.2.

Wavelength	Uniform-Disk		Bright Features			
	Flux	Diam.		Flux	r	θ
633 nm	82 %	60 mas	(1)	12 %	3 mas	-30°
			(2)	5 %	24 mas	115°
			(3)	4 %	21 mas	68°
700 nm	82 %	59 mas	(1)	12 %	5 mas	-45°
			(2)	6 %	10 mas	91°

December 1993: High quality data was obtained at two wavelengths: 633 and 700 nm. As was noted for September 1993 above, phases could be extremely large and exhibit highly complex behaviour with position angle, especially at 633 nm. The 700 nm data has been modeled with a uniform-disk and two unresolved floating spots, whilst the 633 nm data required three spots to obtain good fits. Data from the observation is presented in Figure 4.1 for 700 nm and Figure C.5 for 633 nm, whilst MEM-generated images at both wavelengths can be found in Figure 4.2.

Wavelength	Uniform-Disk		Bright Features			
	Flux	Diam.		Flux	r	θ
633 nm	84 %	54 mas	(1)	11 %	4 mas	-37°
			(2)	3 %	5 mas	174°
			(3)	2 %	26 mas	125°
700 nm	84 %	54 mas	(1)	14 %	3 mas	-29°
			(2)	2 %	19 mas	120°

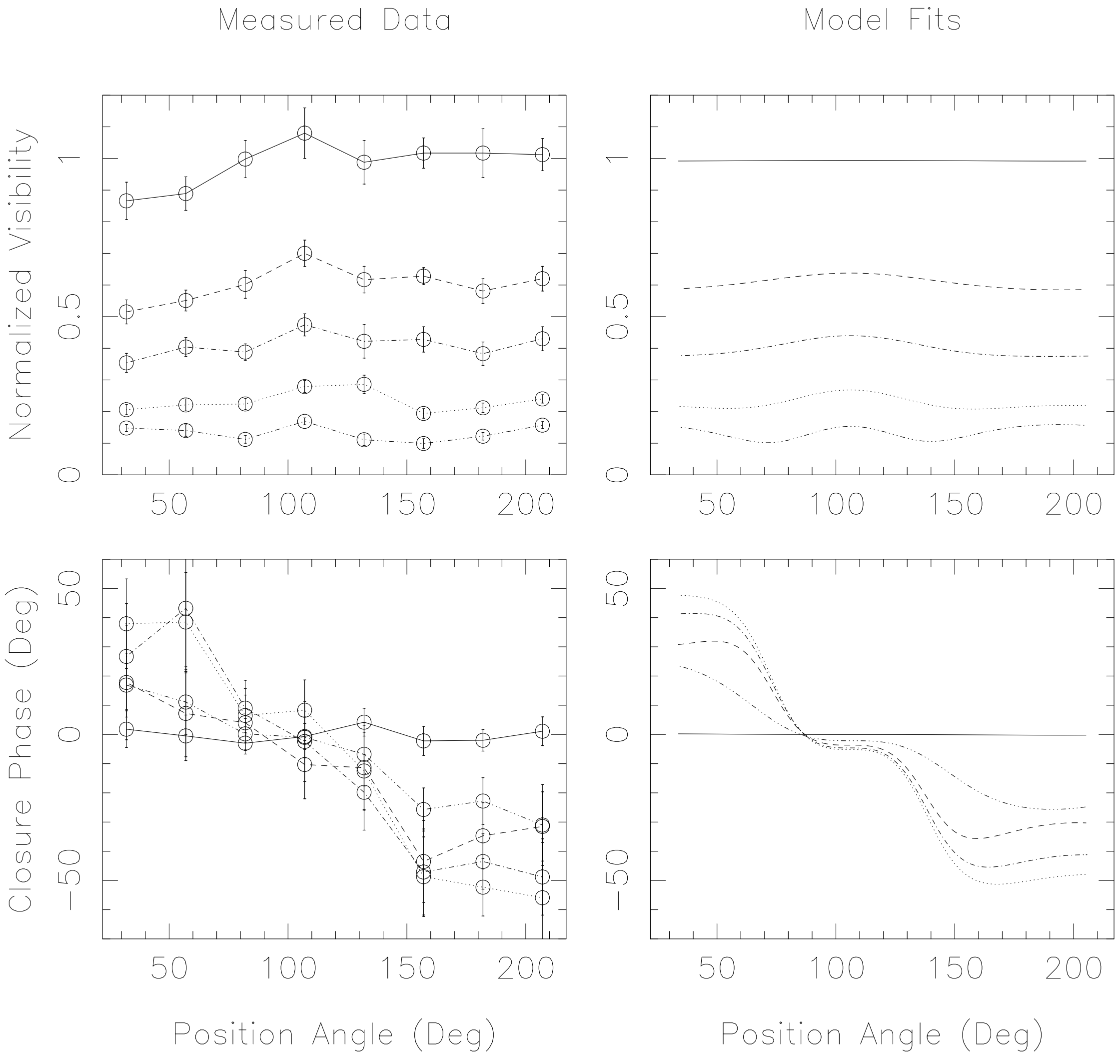

Figure C.1: Visibility data for baselines 1, 6, 7, 9 and 10 of a 5-hole mask taken on Betelgeuse at 700 nm in January 1993 are presented in the upper left panel as a function of the sky position angle of the pupil mask. Closure phases for five different triangles are given in the lower left panel. The corresponding curves in the right-hand panels are fits produced by the 'uniform-disk + 2 spot' model.

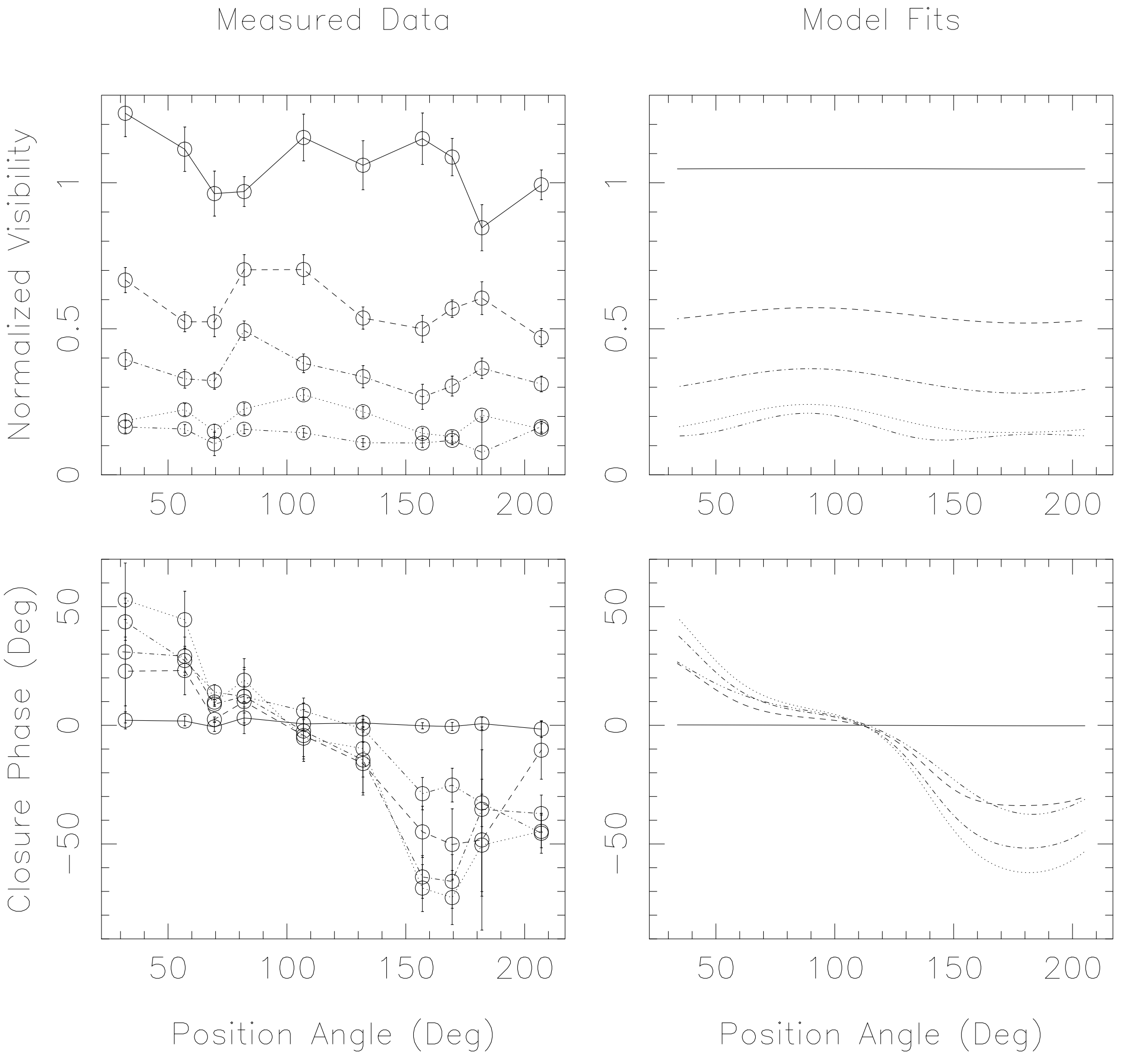

Figure C.2: Visibility data for baselines 1, 6, 7, 9 and 10 of a 5-hole mask taken on Betelgeuse at 710 nm in January 1993 are presented in the upper left panel as a function of the sky position angle of the pupil mask. Closure phases for five different triangles are given in the lower left panel. The corresponding curves in the right-hand panels are fits produced by the 'uniform-disk + 2 spot' model.

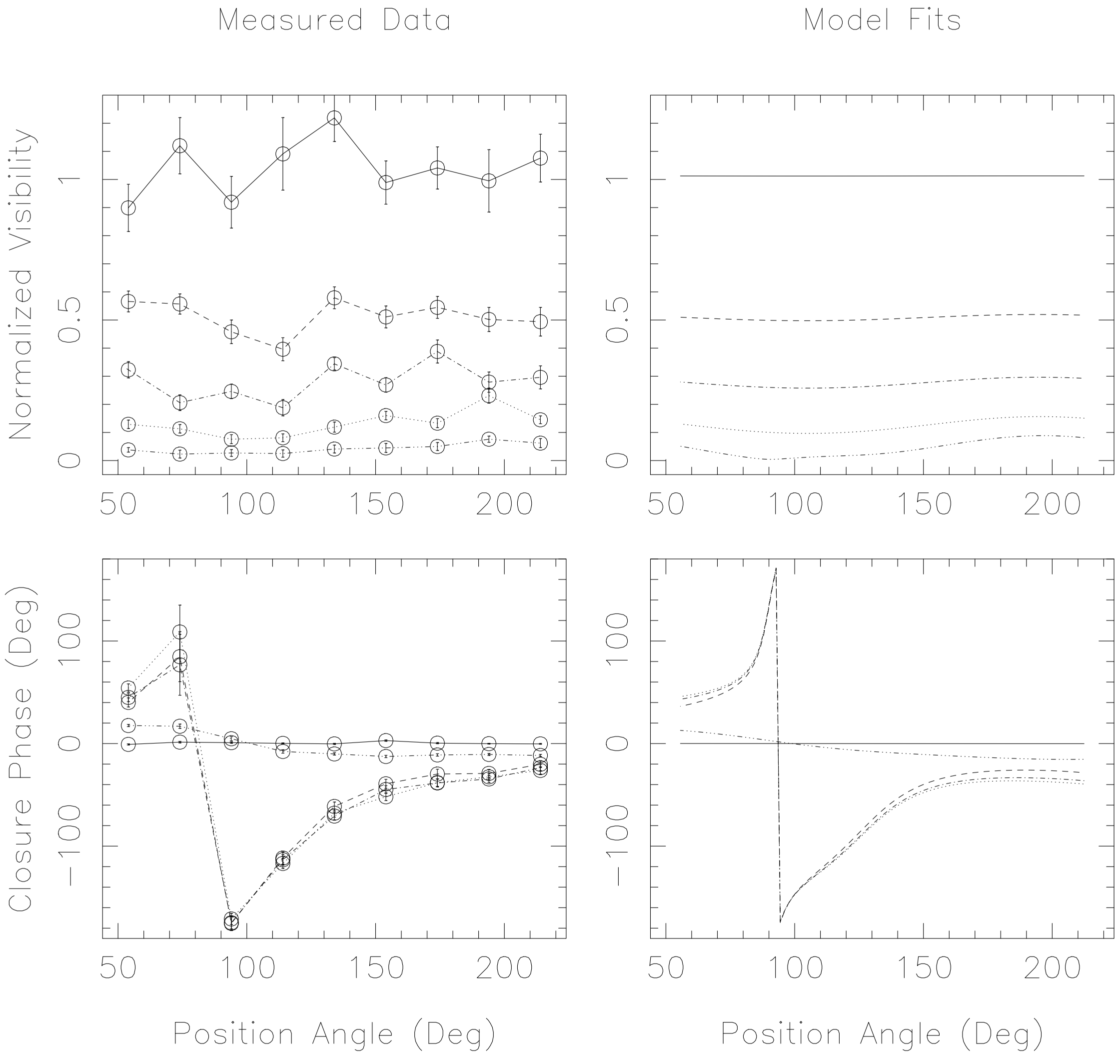

Figure C.3: Visibility data for baselines 1, 6, 7, 9 and 10 of a 5-hole mask taken on Betelgeuse at 700 nm in September 1993 are presented in the upper left panel as a function of the sky position angle of the pupil mask. Closure phases for five different triangles are given in the lower left panel. The corresponding curves in the right-hand panels are fits produced by the 'uniform-disk + 2 spot' model.

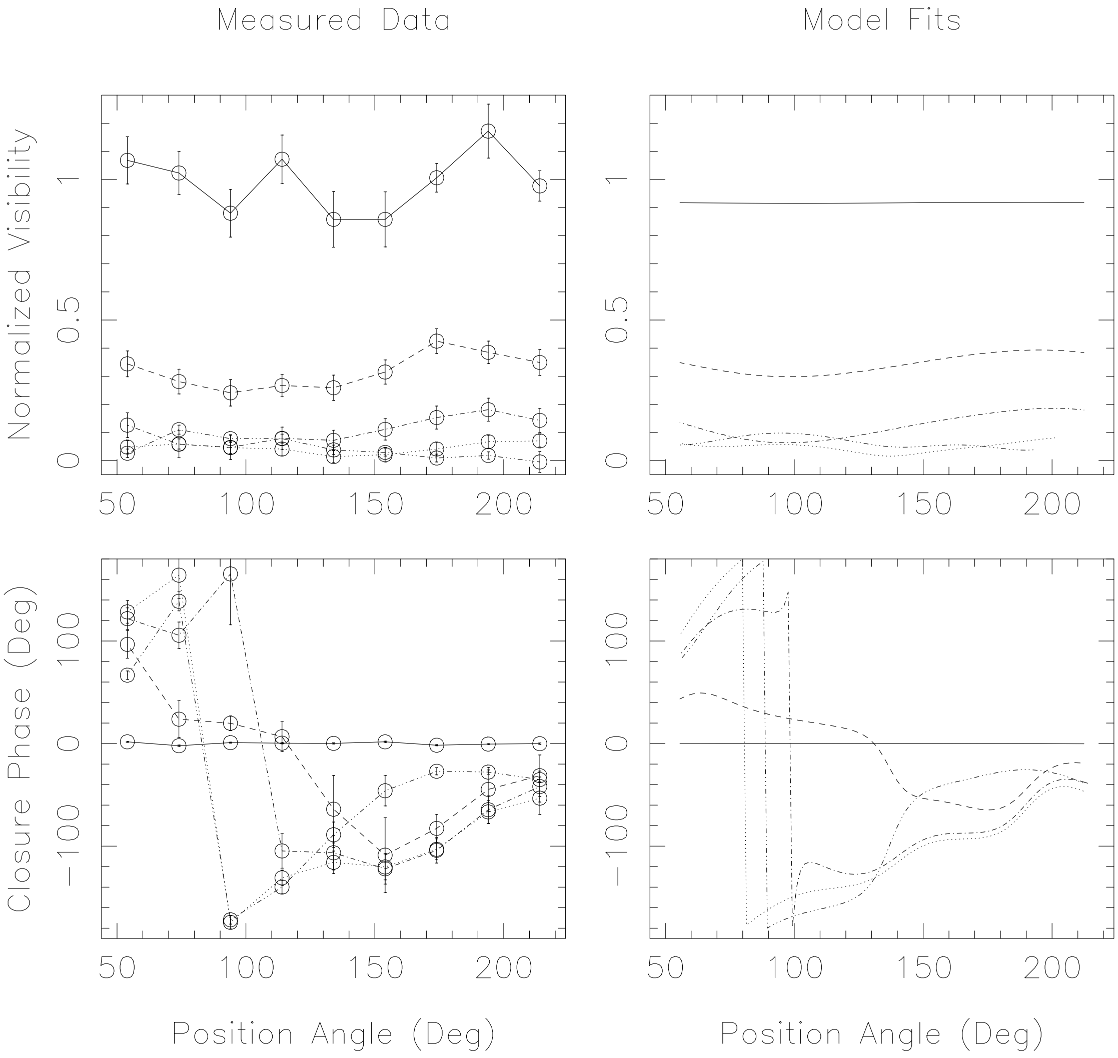

Figure C.4: Visibility data for baselines 1, 6, 7, 9 and 10 of a 5-hole mask taken on Betelgeuse at 633 nm in September 1993 are presented in the upper left panel as a function of the sky position angle of the pupil mask. Closure phases for five different triangles are given in the lower left panel. The corresponding curves in the right-hand panels are fits produced by the 'uniform-disk + 3 spot' model.

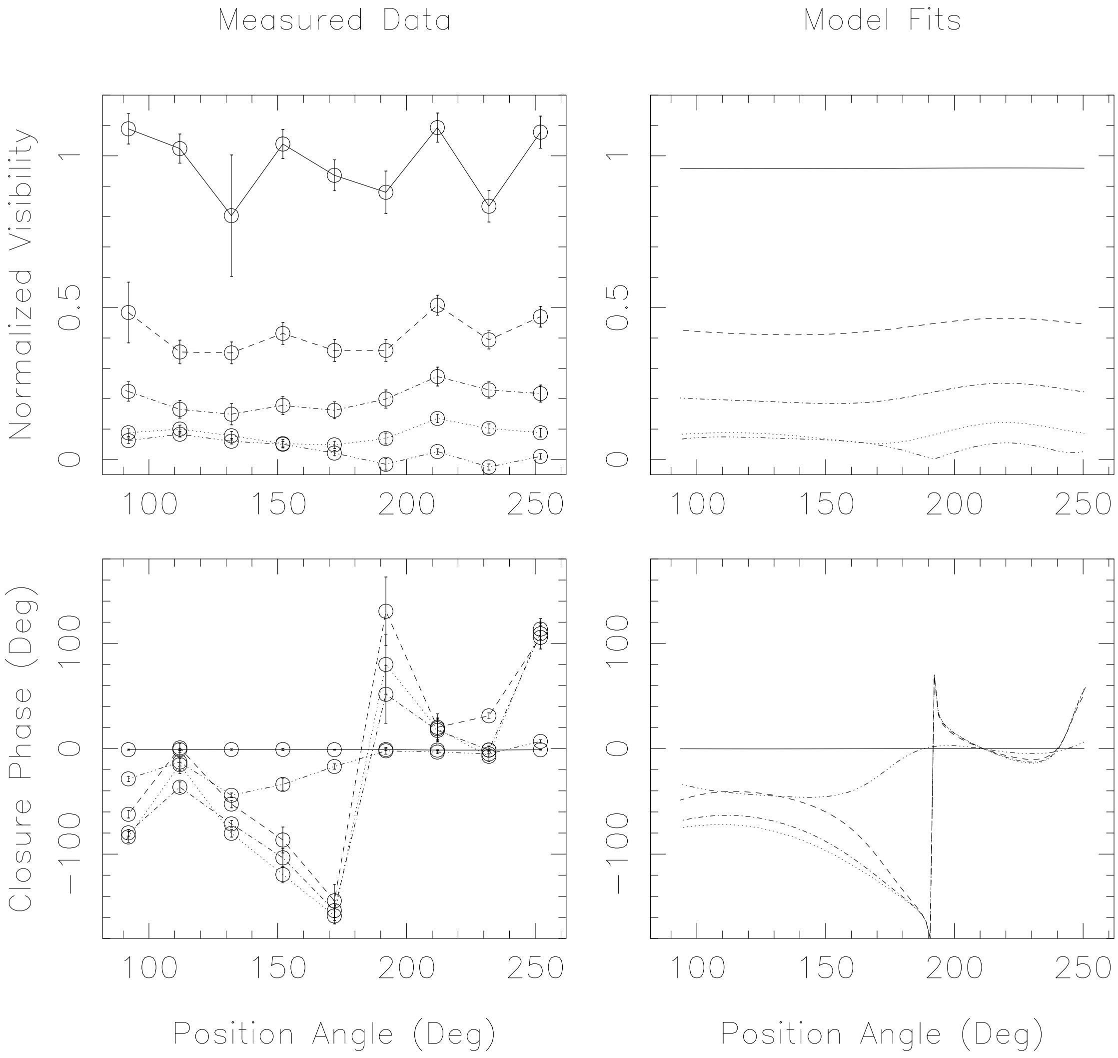

Figure C.5: Visibility data for baselines 1, 6, 7, 9 and 10 of a 5-hole mask taken on Betelgeuse at 633 nm in December 1993 are presented in the upper left panel as a function of the sky position angle of the pupil mask. Closure phases for five different triangles are given in the lower left panel. The corresponding curves in the right-hand panels are fits produced by the 'uniform-disk + 3 spot' model.

C.2 Antares

Observations of Antares (α Sco) suffered serious dispersion problems as from the site of the observatory, this star rose to an elevation of only 40° or so at transit. Thus, although this object was observed a number of times, most datasets were too corrupted to yield morphology information beyond the diameters given in Appendix A which were obtained by fitting profiles to the least-affected position angles. One 700 nm observation on 8 June 1993 did, however, yield data of higher quality.

June 1993: At this epoch α Sco was found to exhibit some distortion from circular symmetry, best fitted by a uniform-disk with a bright spot. Although the details are tentative, the presence of some non-centro-symmetry did seem to be established. A 'disk + 1 spot model' provided a good fit to the data and is given below.

Wavelength	Uniform-Disk			Bright Feature		
	Flux	Diam.		Flux	r	θ
700 nm	95 %	37 mas	(1)	5 %	11 mas	88°

C.3 Rasalgethi

Of the stars discussed in this appendix, Rasalgethi (α Her) was more resolved than any except Betelgeuse. Observations from July 1992 and June 1993 were all taken with non-redundant pupil configurations, and yielded good bispectral information.

July 1992: Although problems with the image rotator affected some of the observations made at this epoch, reliable maps were made at wavelengths of 633 and 710 nm. It was found that signals in the Fourier data indicating a non-symmetric flux distribution could be fitted reasonably well with a model consisting of a uniform-disk upon which one bright unresolved feature was superimposed.

Wavelength	Uniform-Disk			Bright Feature		
	Flux	Diam.		Flux	r	θ
633 nm	85 %	42 mas	(1)	15 %	5 mas	-104°
710 nm	83 %	48 mas	(1)	17 %	3 mas	-94°

Although these two-component fits reproduced most of the excursions in the Fourier data, the residuals appeared to be systematic and similar for the two colours. This could be interpreted as an indication of a second bright feature on the surface of the disk. The model-fitting program established that an additional hotspot with $\sim$ 3 % flux located 19 mas from the centre of the disk and at a position angle of 35° gave an extremely close fit to the data. However, the fainter spot could also converge to other locations (*e.g.* $\sim$ 175° or $\sim$ -85°) and still match well to the observations. Thus although it was probable that some further feature did exist, the data does not constrain its position sufficiently for positive identification. A diffraction-limited image reconstructed by the MEM algorithm for the 633 nm observation is shown in Figure 4.4.

June 1993: It was found that the strong and detailed closure phase signals from data recorded at this epoch necessitated the fitting of more complex models. As is shown in Figure C.6, excellent fits could be obtained with a model consisting of a uniform-disk with two unresolved features.

Wavelength	Uniform-Disk		Bright Features			
	Flux	Diam.		Flux	r	θ
633 nm	80 %	40 mas	(1)	14 %	4 mas	146°
			(2)	6 %	17 mas	-95°
700 nm	79 %	39 mas	(1)	18 %	3 mas	220°
			(2)	3 %	27 mas	-87°
710 nm	82 %	43 mas	(1)	14 %	3 mas	170°
			(2)	4 %	24 mas	-109°

Of the three colours given above, the phase signals for the 700 nm data were barely strong enough to justify the full three-component fit. The fits show good consistency and it seems safe to conclude that two features have been identified, one bright and close to the centre of the disk, and a second fainter and located near the limb at a position angle of about -100°. Figure 4.4 presents a MEM reconstruction of Rasalgethi at 633 nm from this epoch, which can clearly be seen to exhibit regions of enhanced flux away from the centre. Note that the positions of features in these maps match well to the results of the corresponding fitted model given above – lending further weight to the positive identification of the bright spots.

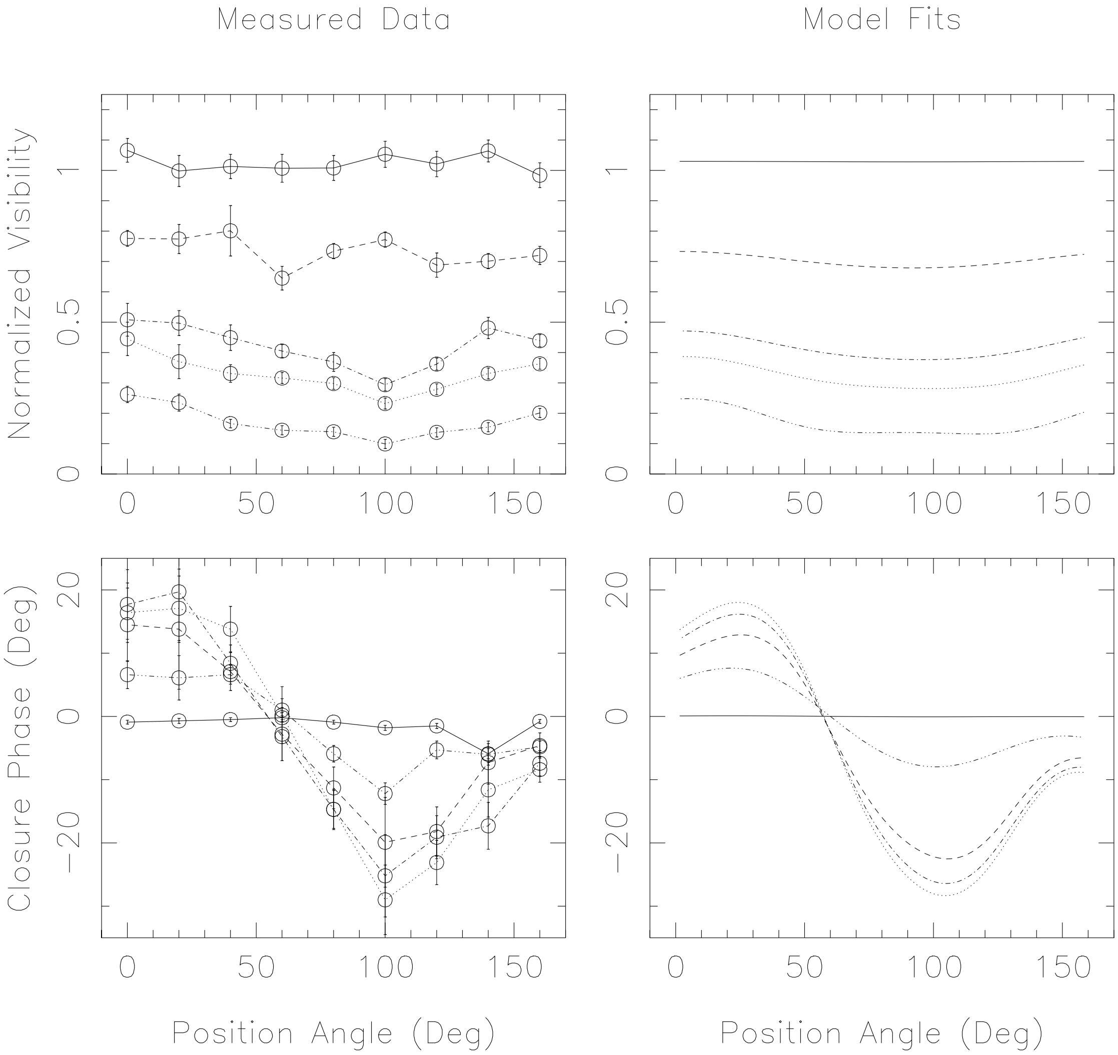

Figure C.6: Visibility data for baselines 1, 6, 8, 9 and 10 of a 5-hole mask taken on Rasalgethi at 633 nm in June 1993 are presented in the upper left panel as a function of the sky position angle of the pupil mask. Closure phases for five different triangles are given in the lower left panel. The corresponding curves in the right-hand panels are fits produced by the 'uniform-disk + 2 spot' model (see text).

C.4 μ Cep

Despite μ Cep's large distance from the sun which leads it to present a relatively small apparent diameter ($\sim$ 30 mas), strong and systematic signals indicating departures from circular symmetry were recorded. The fitting of model distributions to this data was not straightforward. It was found that a model consisting of a very bright (16 $\sim$ 30 %) feature located close to the northern limb of a uniform-disk (hereinafter model 'A') gave a reasonable first order fit to the data at *all* epochs. Without adding further complexity or freedom to the model, it was found that a generally better solution was obtained with the spot fainter (8 $\sim$ 13 %) and further out, located beyond the southern limb (model 'B'). Finally, for some of the best data (June 1993), model 'B' still left some systematic residual and a model comprising two partially resolved uniform-disks (model 'C') was found to produce an extremely good fit. Despite the fact that model 'C' had only 6 free parameters, it was found to be able to produce fits as good as some much more complicated models with more degrees of freedom (*e.g.* a disk with 2 unresolved spots: 8 free parameters). Summaries of the results of observations carried out in July 1992, June 1993 and September 1993 are given below, whilst tables follow containing the results of model-fitting.

July 1992: Although data was gathered at a number of wavelengths under conditions of good seeing, unfortunately a hardware fault with the image rotator control electronics was sufficiently serious to prevent much of this from being usable. For this reason, data taken on July 12th is not described further, however the single 700 nm observation from July 11th was found to be recoverable. The position angle was calibrated using observations of a known binary star taken shortly before the observations of μ Cep. Although the plate orientation so determined was not certain, it was probably no more than 10° or so in error.

Data exhibited clear visibility and closure phase signals, indicative of a strong asymmetric component in the flux distribution of this object. Symmetric elongations such as an elliptical distortion were ruled out by the phase information. Models 'B' and 'C' were found to produce very good fits to the observations, whilst model 'A' reproduced most of the gross behaviour. In this case, model 'C' did not produce a significantly better fit than model 'B', and the results for all models exhibited lower levels of distortion (although similar in other details) than those at subsequent epochs. Details of fits for each model in turn ('A', 'B' & 'C') are given in Tables C.1, C.2 and C.3.

June 1993: 5-hole mask data taken at this epoch was found to be of high quality yielding clear and consistent Fourier information. Simple inspection of this in Figures C.7 and C.8 was sufficient to establish that large asymmetries existed in the flux distribution. This was verified by the fitting of the models, for which the 'A', 'B' and 'C' models respectively gave successively better fits. Visibilities and closure phases, along with the fits produced by the models are given for both the 633 nm and 710 nm μ Cep observations at this epoch in Figures C.7 and C.8 respectively. The strong similarities between the 633 and 710 nm data are clearly evident. This epoch yielded the highest quality Fourier information recorded for μ Cep and it was possible to clearly identify model 'C' as superior to 'B' (and 'A') only for measurements taken at this

Table C.1: Model 'A' fits to μ Cep data over three epochs. Model 'A' consists of a circular uniform-disk upon which a single compact feature of variable flux and position is superimposed. For the 'A' model, the feature is initially started at a small radius.

Date	Wavelength	Uniform-Disk		Bright Feature		
		Flux	Diam.	Flux	r	θ
July 1992	700 nm	84 %	32 mas	16 %	7 mas	13°
June 1993	633 nm	62 %	30 mas	38 %	12 mas	5°
	710 nm	69 %	31 mas	31 %	13 mas	9°
Sep 1993	633 nm	66 %	37 mas	34 %	11 mas	8°
	700 nm	71 %	30 mas	29 %	11 mas	22°
	710 nm	69 %	35 mas	31 %	12 mas	12°

time.

September 1993: All observations at this epoch were made with the use of a slit pupil mask. Visibility information was of high quality, however the closure phases recovered had very large errors due to the poor treatment of phase signals by the slit. Despite the large scatter however, the recovered phases still exhibited a sufficiently systematic trend to establish the presence of a bright asymmetric component in the image. As before, the fitting of the models was found to be successful in reproducing the signals in the Fourier data, and yielded fairly consistent results for the three colours. Although models 'B' and 'C' were significantly preferred over 'A', the data were not of high enough quality to discriminate strongly between these two. Visibilities in Figure C.9, taken at 710 nm can be seen to exhibit very similar signals to those noted earlier for the June 1993 observations. The figure also shows that whilst they are noisy, the phases do show some systematic behaviour with position angle. As a final note to the September 1993 results, the 700 nm observation was taken under conditions of inferior seeing and was not as reliable as those at 710 and 633 nm.

Table C.2: Model 'B' fits to μ Cep data over three epochs. Model 'B' consists of a circular uniform-disk upon which a single compact feature of variable flux and position is superimposed. The 'B' model starts the bright feature at a large radius.

Date	Wavelength	Uniform-Disk		Bright Feature		
		Flux	Diam.	Flux	r	θ
July 1992	700 nm	92 %	27 mas	8 %	21 mas	196°
June 1993	633 nm	87 %	23 mas	13 %	23 mas	181°
	710 nm	89 %	26 mas	11 %	23 mas	187°
Sep 1993	633 nm	91 %	28 mas	9 %	25 mas	185°
	700 nm	90 %	26 mas	10 %	18 mas	200°
	710 nm	91 %	29 mas	9 %	27 mas	192°

Table C.3: Model 'C' fits to μ Cep data over three epochs. Model 'C' consists of two circular uniform-disks, the sizes and fluxes of which are allowed to vary whilst the fainter component's position is also allowed to vary.

Date	Wavelength	Uniform-Disk (centre)		Uniform-Disk (floating)			
		Flux	Diam.	Flux	r	θ	Diam.
July 1992	700 nm	88 %	26 mas	12 %	19 mas	195°	20 mas
June 1993	633 nm	76 %	22 mas	24 %	18 mas	183°	27 mas
	710 nm	79 %	25 mas	21 %	19 mas	188°	28 mas
Sep 1993	633 nm	84 %	27 mas	16 %	21 mas	187°	30 mas
	700 nm	67 %	22 mas	33 %	13 mas	202°	31 mas
	710 nm	88 %	28 mas	12 %	25 mas	192°	25 mas

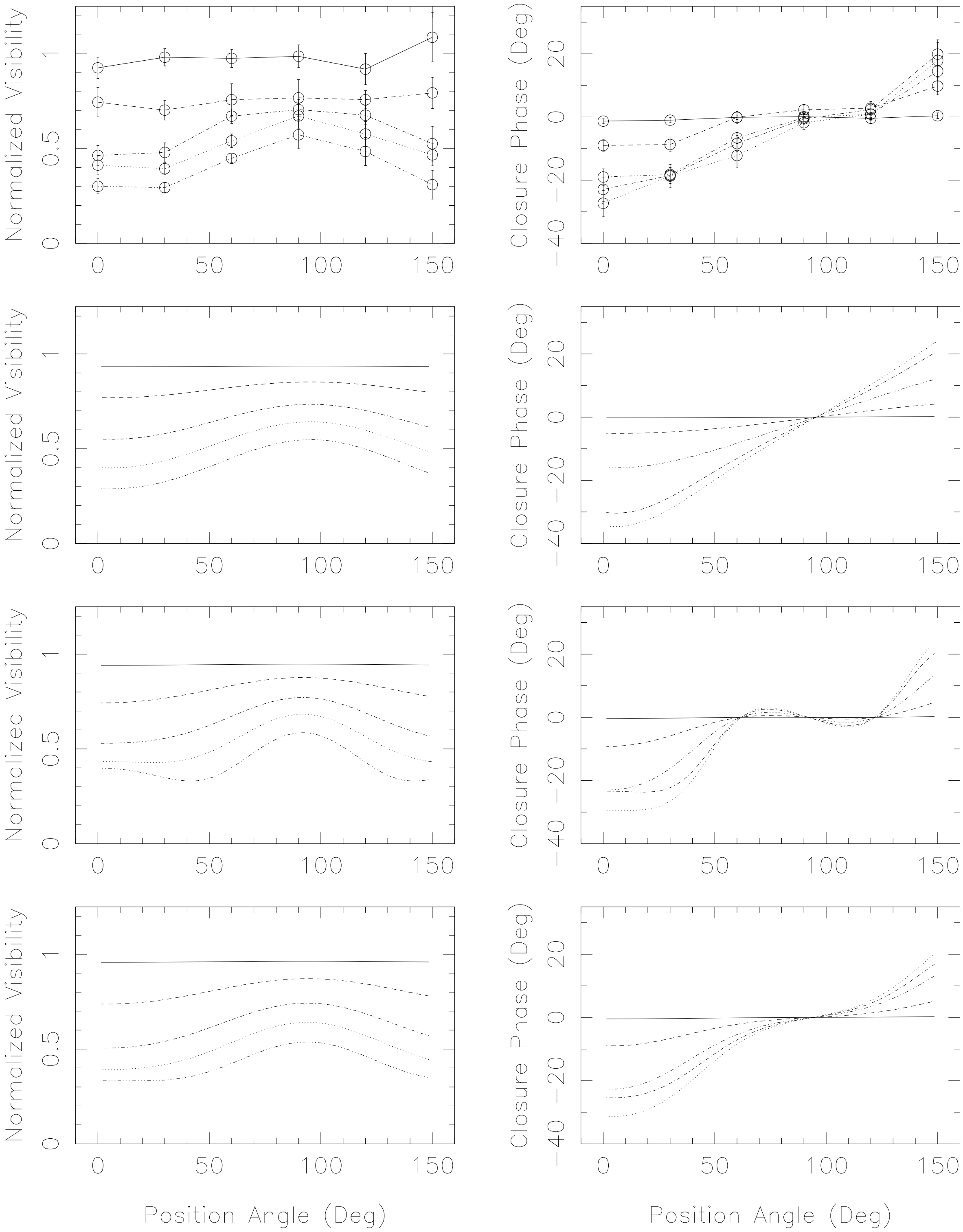

Figure C.7: Visibility and closure phase data for μ Cep at 633 nm in June 1993 taken with a 5-hole mask (top panels). Successive lower pairs of panels present 'A', 'B' & 'C' model-fits respectively.

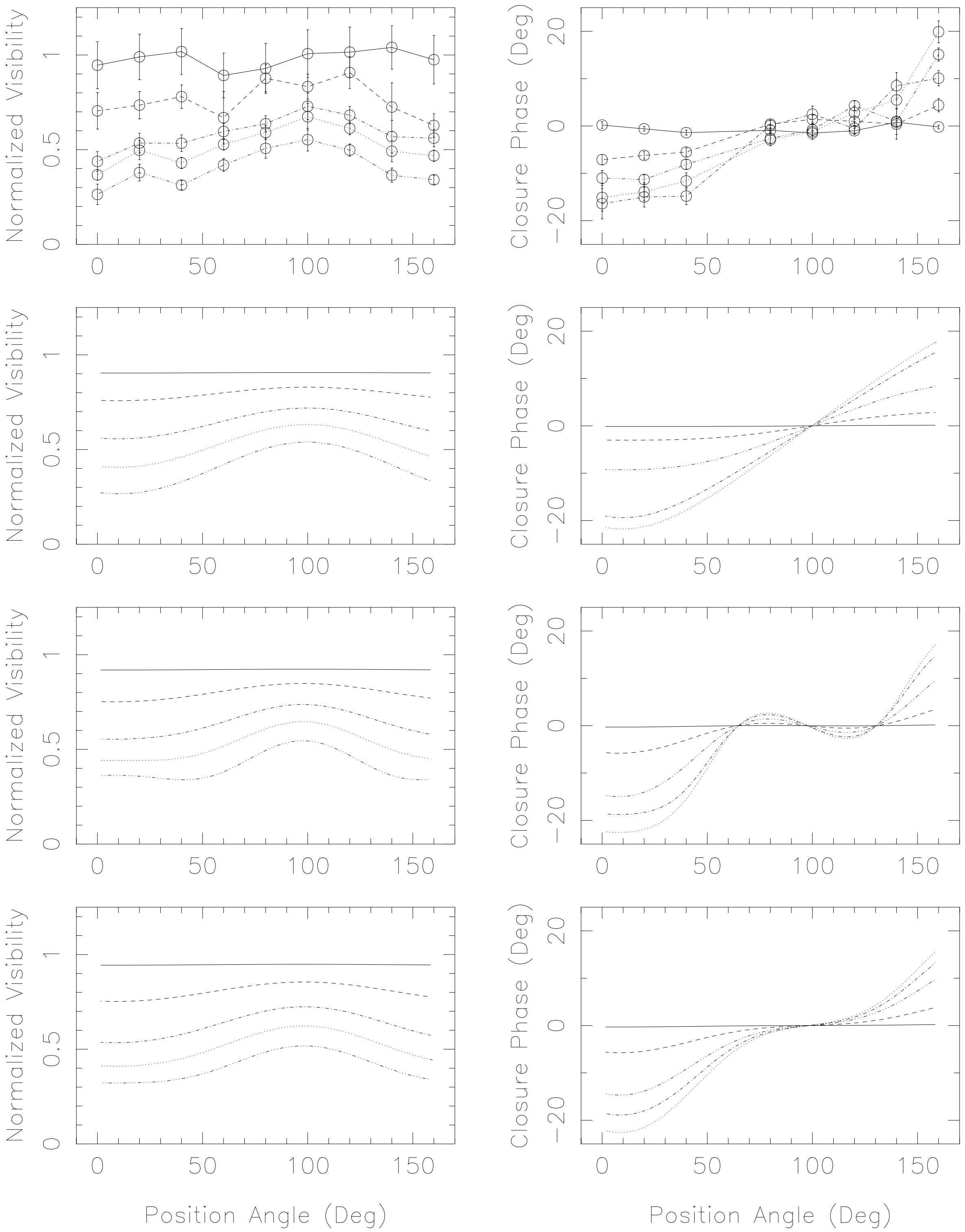

Figure C.8: Visibility and closure phase data for μ Cep at 710 nm in June 1993 taken with a 5-hole mask (top panels). Successive lower pairs of panels present 'A', 'B' & 'C' model-fits respectively.

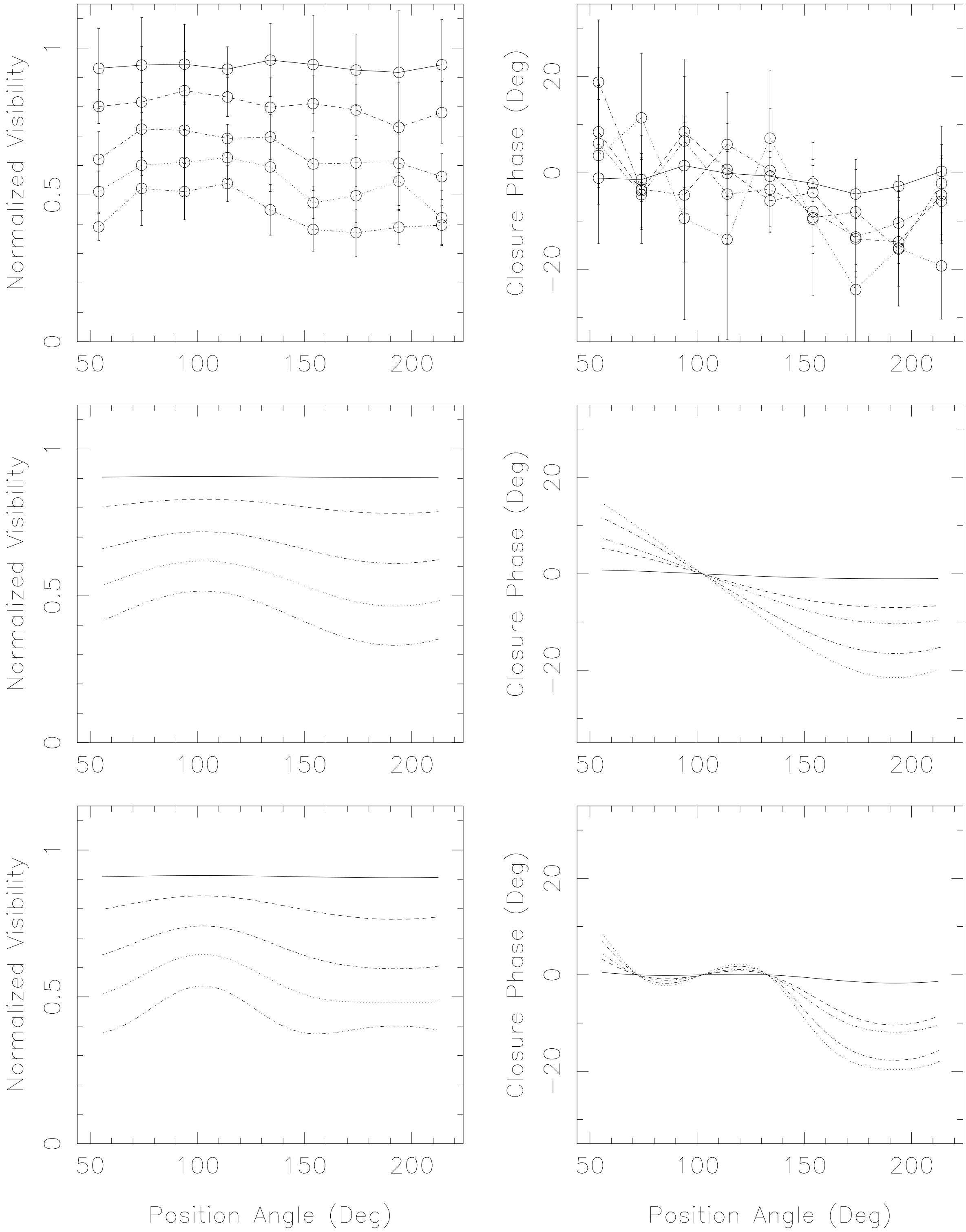

Figure C.9: Visibility and closure phase data for μ Cep at 710 nm in September 1993 taken with a slit mask (top panels). Successive lower pairs of panels present 'A' & 'B' model-fits respectively.

Bibliography

Balega Y., Blazit A., Bonneau D., Koechlin L., Foy R. & Labeyrie A. 1982, *Astr. Astrophys.*, **115**, 253

Baliunas S. & Dupree A.K. 1982, *Astrophys. J.*, **252**, 668

Balmforth N.J., Gough D.O. & Merryfield W.J. 1990, in Mennessier M.O. & Omont A., eds, *From Miras to Planetary Nebulae: Which Path for Stellar Evolution?* Editions Frontières, Gif-sur-Yvette, p. 85

Barthès D. & Tuchman Y. 1994, *Astr. Astrophys.*, **289**, 429

Baschek B., Scholz M. & Wehrse R. 1991, *Astr. Astrophys.*, **246**, 374

Bates R.H.T. & Cady F.M. 1980, *Opt. Commun.*, **32**, 365

Beckers J.M. & Merkle F. (eds) 1994, ESO conference No. 39, *High-Resolution Imaging by Interferometry.* ESO, Garching, Germany

Bedding T.R. 1992, *Ph.D. Dissertation*, University of Sydney

Belvedere G., Chiuderi C., & Paterno L. 1982, *Astr. Astrophys.*, **105**, 133

Benson J.A., Dyck H.M., Ridgway S.T., Dixon D.J., Mason W.L. & Howell R.R. 1991, *Astron. J.*, **102**, 2091

Bernat A.P. 1981, *Astrophys. J.*, **246**, 184

Bessell M.S., Brett J.M., Scholz M. & Wood P.R. 1989, *Astr. Astrophys.*, **213**, 209

Blazit A., Bonneau D., Koechlin L. & Labeyrie A. 1977, *Astrophys. J.*, **214**, L79

Bonneau D., Foy R., Blazit A. & Labeyrie A. 1982, *Astr. Astrophys.*, **106**, 235

Bowen G.H. 1988, *Astrophys. J.*, **329**, 299

Boyle R.P., Aspin C., Coyne G.V. & McLean I.S. 1986, *Astr. Astrophys.*, **164**, 310

Breare M. 1993, *Personal Communication*

Buscher D.F. 1988, *Mon. Not. R. ast. Soc.*, **235**, 1203

Buscher D.F. & Haniff C.A. 1993, *J. Opt. Soc. Am. A*, **10**, 1882

Buscher D.F., Haniff C.A., Baldwin J.E. & Warner P.J. 1990, *Mon. Not. R. ast. Soc.*, **245**, 7P

Cady F.M. & Bates R.H.T. 1980, *Opt. Lett.*, **5**, 438

Cahn J.H. & Wyatt S.P. 1978, *Astrophys. J.*, **221**, 163

Catchpole R.M., Robertson B.S.C., Lloyd Evans T.H.H., Feast M.W., Glass I.S. & Carter B.S. 1979, *SAAO Circular*, **4**, 61

Celis S.L. 1980, *Astr. Astrophys.*, **89**, 145

Celis S.L. 1981, *Astr. Astrophys.*, **99**, 58

Celis S.L. 1984, *Astron. J.*, **89**, 1343

Christou J. & Worden S.P. 1980, *Astron. J.*, **85**, 302

Cheng A.Y.S., Hege E.K., Hubbard E.N., Goldberg L., Strittmatter P.A., & Cocke W.J. 1986, *Astrophys. J.*, **309**, 737

Clarke D. & Schwarz H.E. 1984, *Astr. Astrophys.*, **132**, 375

Colavita M.M. Shao M.J. & Staelin D.H. 1987, *Appl. Opt.*, **26**, 4106

Coulman C.E., Vernin J., Coquegniot Y. & Caccia J.L. 1988, *Appl. Opt.*, **27**, 155

Dainty J.C. 1984, *Topics in Applied Physics: Volume 9*, ed. Dainty J.C., Springer-Verlag, Berlin

Dainty J.C. 1987, *SPIE "Digital Image Recovery and Synthesis"*, **828**, 2

Danchi W.C., Bester C.G., Degiacomi C.G., Greenhill L.J. & Townes C.H. 1994, *Astron. J.*, **107**, 1469

Devaney M.N., Redfern R.M., Ballesteros Ramirez E., Gomez Renasco R., O'Kane P.O. & Rosa F. 1989, *proc. NATO Advanced Study Institute on "Diffraction Limited Imaging with Very Large Telescopes"*, p369, Kluwer, Dordrecht

De Jager C. & Vermue J. 1978, *Astrophys. & Space Sci.*, **62**, 245

Di Giacomo A., Richichi A., Lisi F. & Calamai G. 1991, *Astr. Astrophys.*, **249**, 397

Drinkwater M.J. & Wood P.R. 1985, *Mass Loss from Red Giants* p257, ed. Morris M. & Zuckerman B., Reidel, Dordrecht

Dupree A.K., Baliunas S.L., Guinan E.F., Hartmann L., Nassiopoulos G.E. & Sonneborn G. 1987, *Astrophys. J.*, **317**, L85

Dyck H.M. 1968, *Astron. J.*, **73**, 688

Dyck H.M., Lockwood G.W. & Capps R.W. 1974, *Astrophys. J.*, **189**, 89

Dyck H.M., Zuckerman B., Leinert CH. & Beckwith S. 1984, *Astrophys. J.*, **287**, 801

Evans D.S. 1957, *Astron. J.*, **62**, 83

Feast M.W., Glass I.S., Whitelock P.A. & Catchpole R.M. 1989, *Mon. Not. R. ast. Soc.*, **241**, 375

Fernie J.D. 1959, *Astrophys. J.*, **130**, 611

Fox M.W. & Wood P.R. 1982, *Astrophys. J.*, **259**, 198

Foy R., Heck A. & Mennessier M.O. 1975, *Astr. Astrophys.*, **43**, 175

Fried D.L. 1966, *J. Opt. Soc. Am.*, **56**, 1372

Fried D.L. 1978, *proc. IAU Colloq. No. 50*, ed. Davis J. & Tango W.J., Univ. of Sydney, NSW

Gatewood G. 1992, *Publ. Astr. Soc. Pac.*, **104**, 23

Gillett F.C., Low F.J. & Stein W.A. 1968, *Astrophys. J.*, **154**, 677

Glass I.S. & Feast M.W. 1982, *Mon. Not. R. ast. Soc.*, **199**, 245

Goldberg L. 1986, *NASA special publication* **sp-492**, 245

Goodman J.W. 1985, *Statistical Optics*, Wiley, New York

Gull S.F. & Skilling J. 1984, *IEEE Proceedings*, **131**, Pt. F, No. 6

Gull S.F. 1992, *Personal Communication*

Habing, H.J. 1990, in Mennessier M.O. & Omont A., eds, *From Miras to Planetary Nebulae: Which Path for Stellar Evolution?* Editions Frontières, Gif-sur-Yvette, p. 16

Haniff C.A., Mackay C.D., Titterington D.J., Sivia D., Baldwin J.E. & Warner P.J. 1987, *Nature*, **328**, 694

Haniff C.A. & Buscher D.F. 1992, *J. Opt. Soc. Am. A*, **9**, 203

Haniff C.A., Ghez A.M., Gorham P.W., Kulkarni S.R., Matthews K. & Neugebauer G. 1992, *Astron. J.*, **103**, 1662

Harrington J.P. 1969, *Astrophys. Letters*, **3**, 165

Hayes D.P. 1980, *Astrophys. J.*, **241**, L165

Hayes D.P. 1981, *Publ. Astr. Soc. Pac.*, **93**, 752

Heske A. 1990, *Astr. Astrophys.*, **229**, 494

Hill S.J. & Willson L.A. 1979, *Astrophys. J.*, **229**, 1029

Hughes S.M.G. 1993, in Nemec J.M. & Matthews J.M. (eds.), Proc. IAU Colloq. 139, *New Perspectives on Stellar Pulsations and Pulsating Variable Stars*, Cambridge University Press

Johnson J.J. & Jones T.J. 1991, *Astron. J.*, **101**, 1735

Joy A.H. 1954, *Astrophys. J. Suppl.*, **1**, 39

Karovska M., Nisenson P. & Noyes R. 1986, *Astrophys. J.*, **308**, 260

Karovska M., Nisenson P. & Noyes R. 1989, *Bull. Am. astr. Soc.*, **19**, 755

Karovska M., Nisenson P. & Papaliolios C. 1991, *Astrophys. J.*, **374**, L51

Karovska M., Nisenson P. & Beletic J. 1993, *Astrophys. J.*, **402**, 311

Kenyon S.J & Gallagher J.S. 1983, *Astron. J.*, **88**, 666

Kholopov P.N. 1987, *General Catalogue of Variable Stars, Fourth Edition*, Nakua Publ. House, Moscow.

Knox K.T. & Thompson B.J. 1974, *Astrophys. J.*, **182**, L133

Knox K.T. 1976, *Astr. Astrophys.*, **6**, 85

Kolmogorov A.N. 1941, *Dan. S.S.S.R.*, **30** (4), 229

Krisciunas K. 1990, *Info. Bull. Var. Stars*, No. 3477

Krisciunas K. 1992, *Info. Bull. Var. Stars*, No. 3728

Krisciunas K. 1994, *Info. Bull. Var. Stars*, No. 4028

Kruszewski A., Gehrels T. & Serkowski K. 1968, *Astron. J.*, **73**, 677

Labeyrie A. 1970, *Astr. Astrophys.*, **6**, 85

Labeyrie A., Koechlin L., Bonneau D., Blazit A. & Foy R. 1977, *Astrophys. J.*, **218**, L75

Le Borgne J.F. & Mauron N. 1989, *Astr. Astrophys.*, **210**, 198

Leroy J.L. 1962, *Ann. d'Astrophys*, **25**, 127

Lockwood G.W. 1971, *Astrophys. J.*, **169**, 63

Lynds C.R., Worden S.P. & Harvey J.W. 1976, *Astrophys. J.*, **207**, 174

Manduca A., Bell R.A. & Gustafsson B. 1977, *Astr. Astrophys.*, **61**, 809

Mattei J.A., 1994, *Personal Communication*

Mauron N. & Querci F. 1990, *Astr. Astrophys. Suppl. Ser.*, **86**, 513

McAlister H.A. & Hartkopf W.I. 1984, *Catalogue of Interferometric Measurements of Binary Stars*, CHARA, Georgia State University, Atlanta

McAlister H.A., Hartkopf W.I., Sowell J.R., Dombrowski E.G. & Franz O.J. 1989, *Astron. J.*, **97**, 510

McLean I.S. 1979, *Mon. Not. R. ast. Soc.*, **186**, 21

Michelson A.A. & Pease F.G. 1921, *Astrophys. J.*, **53**, 249

Mullan D.J. & Bell R.A. 1976, *Astrophys. J.*, **204**, 818

Nakajima T., Kulkarni S.R., Gorham P.W., Ghez A.M., Neugebauer G., Oke J.B., Prince T.A. & Readhead A.C.S. 1989, *Astron. J.*, **97**, 1510

Nightingale N.S. & Buscher D.F. 1991, *Mon. Not. R. ast. Soc.*, **251**, 155

Nightingale N.S. 1991, *Ph.D. Dissertation*, Cambridge University

Nordsieck K. 1994, *Personal Communication*

Perl M. & Tuchman Y. 1990, *Astrophys. J.*, **360**, 554

Planesas P., Kenney J.P.D. & Bachiller R. 1990, *Astrophys. J.*, **364**, L9

Polyakova T.A. 1974, *Astrophys.*, **10**, 36

Polyakova T.A. 1984, *Astrophys.*, **20**, 428

Quirrenbach A., Mozurkewich D., Armstrong J.T., Johnston K.J., Colavita M.M. & Shao M. 1992, *Astr. Astrophys.*, **259**, L19

Quirrenbach A., Mozurkewich D., Armstrong J.T., Buscher D.F. & Hummel C.A. 1993, *Astrophys. J.*, **406**, 215

Readhead A.C.S., Nakajima T., Pearson T.J., Neugebauer G., Oke J.B. & Sargent W.L.W. 1988, *Astron. J.*, **95**, 1278

Ribak E., Hege E.K. & Christou J.C. 1985, *proc. SPIE*, **556**, 196

Ribak E. 1986, *proc. SPIE*, *J. Opt. Soc. Am. A*, **3**, 2069

Richichi A. & Lisi F. 1990, *Astr. Astrophys.*, **230**, 355

Ridgeway S. 1981, in *Physical Processes in Red Giants*, p305, ed. Iben I. & Renzini A., Reidel, Dordrecht

Ridgway S.T., Benson J.A., Dyck H.M., Townsley L.K. & Hermann R.A. 1992, *Astron. J.*, **104**, 2224

Robertson B.S.C. & Feast M.W., 1981, *Mon. Not. R. ast. Soc.*, **196**, 111

Robertson J.G. & Tango W.J. (eds) 1994, *Very High Angular Resolution Imaging.* Proc IAU Symposium 158, Kluwer, Dordrecht

Roddier F. 1981, *Prog. Opt.*, **19**, 281

Roddier C. & Roddier F. 1983, *Astrophys. J.*, **270**, L23

Roddier F. 1987, *J. Opt. Soc. Am. A*, **4**, 1396

Roddier F. 1988, *Physics Reports*, **170**, 97

Rowan-Robinson M. & Harris S. 1983, *Mon. Not. R. ast. Soc.*, **202**, 767

Saar S.H. & Huovelin J. 1993, *Astrophys. J.*, **404**, 739

Scholz M. & Takeda Y. 1987, *Astr. Astrophys.*, **186**, 200

Scholz M. 1994, *Personal Communication*

Schwarz H.E. & Clarke D. 1984, *Astr. Astrophys.*, **132**, 370

Schwarzschild M. 1975, *Astrophys. J.*, **195**, 137

Serkowski K. 1970, *Astrophys. J.*, **160**, 1107

Serkowski K. 1971, *Kitt Peak Obs. Contr.*, **554**, 107

Shawl S.J. 1974, *Publ. Astr. Soc. Pac.*, **86**, 843

Shawl S.J. 1975, *Astron. J.*, **80**, 595

Sivia D.S. 1987, *Ph.D. Dissertation*, Cambridge University

Sloan G.C., Grasdalen G.L. & LeVan P.D. 1993, *Astrophys. J.*, **404**, 328

Smith M.A., Patten B.M. & Goldberg L. 1989, *Astron. J.*, **98**, 2233

Stone R.C. 1989, *Astron. J.*, **97**, 1227

Svatoš J. & Šloc M. 1981, *Astrophys. Space Science*, **77**, 511

Tatarski V.I. 1961, *Wave Propagation in a Turbulent Medium*, Dover, New York

Tuchman Y. 1991, *Astrophys. J.*, **383**, 779

Turon *et al.* 1992, *The Hipparcos Input Catalogue*, ESA Publications, Noordwijk, The Netherlands

Tuthill P.G., Haniff C.A. & Baldwin J.E. 1994, in Robertson J.G. & Tango W.J., eds, *Very High Angular Resolution Imaging.* Proc IAU Symposium 158, Kluwer, Dordrecht, p. 395

Tuthill P.G., Haniff C.A., Baldwin J.E. & Feast M.W. 1994, *Mon. Not. R. ast. Soc.*, **266**, 745

Tuthill P.G. & Haniff C.A. 1994, – *in preparation*

Weigelt G. 1977, *Opt. Comm.*, **21**, 55

Welter G.L. & Worden S.P. 1980, *Astrophys. J.*, **242**, 673

White N.M. 1980, *Astrophys. J.*, **242**, 646

Whitelock P.A. 1986, *Mon. Not. R. ast. Soc.*, **219**, 525

Willson L.A. & Hill S.J. 1979, *Astrophys. J.*, **228**, 854

Willson L.A. 1983, in Cox J.P. & Hansen C.J., eds, *Pulsations in Classical and Cataclysmic Variable Stars.* University of Colorado, Boulder, p. 284

Willstrop R.V. 1993, *Personal Communication*

Wilson W.J. Schwartz P.R., Neugebauer G., Harvey P.M., Becklin E.E. 1972, *Astrophys. J.*, **177**, 523

Wilson R.W., Baldwin J.E., Buscher D.F. & Warner P.J. 1992, *Mon. Not. R. ast. Soc.*, **257**, 369

Wilson R.W. 1992, *Ph.D. Dissertation*, Cambridge University

Wirnitzer B. 1985, *J. Opt. Soc. Am. A* **2**, 14

Wood P.R. 1975, *Mon. Not. R. ast. Soc.*, **171**, 15P

Wood P.R. & Cahn J.H. 1977, *Astrophys. J.*, **211**, 499

Wood P.R. 1979, *Astrophys. J.*, **227**, 220

Wood P.R., 1990a, in Mennessier M.O. & Omont A., eds, *From Miras to Planetary Nebulae: Which Path for Stellar Evolution?* Editions Frontières, Gif-sur-Yvette, p. 67

Wood P.R. 1990b, in Cacciari C. & Clementini G., eds, ASP Conf. Series Vol. 11, *Confrontation between Stellar Pulsation and Evolution.* San Fransisco, p. 355

Wyatt S.P. & Cahn J.H. 1983, *Astrophys. J.*, **275**, 225

Zappala R.R. 1967, *Astrophys. J.*, **148**, L81

Zuckerman B. & Aller L. 1986, *Astrophys. J.*, **301**, 772